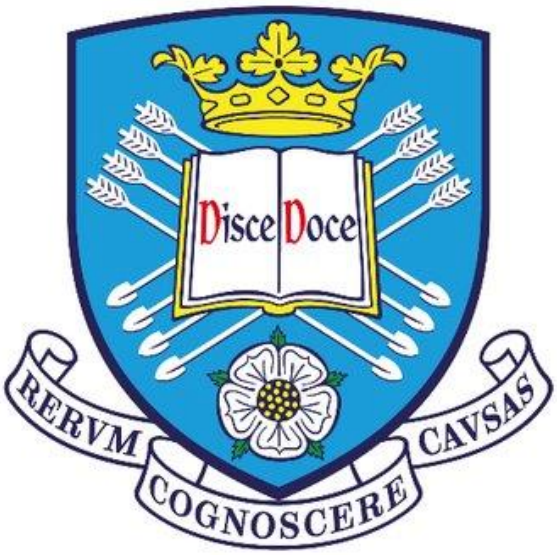

Electromagnetic Design and Advanced Thermal Management of Novel Modular Consequent Pole Permanent Magnet Machines

Rui Zhou

A thesis submitted for the degree of Doctor of Philosophy

Department of Electronic and Electrical Engineering

The University of Sheffield, UK

August 2020

ABSTRACT

This thesis is mainly focused on the investigation of consequent pole permanent magnet machines (CPMs). The main research topics are: 1) investigation of the influence of winding configurations and rotor structures on machine performance, 2) electromagnetic design of the modular CPMs including E-core and C-core stator segments, 3) advanced thermal management using novel forced air and liquid cooling for the modular CPMs.

Firstly, the influences of winding configurations on the electromagnetic performances of fractional-slot (FS-) and integer-slot (IS-) CPMs are investigated. Based on the findings, the CPMs with different rotor structures including the surface-mounted permanent magnet (SPM), the I-shape interior permanent magnet (I-IPM) and the V-shape interior permanent magnet (V-IPM) are further investigated. Furthermore, the modular CPMs with both E-core and C-core stator segments are comprehensively investigated, which have potentially eased manufacture, assembly and transportation processes for large-dimension machines. The operating principle of the investigated modular CPMs are introduced based on mathematical modelling, and the phase back-EMF and electromagnetic torque production mechanisms have been analysed. Moreover, the static and dynamic performances such as on-load losses, torque-speed curves, power-speed curves and efficiency maps have been investigated for modular machines with different slot/pole number combinations.

Finally, to fully take advantages of the flux gaps (FGs), two forced cooling methods including forced air and forced liquid cooling are proposed for the modular CPMs. The FGs in the modular machines are utilized as extra cooling channels to improve the machine cooling efficiency. The effectiveness of both methods has been proven by the numerical results obtained by 3-dimentional computational fluid dynamics (CFD) analyses. Prototype machines including the conventional, E-core and C-core modular CPMs have been built, and the electromagnetic results obtained by finite element analysis (FEA) have been validated by a series of experiments. In addition, some design guidelines and recommendations are provided for machine designers to select the best modular CPMs for different applications having different requirements.

ACKNOWLEDGEMENTS

Upon the completion of this thesis, I owe my heartfelt thanks to my distinguished and cordial supervisor Dr. Guang-Jin Li, who influenced me with his insightful ideas and meaningful inspirations, provided me with excellent academic advice and continuous encouragement. His thought-provoking comments and patiently encouragements are indispensable for my accomplishment of this thesis. My faithful appreciation also goes to the prestigious and distinguished Professor Zi-Qiang Zhu for his instructive advices and upright academic attitude which have been great encouragement for me to finish this thesis and publications from this work.

Ultimately, I would like to express sincere appreciation to my colleagues of the EMD group from the University of Sheffield. Thank you, Dr. Kai Zhang, Dr. Bo Ren, Dr. Xi-Yun Ma, Dr. Yu Wang, Dr. Yan-Xin Li, Dr. Li-Ren Huang, Dr. Shun Cai, Mr. Xi-Meng Wu and Mr. Lei Yang etc. for their valuable suggestions and experimental assistances. I really appreciate the time with all of you at Sheffield.

Last, but not the least, the sincerest thanks go to my parents Mr. Ai-Qun Zhou and Mrs. Yu-Tao Wang, who are always my mentor and guardian through my entire growth. Without their care and provided top educational resources, I could never grow up and study in such a joyous and cosy environment nor have the courage to confront any obstacles on my way to complete my PhD study and this thesis.

CONTENTS

LIST OF ABBREVIATION

2D	2-dimenion
3D	3-dimenion
CFD	Computational fluid dynamics
CP	Consequent pole
CPM	Consequent pole machine
d-axis	Direct axis
DC	Direct current
DL	Double layer
EGW	Ethylene glycol and water
Elec. deg	Electrical degree
EMF	Electromotive force
EV	Electric vehicle
EW	End-winding
FE	Finite element
FEM	Finite element model
FG	Flux gap
FS	Fractional slot
FSCW	Fractional slot concentrated winding
HEV	Hybrid electric vehicle
HTC	Heat transfer coefficient
I-IPM	I-shape interior permanent magnet
IM	Induction machine
IPM	Interior permanent magnet
IS	Integer slot

LMC	Least common multiple
Mech. deg	Mechanical degree
OFC	Open fan-cooled
PM	Permanent magnet
PMa-SynRM	Permanent magnet-assisted synchronous reluctance machine
PMSM	Permanent magnet synchronous machine
q-axis	Quadrature axis
RANS	Reynolds-averaged Navier–Stokes
RE	Rare earth
SL	Single layer
SPM	Surface-mounted permanent magnet
SRM	Switched reluctance machine
SST	Shear stress transport
SynRM	Synchronous reluctance machine
TEFC	Total enclosed fan-cooled
UMF	Unbalanced magnetic force
UNET	Unequal tooth
V-IPM	V-shape interior permanent magnet

NOMENCLATURES

T_{avg}	Average torque	Nm
p	Pole pair number	
φ_m	PM flux linkages	Wb
I_d, I_q	*d*- and *q*-axis currents	A
L_d, L_q	*d*- and *q*-axis inductances	H
N_u	Nusselt number	
h	Heat transfer coefficient	W/m^2·K
L	Characteristic length of the surface	m
λ	Thermal conductivity	W/(m·K)
$N_{u(natural)}$	Dimensionless natural Nusselt number	
a, b	Constants given in the correlation	
G_r	Grashof number	
P_r	Prandtl number	
β	Dimensionless coefficient of the expansion	
g	Gravitational attraction force	m/s^2
ΔT	Temperature difference between surface and fluid	℃
ρ	Density	kg/m^3
μ	Dynamic viscosity	Pa·s
c_p	Specific heat capacity	J/kg
v	Fluid velocity	m/s
$N_{u(forced)}$	Dimensionless Nusselt number	
c	Constant given in the correlation	
α_s	Angular position in the airgap	mech. deg
$\widehat{E_v}$	Magnitude of the v^{th} order back-EMF harmonic	V
k_{wv}	v^{th} order harmonic winding factor	
$\widehat{B_V}$	Magnitude of the v^{th} order flux density	T
N_c	Cogging cycles	
N_s	Stator slot number	
T_{ripple}	Torque ripple	Nm

T_{min}	Minimum torque	Nm
T_{max}	Maximum torque	Nm
P_{Fe}	Iron losses	W
f	Flux density frequency	Hz
B	Amplitude of the flux density	T
k_h, k_e, k_a	Hysteresis loss, eddy current loss and excess or anomalous loss coefficients	
P_{eddy}	PM eddy current losses	W
l_S	Stack length	m
σ	Specific electric conductivity	
v_d, v_q	*d*- and *q*-axis voltages	V
v_{max}	Maximum voltage	V
I_{max}	Maximum current	A
v_{dc}	DC-link voltage	V
ψ_d, ψ_q	*d*- and *q*-axis flux linkages	Wb
T_c	Cogging torque	Nm
L	Length of balance beam	m
$F_{reading}$	Reading from the digital gauge	N
M_{pre_load}	Pre-load weight	kg
ω	Rotation speed	rpm
R	Phase resistance	Ω
P_f	Power factor	
f_{PM}	PM generated MMF	
t	Time	s
Λ_s	Airgap permeance	
N_{s_equiv}	Equivalent stator slot number	
B_{ag_PM}	Airgap flux density due to PMs	T
E_{ph}	Phase back-EMF	V
r_{ag}	Radius of airgap	m
N_{ph}	Phase winding function	
T_{em}	Electromagnetic torque	Nm
i_a, i_b, i_c	Phase current of phases A, B and C	A

e_a, e_b, e_c	Phase back-EMF of phases A, B and C	V
u, v, w	Fluid velocity vector	
P	Fluid pressure	Pa
S_u, S_v, and S_w	Source terms of the momentum equation	
S_T	Volumetric heat source	W/m^3
λ_{slot}	Equivalent slot thermal conductivity	W/(m·K)
S_{slot}	Area of stator slot	m^2
k_f	Stator slot fill factor	

Chapter 1 General Introduction

1.1. General Introduction

With the rapid development of modern society, the world has seen significant increase in the demand for clean and renewable energy in recent decades. However, the majority of industrial equipment are still powered by fossil fuels, especially the combustion engines which are used in the traction systems and thermal power plants where coals or fossil oil are burnt in order to produce electricity. This has raised major concerns about the energy sources, the air pollution caused by fossil fuels and also the unstable supply of fossil fuels which could run out in the next few decades. In order to address these vital issues, growing interest has been paid to clean and renewable energy such as wind power, solar power, etc. As the energy sources are transforming, the aforementioned combustion engines are gradually replaced by more efficient electric traction systems where the key technology is electrical machines and drives. Since electrical machines are the enabling technology in the electrification of transport and also renewable energy, it is pivotal for researchers to keep pushing the boundaries of electrical machines and keep improving their overall performances.

In the process of electrification of transport, electric and hybrid electric vehicles (EV and HEV) are becoming more and more popular. They often adopt induction machines (IM) as traction motors. For example, Tesla roadster, Toyota RAV4 EV, Tesla model S, and so on [1]. This is mainly due to the fact that IMs have the advantages of simple structure, low cost and high robustness. However, the IMs also have the disadvantages such as relatively low efficiency and narrow constant power speed range.

With the increasing demand of high torque/power density, high efficiency and excellent overload capability, permanent magnet (PM) machines have been proven to be better candidates in EV applications. The commonest topologies of PM machines used in existing EV products are the interior permanent magnet (IPM) machines. For example, BMW i3, Nissan Leaf, Toyota Prius, etc all adopt IPM machines for their traction motors [1, 2]. Although the PM machines are good candidates for EV applications, they are suffering from problems such as relatively high costs, complicated manufacturing process and irreversible demagnetization risk caused by high temperature and/or high negative *d*-axis currents during flux weakening operation.

In addition, with the rising concern due to volatile supply of rare-earth (RE) PM materials such as NdFeB, both industry and academia have been seeking for reduced-PM or even PM-free solutions. Amongst the existing solutions, two are the most popular. The first solution is increasing the saliency ratio in the IPMs. This means the reluctance torque can be significantly increased, and for the same torque or power requirements the usage of RE PM materials can be reduced. Typical representatives will be shown in section Chapter 11.2.1.B. Using alternative RE-free materials such as ferrite magnets to replace the RE PM materials is another popular solution. For example, the 2016 Chevrolet Volt has used a 50kW (peak) ferrite-magnet-based IPM machine as the generator. The cost of ferrite magnets is usually much lower compared with RE PM materials. However, the airgap flux densities produced by ferrite magnets are also lower than those produced by the RE PMs, leading to potentially limited torque/power capability.

1.2. Electrical Machines for EV Applications

The most commonly used and feasible electrical machines in EV applications can be classified into three main categories: PM machines, reduced-PM machines and PM-free machines. Their relevant features will be introduced in details in the following sections.

1.2.1. PM Machines

As mentioned above, with the advantages of high torque/power density, high efficiency, PM machines are the most promising candidates for EV applications. In this section, four typical PM machines are reviewed.

A. SPM Machine

The surface-mounted permanent magnet (SPM) machines are the most classic PM machine topologies. An example of a SPM machine is shown in Fig. 1.1. It can be seen that the PMs including north and south poles are alternately mounted on the outer surface of the rotor.

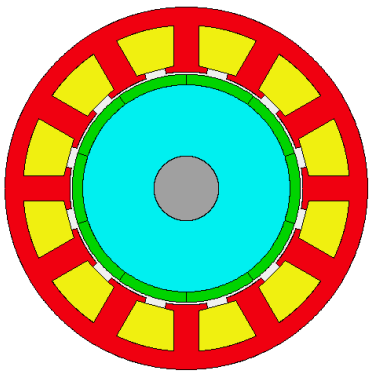

Fig. 1.1. The topology of a typical SPM machine.

The pros and cons of SPM machines can be summarized:

1) Their rotor structure is relatively simple and easy to manufacture.
2) Without significant saliency, the control strategy of SPM machines is relatively simpler compared with IPM machines.
3) The magnet inter-pole flux leakages of SPM machines are usually smaller compared with that of the IPM machines.
4) The PM eddy current losses of SPM machines are usually higher compared with that of IPM machines. This is because that, although the sub-harmonics are the same for both machines with the same stators, the PMs of SPM machines are mounted on the rotor surface and exposed to the harmonic fields more severely compared with the IPM machines.
5) Due to the fact that the PMs are mounted on the rotor outer surface, in high speed applications, rotor sleeves are needed to retain the PMs.
6) The flux-weakening capability of SPM machines is not as good as IPM machines. This disadvantage limits the application of SPM in EV field where a wide constant power speed range is desired. However, this is not an issue for direct-drive wind power application, where flux-weakening capability is not a major concern.

B. IPM Machine

IPM machine is another widely used machine topology, especially in EV applications. In IPM machines, the PMs are buried inside the rotor iron core, leading to the possibility of developing various different IPM rotor structures. The IPM machines with some typical rotor structures are shown in Fig. 1.2. The ‘I-shape’ and double-layer ‘I-shape’ IPM rotors are shown in Fig. 1.2 (a) and (b), while the ‘V-shape’ and double ‘V -shape’ IPM rotors are shown in Fig. 1.2 (c) and (d), respectively.

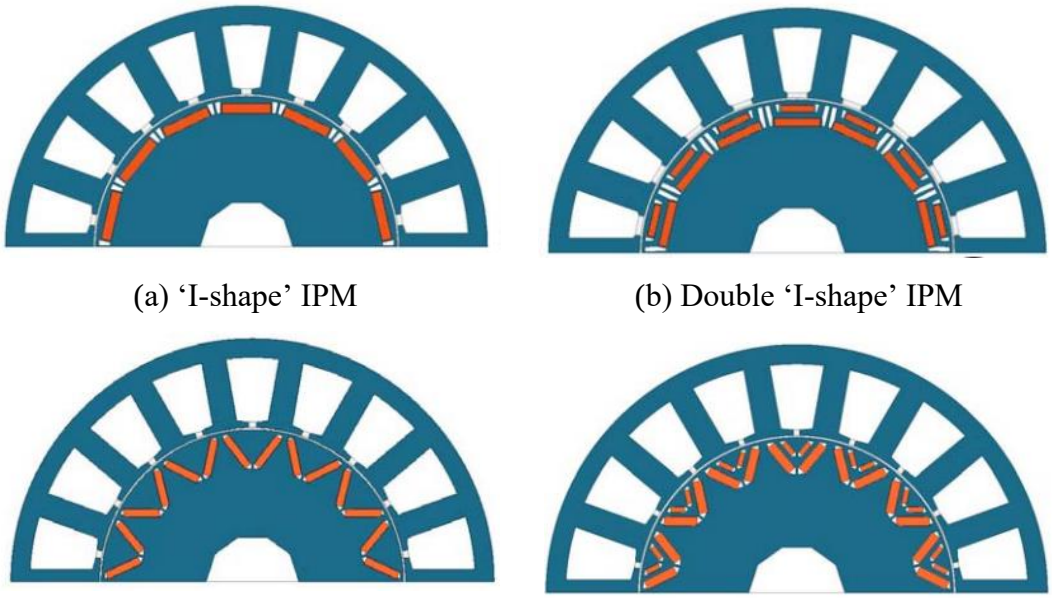

(a) 'I-shape' IPM (b) Double 'I-shape' IPM

(c) 'V-shape' IPM (d) Double 'V-shape' IPM

Fig. 1.2. Typical rotor structures of IPM machines [3].

The average torque (T_{avg}) of the IPM machines can be expressed as:

$$T_{avg} = \frac{3}{2} p\left[\varphi_m I_q + (L_d - L_q) I_d I_q\right] \tag{1.1}$$

where p is the pole pair number, φ_m is the flux linkages due to PMs, I_d and I_q are the *d*- and *q*-axis currents, L_d and L_q are the *d*- and *q*-axis inductances. As the PMs are buried in the rotor iron, the *d*-axis reluctance is often larger compared with *q*-axis reluctance. As a result, L_q is usually larger than L_d. From (1.1), it can be seen that the 2nd term will not be 0 if $L_d \neq L_q$, meaning a reluctance torque component exists in IPM machines. In addition, larger L_q / L_d (saliency ratio) often means higher reluctance torque. This is the major difference between IPM machines and SPM machines.

The pros and cons of IPM machines can be summarized:

1) Due to the existence of reluctance torque, less PM material is often needed for IPM machines to achieve similar torque/power density of the SPM machines.
2) With relatively smaller equivalent air-gap length compared with SPM machines, the *d*-axis inductances of IPM machines are usually larger than those of SPM machines which can lead to better flux-weakening capability and wider constant power speed range [4].

3) Due to the fact that PMs are buried in the rotor iron core, IPM machines usually have a better demagnetization withstand capability and lower PM eddy current losses in comparison with SPM machines. In addition, rotor sleeves are often not necessary in IPM machines for high speed applications.

4) Although the fact that PMs buried in the rotor iron has remarkable advantages, it also has several disadvantages as well. The most significant one is the flux leakages around the magnetic bridges. The iron bridges should be as thin as possible to reduce the flux leakages in order to achieve good torque capability. However, high mechanical stress could be produced with a very thin iron bridge which may cause serious mechanical problems. Therefore, the rotor mechanical stress should be balanced with the electromagnetic performances when designing IPM machines.

Several pictures of different rotor structures used in commercial products from companies such as Toyota, BMW and GM are shown in Fig. 1.3.

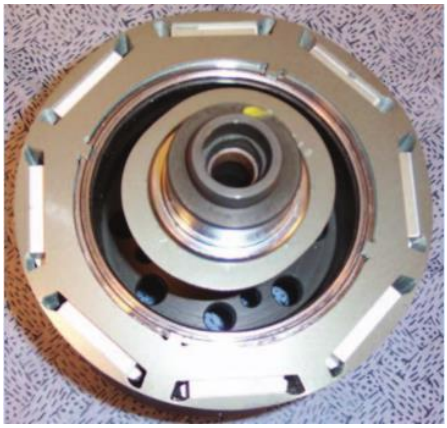

(a) 2003 Toyota Prius

(b) BMW i3

(c) 2010 Toyota Prius

(d) GM Chevy Volt

Fig. 1.3. Photos of the commercial products using IPM rotors [5-8].

1.2.2. Reduced-PM or PM-free Solutions

Although PM machines can achieve high torque/power density and high efficiency, several drawbacks still exist. The main drawbacks are the volatile supply and price of RE PM materials such as NdFeB. This could potentially increase the overall drive system costs [9]. Together with other intrinsic drawbacks such as complicated manufacturing process, potential demagnetization risk of PMs, etc, some other reduced-PM machines or PM-free machines have been attracting attention and their features are briefly reviewed in this section.

A. PM-assisted Synchronous Reluctance Machines

The rotor structure of a PM-assisted synchronous reluctance machine (PMa-SynRM) is similar to that of an IPM machine, as shown in Fig. 1.4, where the PMs are buried in the rotor iron core. The prominent feature of the PMa-SynRM is the multi-layer magnetic barriers in the rotor iron core. By utilizing this structure, the saliency ratio of the rotor can be significantly increased, so does the reluctance torque component.

The main features of PMa-SynRMs can be listed as following:

1) Due to the fact that the reluctance torque is dominant, the PMa-SynRMs could save the usage of PMs in comparison with IPM machines while achieving comparable torque performance [10].
2) As reluctance torque is dominant in the PMa-SynRMs rather than magnet alignment torque, Ferrite magnets could be used in order to replace the RE PMs which have relatively higher price and potential shortage of global supply [11-13].
3) Relatively poor power factor is a major drawback of reluctance machines, thus it requires large reactive power which will increase the size of inverter in the electrical drives.
4) Due to the complex multi-layer magnetic barriers structure in the rotor iron core, the mechanical stress near the iron ribs should be considered when designing the rotor.

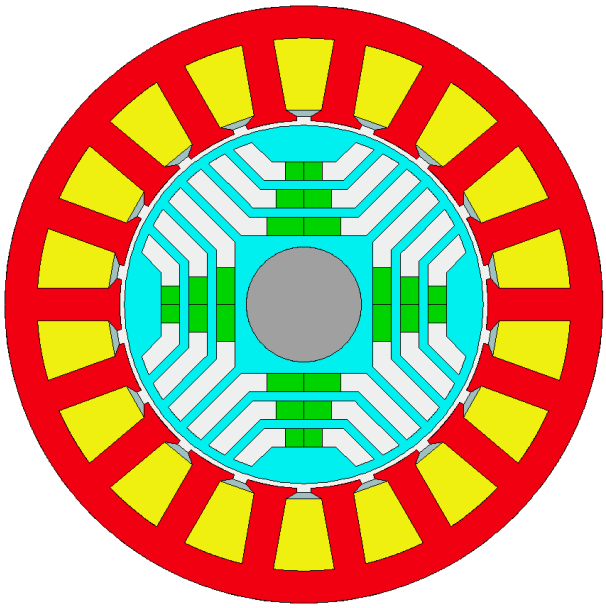

Fig. 1.4. The topology of a PMa-SynRM.

B. Synchronous Reluctance Machines

A classical synchronous reluctance machine (SynRM) is shown in Fig. 1.5. It can be seen that the rotor structure is quite similar to that of the PMa-SynRMs while there are no PMs in rotor iron core. This is a main feature of the SynRMs. Due to such feature, only the reluctance torque produced by saliency effect exists in the SynRMs. Therefore, the key factor to improve the performances of the SynRMs is to increase the saliency of the rotor with multi-layer magnetic barriers together with full-pitched winding structures.

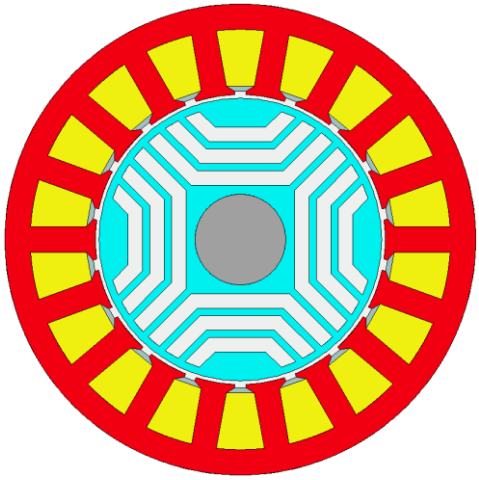

Fig. 1.5. The topology of a SynRM.

The main features of the SynRMs are as follows:

1) Without PMs on the rotor, the material costs could be saved and the assembly process can be simplified.

2) Because the torque is only produced by the saliency of the rotor, the torque density and power density are relatively lower than that of the IPM machines.

3) In addition, since the torque of the SynRM relies only on the *d*- and *q*-axis reluctance difference, the performance of the SynRMs is very sensitive to magnetic saturation which could limit their overload capability [9].

4) Being similar to the PMa-SynRMs, the SynRMs also have relatively poor power factors.

5) Same as the IPM machines and PMa-SynRMs, careful consideration should be paid to the mechanical stress constraints, especially the thin iron bridges near the magnetic barriers.

C. Switched Reluctance Machine

A typical switched reluctance machine (SRM) is shown in Fig. 1.6. It can be seen that the salient rotor structure is quite simple without PMs or field windings. In addition, different from the SynRMs, the SRMs often adopt concentrated non-overlapping windings, leading to much shorter end-windings. Such simple stator and rotor structures are particularly suitable for harsh environment and fault-tolerant operations [14].

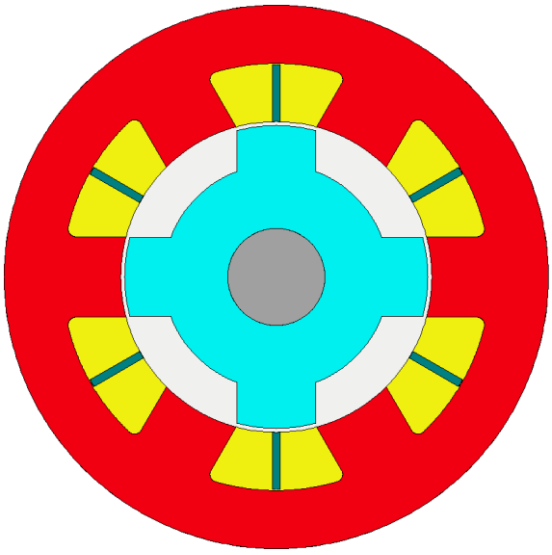

Fig. 1.6. The topology of a SRM.

The features of SRMs can be concluded:

1) Without PMs, the rotors of SRMs are very robust. This makes the manufacturing and assembly process simpler and SRMs suitable candidates in harsh environment and fault-tolerant operations.

2) High iron losses and no PM excitation will result in low efficiency in SRMs compared with that of PM machines [15].

3) Without PM excitation, the SRMs have lower power factors compared with PM machines.

4) High torque ripple and high-acoustic noise are the major problems for SRMs. Thus, noise, vibration and harshness (NVH) performances should be taken into account when designing the SRMs. Proper slot/pole number combinations, stator/rotor pole shaping and current profiling are potential solutions to address these issues [16-18].

D. Induction Machines

The induction machine (IM) is a very well-developed machine technology which has been widely used in various industrial applications. Fig. 1.7 shows a classical induction machine with a copper cage rotor.

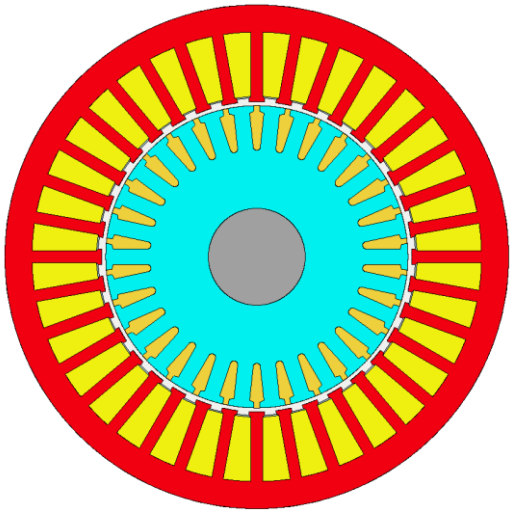

Fig. 1.7. The topology of an IM.

The features of IMs can be concluded:

1) The IMs have no PMs on the rotors which makes them more robust compared with PM machines.

2) The IMs can produce comparable torque in comparison with PM machines and also can have overload power curves not far from that of the IPM machines [19]

3) However, even without PMs on the rotor, copper cages are often used and high copper losses can be produced which has a negative effect on the torque/power density and efficiency [14].
4) With large amount of copper losses on the rotor, the thermal analysis should be considered for the IMs and sufficient cooling should be provided [20].

1.3. Development of the Consequent-pole Machines

1.3.1. Conventional Consequent-pole Machines

As mentioned above, due to the rising concern of the volatile supply of RE PM materials such as NdFeB, both industry and academia have been constantly seeking for reduced-PM or PM-free solutions and a lot of machine topologies have been investigated including the PMa-SynRM, SynRM, SRM and IM. Amongst the solutions, the consequent-pole machines (CPMs) have been deemed as promising candidates.

The CP rotor structure was firstly proposed by Miller in [21]. The rotor of a typical CPM is shown in Fig. 1.8 whilst the stator can be exactly the same as other conventional SPM or IPM machines. In general, in a CPM, for *p* pole pairs only *p* magnets are used. The iron pole between the two adjacent magnets of the same polarity will be reversely magnetized by the magnets themselves, which can be regarded as 'virtual' magnet poles but with opposite polarity to the real magnets [22]. The flux path can be easily understood from Fig. 1.9.

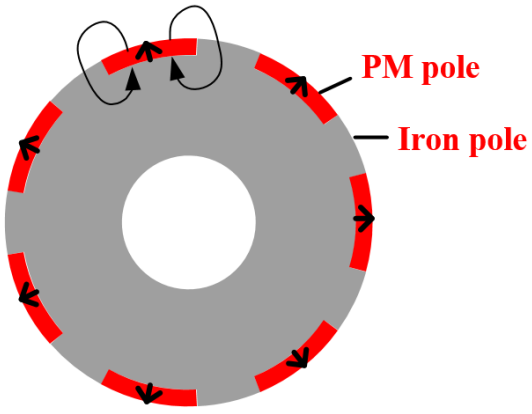

Fig. 1.8. A typical CP rotor [23].

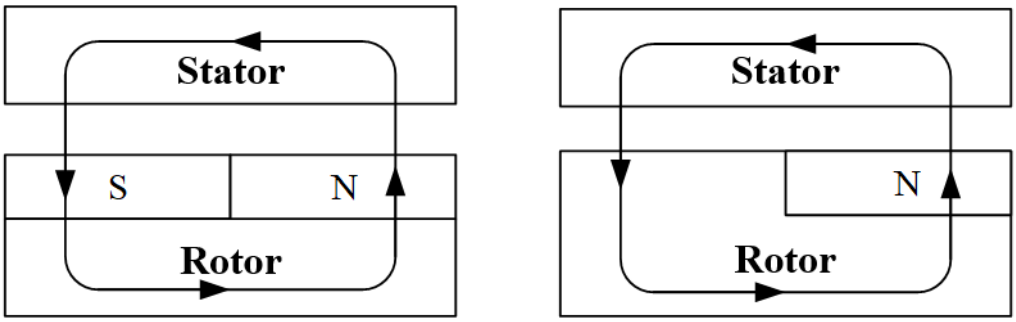

(a) Conventional SPM (b) CPM

Fig. 1.9. Main flux path of the conventional SPM and CPM. (a) Conventional SPM, (b) typical CPM.

Chung *et al* proposed a 48-slot/44-pole fractional slot concentrated winding (FSCW) permanent magnet synchronous machine (PMSM) for a low-speed direct drive in [24, 25]. Two different rotor topologies, a SPM rotor and a CP rotor have been optimized and compared. It is found that by using the CP rotor structure, the machine can acheieve almost the same rated torque and power characteristics while the PM comsumption is reduced by 33%. Although the overload capability of CPM is weaker compared with the SPM due to the fact that CP rotor is more sensitive to the magnetic saturation. The findings prove that the CP rotor topology could be a reduced-PM solution when low cost is desireable. Similarly, Chung *et al* have also validated the feasibility of CP rotor in external-rotor machines and showed their potential for in-wheel direct drive motors used in EVs [26].

In [22], the feasibility of CP rotor in high-speed applications has been investigated. Results showed that the CPM with the Halbach-array magnets used for reducing the iron losses could be an alternative to SPM in high-speed machines. Apart from the classical CP rotor structure, researchers have been investigating other more unconventional CP rotor structures. [27, 28] have investigated the V-shape CP IPM machines used in EV applications. The advantages such as lower PM material consumption, lower cogging torque and wider constant power speed range make them a promising candidate for EV applications. Moreover, a V-shape CP IPM machine shown in Fig. 1.10 has been designed and optimized for refrigeration compressor application [29]. It is found that the proposed V-shape CP-IPM machine can satisfy the targeted load requirement with 33.9% lower usage of PM materials and has therefore great potential for applications such as domestic appliances.

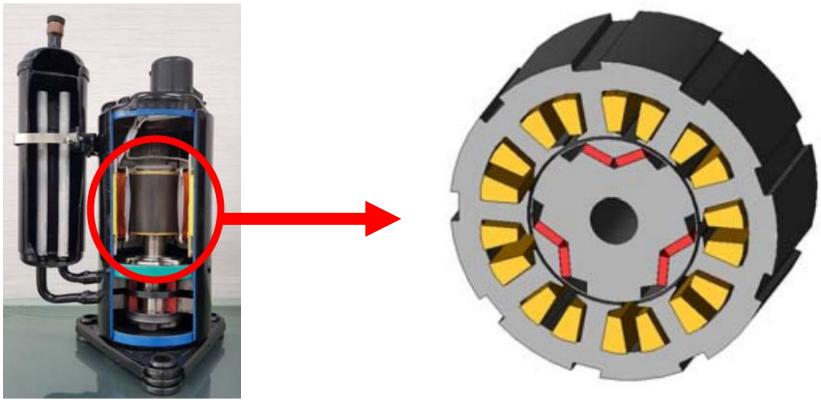

(a) refrigeration compressor (b) proposed V-shape CP IPM machine

Fig. 1.10. Proposed V-shape CP IPM machines used for a refrigeration compressor [29].

1.3.2. Issues in CPMs

Although the CPMs have aforementioned advantages, some intrinsic issues of the CP structure need to be addressed in order to realise their full potential. The main issues and their corresponding solutions will be reviewed in this section.

A. Existence of Even-order Harmonics

For conventional PM machines, because the N-poles and S-poles are symmetrical within the entire machine, normally only odd order harmonics exist in the open-circuit air-gap flux density. However, for the CPMs, even-order harmonics could exist in the air-gap flux density due to the asymmetric rotor structure. This can lead to even order harmonics in phase flux linkages and phase back-EMFs for certain slot/pole number combinations [30]. The even-order open-circuit air-gap flux density harmonics could interact with the armature field and lead to problems such as higher torque ripple, unbalanced magnetic force (UMF), etc. [30].

In order to reduce or to eliminate the even-order harmonics in the back-EMFs, Wang *et al* have proposed two effective solutions: adjusting the winding layouts and modifying the rotor structures. In [30], it is demonstrated that the even-order harmonics in back-EMFs in the CPMs with specific slot/pole number combinations can be suppressed by using the multi-layer windings shown in Fig. 1.11. In [31], Wang *et. al* found that the even-order harmonics in back-EMFs can also be eliminated by modifying the rotor structure as shown in Fig. 1.12. This has the effect of changing the sequences of the magnet polarities. Several other similar rotor structures have also been proposed in [31, 32].

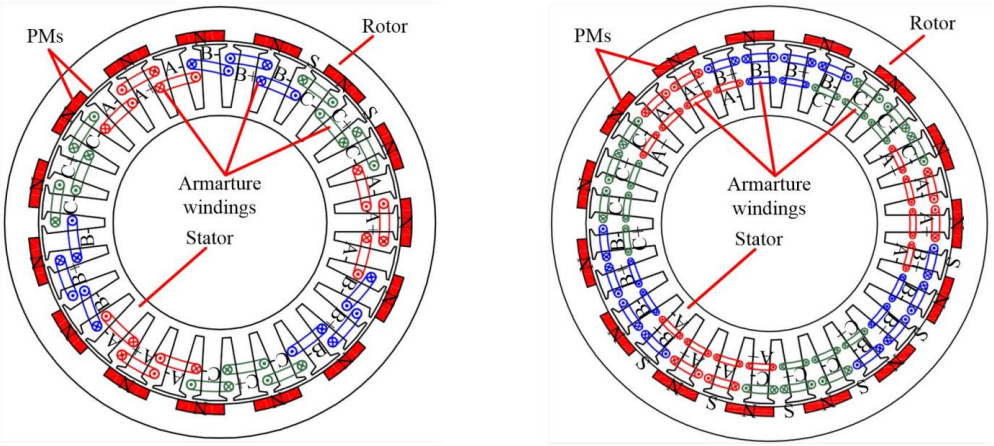

(a) 27-slot/30-pole double-layer CPM (b) 27-slot/30-pole four-layer CPM

Fig. 1.11. Proposed CPMs with muilti-layer windings [30].

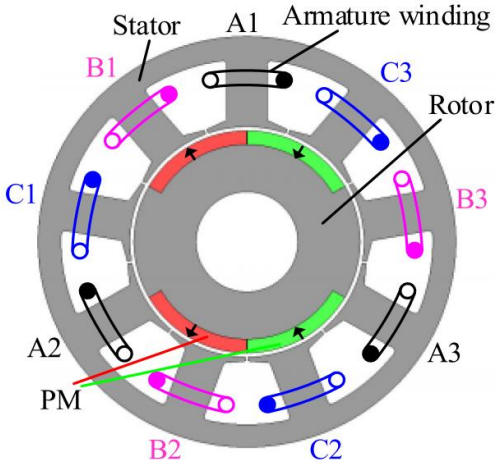

Fig. 1.12. Proposed hybrid rotor for eliminating even-order harmonics [31].

B. Existence of Shaft Unipolar Leakage Flux

Apart from the potential even-order harmonics in the phase back-EMFs caused by the asymmetric rotor structure, the unipolar leakage flux in the end region of the CPMs is another issue which needs to addressed. The mechanical components such as shaft, bearings and bolts could be magnetized by the unipolar leakage flux. This may shorten the lifetime of the components and cause potential system failure [31].

In [31-33], several novel rotor structures have been proposed to mitigate the unipolar leakage flux and two typical structures are shown in Fig. 1.13. Results have shown that the unipolar leakage flux can be transformed into bipolar leakage flux which reduces the magnetization risk of mechanical components by changing the magnet sequence on the rotor.

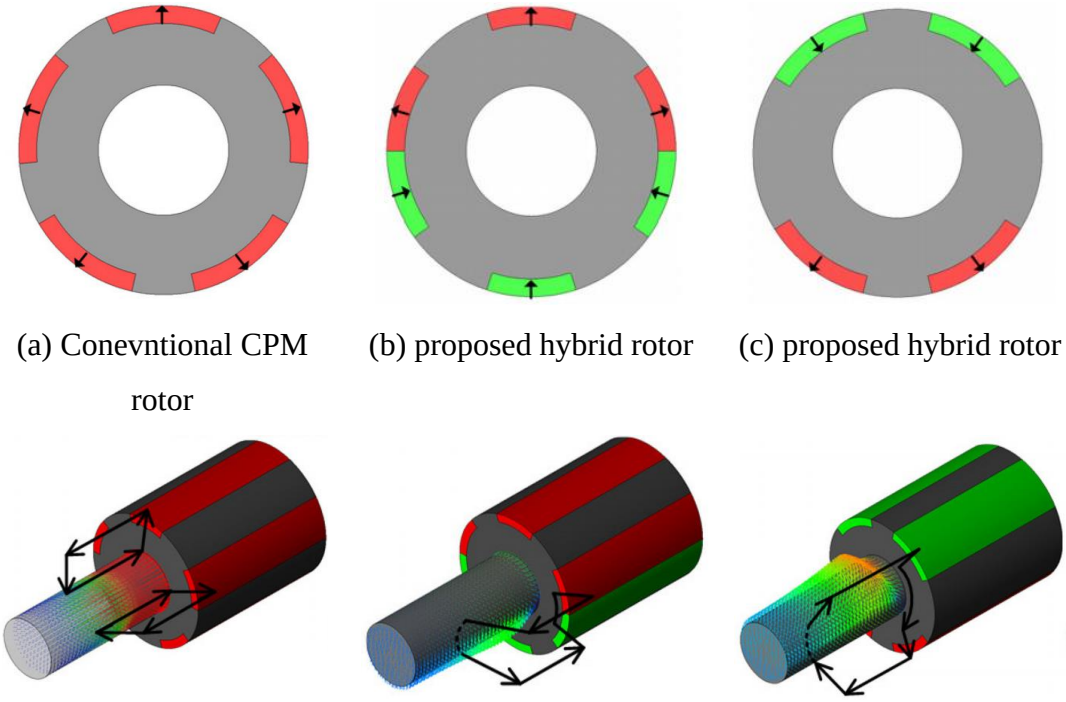

(a) Conevntional CPM rotor (b) proposed hybrid rotor (c) proposed hybrid rotor

(d) corresponding leakage flux path (e) corresponding leakage flux path (f) corresponding leakage flux path

Fig. 1.13. Proposed different rotor strcutures for mitigating unipolar leakage flux and their corresponding leakage flux path [33].

C. High Torque Ripple

High torque ripple is another problem in the CPMs. The even-order harmonics and related sub-harmonics in the air-gap flux densities and phase back-EMFs are the main reasons for high torque ripple in the CPMs. This also means that the torque ripple can be effectively reduced by adopting the methods used to reduce or eliminate the even-order harmonics such as the multi-layer winding configurations and novel rotor structures.

Some other works have been done aiming to improve the electromagnetic performances of CPMs. For example, in [34], a modular consequent-pole rotor is proposed to provide strong flux-focusing effect and the leakage flux near iron bridges can be significantly reduced. Results show that the torque density and PM material utilization can be improved while similar torque ripple and efficiency can be achieved compared with the conventional SPM machines. Moreover, in [35], a CPM with dovetailed CP rotor and quasi-trapezoidal PMs is proposed. By adopting this structure, the non-magnetic sleeve would not be required in high-speed applications. This can significantly reduce the total rotor losses compared with the conventional SPMs which

often have significant sleeve losses. In addition, it is found that due to the removal of rotor sleeve and lower airgap reluctance, the proposed machine structure can have 3% higher average torque with nearly 20% less PM consumption compared with the conventional SPM. Simialr work has also been done in [36-38] including external rotor structure and modular spoke type CP rotor.

1.3.3. Extended CP Concept to other Types of Machines

Apart from the above conventional CPMs, the CP structure has also been adopted in some relatively "unconventional" machine topologies including vernier machines, flux reversal machines and flux switching machines. Their features are briefly reviewed in this section.

A. CP Vernier Machines

[39-49] have investigated the feasibility of CP structure in Vernier machines. A novel Vernier machine with CP rotor structure based on field modulation effect is proposed in [48], as shown in Fig. 1.14 (a). It has proven that the proposed machine is suitable for applications where low speed and high torque are required, such as robotic joints. [49] proposes a novel CP hybrid excited Vernier machine including CP rotor structure, armature winding and dc field winding as can been seen in Fig. 1.14 (b). By combining the hybrid winidng concept and the CP rotor structure, the proposed Vernier can achieve high torque density at low speed and sufficient flux-weakening capability at high speed. These are desirable advantages for EV applications. Some other new concepts which can be used in CP Vernier machines including dual-stator, spoke-type magnets, toroidal winding, etc. are investigated in [39-49].

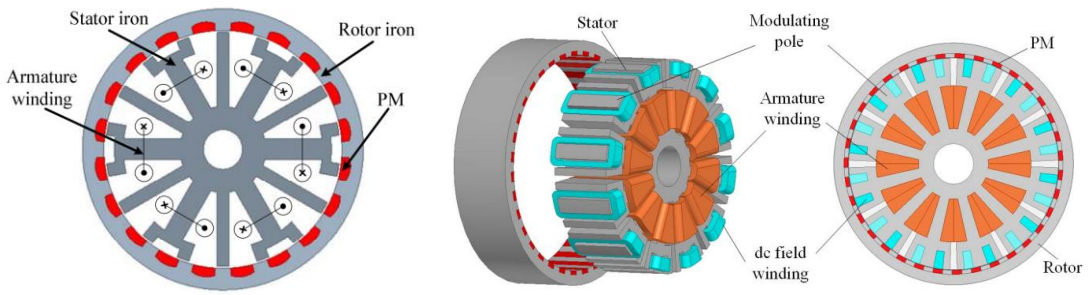

(a) CP Vernier machine (b) CP hybrid excited Vernier machine

Fig. 1.14. CP Vernier machines [48, 49].

B. CP Flux Switching Machines

The CP structure can also be used in flux switching machines. [50] has proposed a novel CP flux switching machine as shown in Fig. 1.15 which can reduce the volume of the PMs while maintaining similar torque density as its conventional counterpart. Moreover, the adoption of two sets of windings improves the flux regulation capability, leading to both high torque capability and wide constant power speed range. A novel CP flux switching machines with flux bridges in stator core is proposed in [51], as shown in Fig. 1.15. The new machine exhibits higher torque capability compared with the conventional flux switching machines due to the reduction of "flux barrier effect". The CP flux switching machines have also been investigated in [52, 53].

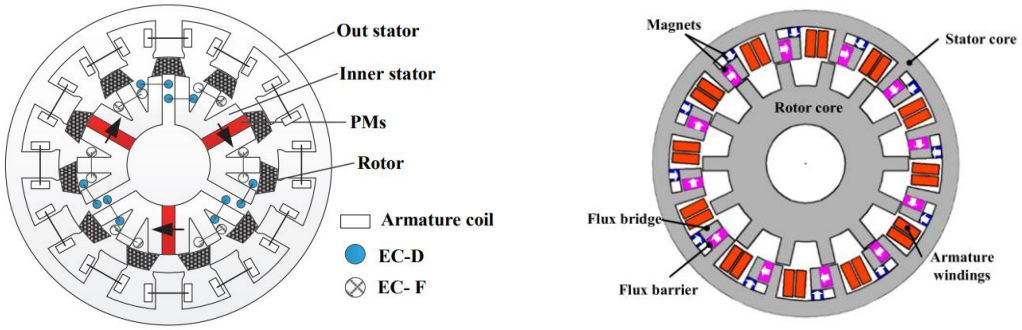

(a) CP flux switching machine, two sets of excitation coils (EC-D&EC-F)

(b) CP flux switching machine with flux bridges

Fig. 1.15. CP flux switching machines [50, 51].

C. CP Flux Reversal Machines

Researchers have also been investigating the feasibility of CP structure in flux reversal machines. A CP flux reversal machines have been proposed in [54] as shown in Fig. 1.16 (a). After optimization, it indicates that the proposed CP flux reversal machines can achieve higher average torque and lower torque ripple with 28% less PM consumption in comparison with a SPM flux reversal machine. Similar as the dual stator CP flux switching machines [50], a 12-stator-pole partitioned stator flux reversal machine having 10-, 11-, 13-, or 14- rotor-pole and a CPM inner stator is proposed in [55], as shown in Fig. 1.16 (b). Their electromagnetic performances are analysed. It is found that the proposed CP flux reversal machines with different rotor pole-pairs are able to generate very much similar torque density (i.e. 98.59%, 96.69%, 95.50%, and 97.15%) compared with the conventional SPM flux reversal machines even with 28.33%, 30%, 30%, and 33.33% less PM consumption, respectively. Meanwhile, the

efficiency of CP flux reversal machines is only 1% lower. Similar works related to the CP flux reversal machines have been reported in [56-59].

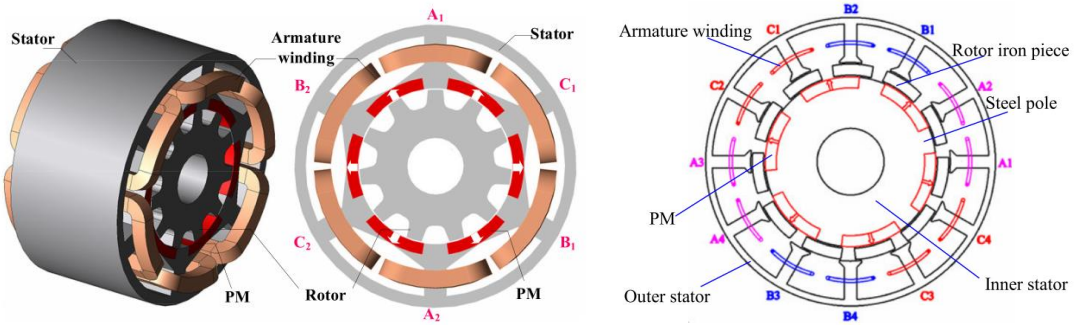

(a) CP flux reversal machine

(b) Partitioned stator CP flux reversal machine

Fig. 1.16. CP flux reversal machines [54, 55].

1.3.4. Summary of CPMs

To conclude, the pros and cons of CP structures can be summarized as follows:

1) The adoption of CP structure can improve the utilization of PM materials without necessarily resulting in a sacrifice in machine electromagnetic performances. This significant advantage makes the CPM a cost-effective solution in various applications, such as EV, wind-power, household appliances, etc.

2) The CP structure is very simple and easy to manufacture and assemble.

3) Rich harmonics caused by the asymmetric rotor structure are beneficial for flux modulation which makes the CP structure a better candidate for Vernier machines used in direct-drive applications.

4) However, the CPMs have some intrinsic issues such as even-order harmonics in the air-gap flux density or phase back-EMFs, high torque ripple and unipolar leakage flux. These issues can be mitigated by modifying the winding configurations and the rotor PM sequences.

1.4. Modular Machines

Apart from the basic electromagnetic performances, for some applications, the manufacturing process of electrical machines should also be taken into account at the design stage. Especially in the wind power generators, modular technology is essential given the dimensions of generators could be very large. By way of example, a 10MW direct drive PM generator used for offshore wind turbines can have an outer diameter

of 13.1m which is quite large [60]. Thus, the manufacturing, transportation and assembly processes are big challenges for larger-scaled machines. The modular technology can be used to solve these issues. Apart from being able to cope with the aforementioned challenges, several other advantages such as simplified winding process, high slot fill factor, good material utilization and possible mass production can also be achieved.

Numerous modular technologies have been proposed for PM machines in the past few decades. Although few solutions of modular rotor have been proposed, most modular technologies focus on the stator structure, which is much easier in comparison with the rotating rotor. According to the stator structures, the modular stator solutions can be classified into 3 categories, i.e. (i) segmented stator with joint-connection, (ii) segmented stator without joint-connection, (iii) segmented stator with flux barriers or flux gaps. Therefore, in the following sections, these three modular stator solutions will be reviewed.

1.4.1. Segmented Stator with Joint-connection

A novel segmented stator with joint-lapped core used in air conditioner compressors has been proposed in [61]. As can be seen in Fig. 1.17, by creating concave and convex joints on the iron core, the modular tooth can be jointed and then rotate with the rotation axis. As each tooth module can rotate freely, a novel flyer winding method can be used as shown in Fig. 1.18. The stator core can be deformed for flyer winding process and then reformed into a conventional circular shape. By doing so, the difficulty during the winding process due to small slot openings can be eliminated and the slot fill factor can be significantly improved. It is reported in [61] that the slot fill factor can be improved up to 75% using the proposed modular stator with joint-lapped core compared with 50% slot fill factor using conventional non-modular core. Although the productivity of this novel stator core can be improved, new manufacturing tools are required for mass production which could lead to higher costs [62]. Moreover, the stator iron losses could be increased because of the large reluctance caused by the joints on the stator modules.

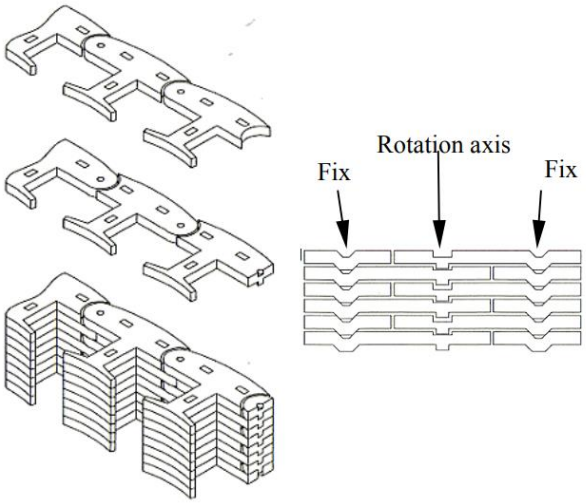

Fig. 1.17. A novel joint-lapped core [61].

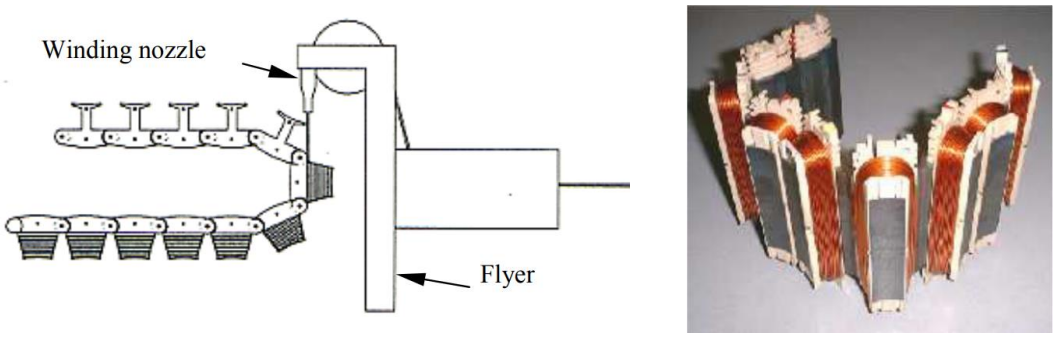

(a) Flyer winding process illustration (b) the joint-lapped core with winding

Fig. 1.18. The joint-lapped core wounded by the flyer winding process.

The influence of the segmented stators with joint-connections have also been investigated in [63]. It is mentioned that the Ω-shape, trapezoid-shape and T-shape are the three main joint-connection shapes, as shown in Fig. 1.19. Here, the Ω-shape joint is the most widely used because it is the easiest to manufacture and to assemble. The stator segments with uniform stator segments or non-uniform stator segments have been proposed as shown in Fig. 1.20 and the influence of the additional stator gaps between the stator segments due to manufacturing tolerance have been analysed. It is found that the presence of these gaps can lead to asymmetric magnetic field which could cause higher cogging torque (both magnitude and period can be increased). Similarly, [64] also investigates the influence of segmented stator on the cogging torques.

(a) Ω-shape (b) Trapezoid-shape (c) T-shape

Fig. 1.19. Different stator segment shapes [63].

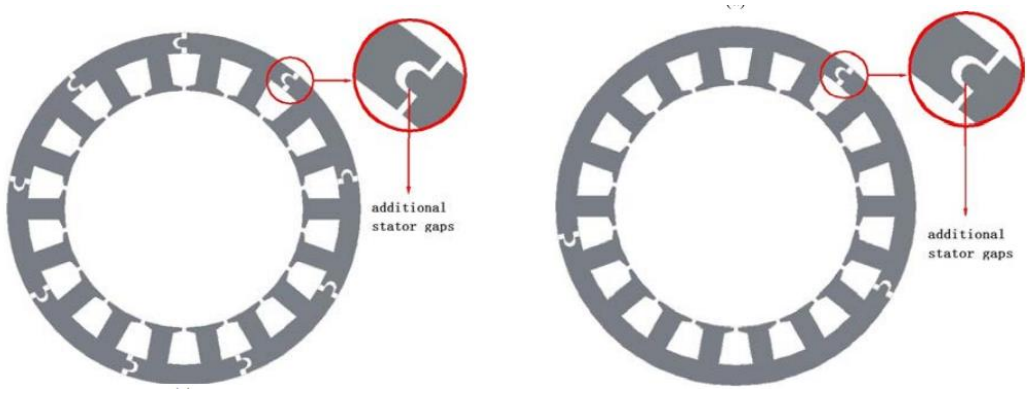

(a) Segmented stators with uniform segments (b) Segmented stators with non-uniform segments

Fig. 1.20. Segmented stators [63].

Baker *et al* in [65] have proposed a PM alternator for aerospace using segmented stators and four power lanes (2 main and 2 safety lanes) are adopted to improve the fault tolerant capability. The segmented stators are interlocked together by the punched notches, as shown in Fig. 1.21 (a). Fig. 1.21 (b) shows the assembled stator segments together with the housing. Results indicate that using the segmented stators can be beneficial for improving the production process, reducing iron losses and removing the magnetic wedges. In the meantime, the vibration and acoustic noise are not significantly deteriorated.

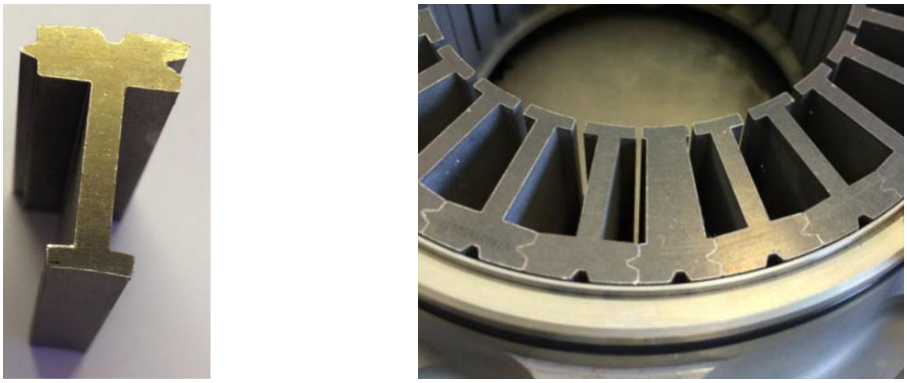

(a) (b)

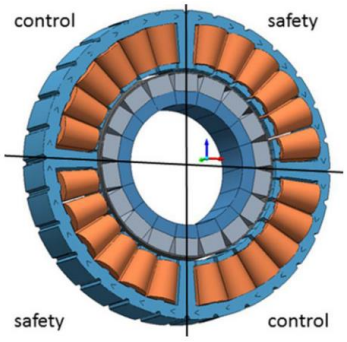

(c)

Fig. 1.21. (a) Single stator segment, (b) assembled stator segments with housing, (c) coil layout [65].

Gerling *et al* in [66] have proposed another type of segmented stators, and the stator segments are joint-connected by the so-called ‘flux-barriers’ in the stator yoke, as shown in Fig. 1.22. It is found that because of the non-magnetic flux barriers in the stator core, reluctance in the stator back iron has been increased. As a result, the sub-harmonics due to armature windings can be reduced and lower rotor losses can be achieved. In the meantime, nearly no influence has been observed on the main flux, leading to unchanged average torque. Machines with this kind of segmented stators have also been investigated in [67, 68]. It is concluded that this modular structure is very promising for EV applications due to higher efficiencies brought by reduced rotor losses.

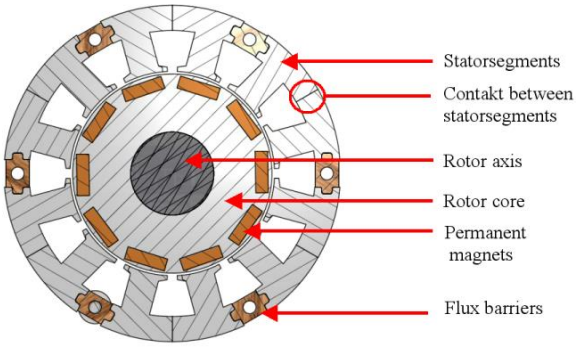

Fig. 1.22. A novel 12-teeth/10-poles PM machine with flux barriers in stator yoke [66].

1.4.2. Segmented Stator without Joint-connection

Another modular stator structure is the segmented stator, where the joint-connection is eliminated. F. Libert *et al* have proposed the segmented stators in [69], as shown in Fig. 1.23. The stator iron can be split into 3 or 6 segments, as shown in Fig. 1.23 (b), (c), respectively. It is claimed that by using this segmentation method, the amount of the wasted iron can be significantly reduced by 30% for 3 segments and by 48% for 6 segments, in comparison with conventional non-segmented stator core. Nevertheless, the segments need to be wielded together in order to form a complete stator iron core which increases the time and manufacture costs for mass production.

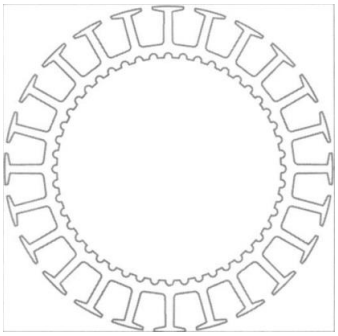

(a) Entire stator

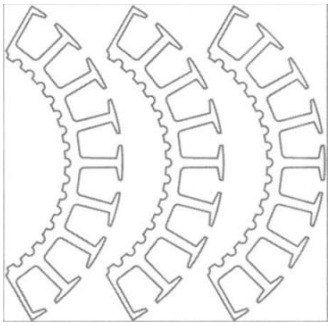

(b) 3 stator segments

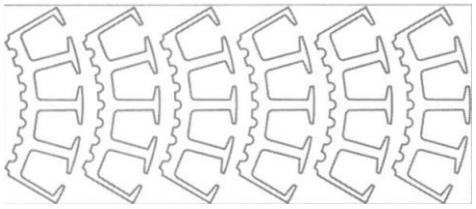

(c) 6 stator segments

Fig. 1.23. (a) Entire stator, (b) 3 stator segments, (c) 6 stator segments [69].

In [70], Heins *et al* have proposed a modular conventional SPM machine with 'U-shape' stator segments, as shown in Fig. 1.24. By removing some parts of the stator yoke, the iron material waste can also be reduced and the manufacture process can be simplified. The authors have developed analytical expressions for the winding factors in machines with such 'U-shape' segmented stators. The electromagnetic performances of the proposed modular machines with different slot/pole number combinations have been investigated. Although it is concluded that such modular structure cannot improve the electromagnetic performances, proper slot/pole number combinations can be selected to reduce the negative impact brought by this modular structure. This makes them attractive for applications requiring for low cost and simple manufacture process. Similarly, 'U-shape' segmented stators have also been used in hybrid-excited doubly salient synchronous machines with stator slot PMs [71], as shown in Fig. 1.25. Again, such segmentation method has the advantages such as simple manufacture, assembly, and transportation processes.

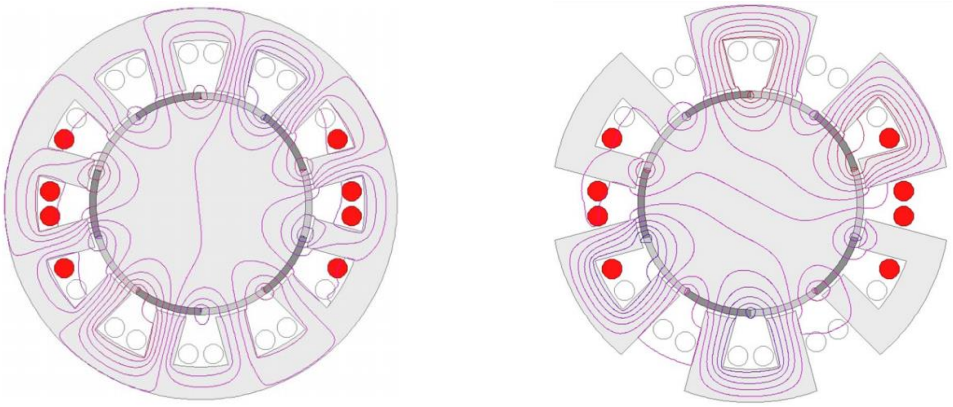

(a) (b)

Fig. 1.24. (a) Conventional SPM, (b) a novel modular SPM with 'U-shape' stator [70].

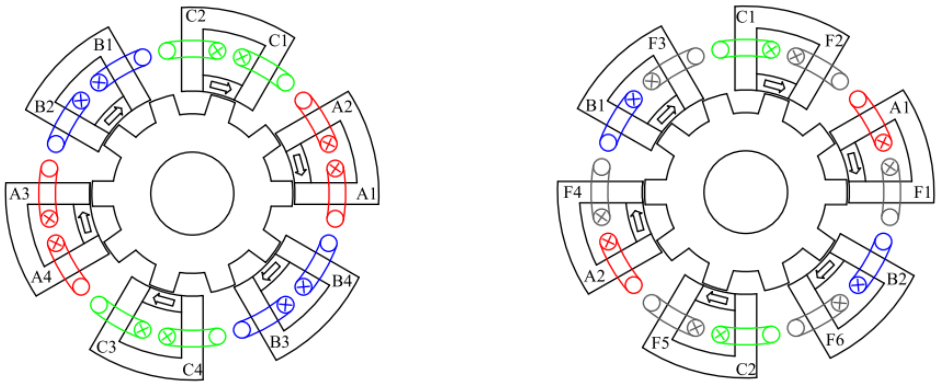

(a) Conventional PM excited (b) Hybrid-excited

Fig. 1.25. Modular machines with slot PMs and 'U-shape' stators [71].

A SRM with segmented stator has been proposed in [72] and the machine topology is shown in Fig. 1.26. Compared with the conventional 12-slot/8-pole SRM, by shortening the flux paths and splitting the common pole tooth into two similar teeth to maximize the total phase flux, the energy conversion capacity of the proposed SRM is significantly improved. It is found that the proposed SRM with segmented stator can exhibit nearly 20% higher average torque. However, complicated manufacture process and increased cost is an evident drawback of such modular SRM. This should be balanced with the improved electromagnetic performances at design stage of such modular SRMs.

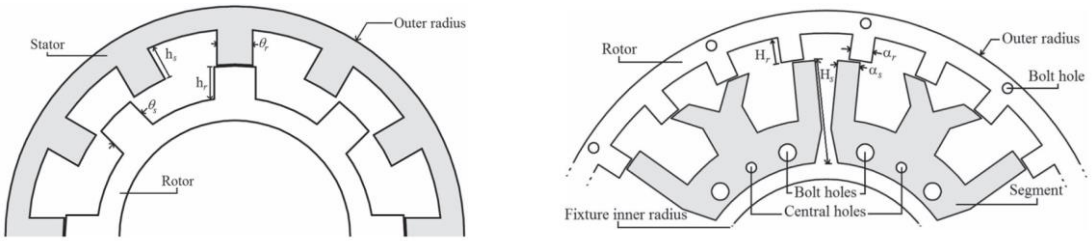

(a) (b)

Fig. 1.26. (a) Conventional 12-slot/8-pole SRM, (b) Novel modular 12-slot/8-pole SRM [72].

Although the segmented stators have various advantages as mentioned above, due to manufacture limits, the additional air gaps between the stator teeth and back-iron segments are inevitable, as shown in Fig. 1.27. Zhu *et al* in [73] have investigated the influence of uniform and non-uniform additional gaps on the cogging torque of PM machines. It is found that the amplitude of cogging torque will be increased due to the existence of uniform additional stator gaps but the periodicity will not be affected. However, the existence non-uniform stator gaps can cause significant increase in both the amplitude and periodicity of the cogging torque. The rotor skewing technology has also be discussed but it is ineffective when the non-uniform additional gaps exist.

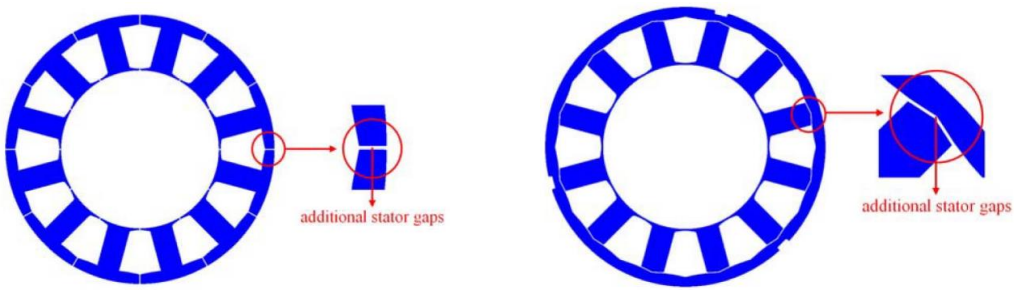

(a) (b)

Fig. 1.27. (a) Additional stator gaps within the back-iron, (b) additional stator gaps between the back-iron and stator tooth body [73].

1.4.3. Segmented Stator with Flux Barriers or Flux Gaps

Spooner *et al* have first proposed some modular PM generators for wind power applications in [74-78], as shown in Fig. 1.28. The stator modules are made of individual laminated E-core segments and each E-core segment can be wounded prior to the assembly of the machine. By using this structure, the manufacture and assembly process of the generators with large dimensions can be eased [74]. It is also pointed out that due to the existence of gaps between stator modules, the active mass of the machine could be slightly reduced which lead to potentially lower cost in comparison with the conventional non-modular counterparts [75]. Moreover, the faulty stator module can be easily repaired or replaced, leading to reduced maintenance cost [75].

Gerling *et al* have proposed several novel modular IPMs in [79]. The modular structures are realized by inserting the so called ‘flux-gaps’ (FGs) between the alternate stator teeth, as shown in Fig. 1.29. This structure is quite similar to the aforementioned segmented stators with the so-called ‘flux-barriers’ in the stator yoke, as shown in Fig. 1.22. Similarly, the sub-harmonics due to armature windings can be reduced and lower rotor losses can be achieved beacuse of the FGs. The results of a 12-slot/14-pole IPM with FGs indicated that the average torque can be increased by about 16% and more than 50% reduction can be aheived in the rotor losses. Very much similar modular structures have also been investigated in [80-83].

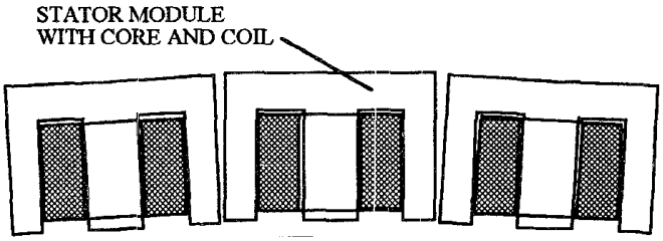

Fig. 1.28. The proposed modular generators with segmented stator [74-78].

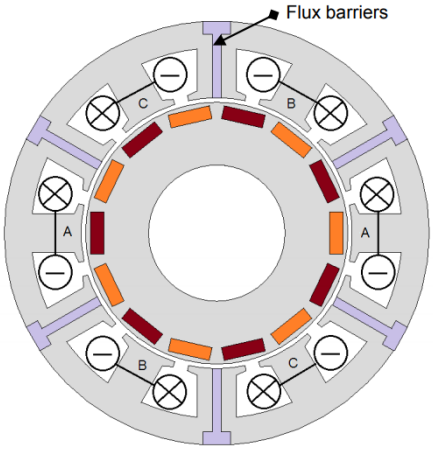

Fig. 1.29. Novel 12-slot/14-pole IPM with flux barriers [79].

Various novel modular SPMs with FGs have been proposed by Li *et al* in [84-89]. In [84], the electromagnetic performances of such kind of modular SPMs with FGs in alternate stator teeth have been comprehensively investigated and the influence of the FGs have been studied. Several general guidelines have been developed for deisgning the modular machines. With regard to the modular machines with FGs in alternate stator teeth, the average torque can be improved by selecting proper FG width if the slot number (N_s) is smaller than the pole number (N_p) such as 12-slot/14-pole. However, the presence of FGs has no positive effect on the torque performance if the slot number (N_s) is higher than the pole number (N_p) such as 12-slot/10-pole, regardless of the FG width. Apart from the average torque, the FGs can also reduce the cogging torque and torque ripple if an approriate FG width is chosen.

Further investigations of similar modular SPMs and unequal teeth (UNET) machines either with or without tooth tips have been done in [85, 86] and the machine topologies are shown in Fig. 1.30. General rules of the influences of FGs have been establsihed and summarized. It is concluded that the overall performance of the modular or UNET machines can be significantly improved with either an approriate FG or UNET width.

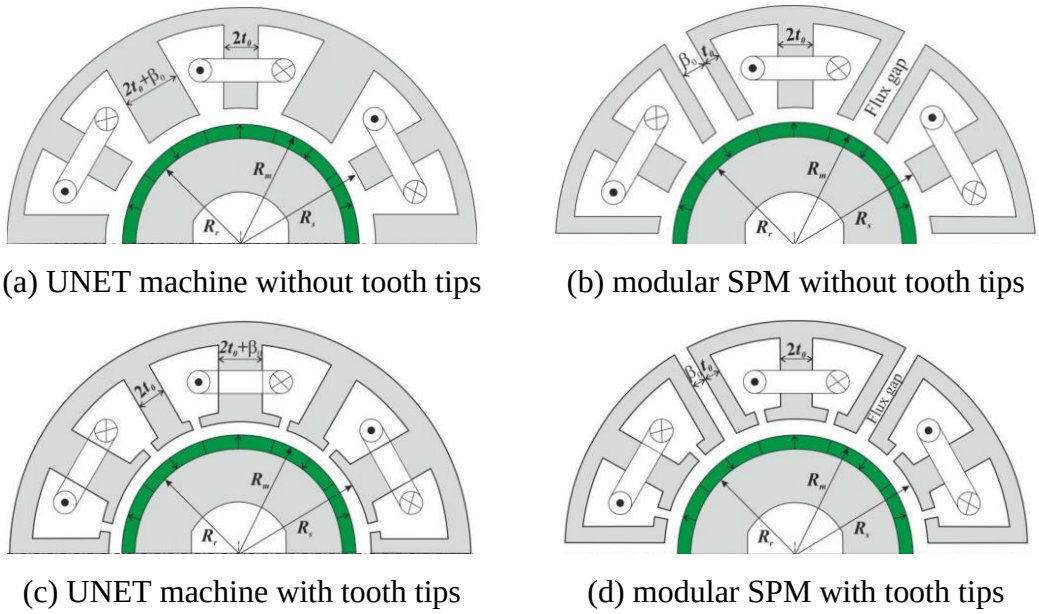

(a) UNET machine without tooth tips (b) modular SPM without tooth tips

(c) UNET machine with tooth tips (d) modular SPM with tooth tips

Fig. 1.30. UNET machines and modular machines either with or without tooth tips [86].

Similarly, the modular PM machines with alternate teeth having tooth tips have been introduced in [89], as shown in Fig. 1.31. General conclusions have been drawn. For machines with $N_s > N_p$, the winding factor is reduced due to the presence of FGs but it can be compensated by having tooth tips on wound teeth which means the average torque can be maintained. However, for machines with $N_s > N_p$, the winding factor can be increased both by FGs and having tooth tips on unwound teeth which means that the average torque can be further increased. In addition, the torque ripples of the investigated machines can be minimized by modifying the FG and also tooth tip widths.

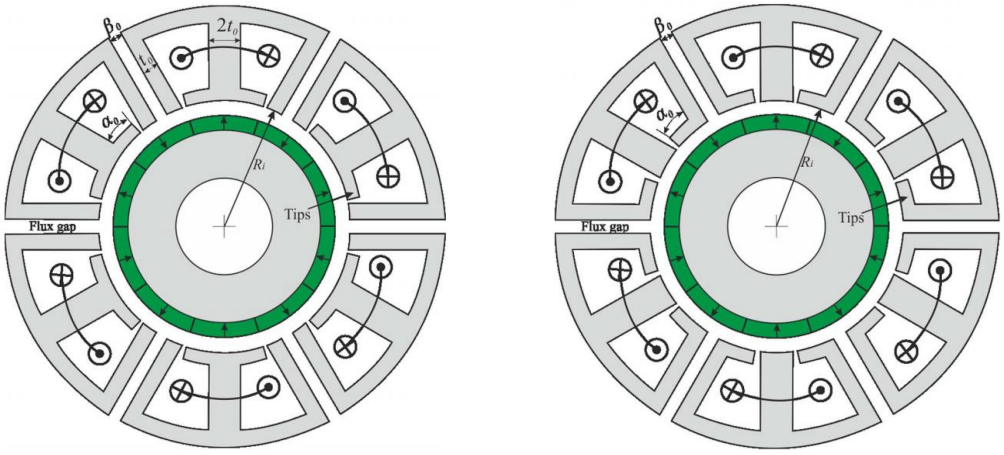

(a) modular SPM with wound teeth having tips (b) modular SPM with unwound teeth having tips

Fig. 1.31. Novel modular SPMs with either wound or unwound teeth having tips [89].

1.5. Thermal Management of Electrical Machines

Although a lot of design methods can be used to reduce the consumption of PM materials and to improve the machine performances, higher power/torque density requirements are often limited by the thermal performances of the PM machines [90]. Thermal management of electrical machines is always a vital factor in machine design. Local high temperatures in the machines may shorten the winding insulation life and demagnetize the PMs [91-93]. In other words, the performances of the electrical machines could be deteriorated due to the influence of high temperatures. Therefore, effective cooling methods are essential for electrical machines in order to reduce the temperature rise. So the cooling is also a major aspect of this PhD research in order to achieve high torque/power density, low cost PM machines. Generally speaking, the most commonly used cooling methods in electrical machines can be broadly classified into 3 categories, i.e. natural cooling, forced air cooling and forced liquid cooling.

1.5.1. Natural Cooling

In a totally enclosed electrical machine without extra cooling equipment, as an example, the heat within the machine is usually transferred by heat conduction and then dissipated to the ambient air from the housing by natural convection and radiation. For the natural convection on the surface of housing, motion of the fluid is caused by the buoyancy forces due to density variations in the fluid. The heat transfer coefficient (HTC) is used to represent the rate of convective heat dissipation. In [94], the typical form of the convection correlation has been developed and the natural Nusselt number is dependent on the Grashof number and Prandtl number as shown in (1.2) and (1.3).

$$N_u = \frac{h \cdot L}{\lambda} \tag{1.2}$$

$$N_{u(natural)} = a \cdot (G_r \cdot P_r)^b \tag{1.3}$$

$$G_r = \frac{\beta g \Delta T \rho^2 L^3}{\mu^2} \tag{1.4}$$

$$P_r = \frac{c_p \cdot \mu}{\lambda} \tag{1.5}$$

where

N_u	Nusselt number	h	Heat transfer coefficient [W/m^2·K]
L	Characteristic length of the surface (m)	λ	Thermal conductivity [W/(m·K)]
$N_{u(natural)}$	Dimensionless natural Nusselt number	a, b	Constants given in the correlation
G_r	Grashof number	P_r	Prandtl number
β	Dimensionless coefficient of the expansion	g	Gravitational attraction force (m/s^2)
ΔT	Temperature difference between surface and fluid	ρ	Density (kg/m^3)
μ	Dynamic viscosity (Pa·s)	c_p	Specific heat capacity (J/kg)

Since the housing surface is the main surface for the heat dissipation, improving the HTC on the housing surface can be an effective solution for temperature reduction. The most commonly used method is adding the cooling fins on the housing. To this end, two types of cooling fins have been proposed, i.e. axial longitudinal fins and radial fins, as shown in Fig. 1.32 [95].

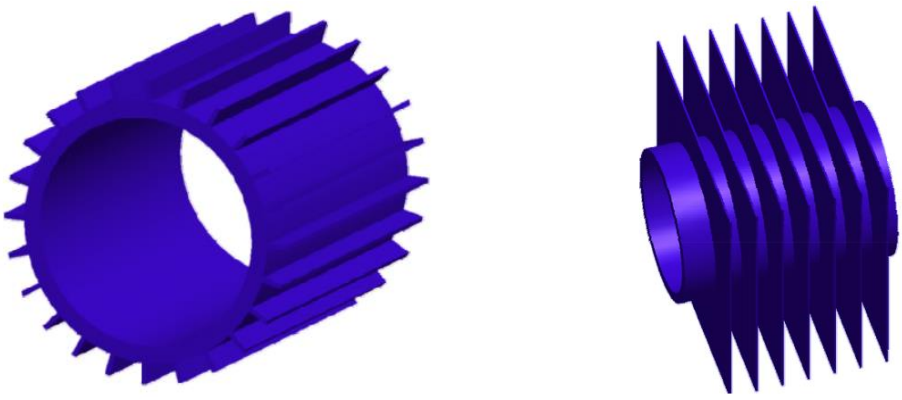

(a) Axial longitudinal fins (b) radial fins

Fig. 1.32. Axial longitudinal fins and radial fins on the housing [95].

With the existence of cooling fins, the contact surface between the housing and ambient environment is significantly increased and the thermal convection is improved. Lots of works have been done and some analytical models have been proposed related

to optimizing the fins such as the thickness, extension, pitch and the number of fins to achieve the highest HTC and best cooling effect [95-98]. Although using the cooling fins can improve the overall cooling effect, the HTC of natural cooling method is very much limited, roughly between 5-30 W/(m·K). This is still much lower than the forced cooling methods, for example, 20-300 W/(m·K) for forced air cooling and 100-25000 W/(m·K) for forced liquid cooling [99]. Thus, the natural cooling method is only suitable for low/medium power machines or machines with enough outer surface for heat dissipation.

1.5.2. Forced Air Cooling

In order to achieve higher heat dissipation rate, forced air cooling methods have been widely used in the medium/high power electrical machines including EV and wind power applications. Similar to the correlation of natural cooling, the typical form of forced convection correlation has been developed and the Nusselt number is treated as a function of Re and Pr [94]:

$$R_e = \frac{\rho v L}{\mu} \tag{1.6}$$

$$N_{u(forced)} = a \cdot (R_e)^b (Pr)^c \tag{1.7}$$

where v is fluid velocity (m/s), $N_{u(forced)}$ is dimensionless Nusselt number and c a constant given in the correlation.

Generally speaking, machines with the forced air cooling can be categorized into the totally-enclosed fan cooled (TEFC) machine and the open fan cooled (OFC) machine [99]. The feature of a TEFC machine is that the inner air is totally enclosed within the machine and will not have the heat exchange with the external ambient air. This kind of machines usually have an internal fan and an external fan or blower which can be seen in Fig. 1.33 (a) and (c). The internal fan is used to accelerate the circulation of internal air which can improve the heat transfer to the housing or frame [100]. Meanwhile, the external fan can boost the air velocity surrounding the housing and increase the heat dissipation rate to the ambient air. Similar to the natural cooling, fins are usually added on the housing outer surface which can significantly increase the contact surface between the housing and ambient environment, leading to better cooling effect.

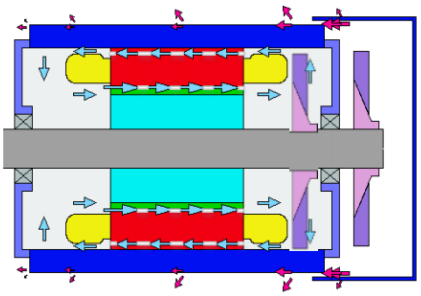

(a) TEFC machine

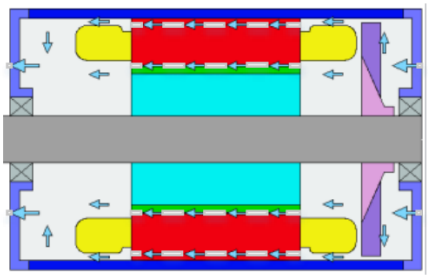

(b) OFC machine

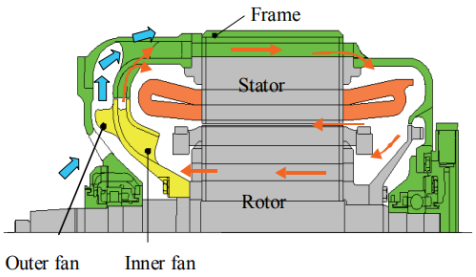

(c) inner structure of a TEFC machine

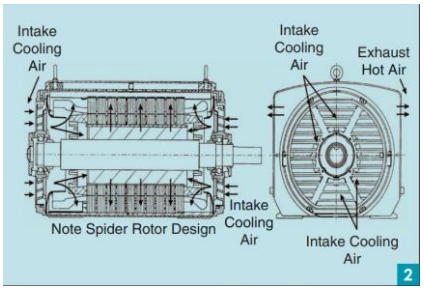

(d) inner structure of a OFC machine

Fig. 1.33. Typical structures of the TEFC and OFC machines [99, 101, 102].

Since in the TEFC machine the internal parts are separated from the ambient air, the external pollutants or contaminants are prevented from entering the machine. This ensures that the air-gap and ventilation ducts are not blocked preventing potential machine electromagnetic performance deterioration due to declined cooling performance. The disadvantage is also evident, extra fans, blower or heat exchanger equipment are needed which could increase the system weight and manufacturing cost.

This might also be a problem for the OFC machine, the air in which is continuously drawn from the ambient air by a shaft-mounted fan or a blower via the inlets into the machine and discharged from the outlets, as shown in Fig. 1.33 (b) and (d). By using this structure, the heat exchange between the machine and ambient air can be significantly increased and good cooling effect can be achieved. A main drawback of this configuration is that the particles or contaminants could be attracted into the machine [101]. Therefore, a hood is usually used to filter the air coolant but in fact the pollutants cannot be totally filtered. Thus, the OFC machines normally need a clean-up process every two or three years [101], leading to increased operation and maintenance costs.

1.5.3. Forced Liquid Cooling

The forced liquid cooling is suitable for high torque/power density applications where forced air cooling cannot provide sufficient cooling. Due to the relatively high heat capacity of liquid such as water, mixed ethylene glycol and water (EGW) 50/50, and engine oil, liquid cooling is able to remove the massive heat generated within the machines [99].

A. Water Jacket Cooling

The most commonly used forced liquid cooling method in industry is the water jacket. With the steady flow of water in the channels within the water jacket, the heat produced in the machine can be dissipated via the convection of the fluid (water). Fig. 1.34 shows some typical water jackets with circumferential, axial and spiral channels. When designing the water jacket, parameters such as number of inlets, channel width and height, axial channel numbers, etc. should be taken in to account in order to achieve the highest HTC for best cooling effect and reasonable pressure drop between the inlet and outlet. Due to the excellent cooling effect and reasonable cost, the housing water jacket is widely used in EV applications. For example, the water jacket with 3 separate channels used in 2013 Nissan Leaf is shown in Fig. 1.35.

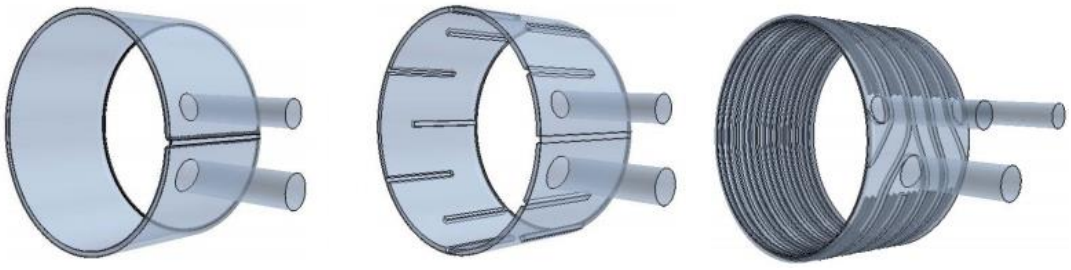

(a) Circumferential (b) axial (c) spiral

Fig. 1.34. Different types of water jackets, (a) circumferential, (b) axial, (c) spiral [103].

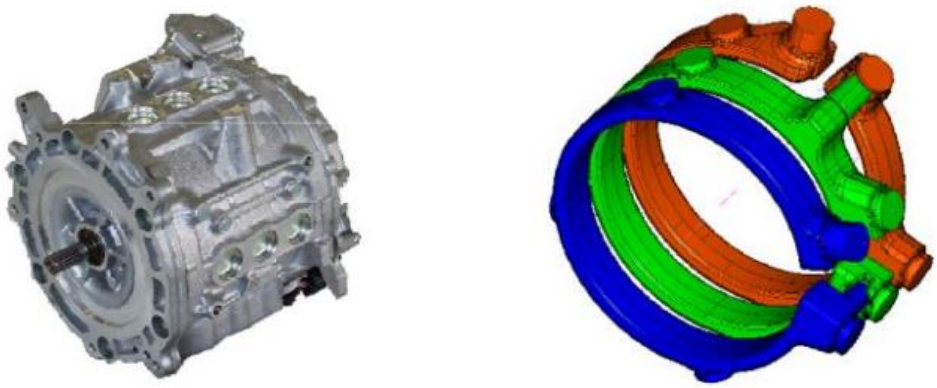

(a) Nissan Leaf electrical machine (b) water jacket used for Nissan Leaf

Fig. 1.35. Electrical machine used in Nissan Leaf and its water jacket [104].

B. Slot Heat Pipe

The windings are usually the hot spots within the machines, therefore, sufficient cooling for the coils is needed. In [105], a novel direct cooling method for the coils are proposed. The rectangular flat wires are used to increase the slot fill factor instead of the round wires which are commonly used in the conventional machines. The unusable triangular free spaces between two adjacent coils in the same stator slot can be used for cooling pipes, as shown in Fig. 1.36. By using this structure, the coils can get direct cooling and the commonly used water jacket is no longer needed. This can lead to lower manufacturing cost and a more compact machine design. Simulation results indicate that this design can provide outstanding cooling effect. However, the major drawback is the high eddy current loss inside the rectangular winding at high fundamental frequencies (high speeds) which should be considered as a compromise. Similar cooling structure or concept have also been investigated in [106, 107]. Generally speaking, the coils can get excellent direct cooling when the slot cooling pipes are adopted and high power density can be achieved. However, a few points should be paid attention to, such as good insulation between the coils and the cooling pipes, good sealing of the slot cooling pipes in case of coolant leakage, decent mechanical support for the slot pipes, etc.

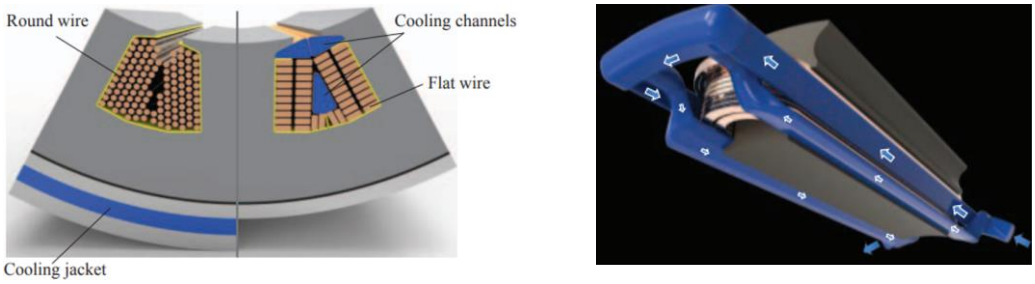

(a) (b)

Fig. 1.36. (a) Flat wires with slot cooling channels compared with round wire with the water jacket, (b) flow path of the slot pipe [105].

C. Oil Spray

The aforementioned slot heat pipes are mainly designed for cooling the active windings and only limited to the cases where there is enough available space in the stator slots. In terms of the direct cooling of the end-windings, the spray cooling method is another effective way of reducing the overall winding temperatures. Some typical examples of the oil spray cooling methods are shown in Fig. 1.37 [108]. In Fig. 1.37 (a) the oil is injected by each single nozzle on top of each corresponding group of end-windings while the oil is injected through a hollow shaft in Fig. 1.37 (b). the cooling effectiveness of these two arrangements has been investigated and validated experimentally using the setup shown in Fig. 1.38 [108]. It is found that the current density and output power of the investigated machine can almost be doubled by replacing the water jacket with the proposed oil spray cooling method.

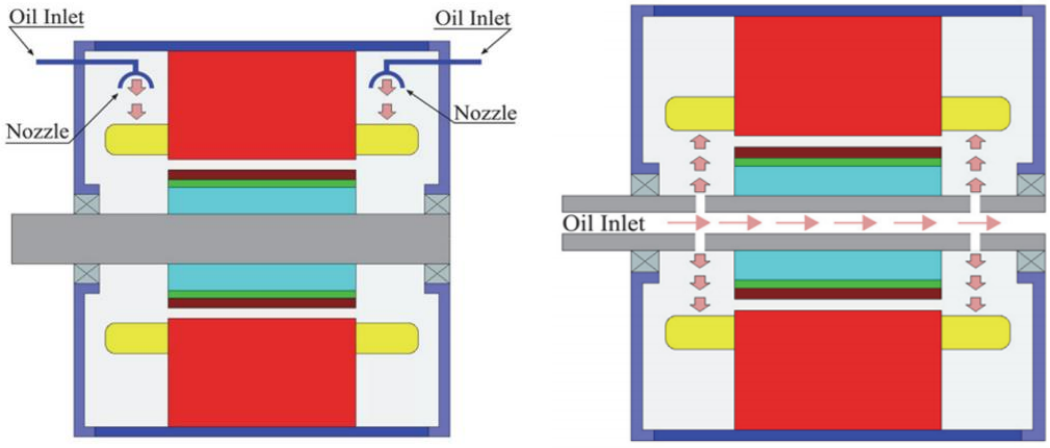

(a) Oil injected by nozzles above the end-windings (b) oil injected via a hollow shaft

Fig. 1.37. Two typical arrangements of oil spray cooling methods [108].

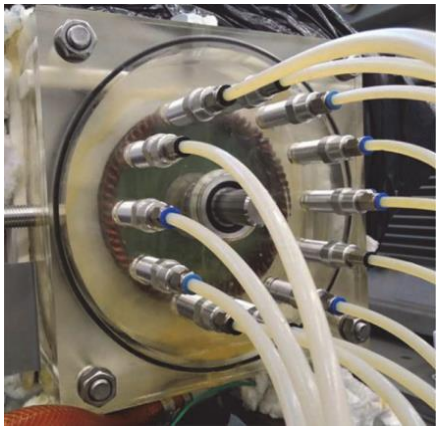

(a) Experimental setup with 12 nozzles for oil spray

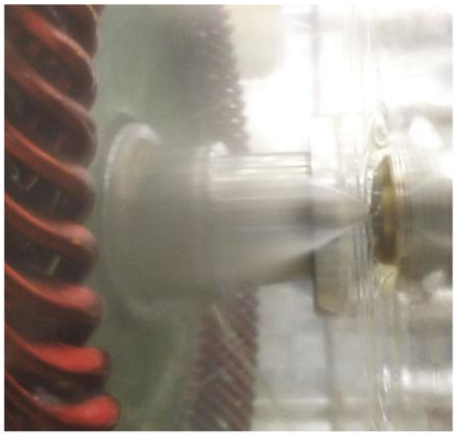

(b) close-up view of a nozzle

Fig. 1.38. (a) Experimental setup with 12 nozzles for oil spray, (b) close-up view of a nozzle [108].

D. Hollow Shaft

For most inner rotor machines, due to the existence of the airgap, it is difficult for the heat generated on the rotor to be dissipated. Poor heat transfer of the rotor could lead to high rotor temperture which could demagnitize the PMs and deterioriate the electrcomagnetic performances. In order to improve the rotor heat transfer, Gai *et al* have proposed a shaft-cooling solution in [109-112]. The structure is shown in Fig. 1.39 and it can be seen that the shaft is manufactured as a hollow cylinder with inlet and outlet for the coolant circulation. Simulation and experimental results have proven the effectiveness of this cooling method. It is found that the rotational speed of the shaft can enhance the HTC of the shaft and the temperature of the rotor can be significantly reduced. The major constraint of this method is the complex mechanical design of the shaft, for example, the sealing the rotating shaft in order to prevent the oil leakages, the mechanical strength of the hollow shaft at high speeds, etc [106]. This needs to be properly addressed in order to realise the full potential of such cooling technology.

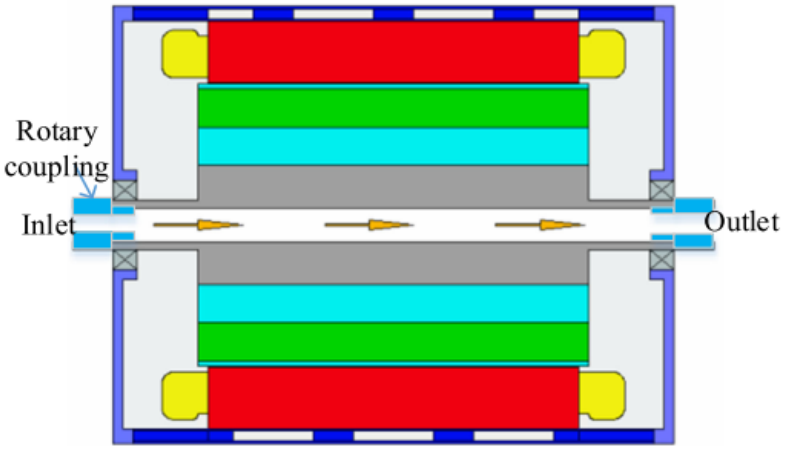

Fig. 1.39. Concept of the rotor cooling using a hollow shaft [109].

1.6. Research Scope and Contributions

In this chapter, different electrical machines are reviewed with a particular focus on the CPM machines, which have been recognized as a cost-effective solution for various applications. In addition, the modular stator technologies adopted in electrical machines are introduced considering their intrinstic advantages attributed from eased manufacturing process and improved electromagnetic performances. Finally, since thermal management is a vital factor for designing high torque/power density electrical machines, the commonly used cooling methods have also been reviewed.

However, so far, the influences of winding configurations and rotor structures of CPM machines have not been investigated in the literature. Moreover, the electromagnetic potential of modular structures have not been exploited in the CPMs and no research has been done with regard to their thermal management. To fill in this knowledge gap, this thesis will focus on these aspects. More details about the the research scope and contirbution of this thesis can be seen in the following sections.

1.6.1. Research Scope

The CPMs are investigated in this thesis, which is mainly focused on two aspects, as shown in Fig. 1.40. The first aspect is the electromagntic performances of CPMs which covers the chapters 2 and 3 while the second aspect is the thermal managements of PM machines which covers the chpater 4, including two forced cooling methods. This thesis contains 5 chapters which are oragnized as follows:

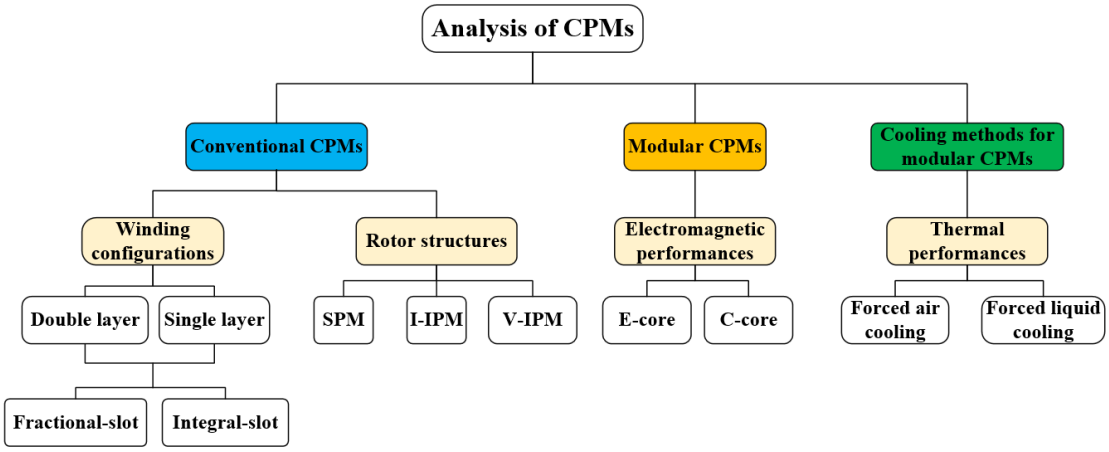

Fig. 1.40. Main research topics of this thesis.

- Chapter 1 provides a general and overview of PM machines widely used in EV and wind power applications. It is followed by the literature review of different types of CPMs which have become increasingly popular in recent decades due to the advantage such as better utilization of PM materials. Apart from the review of electromagnetic performances, exsiting cooling methods are also briefly reviewed. This is because the thermal management is another vital aspect for designing high performance electrical machines. Finally, the research scope and contributions are given.

- Chapter 2 covers two topics. In the first section, electromagnetic performances of CPMs with different winding configurations, i.e. fractional-slot (FS) and integer-slot (IS) CPMs have been investigated. Their open-circuit characteristics such as cogging torque, EMF, etc. and on-load characteristics such as on-load torques, losses and the dynamic performances are evaluated and compared thoroughly. The second section of this chapter focuses on the influence of rotor structures on the electromagnetic performances of the CPMs, especially CPMs with I-IPM or V-IPM rotor structures and FS or IS windings. Again, all open-circuit and on-load performaces are evaluated. Furthermore, the demagnetization withstand capabilities considering thermal influence have also been investigated to provide some useful insight into the performances under fault conditions. Finally, some recommendations related with selection of winding configuration and rotor structure are given in order to achieve optimal

performance. One prototype machine has also been manufactured to validate the predictions.

- ❖ Chapter 3 further investigates the CPMs with modular stators. Both the E-core and C-core modular structures are investigated including the static and dynamic performances such as on-load losses, torque-speed curves, power factor-speed curves and efficiency maps. Different slot/pole number combinations are also covered. The full benefits of modular structures are revealed. Finally, some guidelines and recommendations under different criteria are given in the conclusion for selecting the best candidates from modular CPMs with different stator structures. Two prototype machines have also been manufactured to validate the predictions.

- ❖ Chapter 4 proposes two novel forced cooling methods utilizing the flux gaps (FGs) for the E-core modular CPM with FGs inserted into alternate stator tooth bodies which is investigated in chapter 3. The two cooling methods are forced air cooling with inlets on the endcaps and forced oil cooling with submerged stator. With both methods, the FGs are utilized as cooling channels to improve the internal cooling in such modular machines. Computional fluid dynamics (CFD) have been performed and the effectiveness of utilizing the FGs as cooling channels is proven. Moreover, the influence of FG width, inlet position and inlet dimension are also investigated. At last, some design guidelines of such modular machines for best cooling effect and lowest pressure drop (or highest cooling system efficiency) are provided.

- ❖ Chapter 5 gives a general conclusion based on the investigations carried out in this thesis and some meaningful future works have been proposed.

1.6.2. Contributions

The major novely and contributions of this thesis are summarized as follows:

- Recommendations about the selections of winding configuration and rotor structure for CPMs to achieve good electromagnetic performances are given.

- The modular CPMs with E-core and C-core are proposed and their static and dynamic performances are investigated, especially the dynamic

performances. The influences of FG width are comprehensively investiagted. Some recommendations under different criteria are given for selecting the best candidates for different applications.

- Two novel forced cooling methods utilizing the flux gaps (FGs) in the E-core modular CPM are proposed, including the forced air cooling with inlets on the endcaps and forced oil cooling with submegred stator. The cooling effect of both methods is assessed and some design guidelines of such modular machines for best cooling effect and lowest pressure drop (or highest cooling system efficiency) are given.

Several papers have been published based on the findings of this thesis, and a list of them is given below:

1. R. Zhou, G. J. Li, Z. Q. Zhu, Y. X. Li, M. P. Foster, and D. A. Stone, "Comparative studies of fractional/integer-slot consequent pole permanent magnet machines," in *2019 IEEE International Electric Machines & Drives Conference (IEMDC)*, 2019, pp. 104-111.
2. R. Zhou, G. J. Li, Z. Q. Zhu, Y. X. Li, M. P. Foster, and D. A. Stone, " Investigation of integer/fractional slot consequent pole PM machines with different rotor structures," in *2019 IEEE International Electric Machines & Drives Conference (IEMDC)*, 2019, pp. 119-126.
3. R. Zhou, G. J. Li, Z. Q. Zhu, Y. X. Li, M. P. Foster, and D. A. Stone, " Performance investigation of modular consequent-pole machines," *IEEE Trans. Energy Convers.* 2020 (accepted).
4. R. Zhou, G. Li, Z. Zhu, Y. X. Li, M. Foster, and D. Stone, " Improved Cooling in Modular Electric Machines Utilizing Flux Gaps," in *2020 IEEE Energy Conversion Congress and Exposition (ECCE)* (Accepted).

Chapter 2 Winding Configurations and Rotor Structures of Consequent Pole PM Machines

2.1. Introduction

With the intrinsic advantages such as high torque and power density, high efficiency and excellent overload capability, permanent magnet (PM) machines are being widely used in various industry applications. One of the most classical PM machines is the surface-mounted permanent magnet (SPM) machine where the PMs are mounted on the rotor surface and the torque is only produced by the magnets without contribution from reluctance torque [113]. Due to the advantages of simplicity and also easy to control, SPM machines have been popular in many applications. For example, in [114] a high-speed SPM machine with rotor sleeve was proposed for machine tool applications. A 18-slot/12-pole Halbach magnetized SPM machine was proposed in [115] to provide a better flux-weakening capability.

With the increasing demand of higher torque density, wider speed range and lower total losses, researchers have proposed the interior permanent magnet (IPM) machines. The most common rotor structures for IPMs are the I-shape (I-IPM) and V-shape (V-IPM) ones. [116] made a comparison between SPM machine and I-IPM machine for electrical vehicles (EV) applications. It pointed out that the IPM machine has better flux-weakening capability and lower PM eddy current losses compared with the SPM machine. A V-IPM machine having distributed winding with double-layer PM rotor was proposed in [117] for high efficiency and low-cost applications.

However, due to rising concern for increasing cost and volatile supply of rare-earth PM materials such as NdFeB, many researchers are seeking for cost-effective solutions by reducing magnet consumption in electrical machines [26]. It has been proven that the consequent pole (CP) rotor can improve the PM material utilization in cost sensitive applications [25]. In general, for p pole pairs in a consequent pole machine (CPM), only p magnets are used as shown in Fig. 2.1 (a). The iron pole between the two adjacent magnets of the same polarity will be reversely magnetized by the magnets themselves, which can be regarded as ‘virtual’ magnet poles but with opposite polarity to the real magnets [22]. It is revealed in [25] that, with CP rotor, approximately 33% of PM

materials can be saved while maintaining almost the same performance in comparison with conventional SPM machine. In [22], an SPM with CPM rotor having the optimal pole arc to pole pitch ratio is proposed to improve the torque performance for high-speed applications. In addition, [27] compared the electromagnetic performances between CPM (with V-IPM rotors) and conventional V-IPM machine. It was found that the CPM can achieve higher torque density at rated condition, lower cogging torque and wider speed range, which are all desirable advantages for EV applications. Apart from being adopted in relatively "conventional" machine topologies such as SPM and IPM machines, the CP structure has also a good potential in other new machine topologies. By way of example, a new doubly salient linear PM machine with CP stator was investigated in [118]. [36] proposed a PM machine with external eccentric CP rotor to improve the torque performance.

As for other types of electrical machines, different winding configurations may also have significant influences on the performances (electromagnetic, thermal and mechanical) of the CPMs. It is generally agreed that the integer-slot (IS) machines, often equipped with distributed-windings, are widely used in the field of electric vehicles due to advantages such as high utilization of the reluctance torque, high winding factor, low armature field harmonics, etc. [119]. However, with the benefits of short end-winding, high slot fill factor and high fault tolerant capability brought by single-layer windings (SL), the machines with the fractional-slot (FS), often with concentrated-windings, are becoming increasingly popular for safety-critical applications such as aerospace and marine propulsion [120].

However, so far, little research has been done in terms of the electromagnetic performance comparison between the FS- and IS-CPMs. To fill in this gap, in the first section of this chapter, the electromagnetic performance of CPMs with both winding configurations have been evaluated and compared thoroughly including the open-circuit characteristics such as cogging torque, EMF, etc. and on-load characteristics such as on-load torques, losses and the dynamic performance. It is worth noting that both single-layer (SL) and double-layer (DL) structures are investigated for both the FS- and IS-CPMs, with concentrated windings and distributed windings, respectively. This aims to make the comparison more comprehensive and provide some meaningful design guidelines for such machines in future applications.

Meanwhile, so far, little systematic research has been done regarding the influence of rotor structures on the electromagnetic performances of the CPMs, especially CPMs with I-IPM or V-IPM rotor structures and with fractional-slot (FS) or integer-slot (IS) windings. Therefore, the second section of this chapter will extend the analysis in the first section and focus on this topic in order to reveal the full potential of CPMs. Furthermore, the demagnetization withstand capabilities considering thermal influence have also been investigated to provide some insight into the performances under fault conditions.

This chapter is organized as follows: firstly, two FS- and IS-CPMs with both SL and DL windings are thoroughly compared to investigate the influence of winding configurations, including their static and dynamic performances. Then, CPMs with different rotor structures, especially CPMs with I-IPM or V-IPM rotor structures are investigated to reveal the full potential of CPMs. Their static and dynamic performances are compared.

2.2. Winding Configurations

2.2.1. Comparison of Static Electromagnetic Performances

By way of example, two 12-slot/8-pole and two 48-slot/8-pole CPMs with both the SL and DL windings are employed to compare the electromagnetic performance in order to figure out the influence of winding configurations. The 12-slot/8-pole CPM with SL winding is shown in Fig. 2.1 (a) while Fig. 2.1 (b) shows the 12-slot/8-pole CPM with DL winding. Cross-sections of 48-slot/8-pole CPMs with SL and DL windings are illustrated in Fig. 2.1 (c) and (d), respectively. It is difficult to show all phases of the 48-slot/8-pole CPMs in Fig. 2.1, thus its entire winding layouts are shown in Fig. 2.2.

The design constraints for the comparison are: the stator outer radius, the stack length, the material grades, the PM volume, the number of turns per phase and also the copper losses are all the same. The global optimization method based on genetic algorithm is adopted in the software (Ansys Maxwell) with the aim of maximizing the average torques of the FS-CPM and IS-CPM with SL-windings supplied with 3-phase sinewave currents. The ranges of dimensions used for the optimisation process are shown in Table 2.1 and the corresponding optimal values are shown in the brackets.

Considering the fact that a prototype machine will be built to validate the predictions, several other general parameters of the investigated machines are fixed based on previous lab work [84] and listed in Table 2.2. It is worth noting that since the main focus of this section is on the influence of the FS and IS, for simplicity, the same type of CPMs will have the same rotors. In other words, the rotors of the FS-CPMs with SL and DL windings will be the same and this is the same case for the IS-CPMs with SL and DL windings.

The FS and IS-CPMs have been optimized under the condition of the same copper loss and PM volume. The electromagnetic performance comparison including the open-circuit and on-load characteristics are presented in this section.

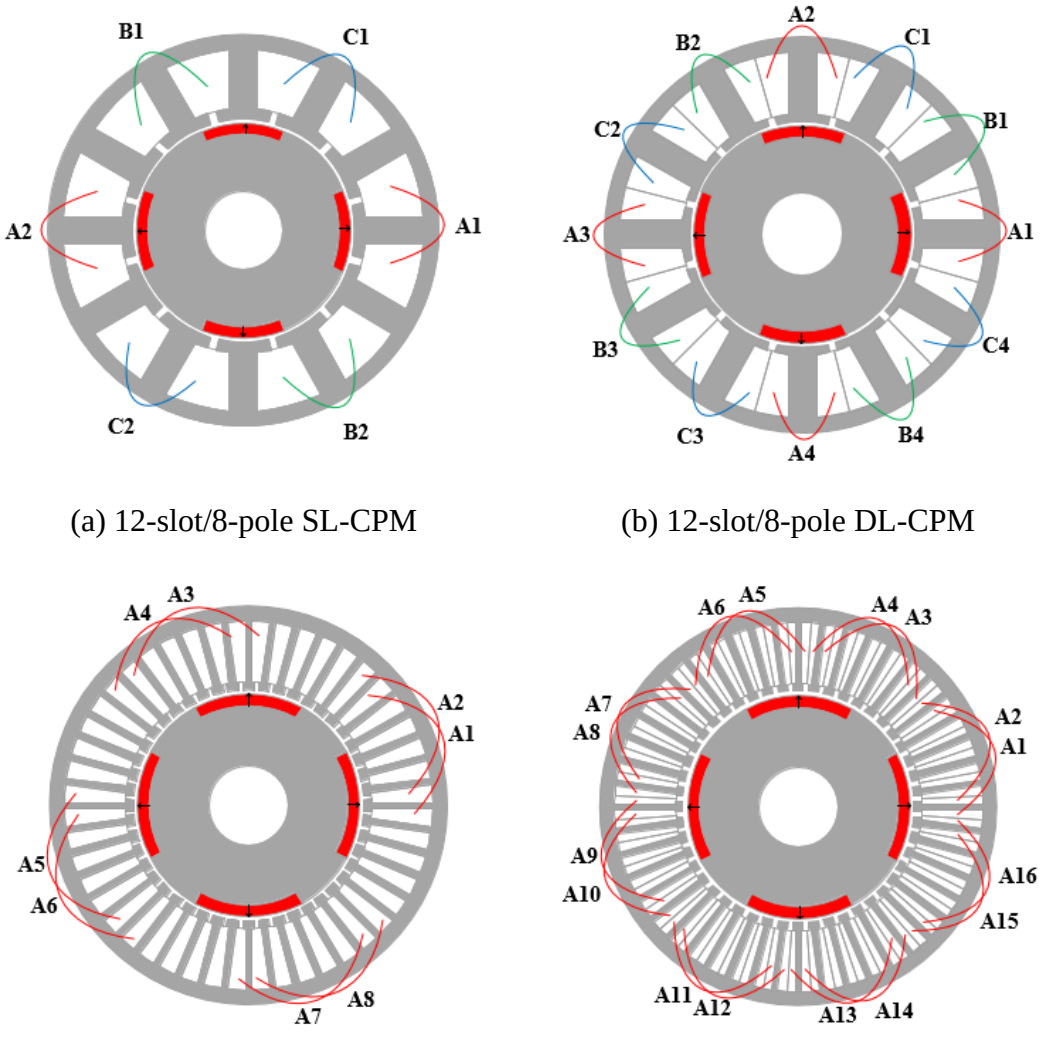

(a) 12-slot/8-pole SL-CPM (b) 12-slot/8-pole DL-CPM

(c) 48-slot/8-pole SL-CPM (d) 48-slot/8-pole DL-CPM

Fig. 2.1. Cross-sections of investigated machines with different winding configurations.

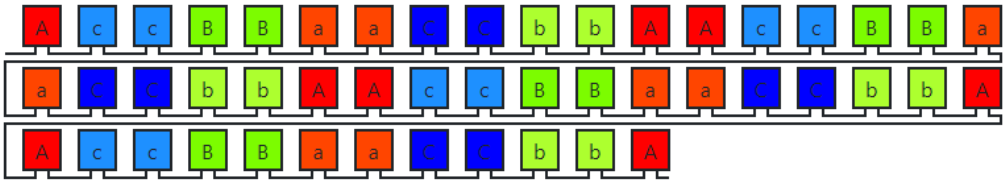

(a)

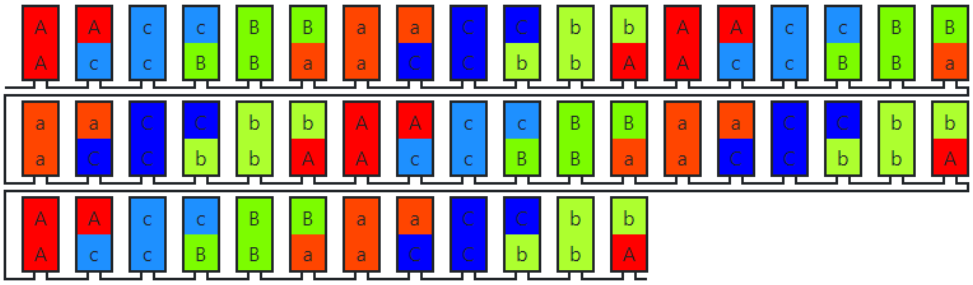

(b)

Fig. 2.2. Winding layouts of 48-slot/8-pole CPMs. (a) SL winding, (b) DL winding.

Table 2.1 The ranges of parameters used in optimisation and optimised values

	FS	IS
Split ratio	0.4-0.7 (0.57)	0.4-0.7 (0.58)
Stator yoke height (mm)	2-5 (3.7)	2-5 (3.58)
Tooth body width (mm)	4-10 (7.1)	0.8-2.5 (1.58)
PM pole arc to pole pitch ratio	0.3-0.8 (0.65)	0.3-0.8 (0.64)
Slot opening (mm)	1-3 (2)	0.5-1.5 (1)
Current advanced angle	0-20 (3)	0-20 (5)

Table 2.2 Main fixed design parameters of the CPMs

	FS & IS
Stator outer radius (mm)	50
Total magnet volume (mm^3)	15928
Magnet remanence (T)	1.2
Filling factor	0.37
Stack length (mm)	50
Rated current (A_{rms})	7.34
Number of turns per phase	128

A. Air-Gap Flux Density Due to PMs

The waveforms of open-circuit air-gap flux density of the investigated machines are shown in Fig. 2.3. Only results for the FS and IS-CPMs with SL windings are shown as examples because the open-circuit air-gap flux density is independent of the winding layout. Meanwhile, the open-circuit flux density distributions are shown in Fig. 2.4.

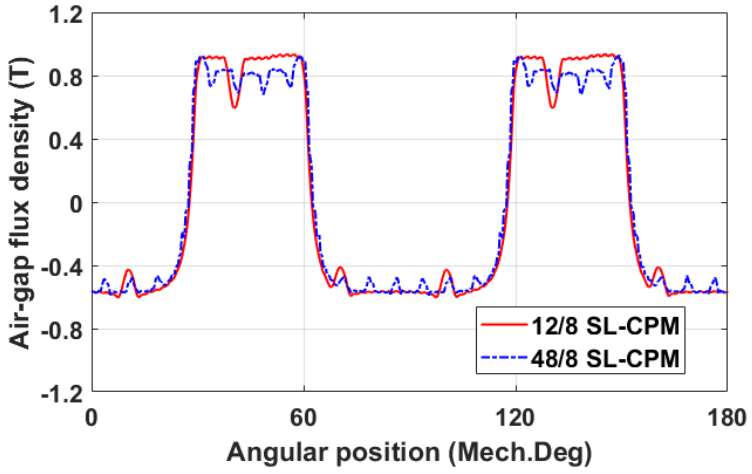

(a) Waveform

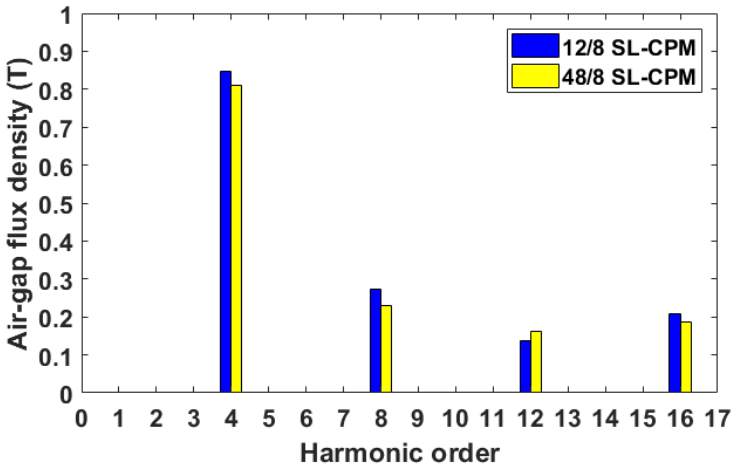

(b) Spectra

Fig. 2.3. Open-circuit air-gap flux density of the 12-slot/8-pole SL winding CPM and 48-slot/8-pole SL winding CPM.

From Fig. 2.3 (a), it is evident that the air-gap flux density waveforms of both investigated CPMs are asymmetric. By way of example, in the 12-slot/8-pole CPM with SL windings, the peak positive airgap flux density can reach up to approximately 0.9T while the peak negative airgap flux density is only around 0.6T. The spectra of both machines are shown in Fig. 2.3 (b). For the 8-pole machines, it is easy to point out that

the working harmonic (fundamental or 1st) order is 4th when the entire airgap circumference is considered in the analysis. It is worth noting that the even order harmonics, such as the 2nd order harmonic (the 8th if the entire airgap circumference is considered), exist. This is mainly due to the asymmetric rotor structure in the CPMs, as shown in Fig. 2.4. To illustrate the rotor asymmetry in the CPMs, the simplified flux paths of conventional SPM and CPM are shown in Fig. 2.5. Due to the removal of the S-poles in the conventional SPM, the iron poles in the CPM act as a 'virtual' magnet pole (S-poles) to provide the return path for the flux. As pointed in [23], the available magnets nowadays have a remanence somewhat smaller than the saturation flux density of iron materials. As a result, the flux density in the airgap over the iron pole will usually be higher than that above the PM pole. Moreover, the modern magnets have a recoil permeability close to the air. All this leads to the rotor asymmetric structure as mentioned above.

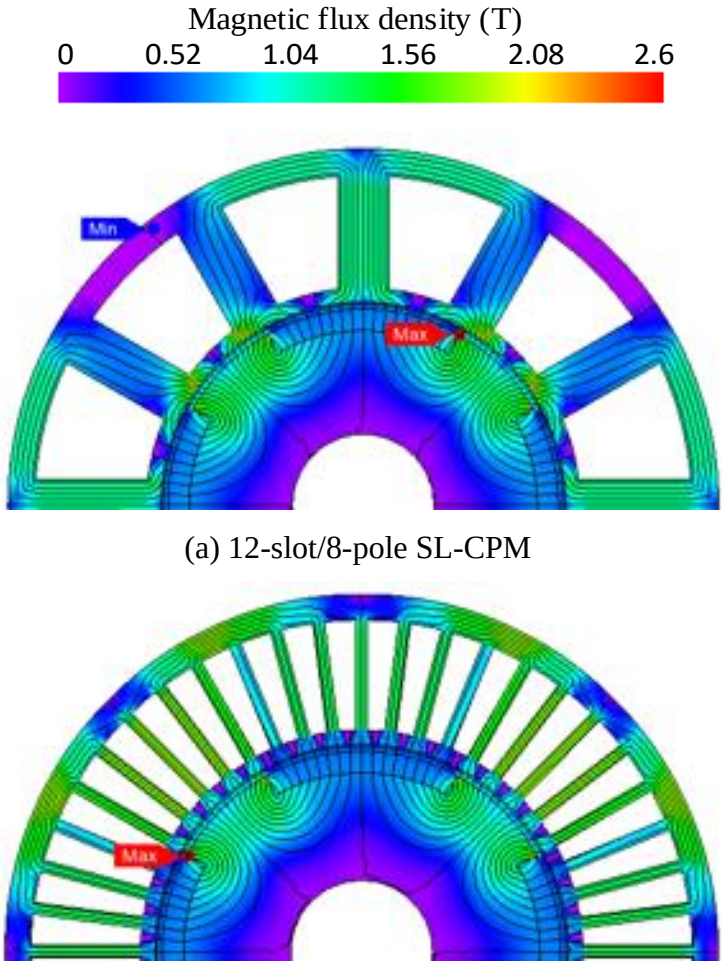

(a) 12-slot/8-pole SL-CPM

(b) 48-slot/8-pole SL-CPM

Fig. 2.4. Open-circuit flux density and flux line distributions of investigated CPMs.

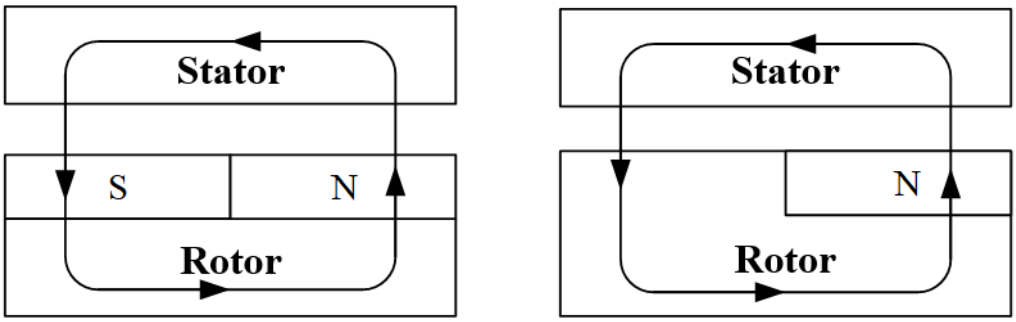

(a) Conventional SPM (b) CPM

Fig. 2.5. Simplified flux paths of different PM machines.

B. Phase Back-EMF

The phase back-EMFs of the investigated CPMs are calculated at 400 rpm and the waveforms and spectra are shown in Fig. 2.21. It is found that FS-CPMs with SL and DL windings almost have the same phase-back-EMFs. This is mainly due to the same winding factor of both winding configurations which is 0.866. It can be seen that the FS-CPMs with SL and DL windings have even-order harmonics, particularly the 2nd order harmonic, in the phase back-EMFs. Such harmonics do not exist in the IS-CPMs with SL and DL windings. This is mainly due to the specific slot-pole number combinations employed in the CPMs as will be explained in the following parts.

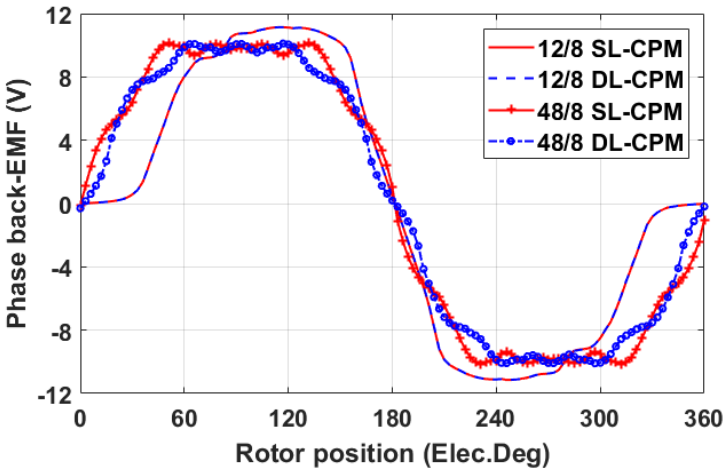

(a) Waveforms

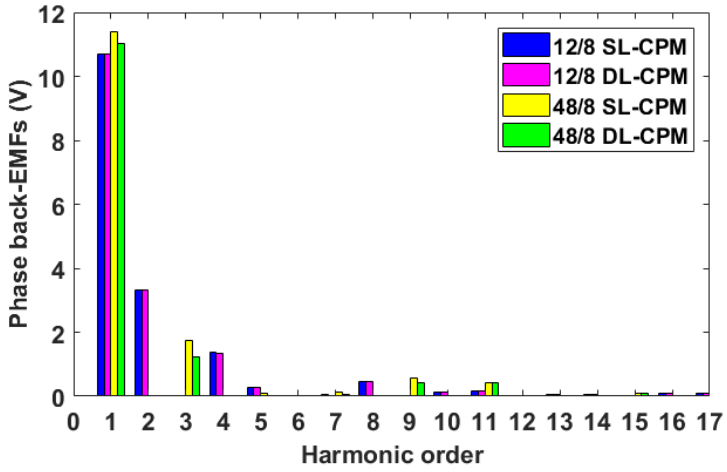

(b) Spectra

Fig. 2.6. Phase back-EMFs at 400 rpm of the investigated CPMs.

For conventional PM machines, because the N-poles and S-poles are symmetrical within the entire machine, normally only odd order harmonics exist in the open-circuit air-gap flux density. However, for the CPMs, even order harmonics will exist due to the asymmetric rotor structure as mentioned previously. The simplified Fourier expression of the open-circuit air-gap flux density can be written as:

$$B(\alpha_s) = \sum_{k=0}^{N} B_v \times \sin(v \times \alpha_s) \tag{2.1}$$

With

$$\begin{cases} v = 2 \times k + 1, for\ conventional\ PM\ machines \\ v = k + 1, for\ CPMs \end{cases}$$

where α_s is the angular position in the airgap, v is the harmonic order, and N is an integer number depending on the harmonics in the open-circuit airgap flux density.

It is established that the phase back-EMF does not only depend on the open-circuit flux density but also on the winding factor. In addition, the ratio of fundamental EMF and harmonic EMF can be written as:

$$\frac{\left|\widehat{E_1}\right|}{\left|\widehat{E_v}\right|} = \frac{\widehat{B_1} \times k_{w1}}{\widehat{B_V} \times k_{wv}} \tag{2.2}$$

where $\widehat{E_v}$ is the magnitude of the v^{th} order back-EMF harmonic, $\widehat{B_V}$ is the magnitude of the v^{th} order flux density while k_{wv} represents the winding factor of the v^{th} order harmonic. (2.2) means that the even order harmonics in the phase back-EMF can be eliminated if k_{wv} for even order harmonics equal to 0, otherwise the even order harmonics will exist in the CPMs due to the existence of even order harmonics in the open-circuit air-gap flux density.

To elaborate this further, the 12-slot/8-pole DL-CPM and 48-slot/8-pole DL-CPM are analysed as an example. It can be clearly seen from Fig. 2.7 (a) that the winding factor of the 2nd order harmonic is not 0. Thus, even order harmonics exist in the phase back-EMF of the 12-slot/8-pole CPM. However, for the 48-slot/8-pole CPM, each phase has two groups of coil EMF vectors, which have the same amplitude but out of phase of π degree, as shown in Fig. 2.7 (b). This means that the winding factor of the 2nd order harmonic is 0 and it is the same for other even order harmonics. As a result, there will be no even harmonics in the phase back-EMF.

Additionally, this can be validated by the results from 2D FE analysis as shown in Fig. 2.8 (a). It can be seen from the spectra of both machines in Fig. 2.8 (b) that the 48-slot/8-pole DL-CPM has no even harmonics while the 12-slot/8-pole DL-CPM has all orders of harmonics except the triplen harmonics in the phase back-EMFs. However, apart from adopting IS machine topology, it is worth mentioning here that the even harmonics can also be eliminated by selecting appropriate slot-pole number combinations for the FS-CPMs. By way of example, the 12-slot/10-pole DL-CPM and 12-slot/14-pole DL-CPM are analysed as well. It can be clearly seen from Fig. 2.8 (a)

and (b) that both the 12-slot/10-pole DL-CPM and the 12-slot/14-pole DL-CPM have no even order harmonics in the phase back-EMFs because the winding factors for even order harmonics are null, as shown in Fig. 2.7 (c) and (d), where the 2nd order harmonic is used as example.

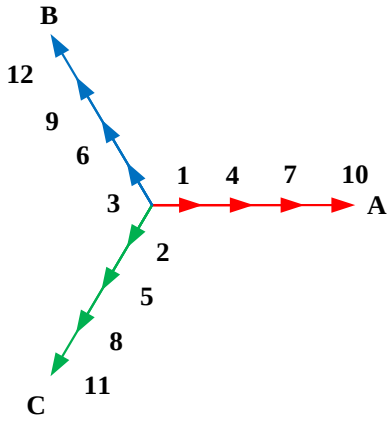

(a) 12-slot/8-pole

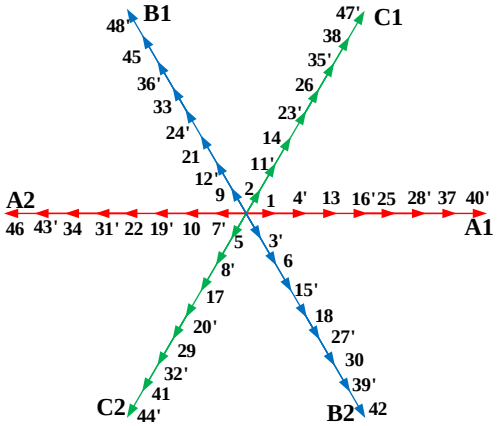

(b) 48-slot/8-pole

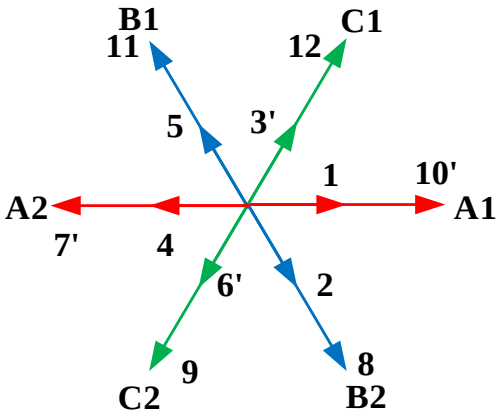

(c) 12-slot/10-pole

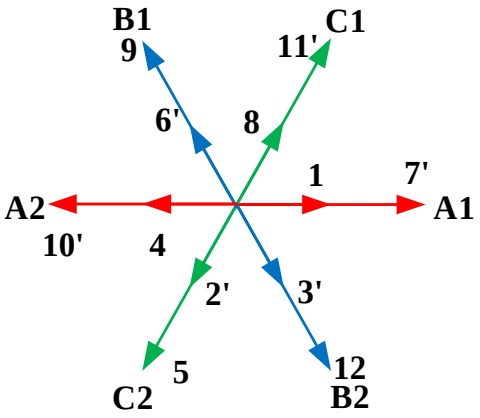

(d) 12-slot/14-pole

Fig. 2.7. Voltage phasors of the 2nd order harmonics. All the machines are DL CPMs.

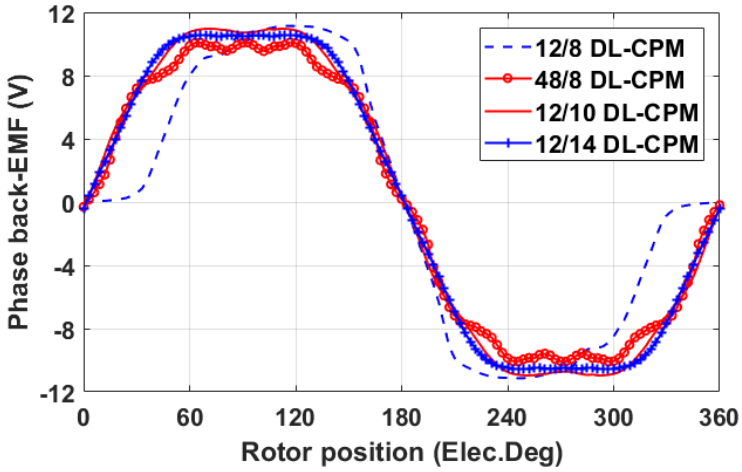

(a) Waveforms

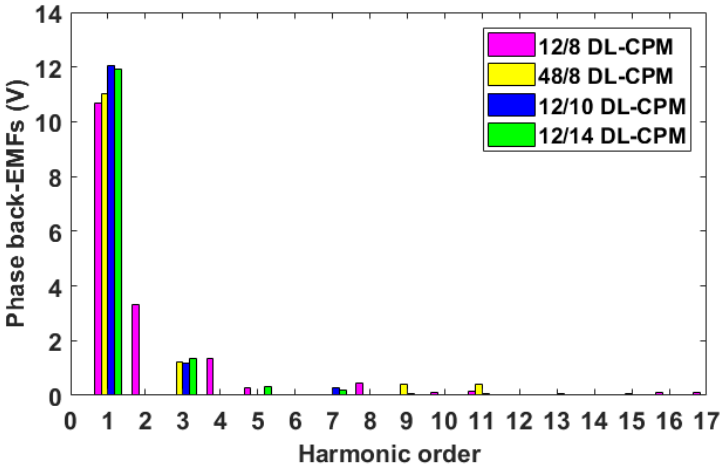

(b) Spectra

Fig. 2.8. Phase back-EMFs at 400 rpm of the 12-slot/8-pole, 48-slot/8-pole, 12-slot/10-pole and 12-slot/14-pole DL-CPMs.

C. Cogging Torque

Cogging torque is produced predominantly due to the fringing fields in the magnet pole and slot regions [121]. It might be a dominant factor in the torque ripple in some cases. The cogging torques of the 12-slot/8-pole FS-CPM and 48-slot/8-pole IS-CPM are shown in Fig. 2.9. It is worth mentioning that cogging torque is independent of winding layout. Therefore, only the results for SL windings are shown. It can be found that the IS-CPM has smaller peak cogging torque in comparison with the FS-CPM. With respect to the electrical period, the FS-CPM has a shorter period than the IS-CPM. Meanwhile, in terms of the cogging torque cycles in one electrical period, it can be calculated by [31]:

$$N_c = \frac{LCM(k, N_s)}{p} \tag{2.3}$$

where LCM is the lowest common multiple, N_s is the number of slots, p is the pole pair number, for conventional CPMs as discussed in this thesis, $k = 1$. As a result, for the 12-slot/8-pole CPM, it has 3 cogging torque cycles per electrical period while the 48-slot/8-pole CPM has 12 cogging torque cycles per electrical period. It is generally valid that more cycles will lead to lower peak cogging torque.

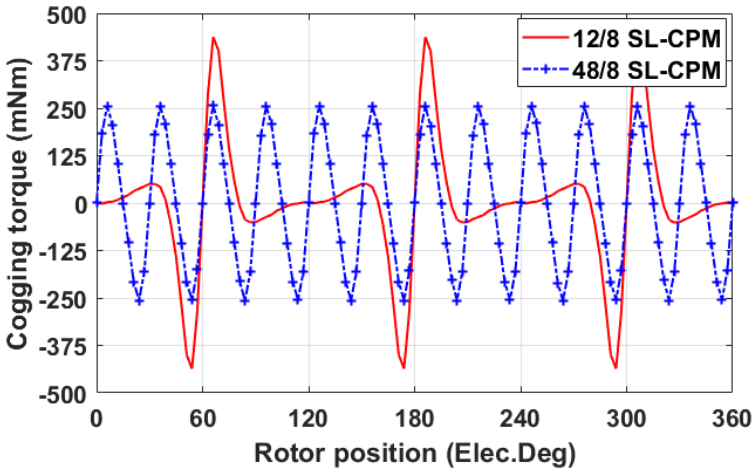

(a) Waveforms

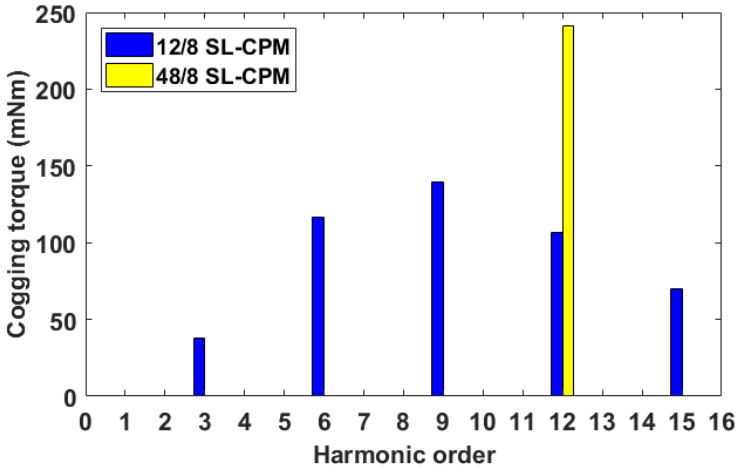

(b) Spectra

Fig. 2.9 Cogging torques of the 12-slot/8-pole CPM and 48-slot/8-pole CPM, both with SL windings.

D. Electromagnetic Torque Characteristics

The torque waveforms at rated current of the investigated CPMs are shown in Fig. 2.10. It can be found that both IS-CPMs have higher average toque in comparison with the FS-CPMs and this matches well with the magnitudes of phase back-EMFs shown in Fig. 2.21. Firstly, this is due to the fact that the winding factors of the investigated IS-CPMs are larger than those of the FS-CPMs, e.g. 0.966 for 48-slot/8-pole SL-CPM, 0.933 for 48-slot/8-pole DL-CPM while 0.866 for 12-slot/8-pole SL-CPM and DL-CPM. Furthermore, the armature field reactions in the FS-CPMs are more significant than the IS-CPMs, leading to higher saturation level.

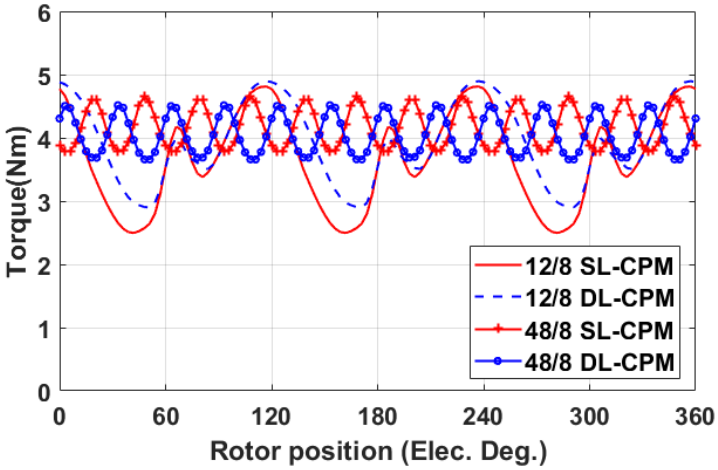

(a) Waveforms

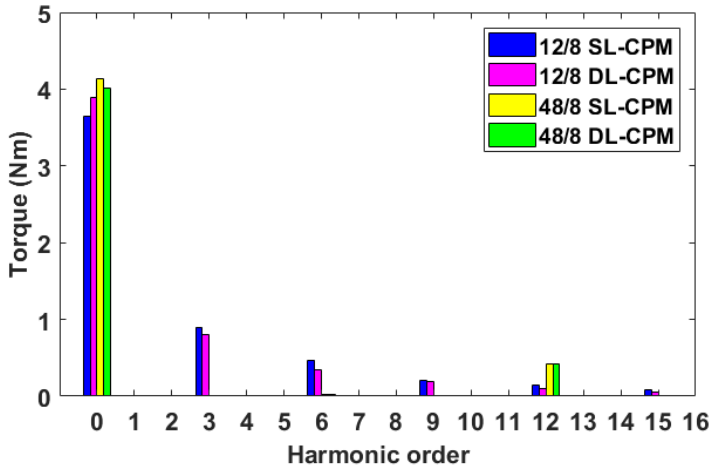

(b) Spectra

Fig. 2.10. Electromagnetic torque of the investigated CPMs at rated current.

The fields of armature winding of the investigated CPMs at rated current are illustrated in Fig. 2.11. It is worth noting that the contour plots shown in Fig. 2.11 are the fields which are only produced by the armature windings with the remanence of the magnets being set to 0. From Fig. 2.11 (a) and (b), it can be observed that in the FS-CPMs, by adopting the DL winding configuration, the armature field can be significantly reduced which means lower saturation level compared to the SL winding configuration. However, for the IS-CPMs, the winding configurations have nearly no influence on the armature field. In general, the saturation levels of IS-CPMs are lower than the FS-CPMs at the same current level as already proven by the results shown in Fig. 2.10. This can also be validated by the average torque versus phase peak current,

as shown Fig. 2.12 (a). It is evident that both the FS-CPMs have smaller average torques in comparison with the IS-CPMs at the same load condition. In addition, when phase peak current increases, the difference becomes larger.

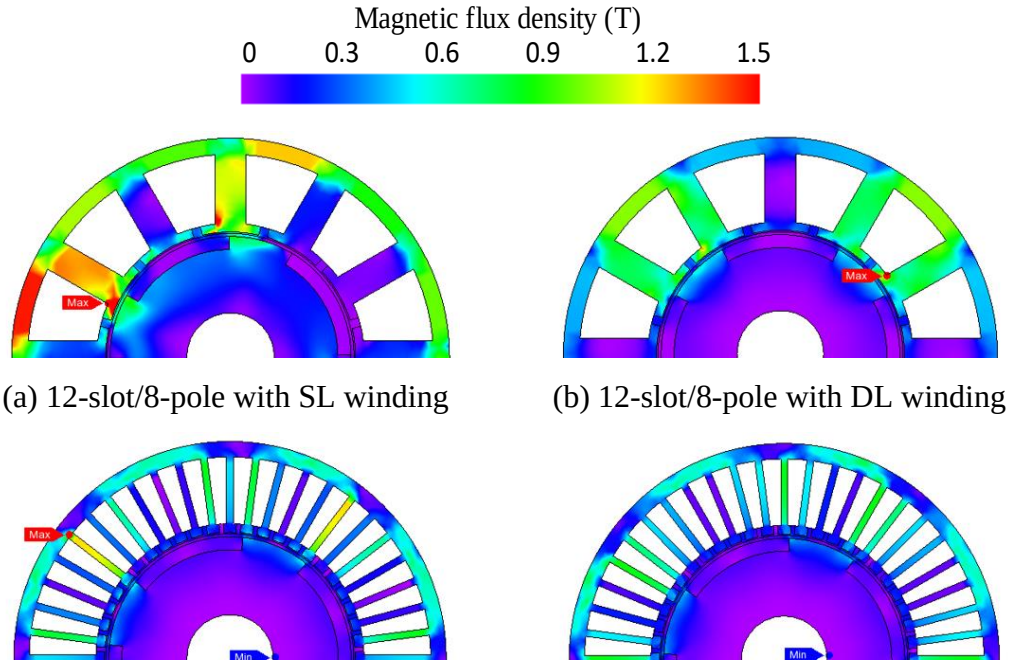

(a) 12-slot/8-pole with SL winding (b) 12-slot/8-pole with DL winding

(c) 48-slot/8-pole with SL winding (d) 48-slot/8-pole with DL winding

Fig. 2.11. Armature reaction fields (without PMs) of the investigated CPMs at rated current.

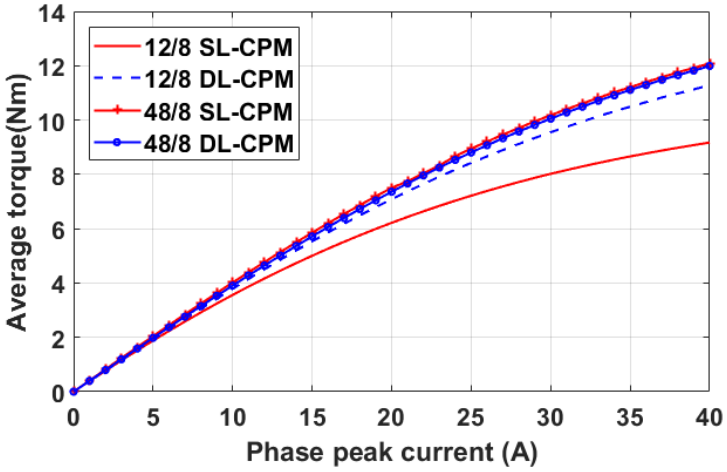

(a) Average torque

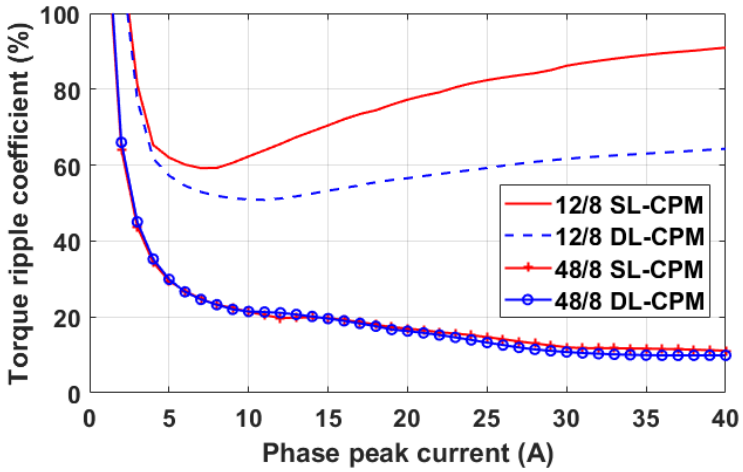

(b) Torque ripple coefficient

Fig. 2.12. Average torque and torque ripple coefficient *vs* phase peak current of the investigated CPMs.

The torque ripple coefficients versus phase peak current are shown in Fig. 2.25 (b). It is worth noting that the torque ripple coefficient is defined as:

$$T_{ripple} = \frac{T_{max} - T_{min}}{T_{ave}} \times 100\% \tag{2.4}$$

It can be seen that the IS-CPMs generally have lower torque ripple than the FS-CPMs. This is mainly due to no even order harmonics in the phase back-EMF and also lower peak cogging torque for the IS-CPMs. In addition, the torque ripple coefficients of the FS-CPMs decrease with the increasing phase peak current at low current levels. When the phase peak current keeps increasing, e.g., after approximately 7A, the torque ripple coefficients of the FS-CPMs start to increase. However, the torque ripple coefficients of both IS-CPMs keep decreasing and the difference between them can be negligible.

E. Core Losses and PM Eddy Current Loss

In this section, the iron loss and PM eddy current loss are investigated for the FS and IS-CPMs. The iron losses can be calculated using the general expression below [122, 123]:

$$P_{Fe} = k_h f B^{\alpha} + k_e f^2 B^2 + k_a f^{1.5} B^{1.5} \tag{2.5}$$

where f is the flux-density frequency, B is the amplitude of the alternating flux density and k_h, k_e, k_a represent the hysteresis loss, eddy current loss and excess or anomalous

loss coefficients, respectively. The iron material used here is China Steel 35CS250H and its corresponding loss coefficients are listed in Table 2.3. These coefficients are obtained from the manufacturer and calibrated based on previous lab work.

Table 2.3. Loss coefficients of the iron material

Coefficients	k_h	$k_{e,}$	k_a
Value	243.95	0.15	5.87

Moreover, the PM eddy-current loss can be roughly calculated according to Joule's law expressed in [124]:

$$P_{eddy} \approx l_S \sum_{j \in \Omega_e} \int_{\Omega_{e,j}} \frac{J_e^2}{\sigma} d\Omega \tag{2.6}$$

where l_S is the axial length of PMs, σ is the specific electric conductivity of PMs, Ω_e is the magnetic scalar with the index number j and J_e represents the harmonic eddy-current density.

Hence, the iron losses and PM eddy current losses of the investigated CPMs versus the phase current and rotation speed are shown in Fig. 2.13 and Fig. 2.14. It can be found that the iron losses of all investigated CPMs will increase more rapidly with the speed than with the phase current. This is mainly due to the fact that in iron losses, the hysteresis loss is proportional to the rotation speed while the eddy current loss is proportional to the square of rotation speed. As a result, the iron losses will be more sensitive to the rotation speed.

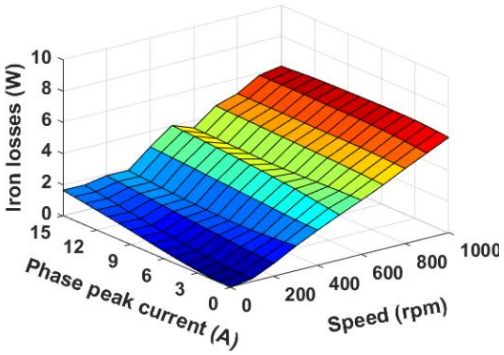

(a) 12-slot/8-pole SL-CPM

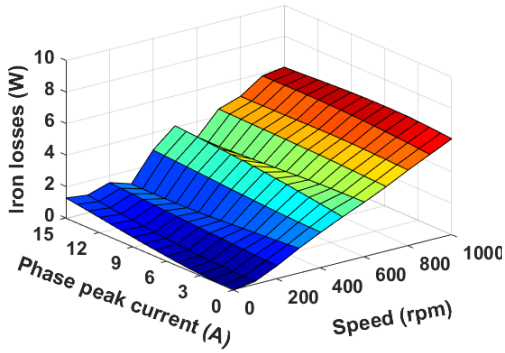

(b) 12-slot/8-pole DL-CPM

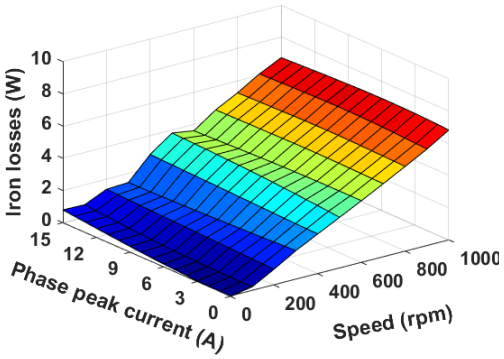

(c) 48-slot/8-pole SL-CPM

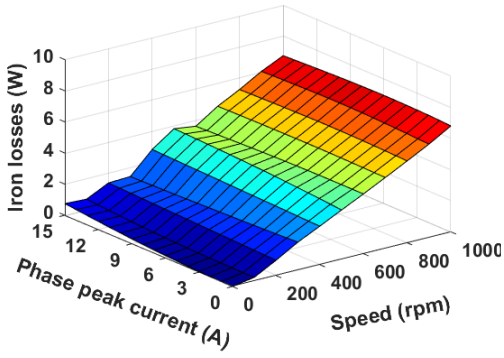

(d) 48-slot/8-pole DL CPM

Fig. 2.13. Iron losses versus current and speed of investigated CPMs.

In terms of PM eddy current losses, it is found that the IS-CPMs have much lower PM eddy current losses than the FS-CPMs, regardless of the load conditions. This can be explained by the spectra of the open-circuit air-gap flux density which is shown in Fig. 2.3. It is evident that except from the working harmonic (4th order harmonic), the magnitudes of the rest harmonics of the FS-CPMs are higher than those of the IS-CPMs. Furthermore, the PM eddy current loss density distributions for open-circuit condition and at rated current are presented in Fig. 2.15 and Fig. 2.16, respectively. It is worth mentioning that the open-circuit PM eddy current losses are independent of winding layout, and therefore, only the results for SL windings are shown in Fig. 2.15. The conclusion is that the FS-CPMs always have higher PM eddy current losses than the IS-CPMs.

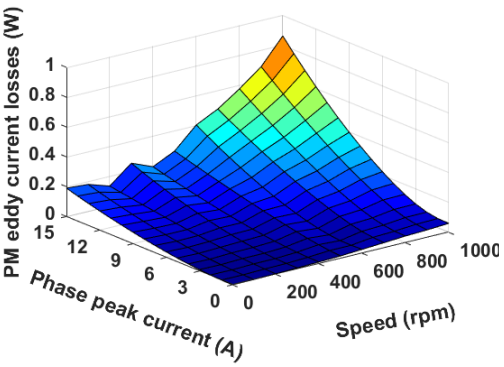

(a) 12-slot/8-pole SL-CPM

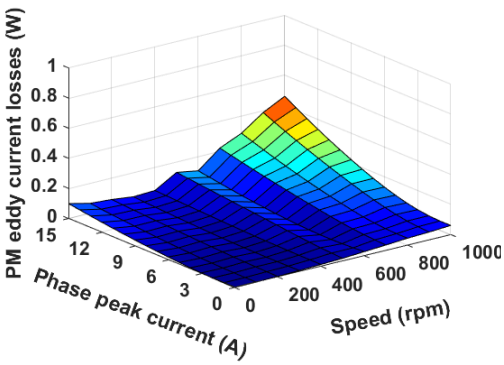

(b) 12-slot/8-pole DL-CPM

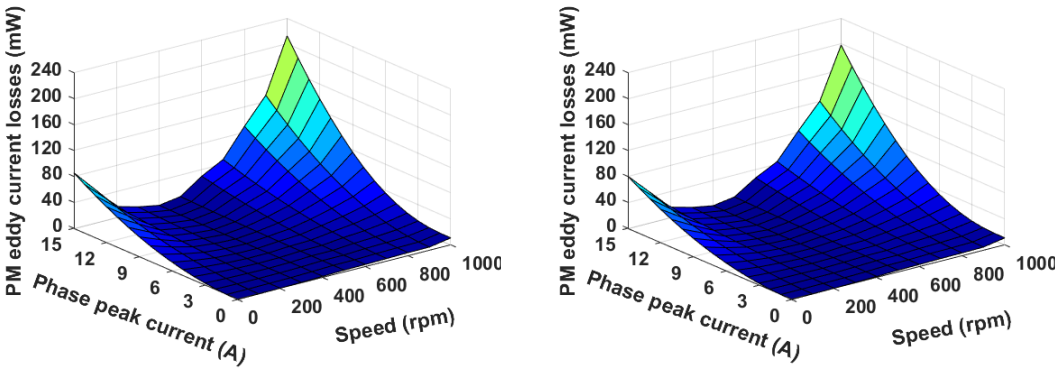

(c) 48-slot/8-pole SL-CPM (d) 48-slot/8-pole DL CPM

Fig. 2.14. PM eddy current losses versus current and speed of investigated CPMs.

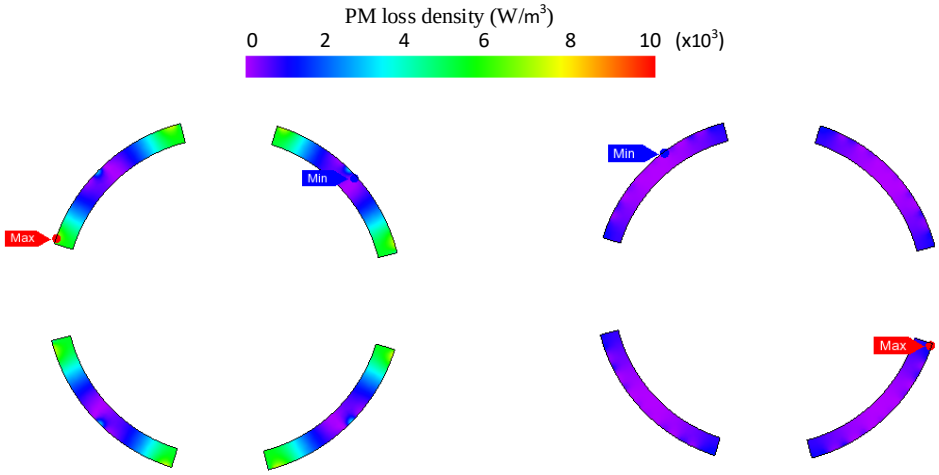

(a) 12-slot/8-pole SL-CPM (b) 48-slot/8-pole SL-CPM

Fig. 2.15. Open-circuit PM eddy current loss density at 400 rpm.

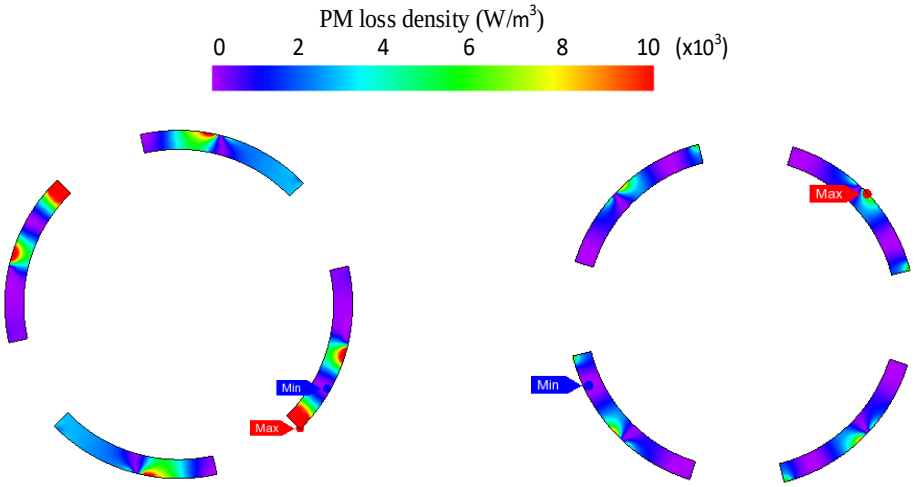

(a) 12-slot/8-pole SL-CPM (b) 12-slot/8-pole DL-CPM

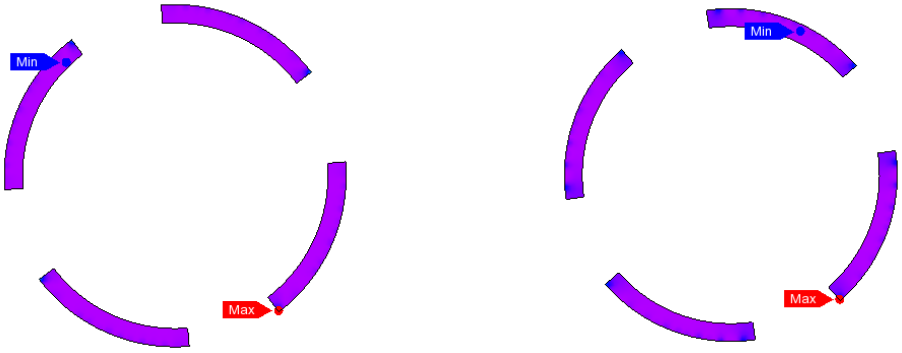

(c) 48-slot/8-pole SL-CPM (d) 48-slot/8-pole DL CPM

Fig. 2.16. PM eddy current loss density at rated current and at 400 rpm.

2.2.2. Comparison of Dynamic Electromagnetic Performances

The dynamic performance such as torque-speed curve, power-speed curve and power factor are also important to evaluate electrical machines.

A. Torque/Power-Speed Characteristics

The torque-speed curves of the investigated CPMs are shown in Fig. 2.17 (a). It is generally known that the torque-speed envelop usually consists of constant-torque region and constant-power region (flux-weakening region) where the phase voltage and current constraints should satisfy (2.7) and (2.8) considering the capacity of the inverter. V_{max} and I_{max} represent the voltage and current constraints of the inverter, respectively. It should be noted that the Space Vector Pulse Width Modulation (SVPWM) control strategy is used here in order to achieve the maximum utilization of DC-bus voltage which means the voltage limitation can be considered as $V_{dc}/\sqrt{3}$.

$$\sqrt{{v_d}^2 + {v_q}^2} \leq V_{max} = \frac{V_{dc}}{\sqrt{3}} \tag{2.7}$$

$$\sqrt{{i_d}^2 + {i_q}^2} \leq I_{max} \tag{2.8}$$

Hence, taking the real conditions into account, it is assumed here that the maximum inverter current (10.38A) and the maximum DC-bus voltage (40V) are the same for all investigated CPMs. It should be noted that the current and voltage limits here are just for simulation to figure out the differences between all the CPMs.

It can be found that both FS-CPMs have wider speed ranges than the IS-CPMs although the maximum torques of the FS-CPMs are lower than those of the IS-CPMs. Here it should be noted that all the CPMs are optimised based on having the same number of turns per phase to make sure their phase back-EMFs are at the similar level. However, it should be kept in mind if a machine has a smaller number of turns then its speed range will be relatively wider. It is established that flux weakening capability is dependent on the ratio defined as $L_d \times I_{max}/\varphi_m$, where I_{max} is the maximum inverter current and φ_m is the PM flux linkage. It is found that the *d*-axis inductances of the FS-CPMs are higher than those of the IS-CPMs while all machines have similar PM flux linkage, the FS-CPMs can achieve wider speed ranges. This is the same case for the power, as shown in Fig. 2.17 (b). As a result, the constant power speed range of the FS-CPMs, particularly the one with SL winding, are wider in comparison with the IS-CPMs. The curves of the power factor versus speed of the investigated CPMs are shown in Fig. 2.17 (c). It can be found that the power factors of the IS-CPMs are generally higher than that of the FS-CPMs at low speed range (<800 rpm), whilst the latter achieve better power factor at higher speed range.

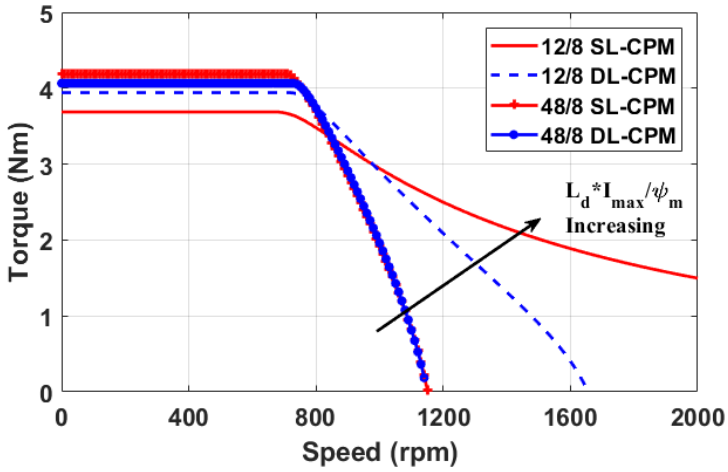

(a) Torque-speed curves

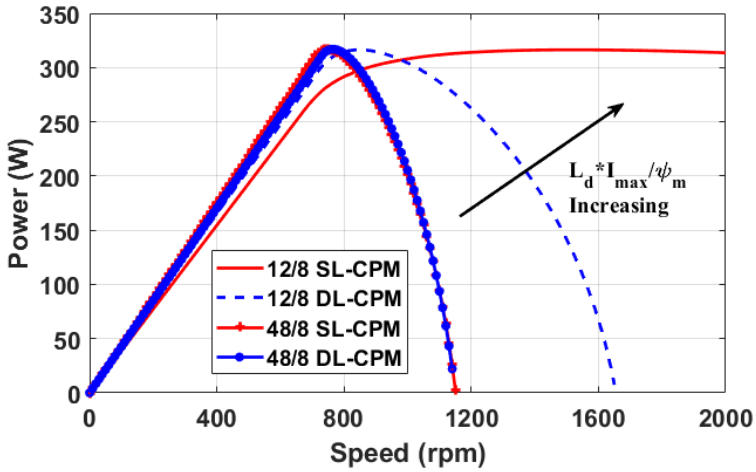

(b) Power-speed curves

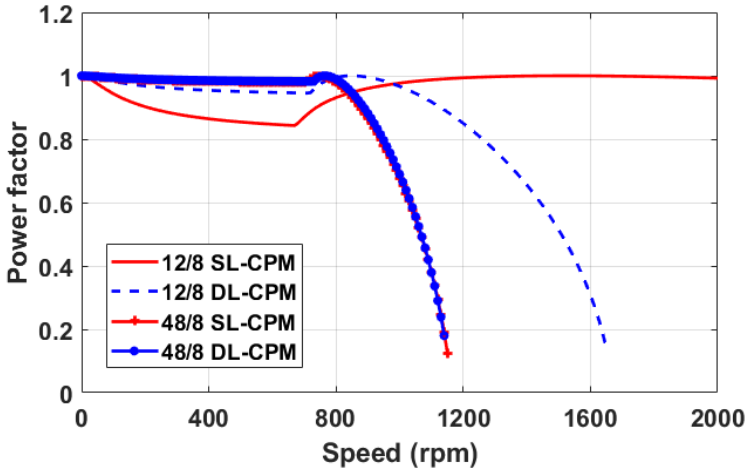

(c) Power factor -speed curves

Fig. 2.17. Torque-speed curves, power-speed curves and power factor -speed curves of the investigated CPMs.

B. Efficiency Map

The efficiency maps of investigated machines are shown in Fig. 2.18. Although the efficiency differences are quite small which is mainly because the relatively small sizes of the investigated machines, the overall efficiencies of the FS-CPMs are slightly lower in comparison with the IS-CPMs, especially for the 12-slot/8-pole SL-CPM. This is mainly due to the fact that the FS-CPMs have higher losses than the IS-CPMs at the same load condition which has been illustrated in the previous section.

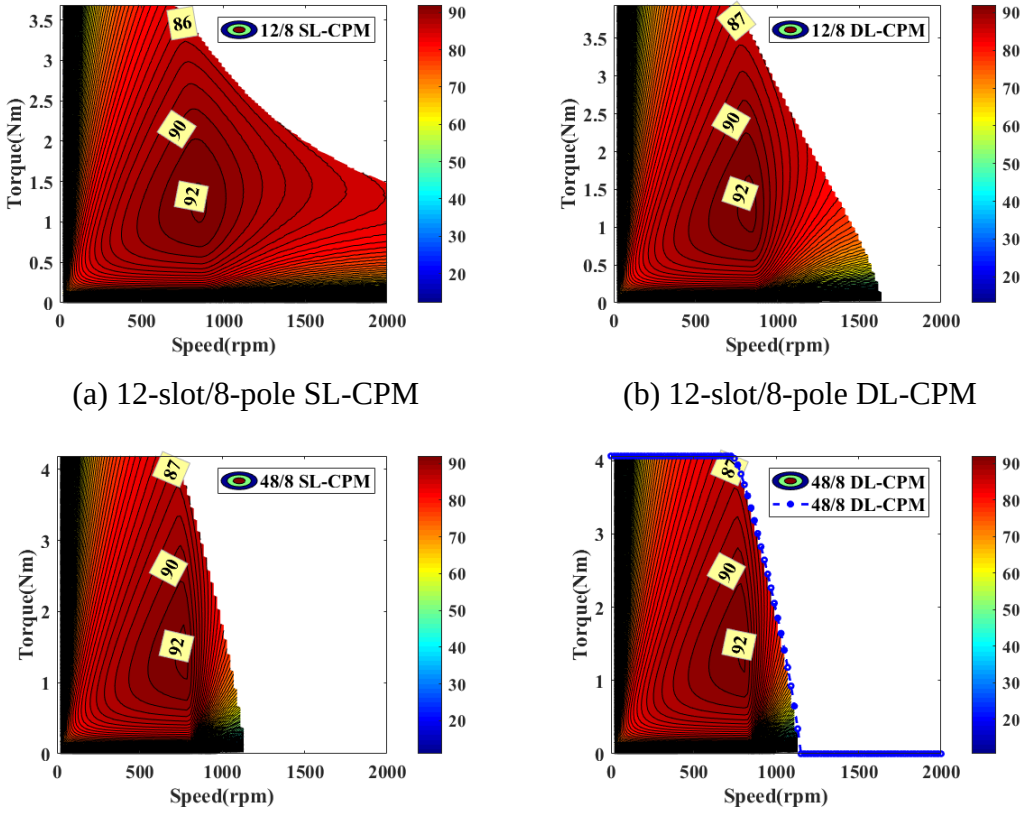

(a) 12-slot/8-pole SL-CPM (b) 12-slot/8-pole DL-CPM

(c) 48-slot/8-pole SL-CPM (d) 48-slot/8-pole DL-CPM

Fig. 2.18. Efficiency maps of investigated machines.

2.3. Different Rotor Structures

As mentioned in the introduction, CPMs with different rotor structures, especially the CPMs with I-IPM or V-IPM rotor structures need to be investigated to reveal the full potential of such machines. All rotors are laminated and using the material China Steel 35CS250H with 0.35mm lamination thickness. By way of example, two groups of FS and IS CPMs with SPM, I-IPM and V-IPM rotors, as shown in Fig. 2.19, have been chosen to compare the electromagnetic performance. For IS machines, only the windings for phase A have been given. 12-slot/8-pole is selected for FS winding while 48-slot/8-pole is for IS winding. It has been demonstrated in section 2.2 that the CPMs are generally sensitive to magnetic saturation due to reduced effective air-gap length (thanks to the iron “virtual” pole). Thus, all investigated machines in this section have

adopted the double layer winding configuration to reduce the saturation effect due to armature field.

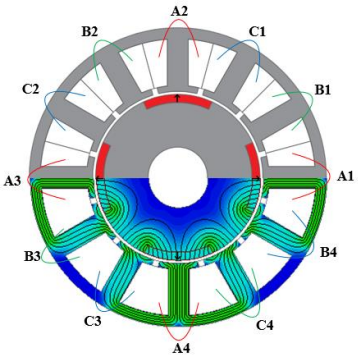

(a) 12-slot/8-pole SPM

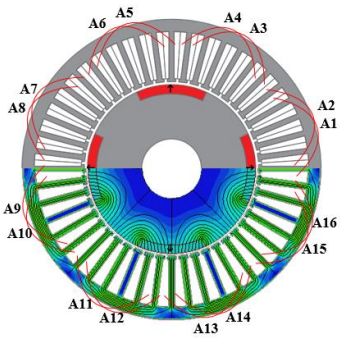

(b) 48-slot/8-pole SPM

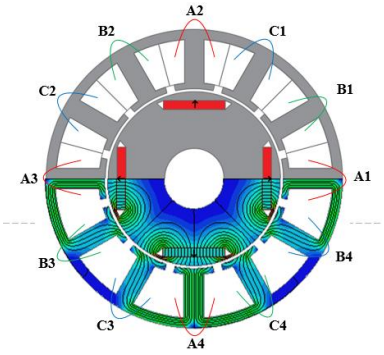

(c) 12-slot/8-pole I-IPM

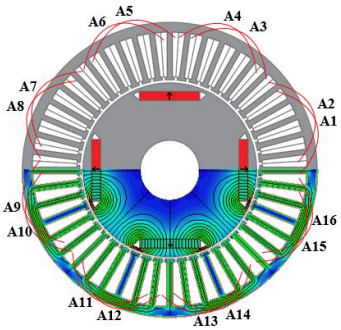

(d) 48-slot/8-pole I-IPM

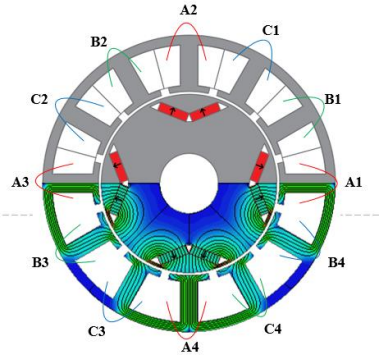

(e) 12-slot/8-pole V-IPM

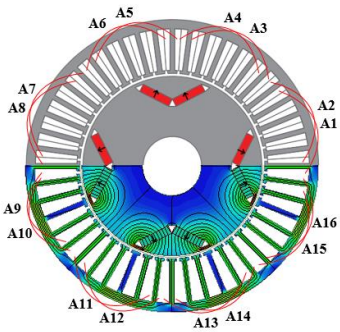

(f) 48-slot/8-pole V-IPM

Fig. 2.19. Cross-sections of the investigated CPMs with different rotors and also different winding structures.

Table 2.4 General specifications of the globally optimized CPMs

	FS-SPM	FS-I-IPM	FS-V-IPM	IS-SPM	IS-I-IPM	IS-V-IPM
Stator outer radius (mm)	50					
Air-gap length (mm)	1					
Split ratio	0.57	0.6	0.62	0.59	0.61	0.63
Stator yoke height (mm)	3.7	3.3	3.2	4.02	3.34	3.14
Tooth body width (mm)	7	6.6	6	1.7	1.7	1.6
Magnet thickness (mm)	2.75	3	3	2.8	3.04	2.81
PM pole arc to pole pitch ratio	1.1	1.08	1.04	1.06	1.05	1.08
Stack length (mm)	50					
Rated current (A_{rms})	7.34					
Rated speed (rpm)	400					
Number of turns per phase	128					

2.3.1. Static Performances

With the globally optimised topologies shown in section 2.3, the open-circuit electromagnetic performances comparison including the open-circuit air-gap flux density, phase back-EMF and cogging torque are presented in this section.

A. Open-circuit Air-gap Flux Density Phase Back-EMF

The flux line distributions of the investigated CPMs are shown in Fig. 2.19 and the waveforms of open-circuit air-gap flux density are shown in Fig. 2.20. It can be found from their spectra that the CPMs with IPM rotors have lower fundamental air-gap flux density compared to the CPMs with SPM rotors, regardless of FS or IS winding. This is mainly due to the existence of flux leakages around the flux barriers in the CPMs having IPM rotors, as shown in Fig. 2.19. The same phenomenon can be observed in a conventional IPM machine. As a result, the CPMs with SPM rotors also have the highest fundamental phase back-EMF in comparison with the CPMs having IPM rotors, as shown in Fig. 2.21.

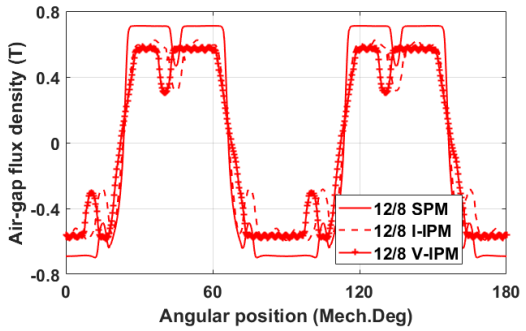

(a) Waveforms of the FS CPMs

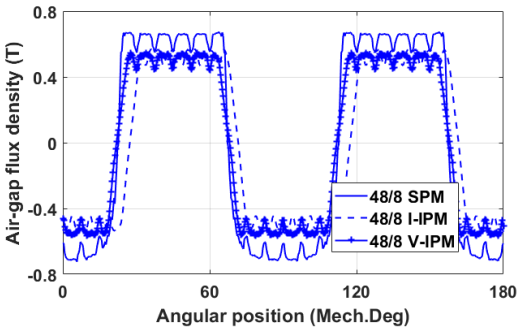

(b) Waveforms of the IS CPMs

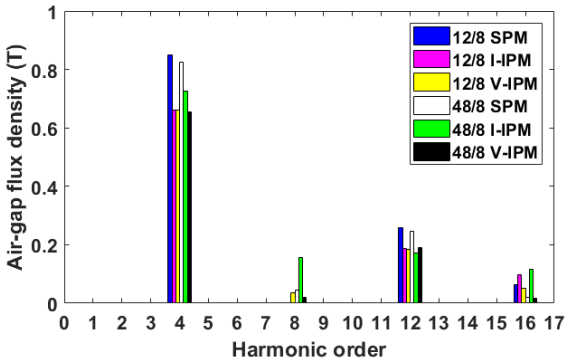

(c) Spectra

Fig. 2.20. Open-circuit air-gap flux density of the investigated FS and IS CPMs.

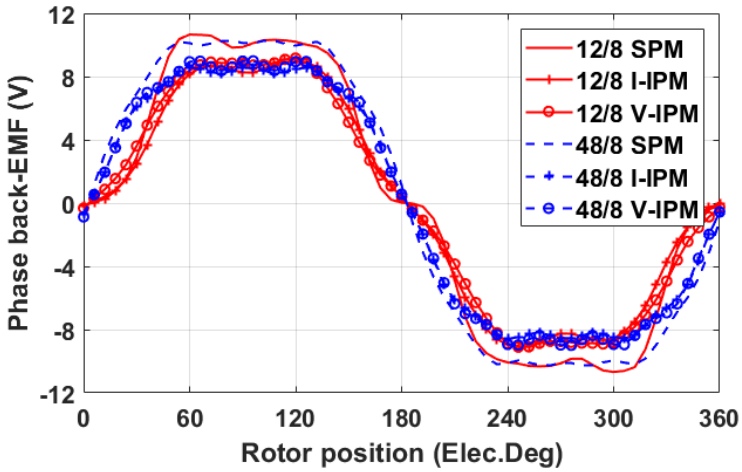

(a) Waveforms

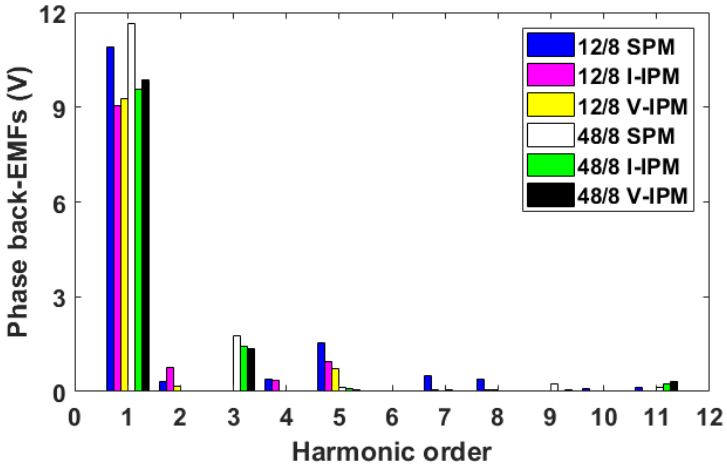

(b) Spectra

Fig. 2.21. Phase back-EMFs at 400 rpm of the investigated CPMs.

B. Cogging Torque

The cogging torques of the investigated CPMs are shown in Fig. 2.22. It can be found that the CPMs with V-IPM rotors have the smallest peak cogging torques compared with the CPMs with other two rotors, regardless of FS or IS windings. Moreover, it is clear that the cogging torques of the CPMs with IS windings are much lower in comparison with their FS counterparts with the same rotor structures. This is mainly due to fact that the IS machines have higher lowest common multiple (LMC) between the number of stator slots (N_s) and rotor poles ($2p$) [121], e.g. for the IS machines, their LMC(N_s, $2p$) is 48 whilst for the FS machines it is 24.

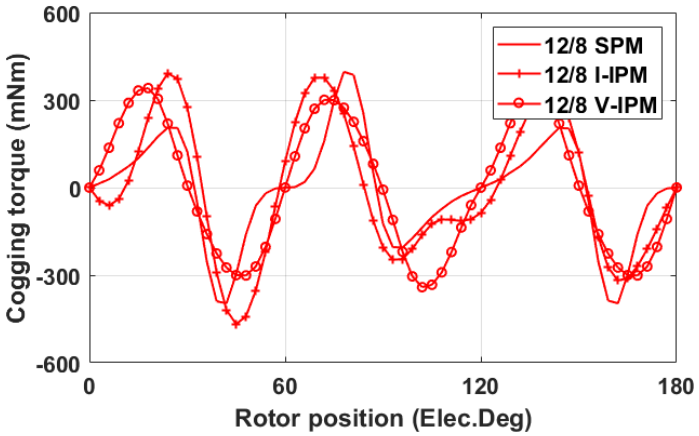

(a) Cogging torque waveforms of FS CPMs

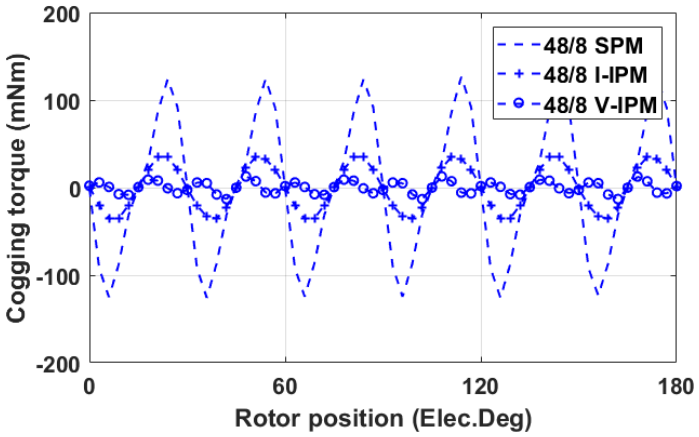

(b) Cogging torque waveforms of IS CPMs

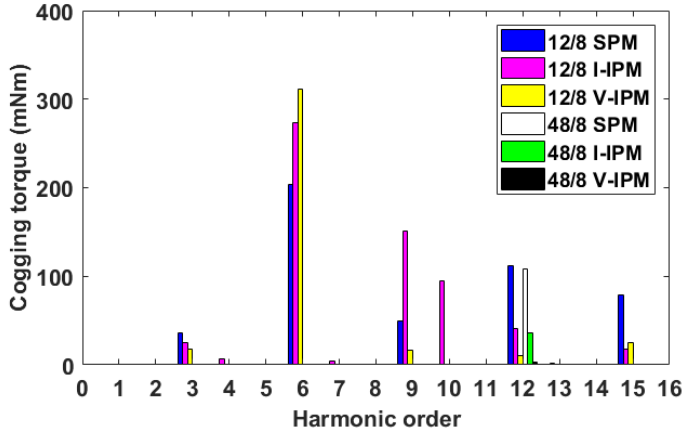

(c) Spectra

Fig. 2.22. Cogging torques of FS- and IS-CPMs.

C. On-Load Electromagnetic Torques

The average torques versus current phase angle of the investigated CPMs at rated current are shown in Fig. 2.23. It can be seen that the reluctance torque due to saliency of both CPMs with SPM rotors are quite small and can be negligible. However, for the CPMs with I-IPM and V-IPM rotors, both FS and IS windings have similar but more significant saliency performances. The instantaneous torque waveforms at rated current of the investigated CPMs are shown in Fig. 2.24, and Fig. 2.25 shows the average torques versus phase RMS current. It can be found that the CPMs with SPM rotors have the highest average torques in comparison with the CPMs with IPM rotors. It is already mentioned that due to the existence of flux leakages around the flux barriers in the CPMs with IPM rotors, they have lower fundamental phase back-EMF compared with their counterparts with SPM rotors, which in turn leads to lower average torques.

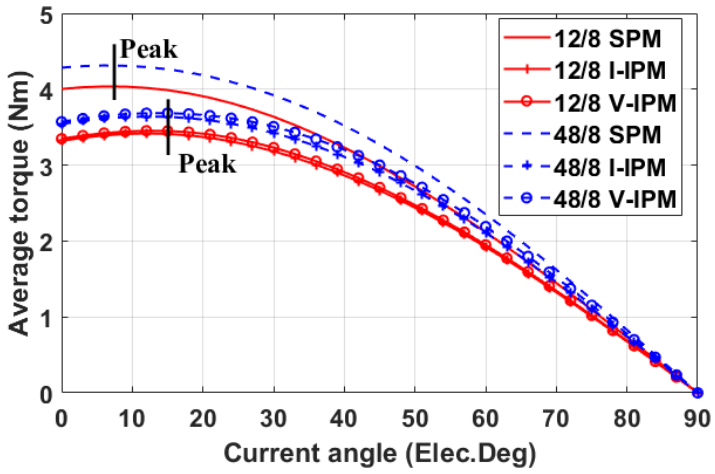

Fig. 2.23. Average torque *vs* current phase angle of the investigated CPMs. Rated current ($7.34A_{rms}$) is used to supply the machines.

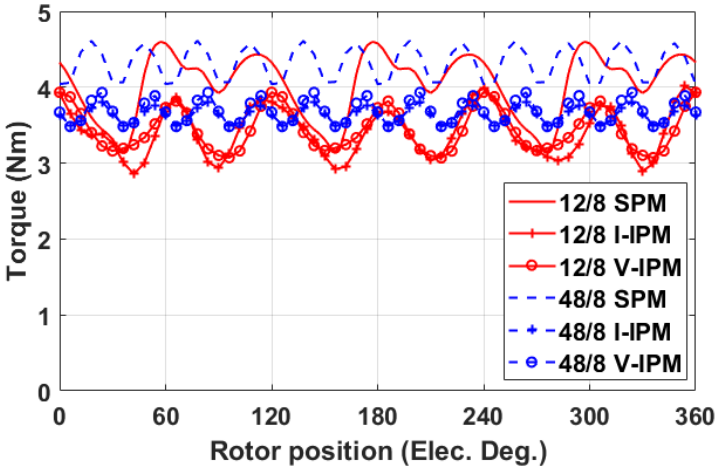

(a) Waveforms

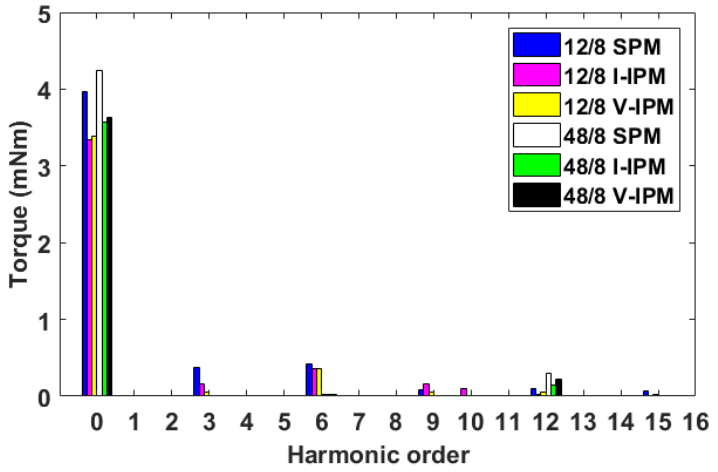

(b) Spectra

Fig. 2.24. Instantaneous torque of the investigated CPMs at rated current ($7.34A_{rms}$). The optimal current phase angles have been chosen for relevant machines.

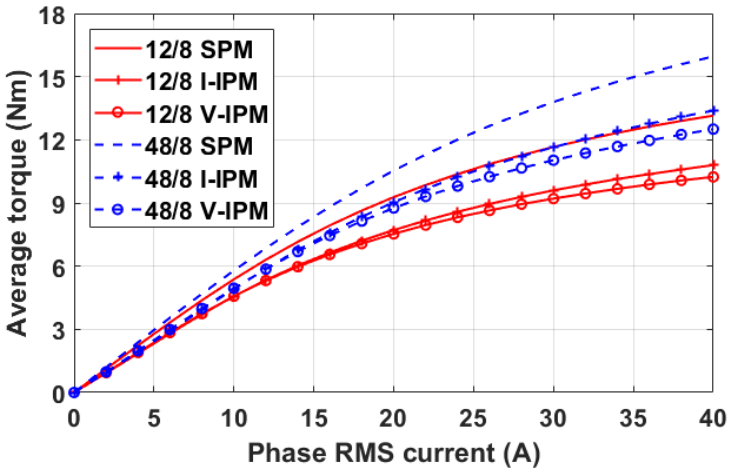

Fig. 2.25. Average torque *vs* phase RMS current of the investigated CPMs. The optimal current phase angles have been chosen for relevant machines.

It can also be observed from Fig. 2.25 that the CPMs with IS windings have better torque performances compared with the FS CPMs with the same rotors. It is the same case for three different rotor structures. The reason is two-fold: first, the IS winding achieves higher winding factor than the FS winding; second, by adopting the IS windings, the armature reaction field can be significantly reduced and hence the magnetic saturation is relieved.

D. *D*- and *q*-Axis Inductances

The *d*- and *q*-axis inductances are key factors to electromagnetic torque and flux-weakening capability and they can be influenced by the armature fields. Thus, the *d*- and *q*-axis inductance variations with the *d*- and *q*-axis currents have been calculated, as shown in Fig. 2.26. Here the cross-coupling effect has been taken into consideration. The inductances accounting for the influence of cross-coupling are given by [125]:

$$L_d(I_d, I_q) = \frac{\varphi_d(I_d, I_q) - \varphi_{PM}(I_q)}{i_d} \tag{2.9}$$

$$L_q(I_d, I_q) = \frac{\varphi_q(I_d, I_q)}{I_q} \tag{2.10}$$

where $L_d(I_d, I_q)$ and $L_q(I_d, I_q)$ are the *d*- and *q*-axis inductances, $\varphi_d(I_d, I_q)$ and $\varphi_q(I_d, I_q)$ are the *d*- and *q*-axis flux linkages, $\varphi_{PM}(I_q)$ is the PM flux linkage accounting for the influence of *q*-axis current.

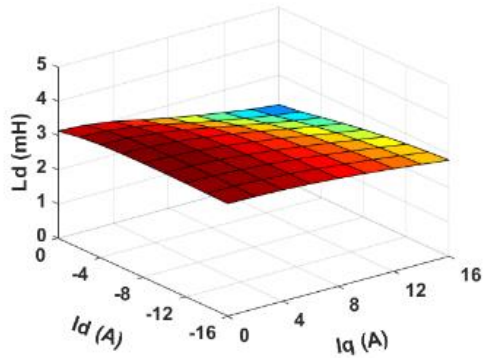

(a) 12-slot/8-pole SPM

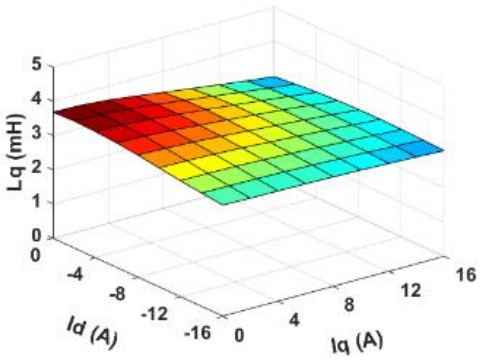

(b) 12-slot/8-pole SPM

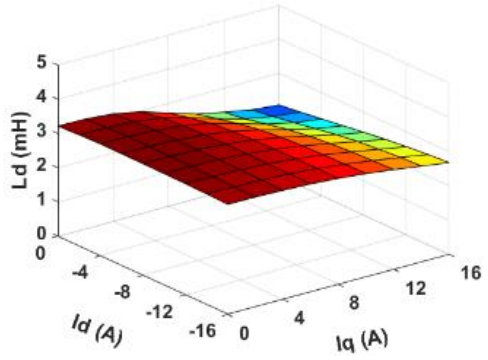

(c) 12-slot/8-pole I-IPM

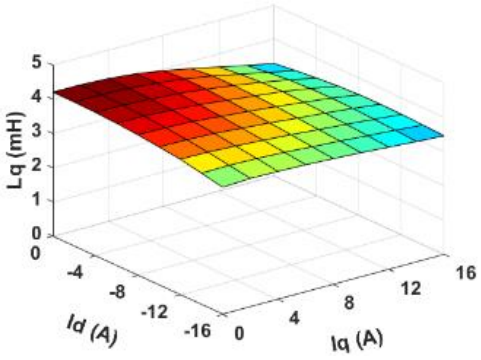

(d) 12-slot/8-pole I-IPM

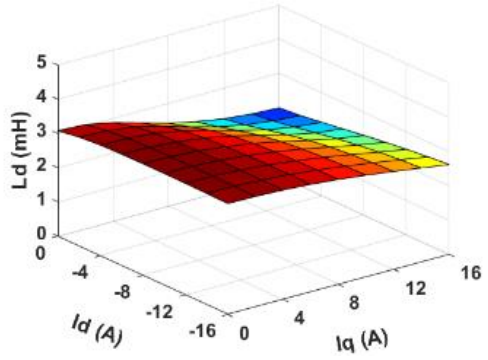

(e) 12-slot/8-pole V-IPM

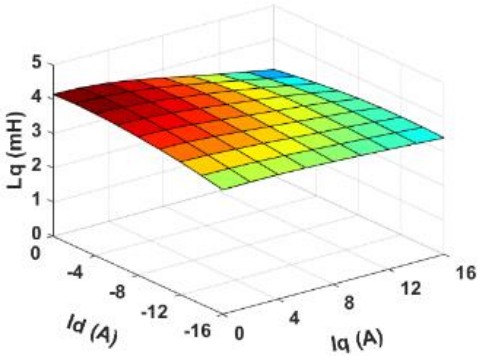

(f) 12-slot/8-pole V-IPM

Fig. 2.26. *D*-axis inductances *vs d*- and *q*-axis currents of FS-CPMs.

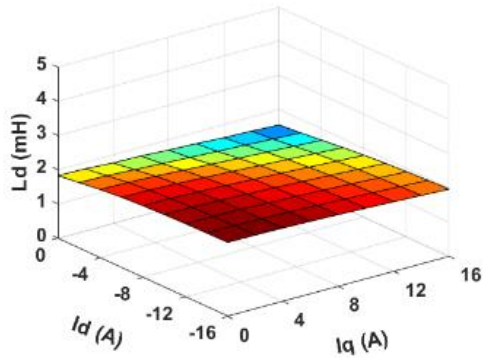

(a) 48-slot/8-pole SPM

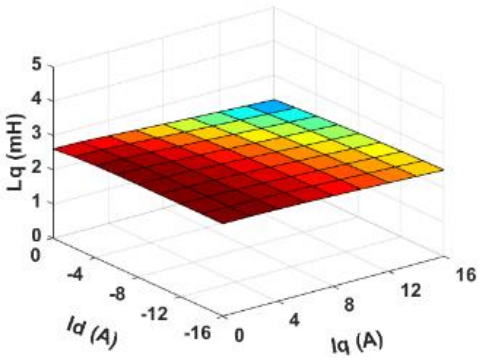

(b) 48-slot/8-pole SPM

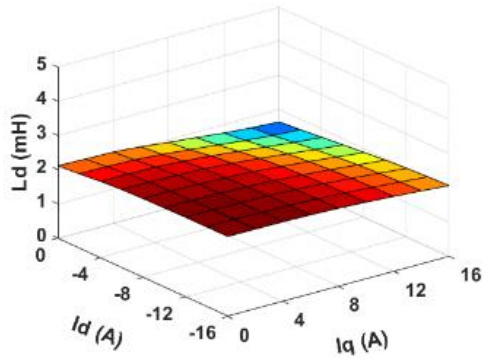

(c) 48-slot/8-pole I-IPM

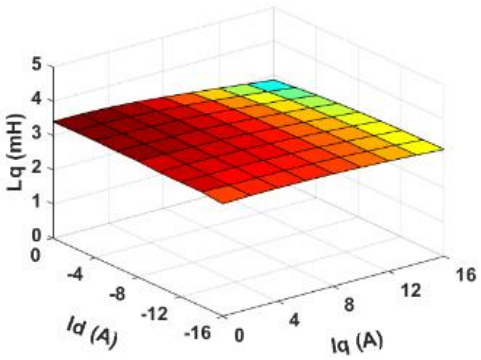

(d) 48-slot/8-pole I-IPM

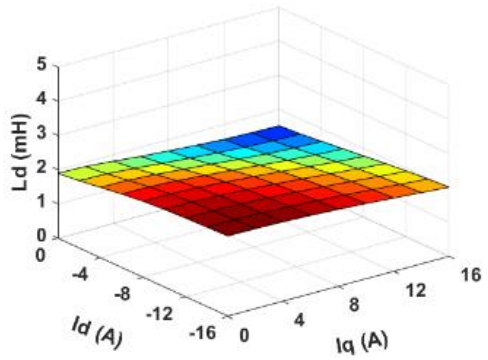

(e) 48-slot/8-pole V-IPM

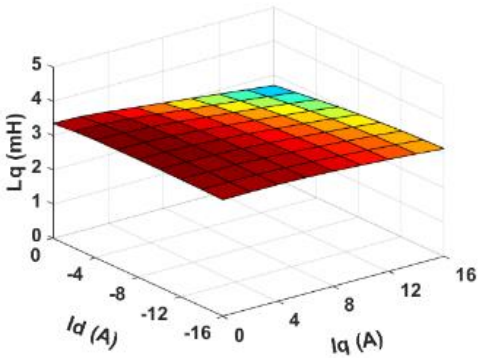

(f) 48-slot/8-pole V-IPM

Fig. 2.27. *D*-axis inductances *vs d*- and *q*-axis currents of IS-CPMs.

It can be observed from Fig. 2.27 that the FS CPMs have larger *d*- and *q*-axis inductances in comparison with the IS CPMs. Moreover, it can be found that, with increasing *d*-axis currents (from 0A to -16A), the *d*-axis inductances of all investigated CPMs will increase. This is due to the fact that the saturation level of the *d*-axis path will be reduced with the increasing negative *d*-axis currents. However, this is opposite for the *q*-axis inductances. It will decrease with the increasing *q*-axis currents because of the more saturated *q*-axis path caused by the increasing positive *q*-axis currents. In addition, it can be found that the influences of *d*- and *q*-axis currents on the *d*- and *q*-

axis inductances of the FS CPMs are more significant than the IS CPMs. This is mainly due to the fact that the saturation levels of the FS CPMs are higher than those of the IS CPMs, as discussed before.

E. PM Eddy Current Losses

In this section, the PM eddy current losses at rated current are investigated for the CPMs with different rotor structures and also winding configurations. The PM eddy current losses of investigated CPMs at rated current and at 400rpm are shown in Table 2.5. The overall PM eddy current losses are quite low for all machines mainly due to relatively low rotor speed and small machine size. However, relatively speaking, it can be found that the PM eddy current losses of the CPMs with IPM rotors, especially with the V-IPM rotors, are significantly lower in comparison with the CPMs with SPM rotors, regardless of FS or IS winding. The reason is that the iron bridges in IPM rotors above the flux barriers are able to divert the armature space-harmonic fluxes away from the PMs, and such fluxes are regarded as the main cause of induced PM eddy current losses [126]. This phenomenon can also be validated by the flux density vector distributions of all the investigated CPMs as shown in Fig. 2.33.

Table 2.5 PM eddy current losses of investigated CPMs @ rated current (7.34Arms) and @ 400rpm.

	FS	IS
SPM	20 (mW)	0.4 (mW)
I-IPM	0.3 (mW)	0.2 (mW)
V-IPM	0.1 (mW)	0.2 (mW)

2.3.2. Dynamic Characteristics

The dynamic characteristics of the investigated CPMs including the torque-speed, the power-speed and the power factor-speed curves are shown in Fig. 2.28. The control strategy is still SVPWM which is the same as section 2.2.2.A. It is assumed that the maximum inverter current (10.38A) and the maximum DC-bus voltage (40V) are the same for all investigated CPMs. It can be found that the CPMs with IPM rotors have wider speed ranges compared with their counterparts with SPM rotors, regardless of FS or IS winding. It is well established in [127] that flux weakening capability is dependent on the ratio defined as $L_d \times I_{max}/\varphi_m$, where I_{max} is the maximum inverter current and φ_m is the PM flux linkage. For the FS CPMs, their *d*-axis inductances are quite similar

but the FS CPMs with IPM rotors have lower PM flux linkages than the FS CPM with SPM rotor. As a result, the former will have better flux weakening capabilities. It is the same conclusion for the IS CPMs.

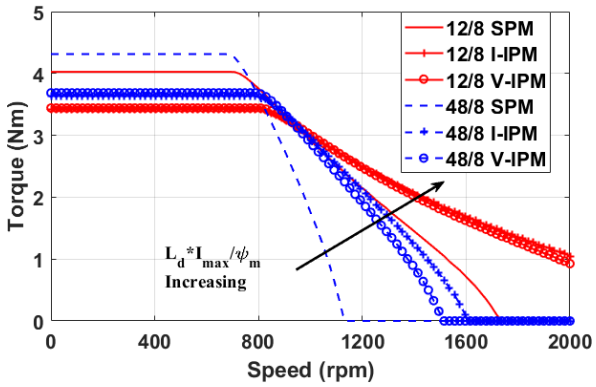

(a) Torque-speed curves

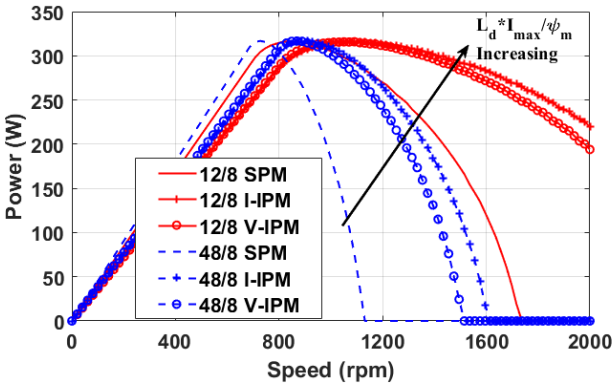

(b) Power-speed curves

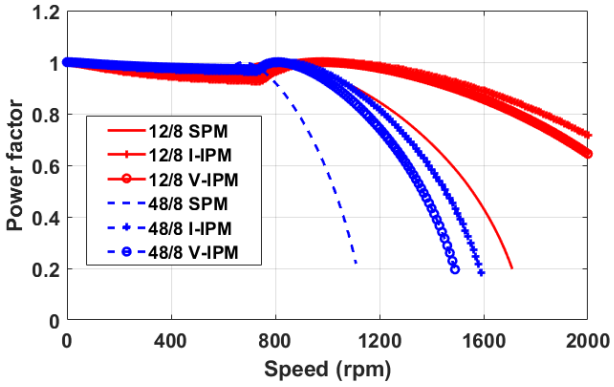

(c) Power factor-speed curves

Fig. 2.28. Torque-speed curves, power-speed curves and power factor-speed curves of the investigated CPMs.

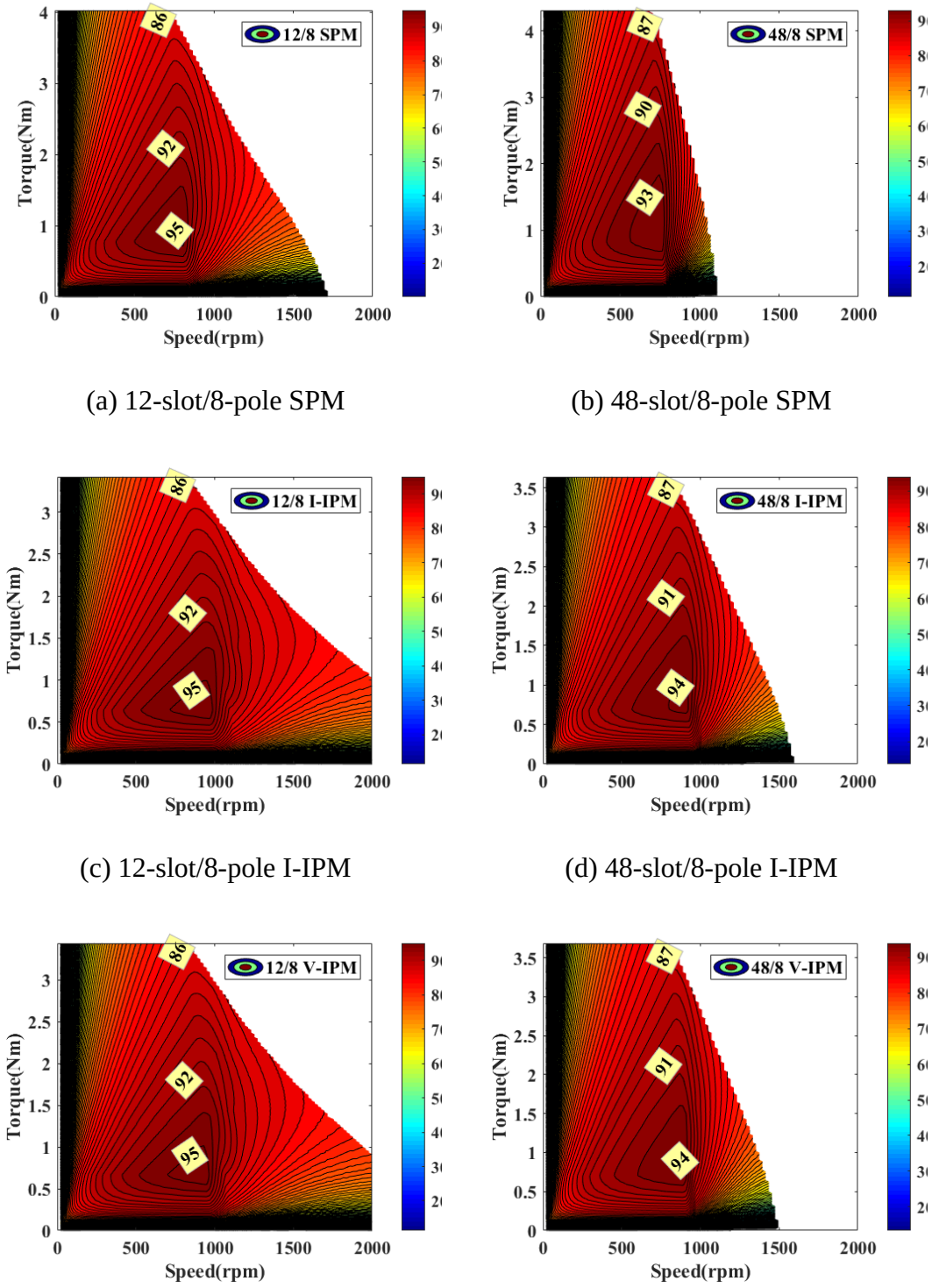

(a) 12-slot/8-pole SPM (b) 48-slot/8-pole SPM

(c) 12-slot/8-pole I-IPM (d) 48-slot/8-pole I-IPM

(e) 12-slot/8-pole V-IPM (f) 48-slot/8-pole V-IPM

Fig. 2.29. Efficiency maps of the investigated CPMs.

The efficiency maps of investigated CPMs are shown in Fig. 2.29. It is worth noting that the efficiency differences between the CPMs with different rotor structures are quite small. This is mainly due to the relatively small size of the investigated machines

leading to negligible iron losses and PM eddy current losses. The overall efficiencies of the IS-CPMs are slightly lower in comparison with the FS-CPMs, this is mainly due to the fact that the IS-CPMs have longer end-windings compared with the FS-CPMs and the copper losses are dominant in the investigated CPMs with such small dimensions.

2.3.3. Demagnetization Withstand Capability

The irreversible demagnetization of permanent magnets is usually caused by high temperature and/or high *d*-axis current. This is particularly the case for EV applications where the traction machines are often operating at high temperature environment and high *d*-axis current is also needed for flux weakening. Therefore, this section will focus on the investigation of the demagnetization withstand capabilities of CPMs with different rotor structures.

When an electrical machine is operating at the rated condition, it will have a stable temperature rise when it reaches the thermal steady state. In the meantime, the characteristic of permanent magnets changes with the temperature. This means that the electromagnetic performances such as open-circuit flux linkages at thermal steady-state could be lower than the initial state, i.e. reversible or irreversible magnet demagnetization. In order to have a clear comparison of the demagnetization of all investigated CPMs, a three-phase short-circuit fault is introduced when the CPMs reach their highest temperatures at thermal steady state. Under such condition, the short-circuit current will experience an electrical transient state with the highest peak amplitude before it reaches the electrical steady state. Although the duration of the electrical transient state is quite short compared to the thermal transient state, the peak *d*-axis current may cause a significant demagnetization which might be irreversible. Therefore, the demagnetization is analysed in this section. A 3D FEM thermal model including end-windings and end-caps is built for each CPM and their steady state temperature distributions are calculated by using the losses obtained from the 2D electromagnetic FEM as the heat sources. Then the steady-state temperatures are fed into the 2D electromagnetic FEMs to analyse the demagnetization caused by the peak short-circuit currents when the three-phase short-circuit fault is introduced.

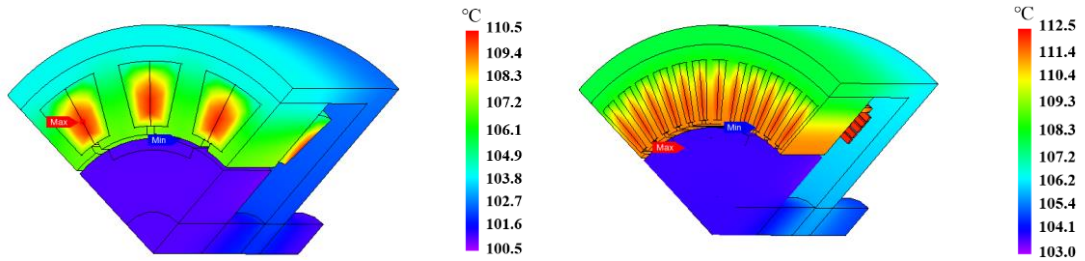

(a) 12-slot/8-pole SPM

(b) 48-slot/8-pole SPM

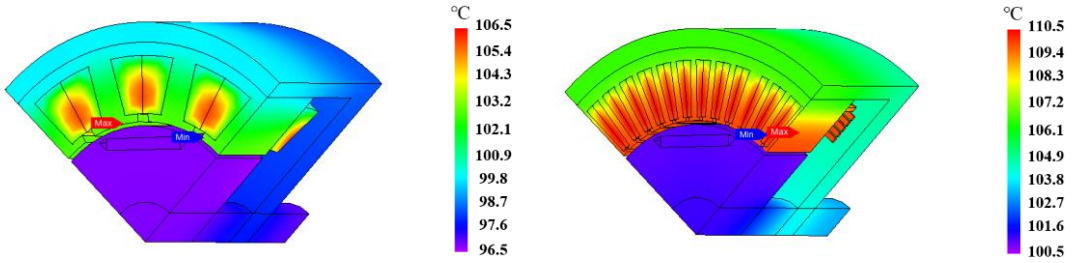

(c) 12-slot/8-pole I-IPM

(d) 48-slot/8-pole I-IPM

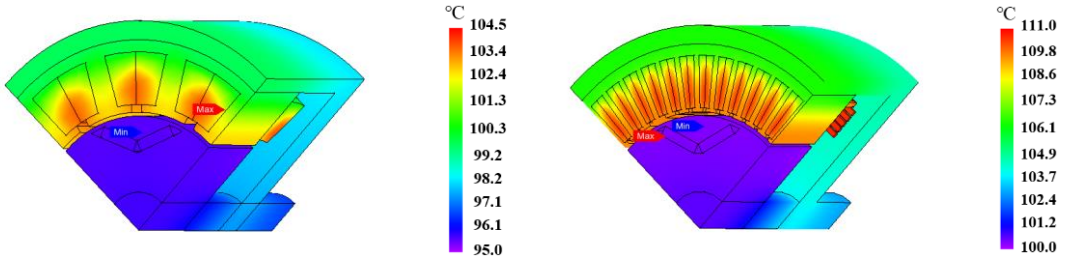

(e) 12-slot/8-pole V-IPM

(f) 48-slot/8-pole V-IPM

Fig. 2.30. Steady-state temperature distributions of the investigated CPMs with rated current (7.34A$_{rms}$) and at 400rpm.

Temperature distributions of all the investigated CPMs at steady state are shown in Fig. 2.30, where the speed and currents are both at rated values and the ambient temperature is 20℃. It can be seen that the highest temperature (around 110℃) is in the windings and the magnets have temperatures of around 100℃. Then a three-phase short-circuit fault is introduced, which will generate demagnetizing flux just like the *d*-axis flux generated by armature currents during flux weakening operation. Under this situation, the short-circuit current can be calculated, as shown in Fig. 2.31. It can be found that the CPMs with SPM rotors have the highest peak short-circuit *d*-axis currents compared with their counterparts with IPM rotors. This is mainly due to their relatively high PM flux linkages but low *d*-axis inductance.

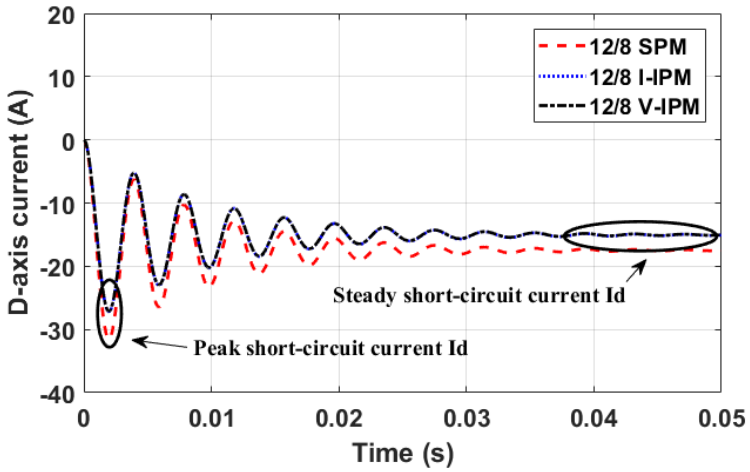

(a) FS CPMs

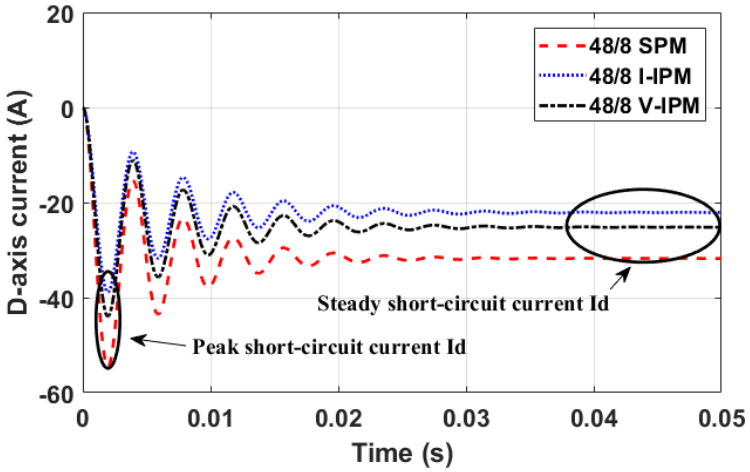

(b) IS CPMs

Fig. 2.31. Transient *d*-axis short-circuit currents of FS and IS CPMs.

Then, the CPMs are supplied with their corresponding peak short-circuit *d*-axis currents and the flux densities within the PMs when the rotors are fixed at the *d*-axis are shown in Fig. 2.32. It is worth noting that the upper limit of the flux density is set as 0.28T here which is the knee point for the N35H PM material at 100℃. Thus, the coloured parts of the PMs indicate the areas that have been irreversibly demagnetized. It can be observed that the irreversible demagnetizations are very slight for all investigated CPMs having IPM rotors with only the edges of magnets demagnetized. However, for CPMs having SPM rotors, their magnets will experience severe demagnetization around the centre area. On one hand, this is because the relatively large peak transient short-circuit currents as shown in Fig. 2.31. On the other hand, due to

the proximity to the air-gap, the demagnetization currents can easily penetrate into the PMs, which could cause demagnetization.

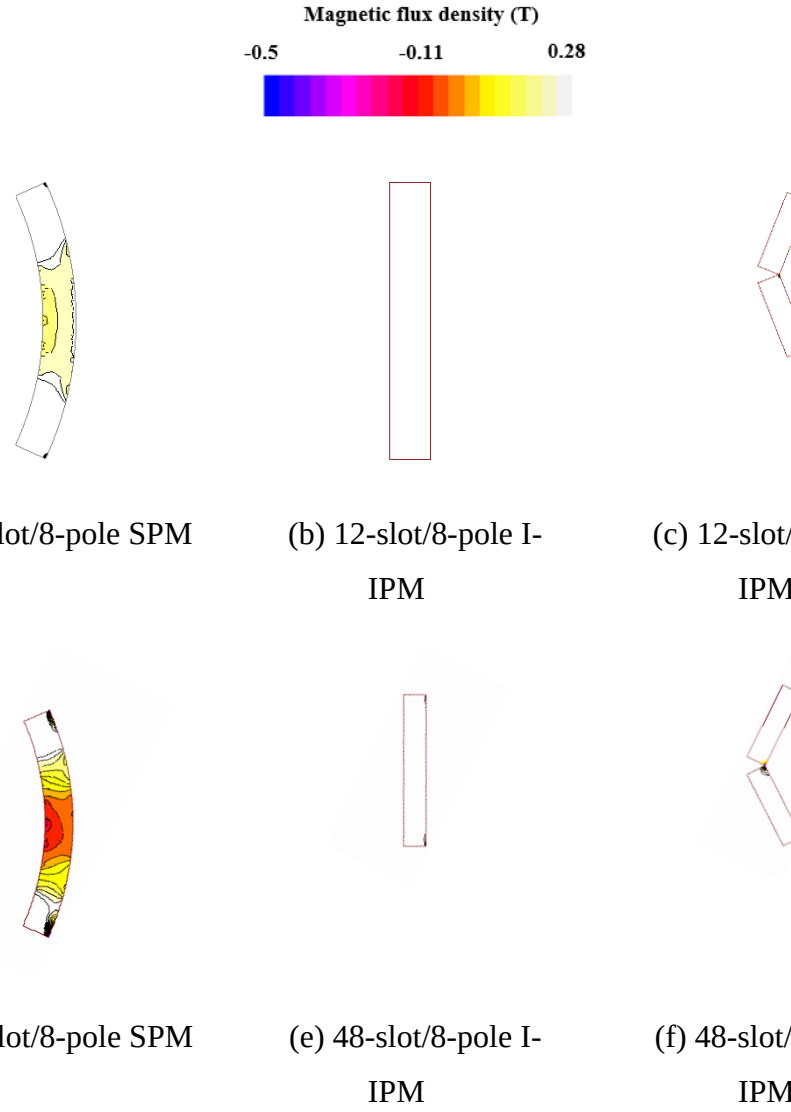

(a) 12-slot/8-pole SPM (b) 12-slot/8-pole I-IPM (c) 12-slot/8-pole V-IPM

(d) 48-slot/8-pole SPM (e) 48-slot/8-pole I-IPM (f) 48-slot/8-pole V-IPM

Fig. 2.32. Flux density distribution within one magnet that experiences the highest demagnetization.

This finding can also be supported by the distributions of the flux density vectors of all the investigated CPMs as shown in Fig. 2.33. It can be observed from Fig. 2.33 (a) and (d) that significant amount of demagnetizing fluxes can penetrate into the PMs directly. However, this is less significant for the CPMs with IPM rotors which are shown Fig. 2.33 (b), (c), (e) and (f). This is due to the fact that the PMs in the CPMs with IPM rotors are buried into the rotor iron. The rotor iron has shielding effect for the armature flux and the iron bridges around the flux barriers can divert the armature flux away from the PMs. Thus, under the three-phase short-circuit conditions, the

demagnetization withstand capabilities of the CPMs with IPM rotors are much better than their counterparts with SPM rotors.

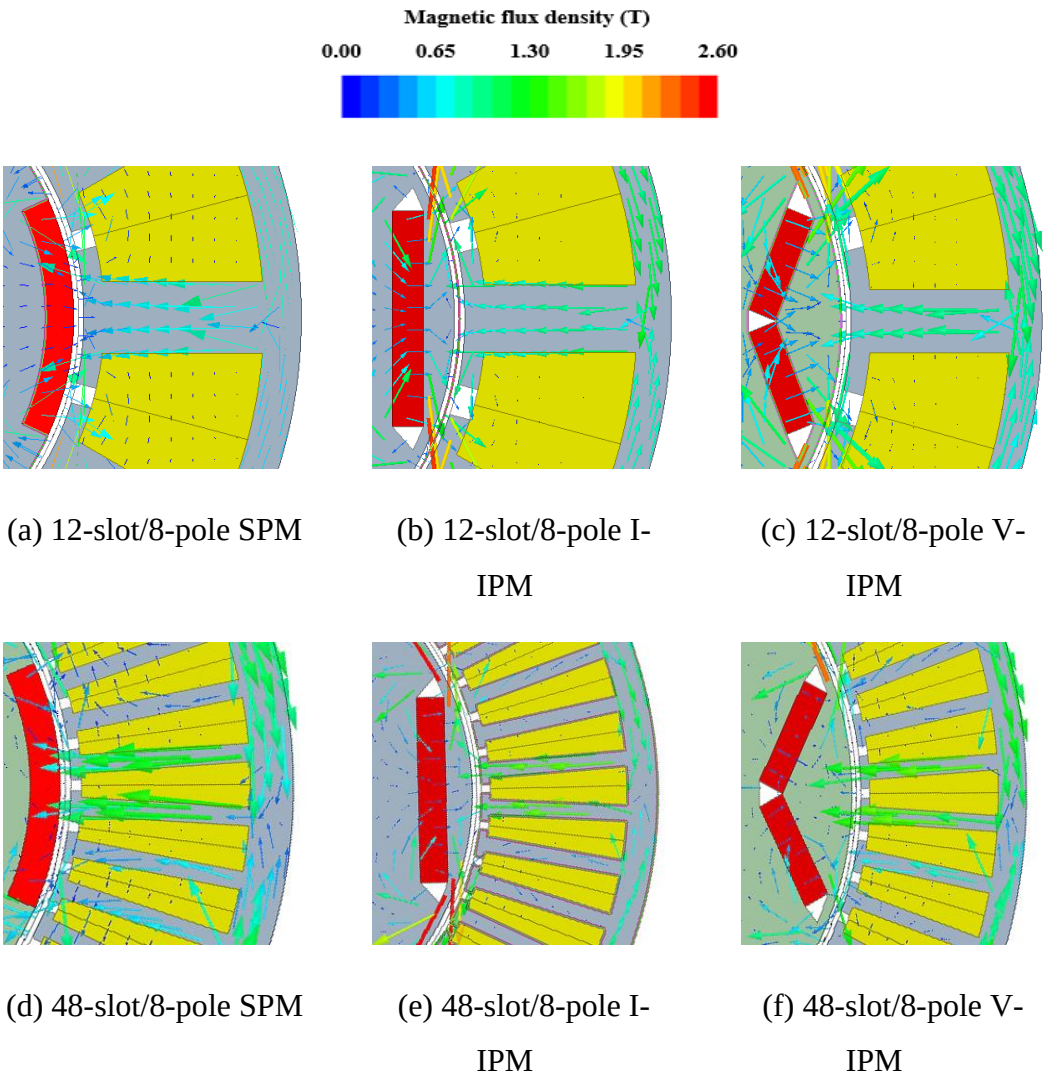

(a) 12-slot/8-pole SPM (b) 12-slot/8-pole I-IPM (c) 12-slot/8-pole V-IPM

(d) 48-slot/8-pole SPM (e) 48-slot/8-pole I-IPM (f) 48-slot/8-pole V-IPM

Fig. 2.33. Flux density vector distributions. Each magnet is experiencing the highest demagnetization.

2.3.4. Experimental Validation

All results shown in previous sections are from FEA predictions. The experimental tests are needed to validate the FEA results. Based on the FEA predictions, the CPMs with SPM rotor structure have the highest average torques and considering the fact that FS machines are relatively easy to be built, thus the FS (12-slot/8-pole) SPM CPM is selected to be the prototype machine.

A. Prototypes of FS-SPM CPM

A 12-slot/8-pole CPM prototype with the SPM rotor structure has been built and the machine parameters are given in Table 2.4. The rotor and stator of prototype machine are shown in Fig. 2.34.

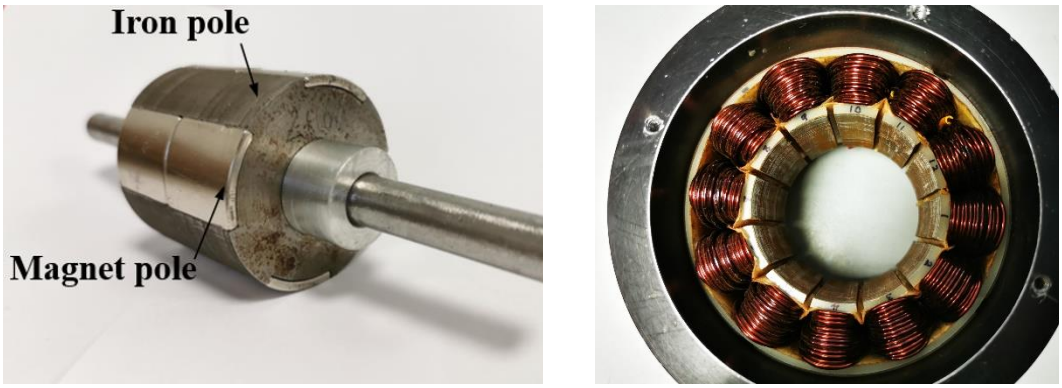

(a) 8-pole SPM CP rotor

(b) 12-slot stator with DL winding configuration

Fig. 2.34. Prototype machine.

B. Phase Back-EMF

The waveforms and spectra of the measured and predicted phase back-EMFs are shown in Fig. 2.35. A good agreement can be observed between the measured and predicted results. The slight difference is mainly due to the PM end flux leakage in CPM and this end effect is neglected in the 2D FE model [56].

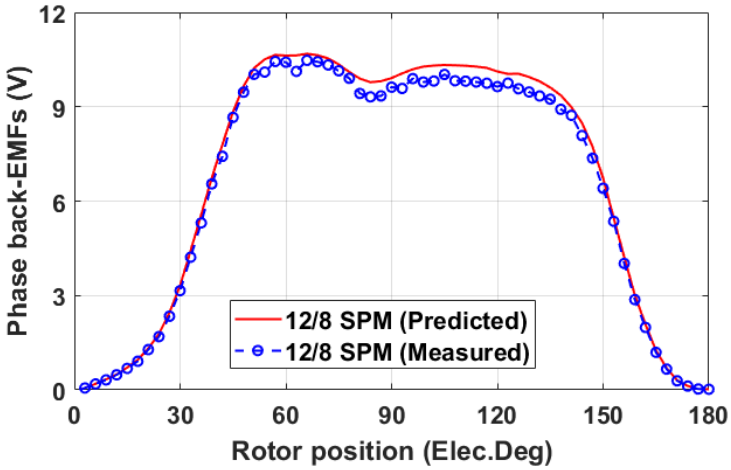

(a) Waveforms

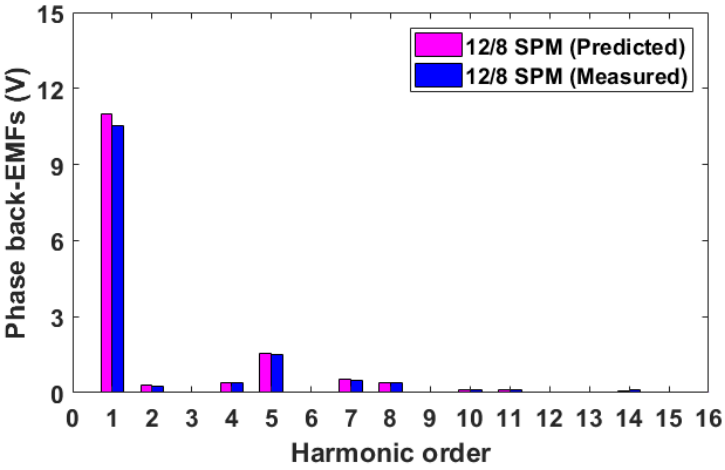

(b) Spectra

Fig. 2.35. Predicted and measured phase back-EMFs at 400 rpm.

C. Cogging Torque

In order to measure the cogging torque, a test rig can be set up as shown in Fig. 2.36 using the method proposed in [128]. It can be seen that the prototype machine is fixed by the jaw of lathe and the rotor shaft is equipped with a balance beam whose end is pointed on a digital weight gauge. When the lathe rotates, the stator can be rotated following the lathe which means the relative position between the stator and rotor is changing. Thus, the cogging torque at each rotor position can be calculated using (2.11) by reading the weight which is shown on the digital weight gauge. In (2.11), L is the length from the centre of rotor shaft to the position of the balance beam on the digital weight gauge, $F_{reading}$ is the reading from the digital gauge and the M_{pre_load} is the pre-

load weight which is shown in Fig. 2.36. Moreover, this method can also be utilized to measure the static torque which is shown in the following section.

$$T_c = L(F_{reading} - M_{pre\_load}) \tag{2.11}$$

The cogging torque of the 12-slot/8-pole SPM CPM has been measured and shown in Fig. 2.37. A general good agreement can be reached. There are some unexpected harmonics in the measured cogging torque, this is mainly due to the manufacturing tolerance.

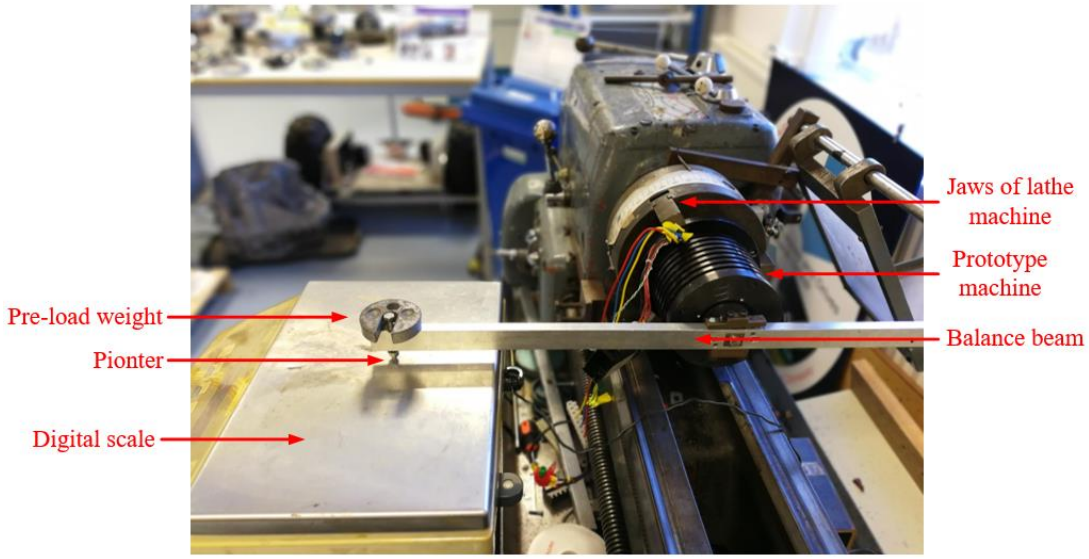

Fig. 2.36. Test rig set-up for measuring the cogging torque.

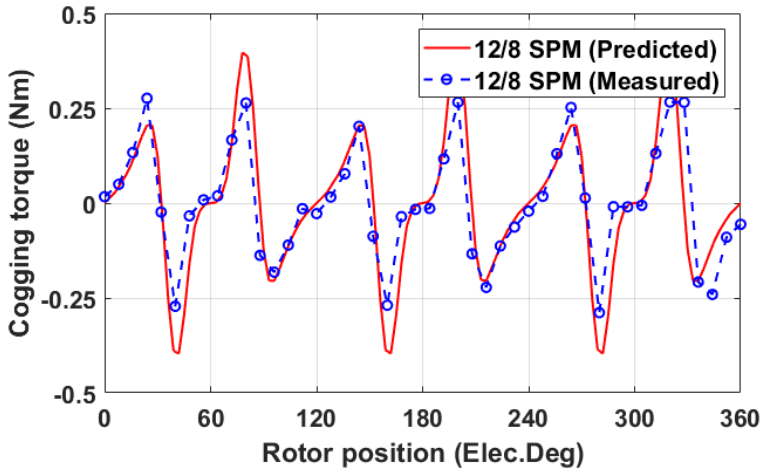

(a) Waveforms

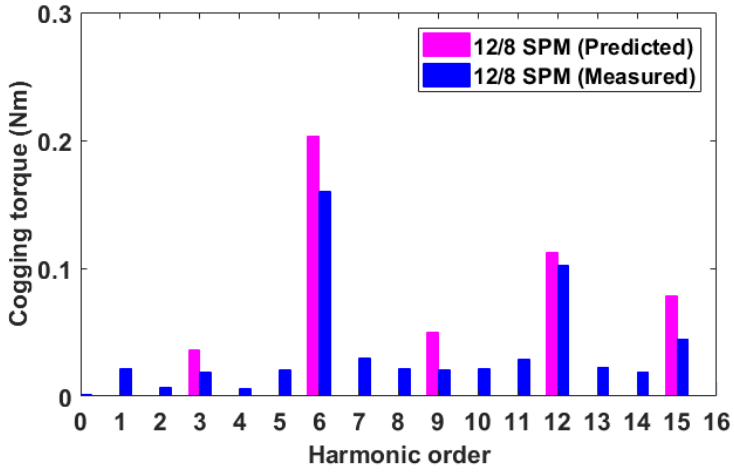

(b) Spectra

Fig. 2.37. Predicted and measured cogging torques.

D. On-load Static Torque

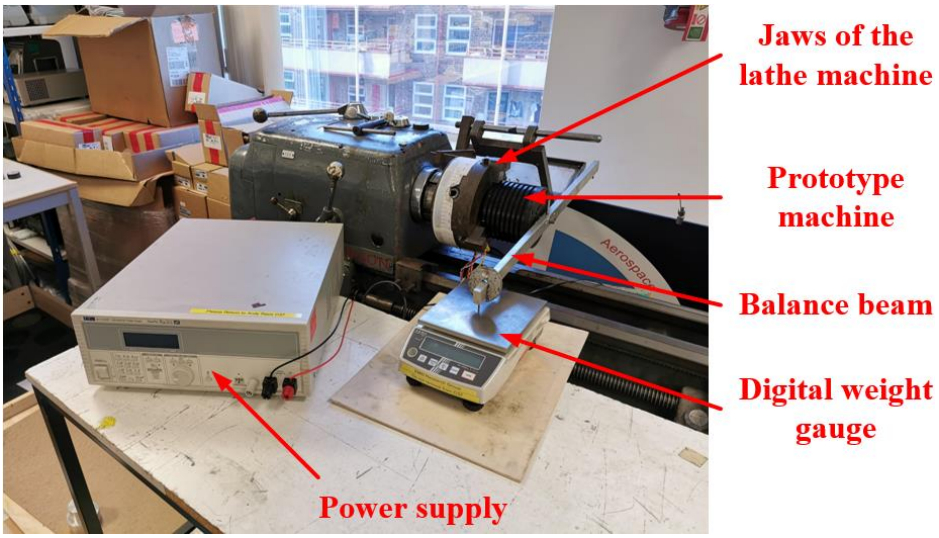

Fig. 2.38 Test rig set-up for measuring the on-load static torque.

The on-load static torque has also been measured by using the method mentioned in the cogging torque section and test rig is shown in Fig. 2.38 while supplying the 3-phase currents such as $I_A = I$, $I_B = -I/2$ and $I_C = -I/2$, where I is a dc current, which can be changed to simulate different load conditions. I also represents the current amplitude of an equivalent 3-phase sinewave current supply. To avoid the overheating of the prototype machine, 3A is selected as the dc current to achieve the waveform of static torque versus rotor position which is presented Fig. 2.39. The different rotor positions here can be considered as the equivalent changing current phase current angle. Moreover, the static torque under different phase *RMS* currents are measured and compared with the predicted results. It is worth noting that the rotor is fixed at the position where the maximum average torque can be obtained. The predicted and measured results are shown in Fig. 2.39. The slight difference between the measured and predicted static torque is due to neglecting the end effect in the 2D FE model.

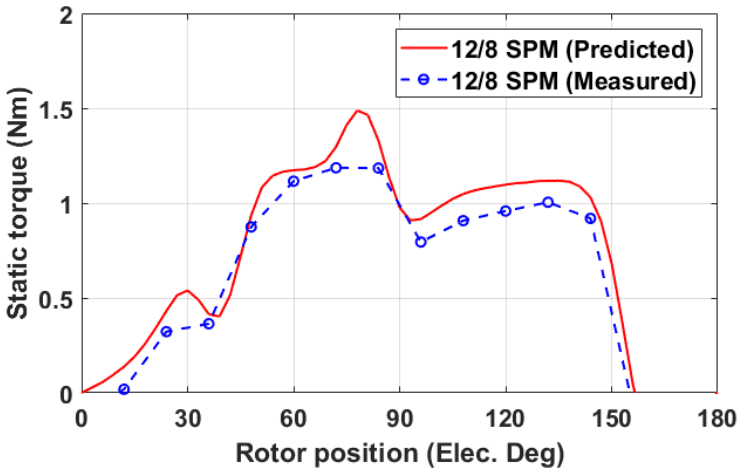

(a) Predicted and measured static torques *vs* rotor position

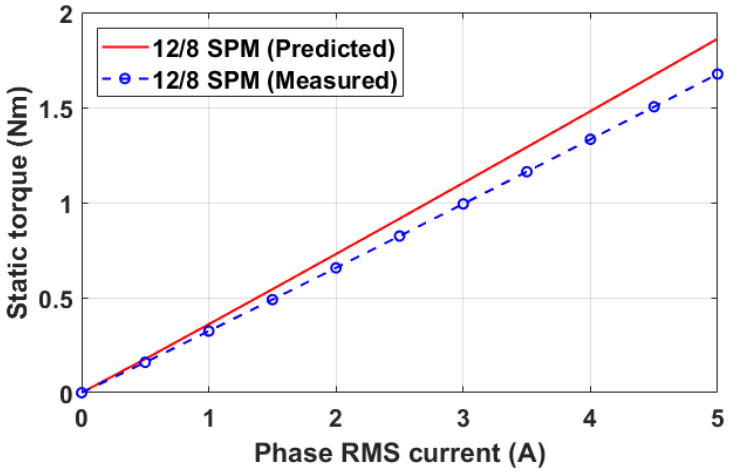

(b) Predicted and measured static torques *vs* phase RMS current

Fig. 2.39. Predicted and measured static torques.

E. Self- and Mutual Inductances

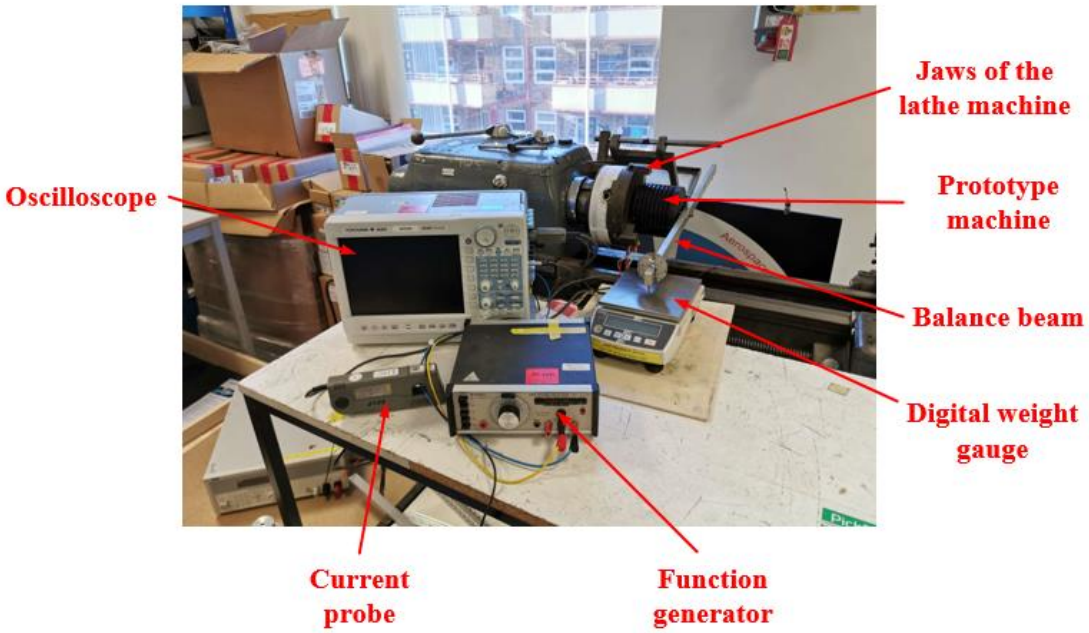

Fig. 2.40. Test rig set-up for measuring the inductances.

$$\begin{cases} L_i(\theta) = \sqrt{\dfrac{(V_i/I_i)^2 - R^2}{2\pi f}} \\ M_{ij}(\theta) = \dfrac{V_j}{2\pi f I_i} \end{cases} \tag{2.12}$$

where V_i and V_j are the amplitude of the measured voltages in phase *i* and *j*, while I_i is the amplitude of the measured phase current in phase *i*.

In order to measure the phase self- and mutual inductances at different rotor positions, the test rig is set up as shown in Fig. 2.40. It can be seen that the prototype machine is fixed on the lathe and the stator can be rotated while the rotor is locked. The phase A is supplied with a sinusoidal voltage with the amplitude of 3V and frequency of 100Hz. The phase resistance is approximately 0.6 Ω. Then the self $[L_i(\theta)]$ and mutual $[M_{ij}(\theta)]$ inductances can be calculated by (2.12) [84].

The measured and predicted results are shown in Fig. 2.41. The trend of the measured inductances matches well with the predicted inductances. It is worth noting that neglecting the end-winding effect in the 2D-FE model results in the difference between the measured and predicted inductances which means the measured inductances are slightly higher than the predicted results.

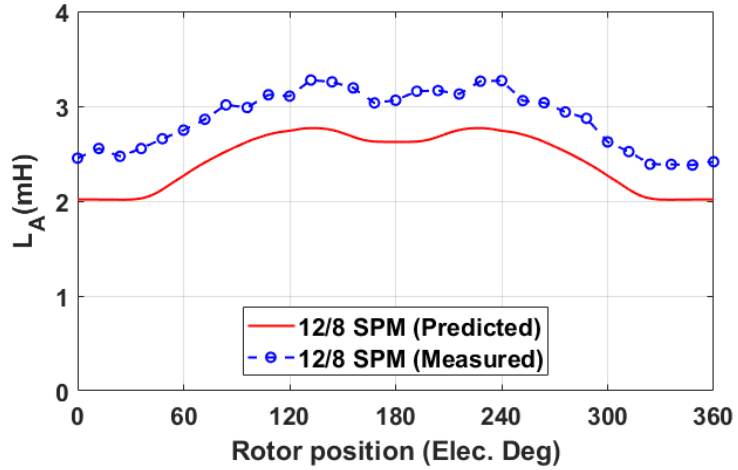

(a) Predicted and measured self-inductances *vs* rotor position

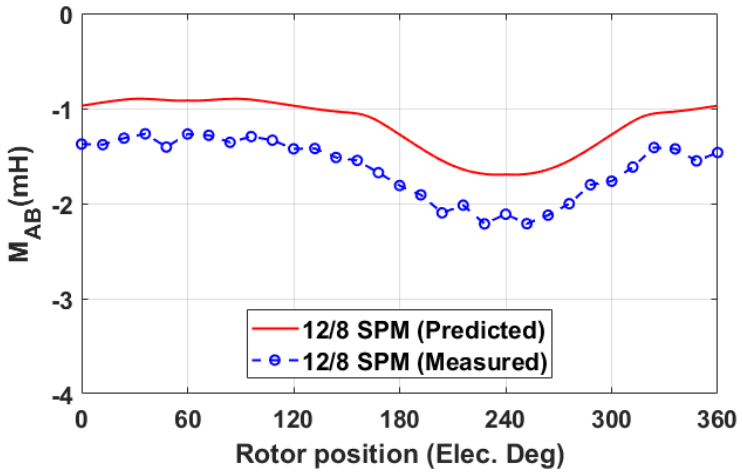

(b) Predicted and measured mutual inductances *vs* rotor position

Fig. 2.41. Predicted and measured self- and mutual inductances.

F. Dynamic Test

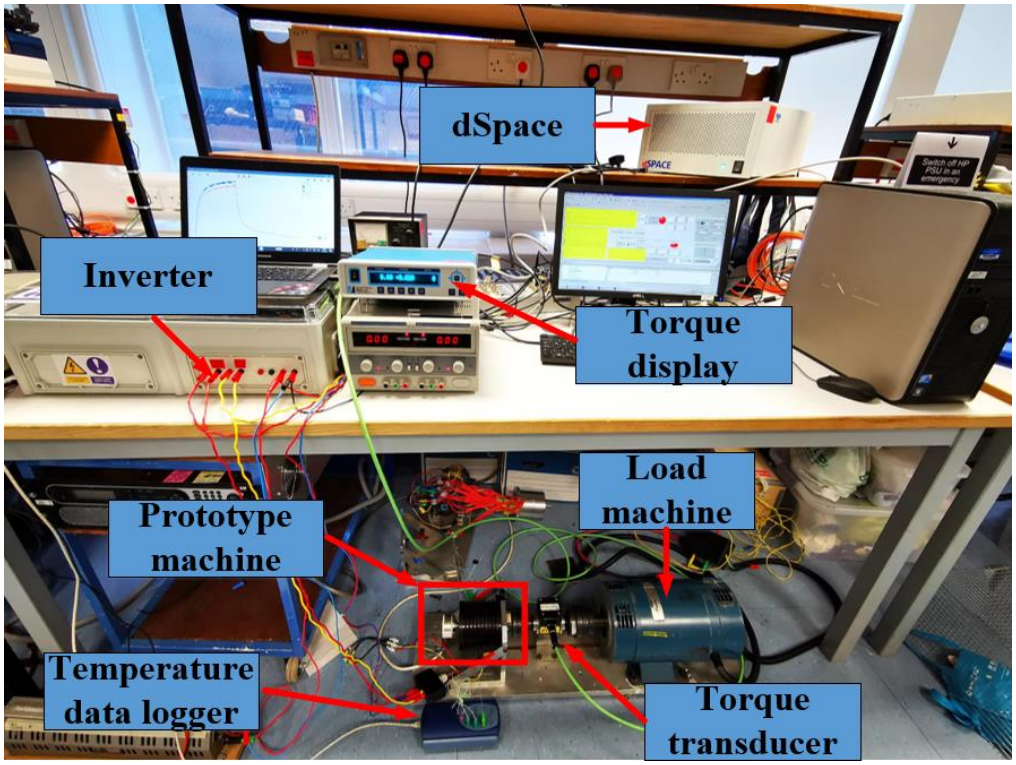

Fig. 2.42. Test rig set-up for the dynamic test.

Apart from the static tests, some dynamic tests including the torque- and efficiency-speed curves are also carried out. The test rig is shown in Fig. 2.42. It should be noting here that the dc link voltage for all dynamic tests is set to 18 V and the maximum phase peak current is 6 A, which is limited by the inverter capacity.

As mentioned before, the SVPWM control strategy is used here in order to achieve the maximum utilization of DC-bus voltage which means the voltage limitation can be considered as $V_{dc}/\sqrt{3}$ and the voltage, current limitations should satisfy (2.7) and (2.8).

When considering the voltage limitations as expressed in (2.8), the variations of *dq*-axis flux linkages caused by the different rotor positions are usually neglected which can be seen from (2.13) and the average values are usually adopted. However, it is worth noting that the prototype machine has severe voltage distortion (VD) due to rich harmonics in the phase back-EMFs, especially the even-harmonics as can be seen in Fig. 2.21. This means that it is essential to take the variations of *dq*-axis flux linkages into account when calculating the torque-speed curve and the voltages can then be expressed as (2.14), where $\psi_d(i_d, \theta)$ and $\psi_q(i_q, \theta)$ represent the *d*-axis flux linkages

vs d-axis currents and rotor positions, *q*-axis flux linkages *vs q*-axis currents and rotor positions, respectively.

$$\begin{bmatrix} v_d \\ v_q \end{bmatrix} = R \begin{bmatrix} i_d \\ i_q \end{bmatrix} + \begin{bmatrix} 0 & -\omega & 0 \\ \omega & 0 & 0 \end{bmatrix} \begin{bmatrix} \psi_d \\ \psi_q \end{bmatrix} + \frac{d}{dt} \begin{bmatrix} \psi_d \\ \psi_q \end{bmatrix} \tag{2.13}$$

$$\begin{bmatrix} v_d \\ v_q \end{bmatrix} = R \begin{bmatrix} i_d \\ i_q \end{bmatrix} + \begin{bmatrix} 0 & -\omega & 0 \\ \omega & 0 & 0 \end{bmatrix} \begin{bmatrix} \psi_d(i_d, \theta) \\ \psi_q(i_q, \theta) \end{bmatrix} + \frac{d}{dt} \begin{bmatrix} \psi_d(i_d, \theta) \\ \psi_q(i_q, \theta) \end{bmatrix} \tag{2.14}$$

According to the theory in [129], the machine will enter into flux-weakening operation earlier due to the VD, meaning that the flux weakening capability will be deteriorated. Therefore, the torque-speed curves with (real case) or without (ideal case) the VD being considered have been calculated using the method proposed in [129], as shown in Fig. 2.43. It is evident that the measured torque-speed curve matches well with the predicted curve when the VD is considered. The slight difference in the average torque is mainly due to the fact that the shaft flux-leakage and end-effect have not been taken into account in the 2D FE model.

Similarly, the efficiency-speed curves under conditions with and without the VD being considered are also calculated and compared to the measured results, as shown in Fig. 2.43 (b). It can be observed that the measured efficiency-speed curve shows a better agreement with the predicted one when the VD is considered, especially in the flux weakening region. This is mainly due to the fact that the input current needs to be reduced in the flux weakening region when the VD is considered according to [129], leading to a reduction in the total input power and to a potential increase in the efficiency. It is worth noting that the measured overall efficiency is lower in comparison with the results shown in section 2.3.2, the reason is that copper wires with smaller diameter are used in the prototype machine to make the winding process easier, resulting in lower filling factor and higher copper losses.

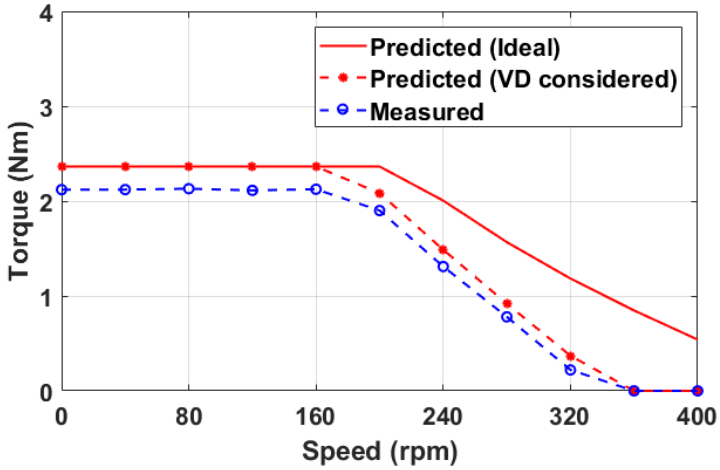

(a) Predicted and measured torque-speed curves

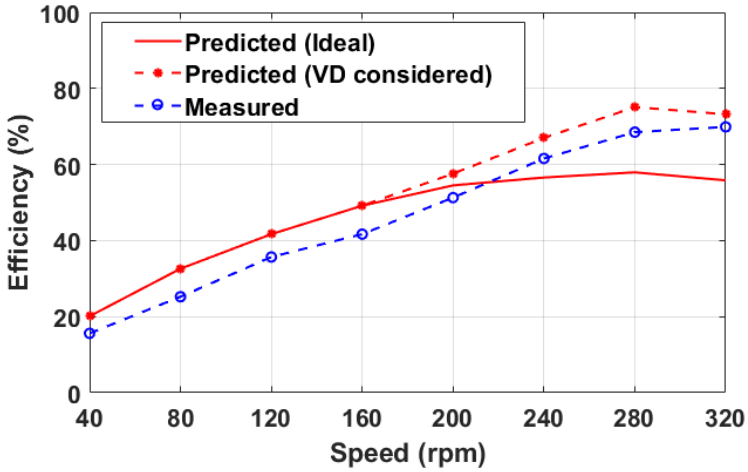

(b) Predicted and measured efficiency-speed curves

Fig. 2.43. Predicted and measured torque-speed curves, and efficiency-speed curves. V_{dc}=18V and I_{max}=6A.

G. Thermal Test

In order to validate the 3D FEA thermal model, two K type thermocouples are put inside the winding of the prototype machine for measuring the transient temperatures as shown in Fig. 2.44 and their physical locations are shown in Fig. 2.45. One is to measure the temperature of the active winding (AW) in stator slots and the other is for the end-winding (EW) temperature measurement. To avoid potential overheating of the prototype machine, the thermal test condition is set as constant speed control (at 400 rpm) with a mechanical load of 55% of the rated torque. The room temperature is approximately 25°C. After 2 hours of operation, the machine is stopped and the

temperature variation during the natural cooling down process is also recorded. The measured and predicted temperature variations are shown in Fig. 2.46. The slight discrepancy is mainly due to the uncertain thermal parameters such as the convection coefficient, contact thermal resistance between different machine components and also the AC losses caused by the current harmonics that are not taken into account in the FEA thermal model.

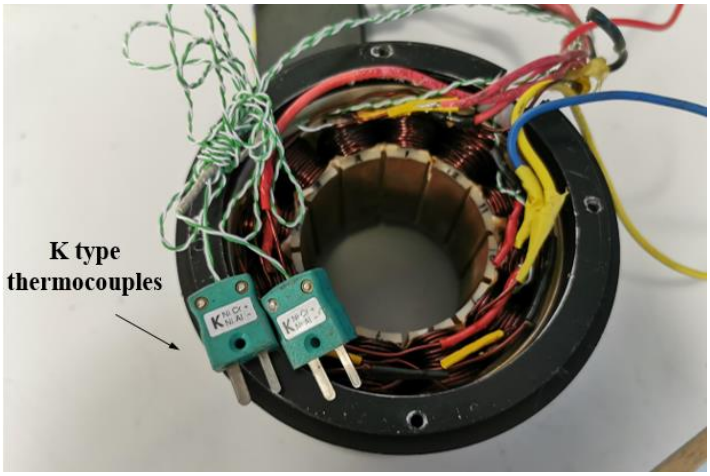

Fig. 2.44. 12-slot DL stator with K type thermocouples.

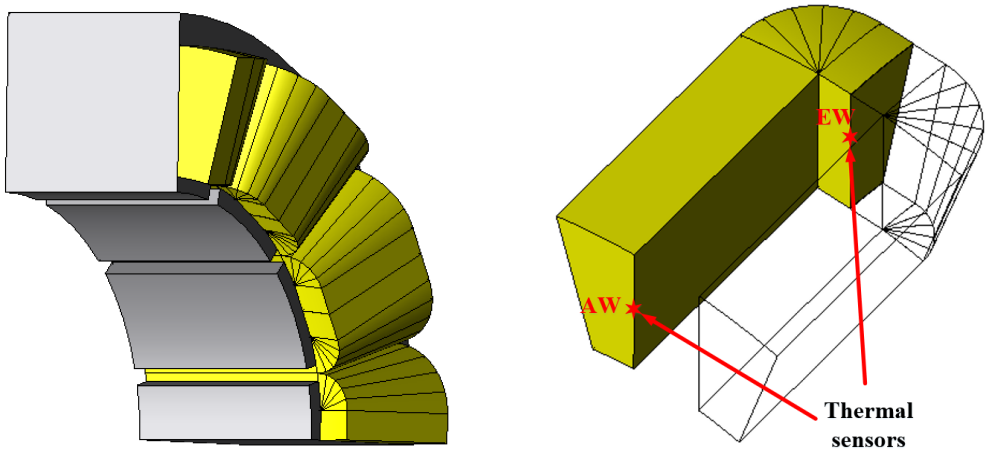

(a) (b)

Fig. 2.45. (a) 1/4 partial FEA thermal model with the end-windings included (stator). (b) locations of thermocouples.

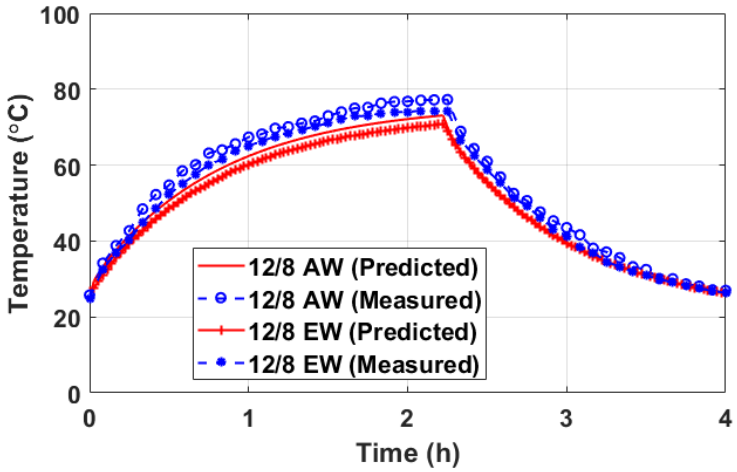

Fig. 2.46. Measured and predicted temperature variations *vs* time @ 400rpm and 55% rated torque.

2.4. Conclusion

In this chapter, the influence of winding configurations on electromagnetic performances of FS and IS-CPMs is firstly investigated. Then, the influences of different rotor structures in CPMs are investigated, including phase back-EMF, on-load torque, losses, dynamic characteristics and also demagnetization withstand capability. It is found that:

(a) The torque capability of IS-CPMs is better than the FS-CPMs. However, by adopting the DL winding configuration, the armature field reaction of the FS-CPM can be significantly reduced and the torque performance can be improved as a result.

(b) Moreover, the IS-CPMs have much lower PM eddy current losses in comparison with the FS-CPMs, which can lead to higher efficiency of the IS-CPMs. However, with larger *d*-axis inductances, the flux-weakening capability of the FS-CPMs are much better than the IS-CPMs, leading to wider speed range and wider constant power region.

(c) With the same PM volume, the CPMs with SPM rotor have better torque capability in comparison with IPM rotors, regardless of FS or IS winding.

(d) In terms of the PM eddy current losses, the CPMs with IPM rotors have much lower PM eddy current losses compared with SPM rotors, regardless of FS or IS winding.

(e) Regarding the dynamic performances, with lower phase flux linkages, the flux-weakening capabilities of the CPMs with IPM rotors are better than their counterparts with SPM rotors. With larger *d*-axis inductances, the flux-weakening capability of the FS CPMs are better than the IS CPMs.

(f) In addition, by taking the influence of temperature on the magnet working point into consideration, it is found that the demagnetization withstand capabilities of the CPMs with IPM rotors are much better than their counterparts with SPM rotors.

(g) Finally, to achieve optimal performance, some recommendations are given in Table 2.6 and Table 2.7 for selecting the best winding and rotor structures.

Table 2.6 Best windings for CPMs

Torque performance	PM loss	Flux-weakening capability	Demagnetization withstand capability	Overall losses	Efficiency
IS	IS	FS	FS/IS	IS	IS

Table 2.7 Best rotor structures for CPMs

Torque performance	PM loss	Flux-weakening capability	Demagnetization withstand capability
SPM	IPM	IPM	IPM

Chapter 3 Consequent-Pole PM Machines with E-core and C-core Modular Stators

3.1. Introduction

As mentioned in the previous chapters, the permanent magnet (PM) machines have been widely used in various applications such as electrical vehicles, more electric aircraft and renewables, etc. thanks to their advantages in terms of high torque/power density and high efficiency [130]. Meanwhile, it is also known from literature review that the consequent pole (CP) concept could be a reasonable cost-saving solution. The influences of winding configurations and rotor structures on the electromagnetic performances of CPMs have been investigated in Chapter 2.

Apart from the electromagnetic performances, the mechanical aspect and manufacturing process also need to be considered when designing electric machines, especially in wind power applications. This is because most wind power generators have large dimensions which makes the manufacturing process difficult and segmented stator are often necessary. To cope with such challenges, a modular wind generator with E-core stator and segmented rotor is proposed in [75]. Another new single tooth segmented stator core without laminated-joint has been proposed in [131]. The laminated tooth modules with pre-wound coils are coupled with a solid back iron, which ease significantly the winding process and also increase the slot fill factor. However, considerable iron losses in the solid stator holder makes such topologies less attractive in large machines. The modular structure is not only necessary in the wind power applications, but also attractive for electric vehicle (EV) applications. For example, [61] proposes a new modular stator core called 'joint-lapped core' which could be used in EV applications. The stator core can be deformed for flyer winding process and then reformed into a conventional circular shape. By using this structure and winding process, the difficulty when inserting coils into stator slots due to small slot openings can be eliminated and higher slot filling factor can be achieved, which can lead to higher overall efficiency as a result.

Moreover, modular machines with so-called 'flux gaps (FGs)' inserted in alternate stator teeth have also been proposed [79] and [84]. Such modular machines have been

investigated thoroughly in [84, 85, 89]. It is concluded that the electromagnetic performances of the machines with slot number (Ns) lower than pole number ($2p$) can be improved by selecting an appropriate FG width. In such E-core modular machines, the average torque can be significantly increased without extra PM material consumption. In other words, the PM volume usage can be effectively reduced by utilizing the modular stator structure while maintaining the same torque level compared with their non-modular counterparts.

So far, little researches have been done with regard to the feasibility of modular structures in the CPMs. Although the E-core modular CP machines (CPMs) have been compared with the modular inset SPM machines in [132], the investigation is far from being complete and only the static performances are investigated. The dynamic performances are key factors to evaluate the machines which can determine their suitability in different applications. Therefore, apart from the static performances, the dynamic performances such as on-load losses, torque-speed curves, power factor-speed curves and efficiency maps over the whole speed range will be investigated in this chapter. Therefore, the main contribution of this chapter is to reveal the full potential of modular stator structures in CPMs by investigating both the E-core and C-core modular CPMs. In addition, given the fact that the slot/pole number combinations have influence on the performances of modular machines, different slot/pole number combinations are also considered to make the investigation more comprehensive. Finally, some guidelines and recommendations under different criteria are given in the conclusion for selecting the best candidates from modular CPMs with different stator structures.

This chapter is organized as follows: firstly, the operating principle of the investigated modular CPMs is introduced based on mathematical modelling, and the phase back-EMF and electromagnetic torque production mechanisms are analysed. Then, the static performances of modular CPMs with E-core and C-core structures are thoroughly compared. Further, their dynamic performances are investigated to reveal the full potential of modular CPMs. The power factor characteristics are emphasized to consider the inverter capacity from the drive end. Finally, in order to validate the general conclusion, modular CPMs with larger dimensions are investigated.

3.2. Design Features of the Modular CPMs

The topologies of E-core and C-core modular CPMs are shown in Fig. 1. By way of example, the 12-slot/10-pole and 12-slot/14-pole are chosen for investigation in this chapter. Some general design specifications of the stators have been optimised in previous work [132] and they are kept the same for all the investigated machines, as listed in Table 1. It is also worth noting that the total PM volume of each machine is the same for a fairer comparison. In addition, the PM thicknesses of the non-modular CPMs are optimized with the aim of achieving the highest torque at the rated current. Since the total PM volume is fixed, the PM pole arc to pole pitch ratio can be easily determined according to the optimal PM thickness. As a result, the optimal PM thicknesses of the machines with 12-slot/10-pole and 12-slot/14-pole are 2.7mm, and 2.5mm, respectively. In addition, to get a clear understanding of the FG width, 12-slot/10-pole modular CPMs with two different FG widths (2mm and 4mm) are given in Fig. 3.2.

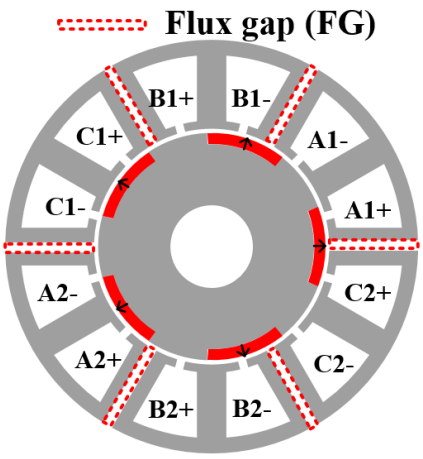

(a) 12-slot/10-pole E-core CPM

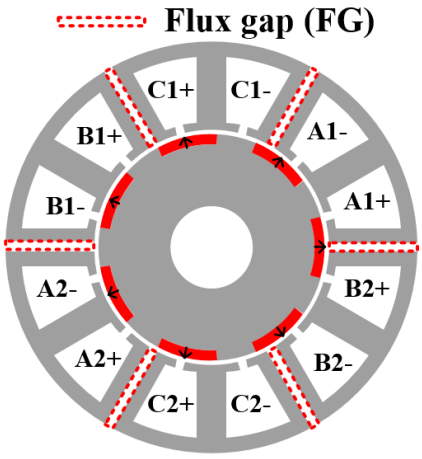

(b) 12-slot/14-pole E-core CPM

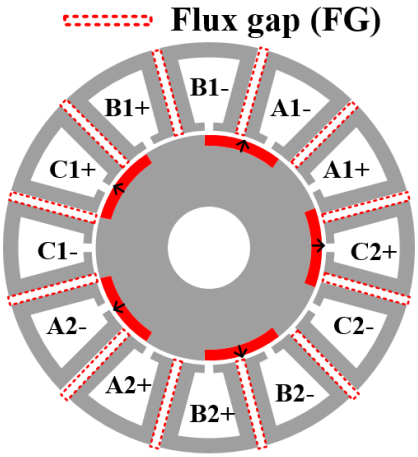

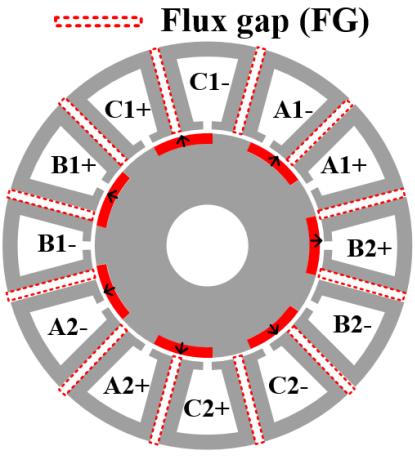

(c) 12-slot/10-pole C-core CPM (d) 12-slot/14-pole C-core CPM

Fig. 3.1. Cross-sections of the investigated modular CPMs.

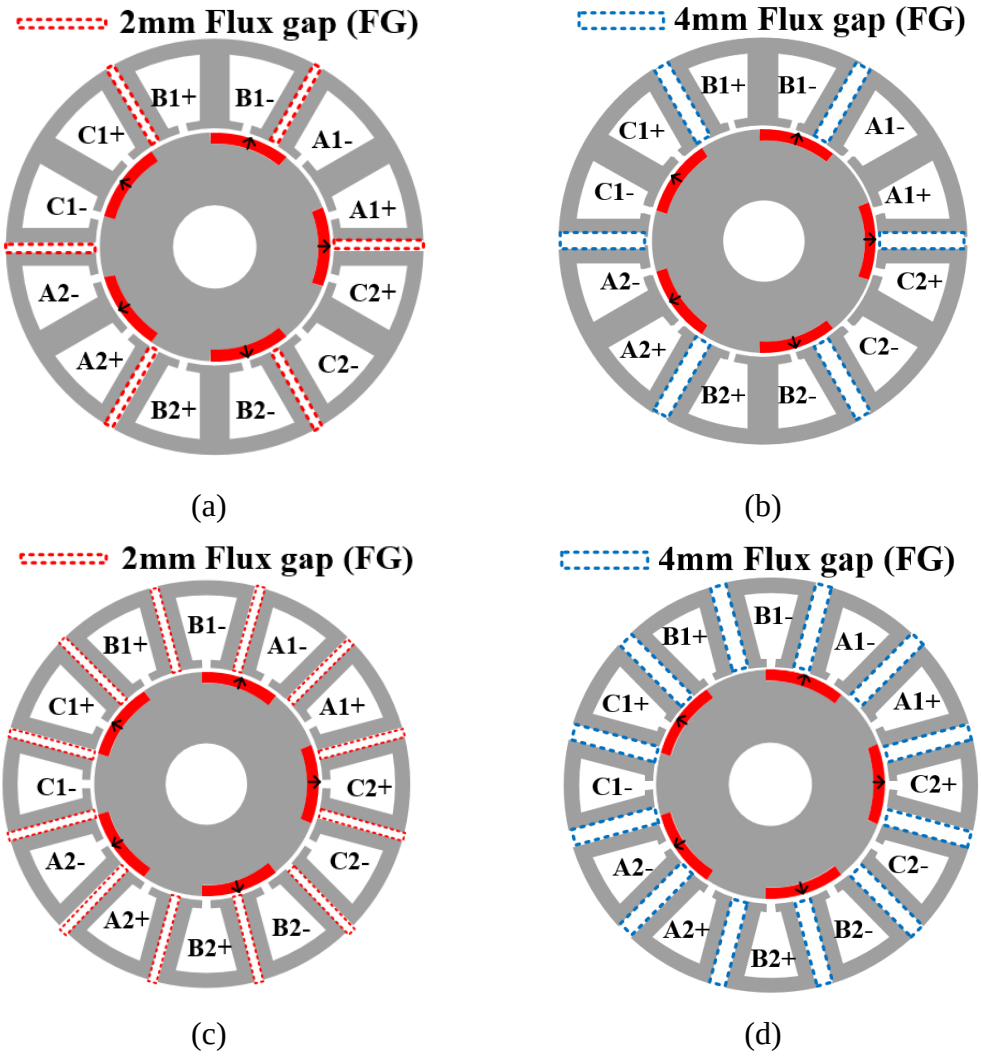

Fig. 3.2. 12-slot/10-pole E-core CPMs, (a) FG=2mm, (b) FG=4mm; 12-slot/10-pole C-core CPMs, (c) FG=2mm, (d) FG=4mm.

Table 3.1 General specifications of the modular CPMs [132]

Stator outer radius (mm)	50	Split ratio	0.57
Tooth body width (mm)	7.2	Stator yoke height (mm)	3.7
Air-gap length (mm)	1	Stack length (mm)	50
Rated current (A_{rms})	7.34	Number of turns per phase	132

For the CPMs (modular or not), their operating principle can be explained using the following mathematical models. The PM excited MMF generated by the CP rotor shown in Fig. 3.1 can be expressed by [133]:

$$f_{PM}(\theta,t)=\sum_{i=1,2,3\ldots}^{\infty}F_{PM_i}cos[ip_r(\theta-\omega_r t)] \tag{3.1}$$

where F_{PM_i} is the i-order Fourier coefficients of PM generated MMF, p_r is the rotor pole pair number, θ is the mechanical position in stationary coordinate, ω_r is the rotor speed and t is the time. Moreover, the airgap permeance model considering both stator slot openings and also flux gaps can be expressed as:

$$\Lambda_s(\theta)=\sum_{j=0,1,2,}^{\infty}\Lambda_{sj}cos(jN_{s\_equiv}\theta) \tag{3.2}$$

where Λ_{sj} is the j^{th}-order Fourier coefficients of the airgap permeance model considering both stator slot openings and also flux gaps, N_{s_equiv} is the equivalent number of stator slots. It should be noted that introducing the FGs in modular machines could change the periodicity of airgap permeance and this is the reason why the equivalent number of stator slots N_{s_equiv} is used to replace the actual number of stator slots in (3.2). In addition, N_{s_equiv} are 12, 6 and 12 for non-modular, E-core and C-core modular machines, respectively.

With the PM excited MMF and airgap permeance, the air-gap flux density produced by the PMs can be derived as:

$$\begin{aligned}B_{ag\_PM}(\theta,t)&=f_{PM}(\theta,t)\Lambda_s(\theta)\\&=\sum_{i=1,2,3\ldots}^{\infty}\sum_{j=0,1,2\ldots}^{\infty}B_{PM_{(i,j)}}cos[(ip_r\pm jN_s)\theta-ip_r\omega_r t]\end{aligned} \tag{3.3}$$

Then, the phase back-EMF can be calculated by:

$$E_{ph}(t)=-\frac{d}{dt}[r_{ag}l_s\int_0^{2\pi}B_{ag\_PM}(\theta,t)N_{ph}(\theta)d\theta] \tag{3.4}$$

where r_{ag} is the air-gap radius, l_{st} is the stack length and N_{ph} is the phase winding function. N_{ph} for both the 12-slot/14-pole and 12-slot/10-pole single layer windings shown in Fig. 2.19 is the same and can be expressed as:

$$N_{ph}(\theta)=\sum_{m=1.3,5\ldots}^{\infty}N_{ph_m}cos(m\theta) \tag{3.5}$$

According to [133], only the harmonics such as the 1st, 5th (fundamental for 10-pole), 7th (fundamental for 14-pole), 11th… exist. Other triplen harmonics are cancelled in three-phase windings. With (3.3)-(3.5), the fundamental phase back-EMFs can be expressed in (3.6), which are not zero if m_{PM} satisfies (3.7).

$$E_{ph\_PM}(t) = r_{ag} l_s \sum_{i=1,2,3\ldots}^{\infty} \sum_{j=0,1,2\ldots}^{\infty} \sum_{m=1,3,5\cdots}^{m=|ip_r \pm jN_{s\_equiv}|} E_{PM_{(i,j)}} cos(ip_r \omega_r t) \quad (3.6)$$

$$m_{PM} = |p_r \pm jN_{s\_equiv}|, j = 0,1,2 \ldots \quad (3.7)$$

It is evident that not only the fundamental harmonics, i.e. 5th order ($p_r = 5$ for the 12-slot/10-pole machine) and 7th order ($p_r = 7$ for the 12-slot/14-pole machine), other harmonics in the winding function listed in Table 3.2 also contribute to fundamental back-EMF.

Table 3.2. Harmonic orders contributing to fundamental phase back-EMF

	Non-modular	E-core stator	C-core stator
12-slot/10-pole	$\|5 \pm 12j\|$=5th, 7th, 19th…	$\|5 \pm 6j\|$=1th, 5th, 7th…	$\|5 \pm 12j\|$=5th, 7th, 19th…
12-slot/14-pole	$\|7 \pm 12j\|$=5th, 7th, 17th…	$\|7 \pm 6j\|$=1th, 5th, 7th…	$\|7 \pm 12j\|$=5th, 7th, 17th…

$$T_{em} = \frac{e_a i_a + e_b i_b + e_c i_c}{\omega_r} \quad (3.8)$$

Finally, according to (3.8), the electromagnetic torque can be calculated. Here i_a, i_b and i_c are 3-phase currents.

3.3. Open-circuit Performances

3.3.1. Phase Back-EMFs and Flux Linkages

The waveforms and spectra of the phase back-EMFs are shown in Fig. 3.3 and Fig. 3.4. It is found that for the 12-slot/10-pole modular CPMs, the magnitude of fundamental phase back-EMF is decreasing with the increasing FG width, regardless of the E-core or C-core structure. However, the C-core structure could be able to weaken the influence of the FGs on the phase back-EMFs. As for the 12-slot/14-pole modular CPMs, the E-core and C-core structures have different influences. In terms of the E-core 12-slot/14-pole modular CPMs, the magnitude of fundamental phase back-EMFs will first increase with the increasing FG width and then start to decrease if the FG width continues to increase.

The phenomenon of the phase back-EMFs can be explained by observing the open-circuit phase flux linkages of different structures which are shown in Fig. 3.5. In order

to have a clear quantitative comparison, the spectra of the open-circuit phase flux linkages with different FG width are shown in Fig. 3.5. It is evident that the FG has a 'flux-focusing' effect in the E-core 12-slot/14-pole modular CPMs with an appropriate FG width. However, the FG only has a negative effect on the C-core 12-slot/14-pole modular CPMs, i.e. the fundamental phase flux linkage always decreases with the increasing FG width.

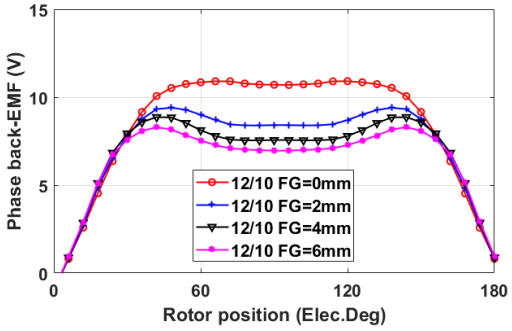

(a) 12-slot/10-pole E-core CPM

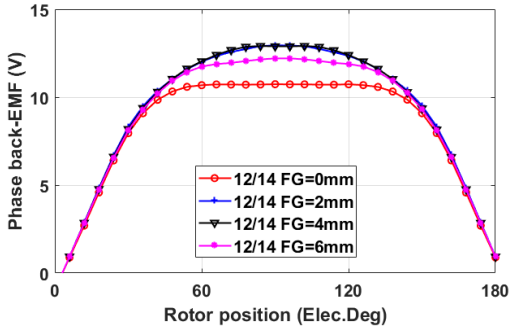

(b) 12-slot/14-pole E-core CPM

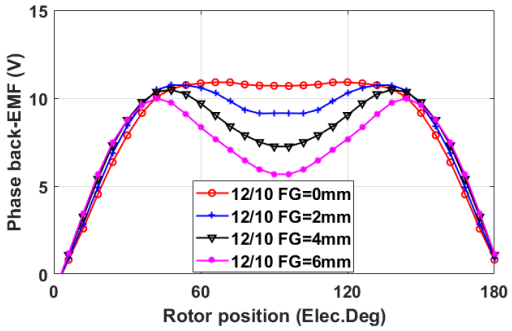

(c) 12-slot/10-pole C-core CPM

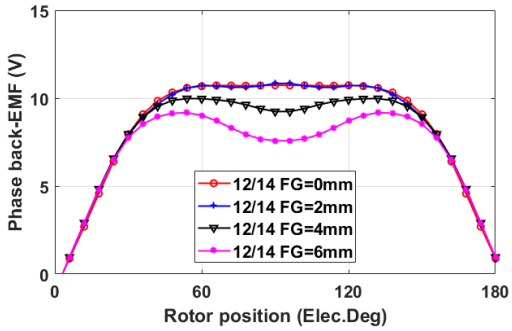

(d) 12-slot/14-pole C-core CPM

Fig. 3.3. Waveforms of the phase back-EMFs for different FG widths at 400 rpm.

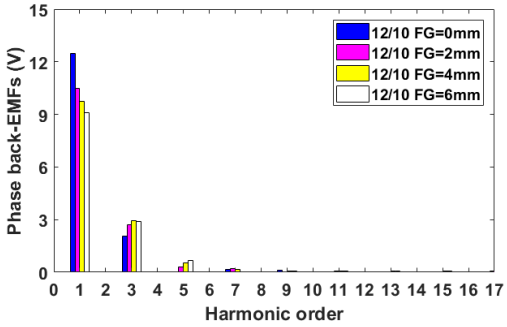

(a) 12-slot/10-pole E-core CPM

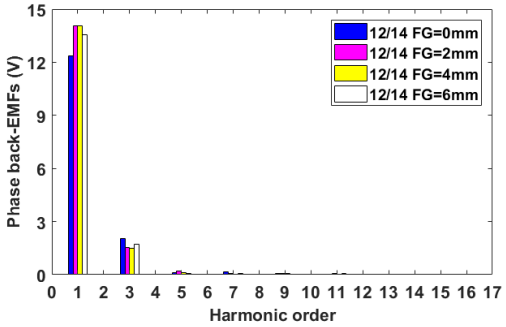

(b) 12-slot/14-pole E-core CPM

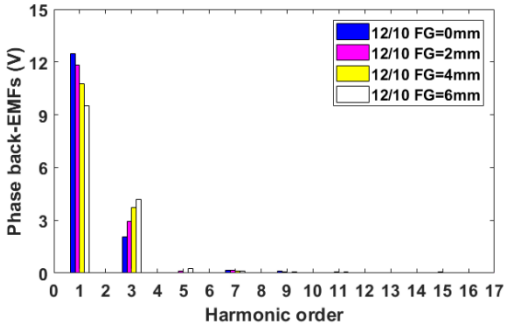

(c) 12-slot/10-pole C-core CPM

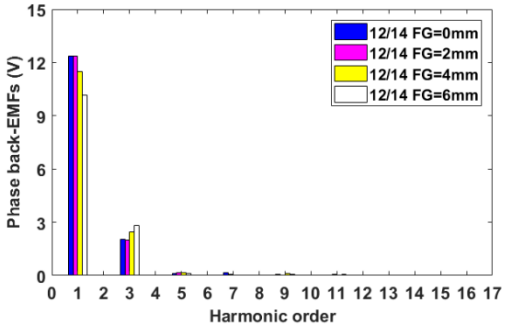

(d) 12-slot/14-pole C-core CPM

Fig. 3.4. Spectra of the phase back-EMFs for different FG widths at 400 rpm.

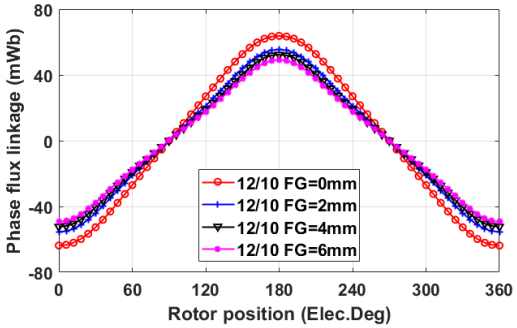

(a) 12-slot/10-pole E-core CPM

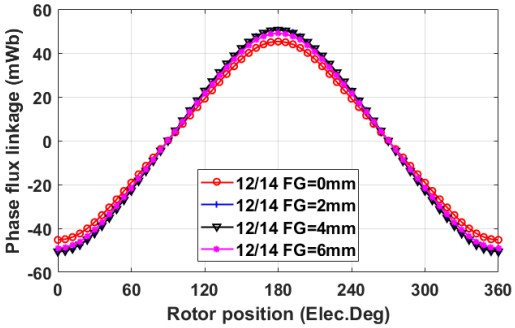

(b) 12-slot/14-pole E-core CPM

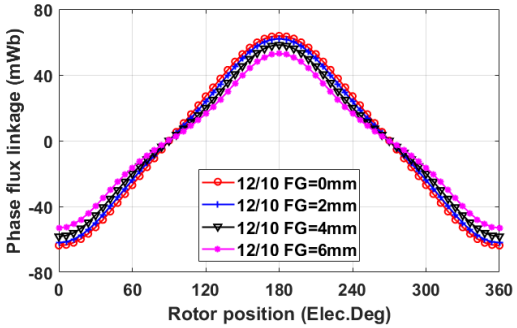

(c) 12-slot/10-pole C-core CPM

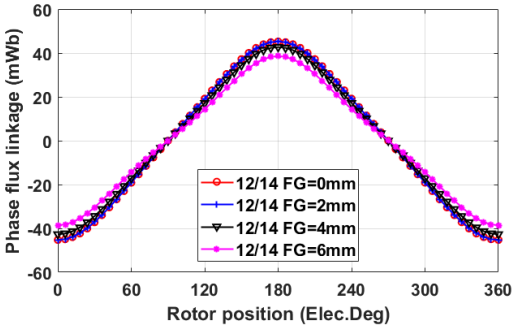

(d) 12-slot/14-pole C-core CPM

Fig. 3.5. Waveforms of the phase flux linkages for different FG widths at 400 rpm.

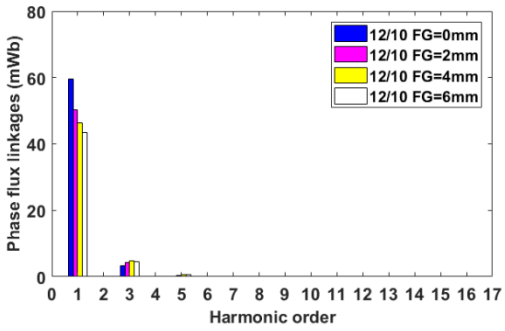

(a) 12-slot/10-pole E-core CPM

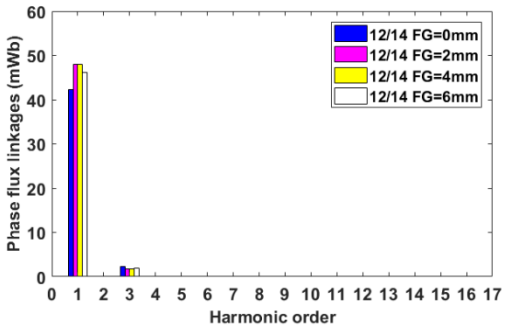

(b) 12-slot/14-pole E-core CPM

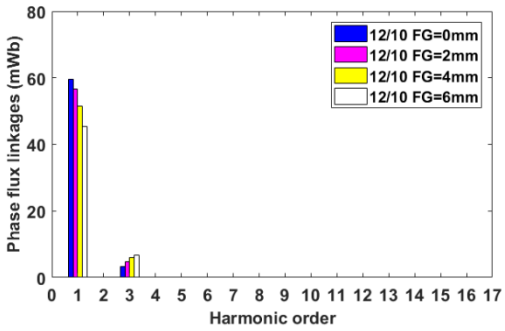

(c) 12-slot/10-pole C-core CPM

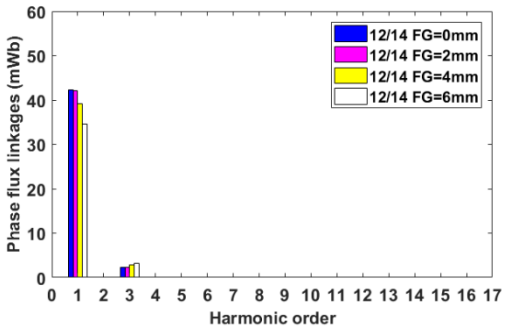

(d) 12-slot/14-pole C-core CPM

Fig. 3.6. Spectra of the phase flux linkages for different FG widths at 400 rpm.

3.3.2. Cogging Torque

It is essential to evaluate the cogging torques due to the fact that sometimes the cogging torque might be a dominant factor in the torque ripple. In order to figure out the influence of the FGs on the cogging torque, the waveforms and spectra of the investigated modular CPMs with different FG widths are shown in Fig. 3.7, to Fig. 3.10. It can be observed from the spectra that the fundamental cogging torques for the E-core 12-slot/10-pole and 12-slot/14-pole CPMs change from 12^{th} to 6^{th} after introducing the FGs whilst the order of the fundamental cogging torques of the C-core 12-slot/10-pole and 12-slot/14-pole CPMs remain unchanged, which is the 12^{th} order. In terms of the number of cogging torque cycles in one electrical period, it can be calculated by [31]:

$$N_c = \frac{LCM(k, N_s)}{p} \tag{3.9}$$

where LCM is the least common multiple (LMC), N_s is the number of slots, p is the pole pair number, $k = 1$ for conventional CPMs in this chapter. As a result, the non-modular CPMs have 12 cycles in one electrical period. However, when the FGs are introduced,

the slot number of E-core structure can be considered as 6 rather than 12 which can reduce the cycle number per electrical period from 12 to 6.

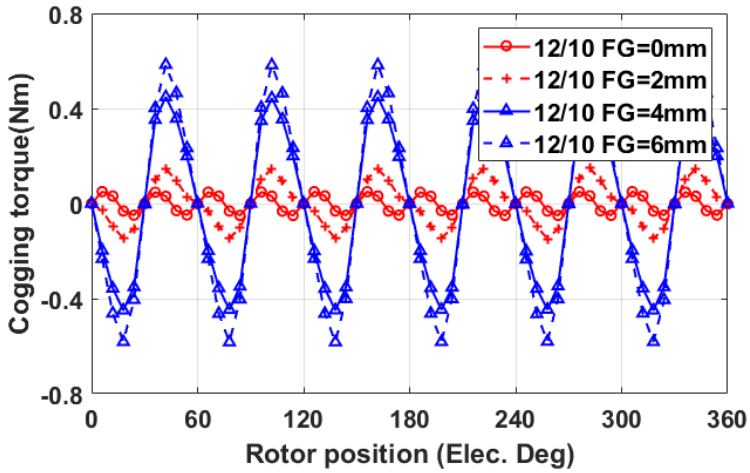

(a) 12-slot/10-pole E-core CPM

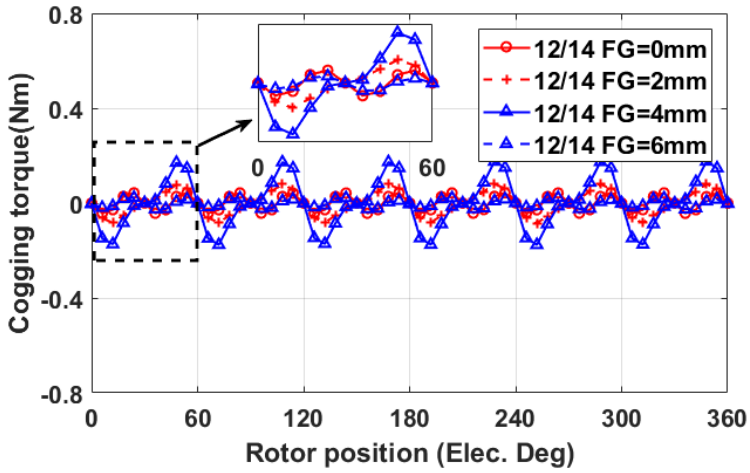

(b) 12-slot/14-pole E-core CPM

Fig. 3.7. Waveforms of the cogging torques of E-core CPM.

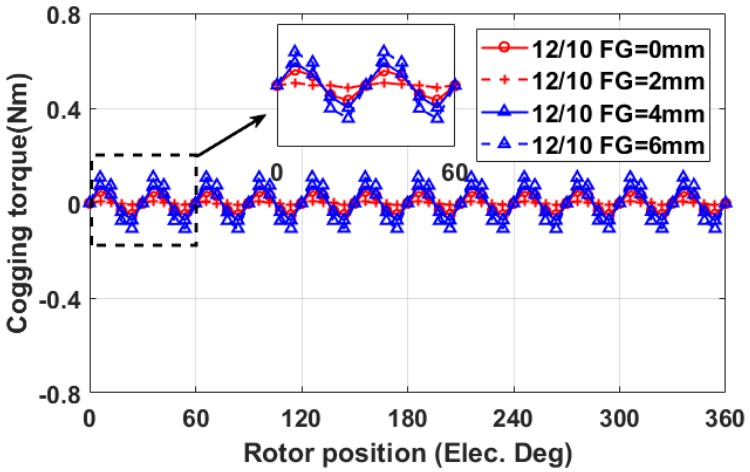

(a) 12-slot/10-pole C-core

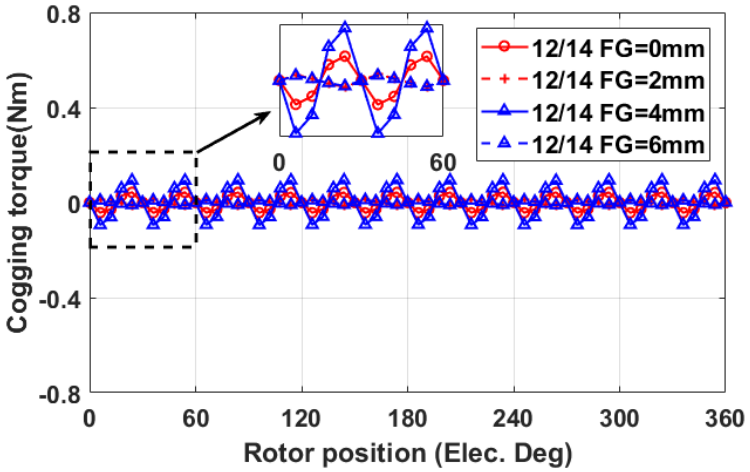

(b) 12-slot/14-pole C-core

Fig. 3.8. Waveforms of the cogging torques of C-core CPMs.

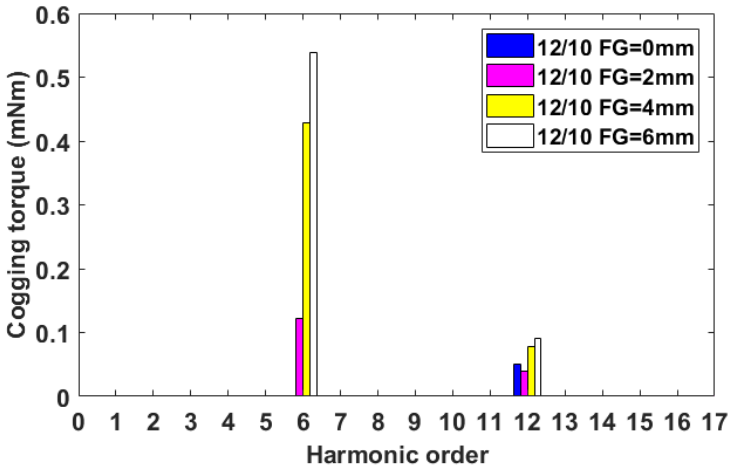

(a) 12-slot/10-pole E-core CPMs

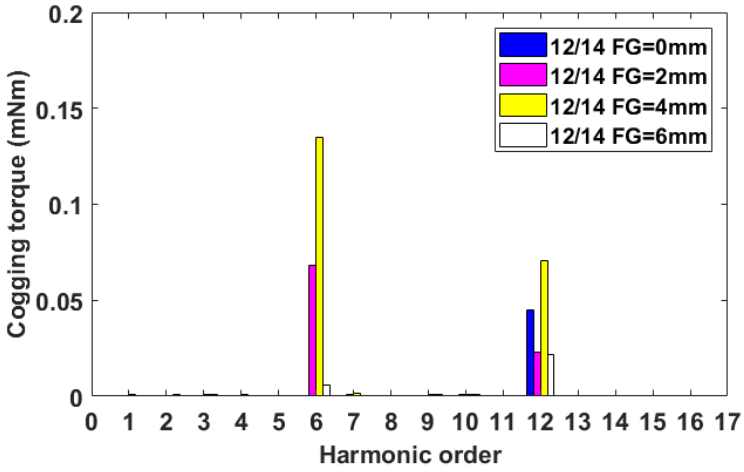

(b) 12-slot/14-pole E-core CPMs

Fig. 3.9. Spectra of the cogging torques of E-core CPMs.

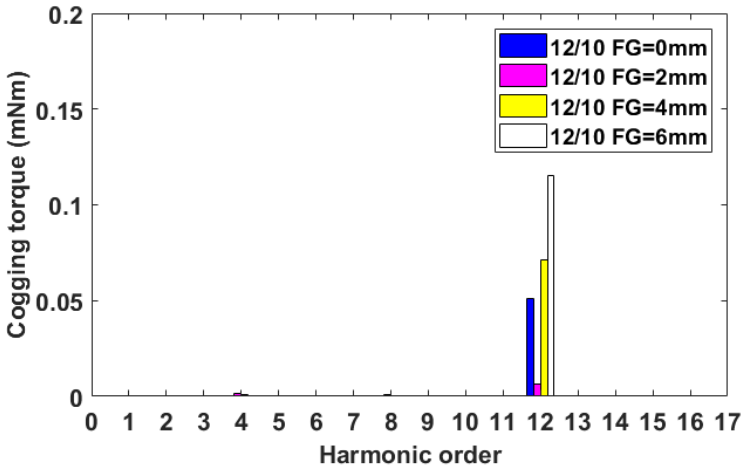

(a) 12-slot/10-pole C-core CPMs

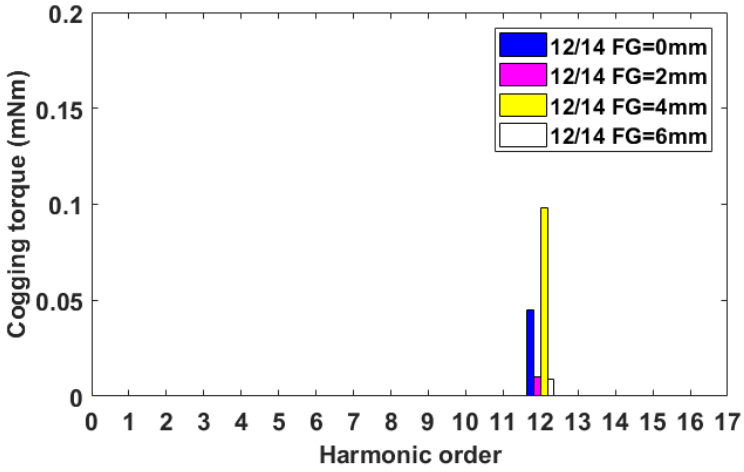

(b) 12-slot/14-pole C-core CPMs

Fig. 3.10. Spectra of the cogging torques of C-core CPMs.

Moreover, the peak-to-peak cogging torque versus the FG width of the investigated modular CPMs are shown in Fig. 3.11. It can be observed that the C-core CPMs have smaller peak-to-peak cogging torques compared with their E-core counterparts, regardless of the slot/pole number combination. This is mainly due to fact that, in general, the value of cogging torques are also determined by the LMC as discussed in [121]. It is generally valid that more cycles will lead to lower peak cogging torque. Therefore, by choosing a proper FG width (e.g. 2mm and 3mm) in the C-core CPMs, the cogging torque can be significantly reduced.

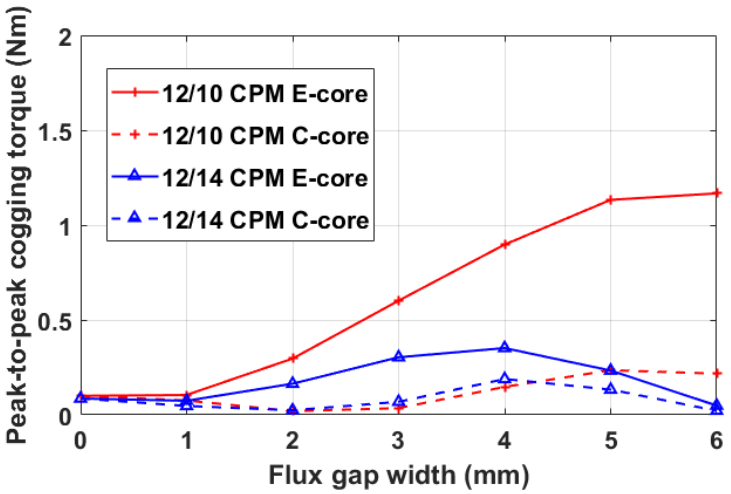

Fig. 3.11. Peak-to-peak cogging torque *vs* FG width of the investigated CPMs.

3.4. On-Load Performances

3.4.1. On-Load Torques

The average torques and torque ripple coefficients of the investigated CPMs at rated condition against different FG widths are shown in Fig. 3.12 and Fig. 2.25. Similar to the phase back-EMF investigated previously, the FGs also have a significant torque improvement effect on the E-core 12-slot/14-pole CPM if a proper FG width is selected. However, for all the other machines, the torque performance will be deteriorated with increasing FG width. In terms of torque ripple, for all the modular CPMs, the adoption of C-core structure can reduce the torque ripple, especially for the 12-slot/10-pole CPMs. This is due to the same reason as for the cogging torque.

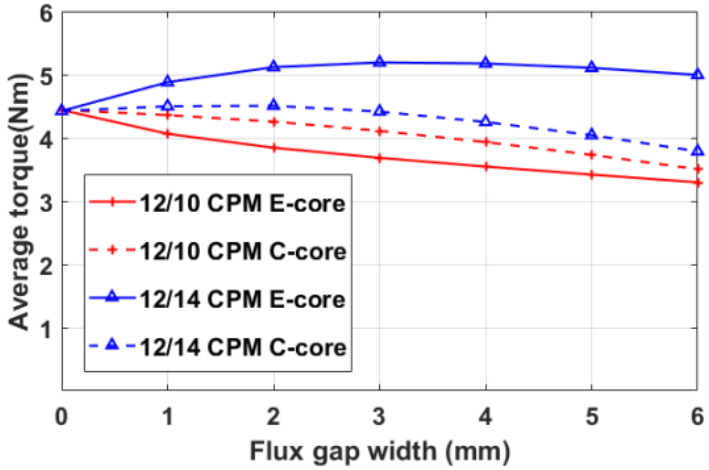

Fig. 3.12. Average torque *vs* FG width of the investigated modular CPMs at the rated current (I_{rms}=7.34A).

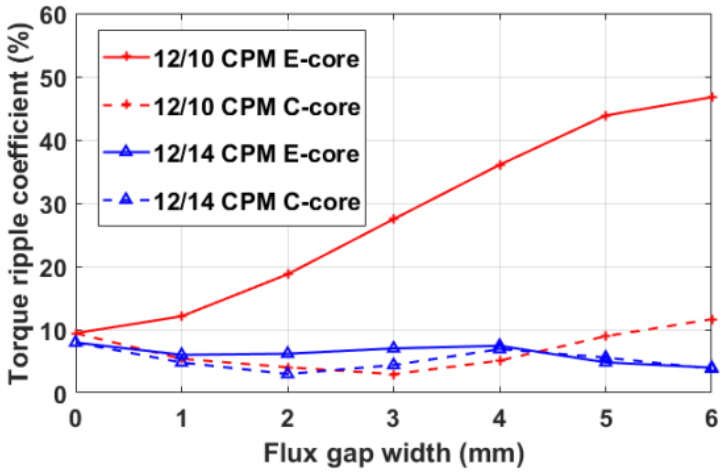

Fig. 3.13. Torque ripple coefficient *vs* FG width of the investigated modular CPMs at the rated current (I_{rms}=7.34A).

To investigate the torque performance under different load conditions, the average torques against phase RMS current have been calculated, as shown in Fig. 3.14. It can be seen that the trend is the same for all machines, i.e. the toque will always increase with phase RMS current, but the rate of increase will be reduced after 15A due to saturation effect, which is almost twice the rated current. However, it should be noted that the load condition will not change the influence of FG width on the average torques, as a proper FG width can improve the torque of E-core 12-slot/14-pole CPM while for all the other machines, the torque will be reduced with increasing FG width.

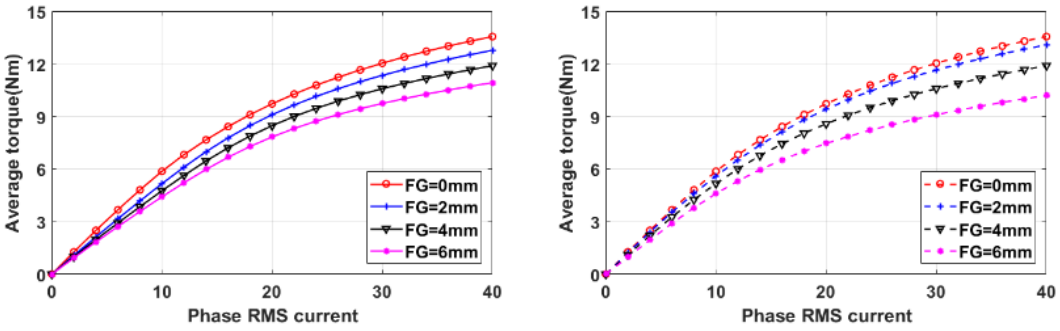

(a) 12-slot/10-pole E-core CPM (b) 12-slot/14-pole E-core CPM

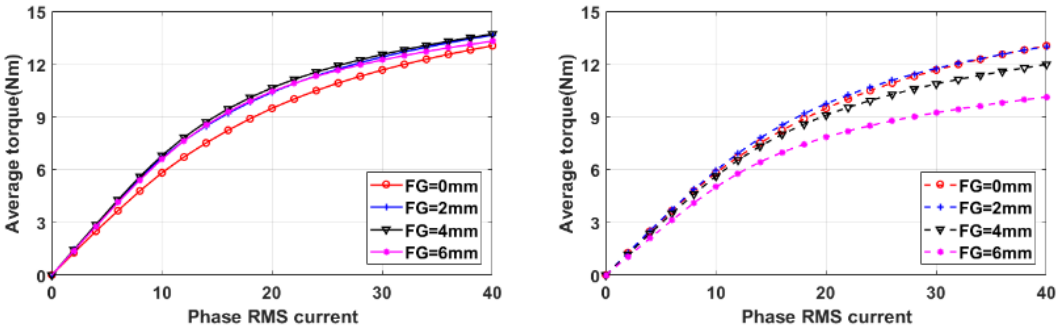

(c) 12-slot/10-pole C-core CPM (d) 12-slot/14-pole C-core CPM

Fig. 3.14. Average torque *vs* phase RMS current with different FG width of the investigated modular CPMs.

3.4.2. *D*-*Q* Axis Inductances

In order to account for the cross-coupling effect between the *d*- and *q*-axes, it is essential to evaluate the *d*- and *q*-axis inductances under different *d*- and *q*-axis currents, i.e. different load conditions. Therefore, the *d*- and *q*-axis inductances versus *d*- and *q*-axis currents with different FG widths have been calculated and shown in Fig. 3.15 and Fig. 3.16.

It has found that the *d*-axis inductances will be reduced in all machines after the introduction of modular structures, especially when the *d*-axis current is relatively low, regardless of the E-core or C-core stator. This is due to the fact the existence of FGs will increase the *d*-axis magnetic reluctance which can lead to lower inductances. On the other hand, the modular structures have almost no influence on the *q*-axis inductances, except conditions when the *d*-axis current is relatively low. When the *d*-axis current is low, the *q*-axis inductances will be reduced slightly when the FGs are introduced. This is due to the influence of cross-coupling effect. Generally speaking,

the introduction of FGs will have influence on the inductances, especially on the *d*-axis inductances, but the impact of FG width is quite minor.

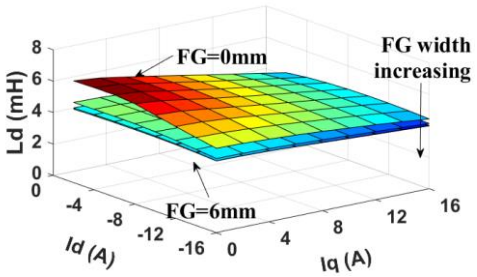

(a) 12-slot/10-pole E-core CPM

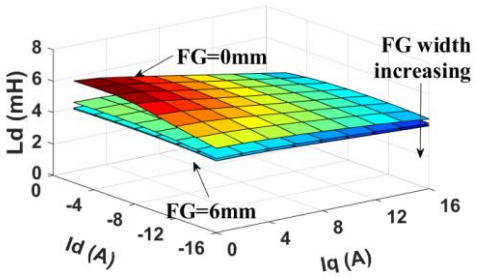

(b) 12-slot/10-pole E-core CPM

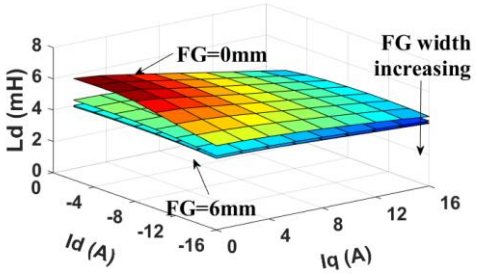

(c) 12-slot/10-pole E-core CPM

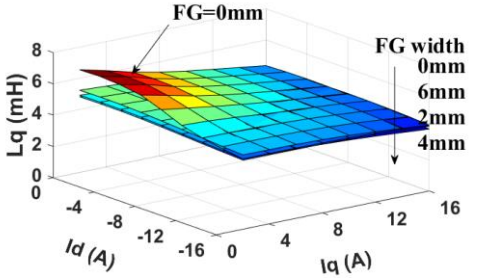

(d) 12-slot/10-pole E-core CPM

Fig. 3.15. *D-q* axis inductances *vs d-q* axis currents of E-core CPM.

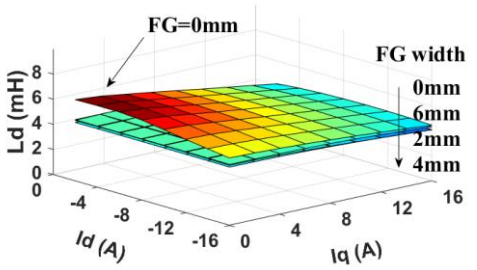

(a) 12-slot/10-pole C-core CPM

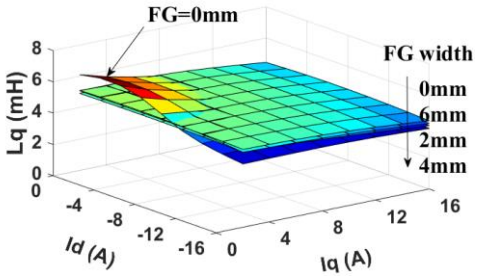

(b) 12-slot/10-pole C-core CPM

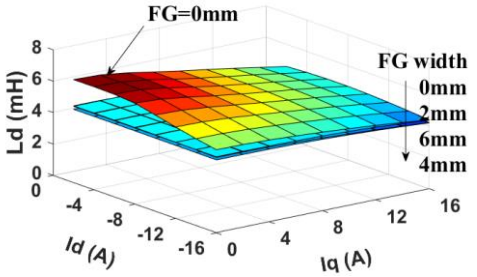

(c) 12-slot/14-pole C-core CPM

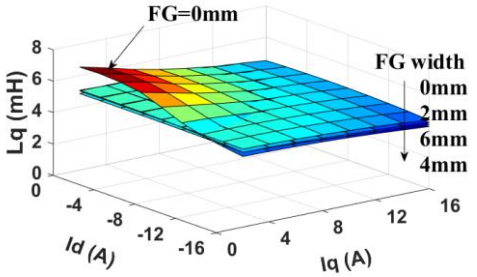

(d) 12-slot/14-pole C-core CPM

Fig. 3.16. *D-q* axis inductances *vs d-q* axis currents of C-core CPM.

3.4.3. Iron Losses and Magnet Eddy Current Loss

The FGs can be regarded as "dummy slots" on the stator iron core and may cause extra variation in the airgap permeance. This will have impact on the loss performances including stator and rotor core iron losses and PM eddy current losses. Since the E-core stator has 6 FGs whilst the C-core stator has 12 FGs, it is necessary to figure out the influences of different structures on the losses. Therefore, the stator iron losses and PM eddy current losses at rated condition are calculated and shown in Fig. 3.17.

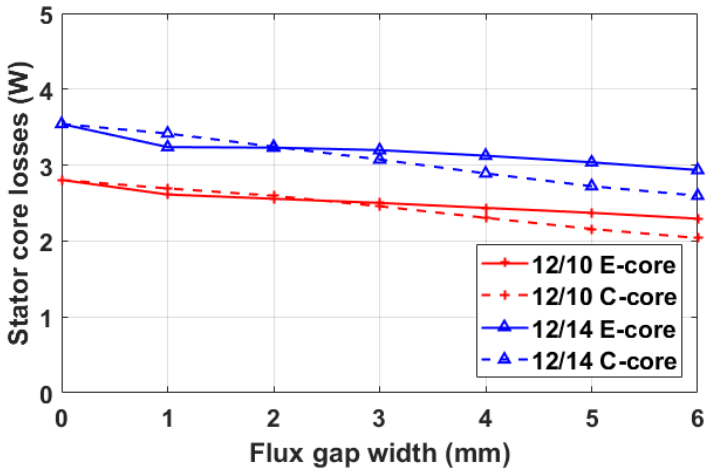

(a) Stator iron losses *vs* FG width

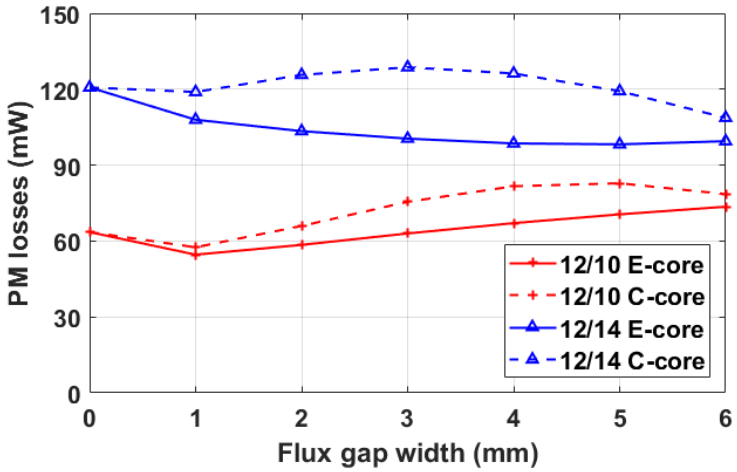

(b) PM eddy current losses *vs* FG width

Fig. 3.17. Stator iron losses and PM eddy current losses *vs* FG width. The phase current is 7.34A*rms* and the rotor speed is 400rpm.

It is generally known that the rotor iron losses are often much smaller than the stator iron losses in synchronous machines with laminated iron core. Therefore, they are neglected in this chapter (the calculated highest rotor iron loss amongst all investigated

CPMs is only 0.2W). Moreover, it should be noted here that the PM eddy current losses are relatively small due to the relatively low rated rotor speed (400rpm) and small dimensions of the investigated machines. It is well known that, in the iron losses, the hysteresis loss is proportional to the rotation speed while the PM eddy current loss is proportional to the square of rotation speed. This can also be validated by the results shown in Fig. 3.18, where a FG width of 2mm is chosen as example.

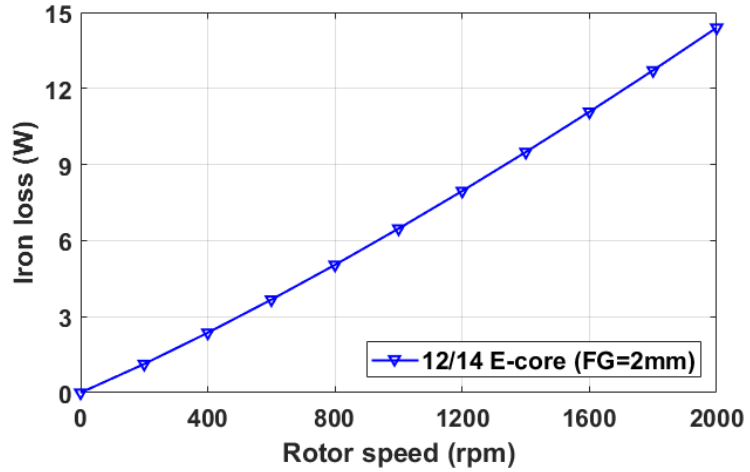

(a) Stator iron losses *vs* rotor speed

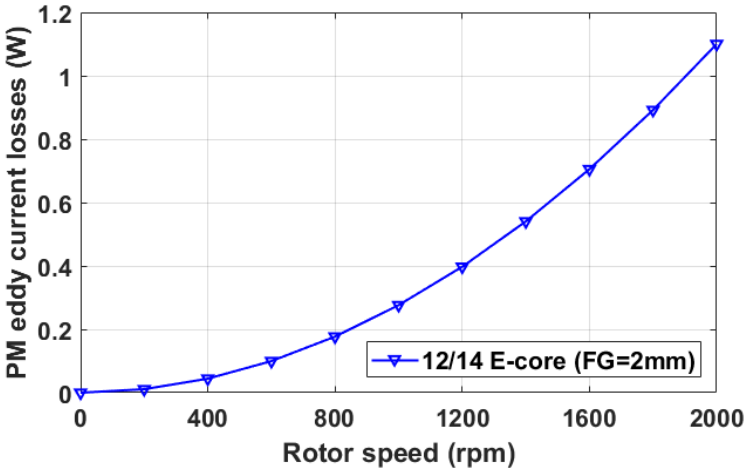

(b) PM eddy current losses *vs* rotor speed

Fig. 3.18. Stator iron losses and PM eddy current losses *vs* rotor speed of the 12-slot/14-pole CPM with 2mm FG. The phase current is 7.34A*rms*.

It can be observed that for all the investigated modular CPMs, the stator iron losses can be reduced by increasing the FG width and the C-core structure can reduce more stator iron losses than the E-core structure with larger FG width (≥2.5mm), regardless

of the slot/pole number combinations. This phenomenon can be explained by analysing the spectra of on-load air-gap flux densities, as shown in Fig. 3.19.

It is apparent that the main working harmonics, e.g. the 5th order harmonic for the 12-slot/10-pole machines and the 7th order harmonic for the 12-slot/14-pole machines, are reducing with increasing FG width. Since the working harmonics are dominant in the stator iron losses, the stator iron losses will be reduced with increasing FG width.

The PM eddy current losses are mainly caused by the sub-harmonics rather than the working harmonics. In terms of the 12-slot/10-pole machines, although the 1st order harmonics are reduced slightly with the increasing FG width, some increase can be observed in the magnitudes of other dominant harmonics such as the 7th, 11th and 13th. Taking all these into account, for the 12-slot/10-pole CPMs, the FGs have nearly no positive effect on the PM eddy current losses although they can be reduced very slightly at a 1mm FG width.

In terms of the 12-slot/14-pole E-core CPMs, most lower and dominant order harmonics such as 1st, 2nd, 5th and 8th order harmonics keep reducing with the FG width, this is the reason that PM eddy current losses of the 12-slot/14-pole E-core CPMs are reduced with increasing FG width. However, for the 12-slot/14-pole C-core CPMs, the reduction in the magnitude of the 5th order harmonic is not significant when the FG width is smaller than 3mm, with a small increase in the 9th order harmonics at small FG width, the PM eddy current losses of the 12-slot/14-pole C-core CPMs will first increase slightly and then starts to decrease (after 3mm FG width).

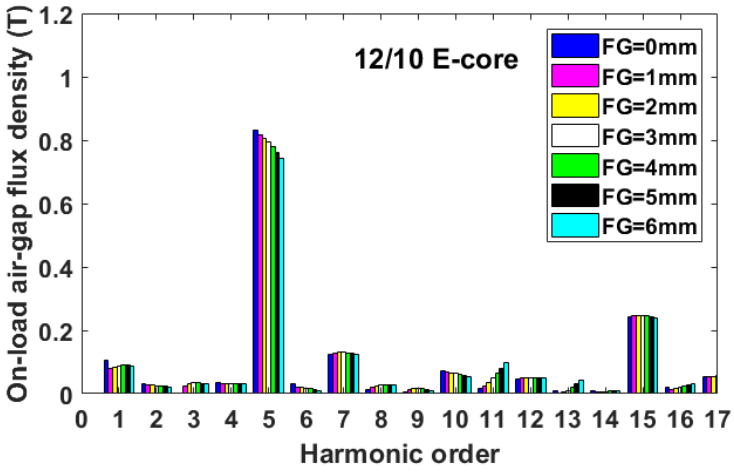

(a) E-core

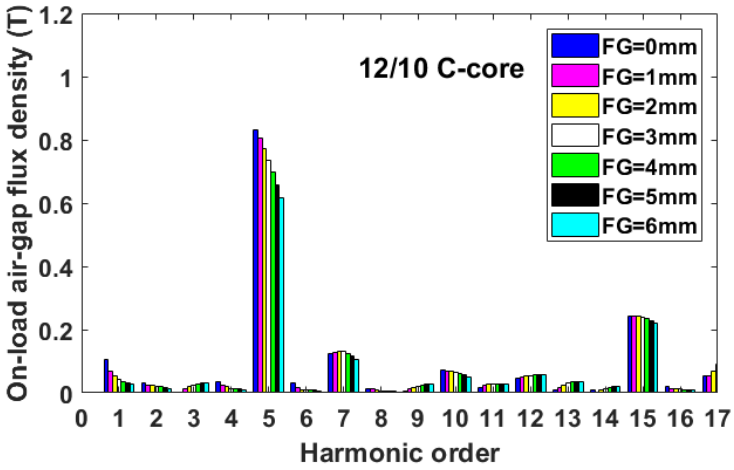

(b) C-core

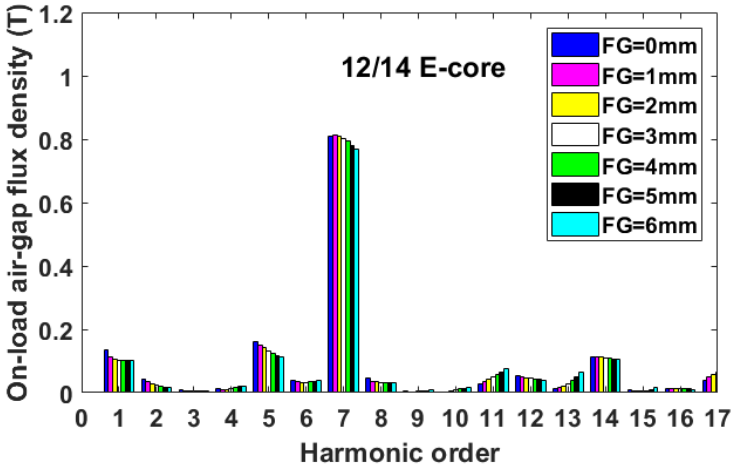

(c) E-core

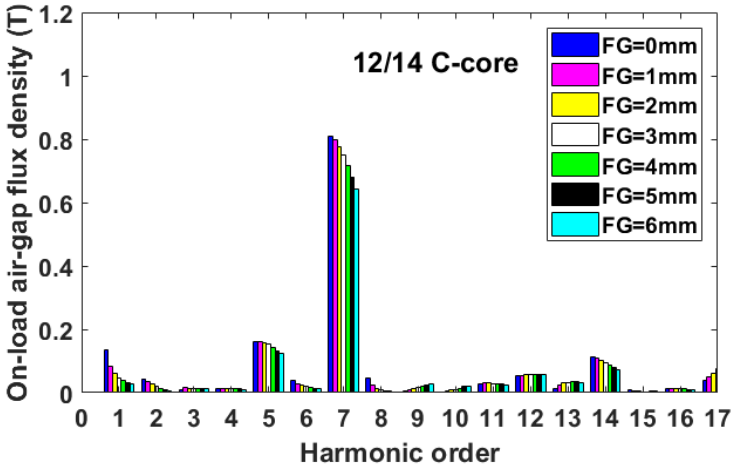

(d) C-core

Fig. 3.19. Spectra of the on-load air-gap flux density of the 12-slot/10-pole modular CPMs and 12-slot/14-pole modular CPMs.

3.4.4. Unbalanced Magnetic Force

Due to the asymmetric rotor structures, the unbalanced magnetic force (UMF) often exists in the CPMs and it is important to analyze the influence of FGs on the UMF. The open-circuit and the rated UMFs of all the modular CPMs versus FG width are shown in Fig. 3.20. In terms of the open-circuit UMFs, it can be seen that the C-core modular CPMs have much lower UMFs compared with those of the E-core modular CPMs, regardless of the FG width. The FG width generally has negative effect on the E-core machines which will increases the open-circuit UMF with increasing FG width. To explain this, the spectra of air-gap flux density only due to PMs in the 12-slot/14-pole E-core machines is shown in Fig. 3.21 (a). According to [134], the UMF is dependent on the working harmonic and its main sub-harmonics. It is found in Fig. 3.21 (a) that, although the 7^{th} working harmonic reduces slightly with the FG width, the other harmonics such as 1^{st}, 6^{th}, 11^{th}, 13^{th}, etc. increase with the FG width. This contributes to the overall increase of the open-circuit UMFs in the E-core machines.

For the rated UMFs, except for some cases of the 12-slot/10-pole E-core machine, they can be significantly reduced by introducing FGs. Again, the spectra of air-gap flux density only due to armatures in the 12-slot/14-pole E-core machines are selected as an example. It can be seen that, although the 7^{th} working harmonic varies slightly with the FG width, the 1^{st}, 2^{nd}, 5^{th}, 6^{th}, 8^{th}, etc. harmonics all reduce with the FG width, leading to the overall reduced rated UMFs. To conclude, on one hand, the C-core structure can achieve much lower open-circuit UMF compared with the E-core structure, regardless of slot/pole number combinations. On the other hand, except for the 12-slot/10-pole E-core machine, the FGs can significantly reduce the on-load UMFs in all other machines and the 12-slot/14-pole C-core machines have the lowest UMFs.

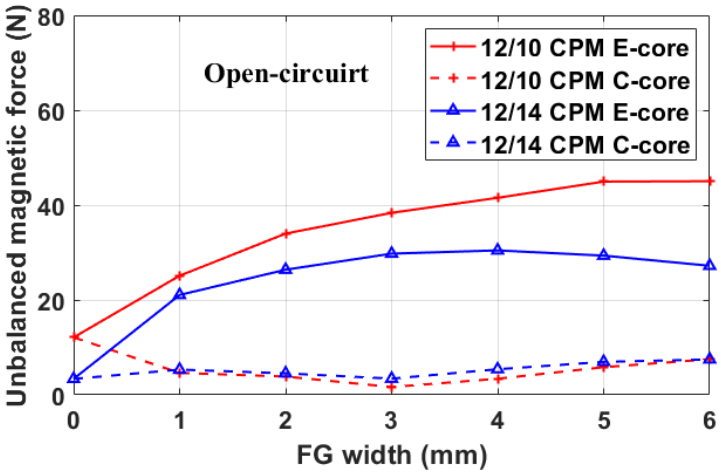

(a) Open-circuit UMF *vs* FG width

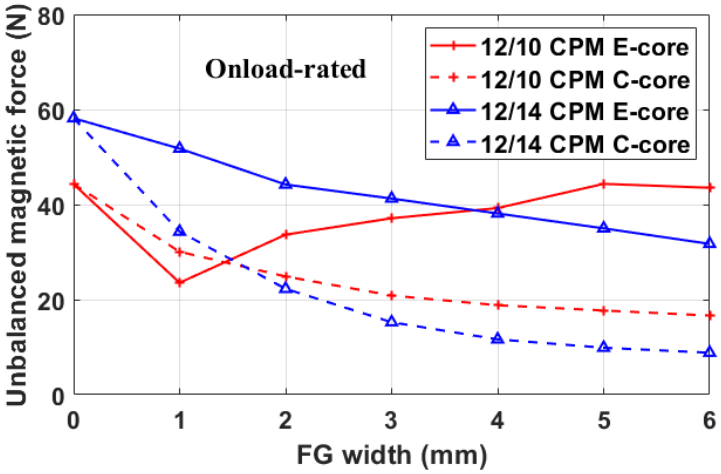

(b) Onload UMF *vs* FG width

Fig. 3.20. Open-circuit and on-load UMFs *vs* FG width.

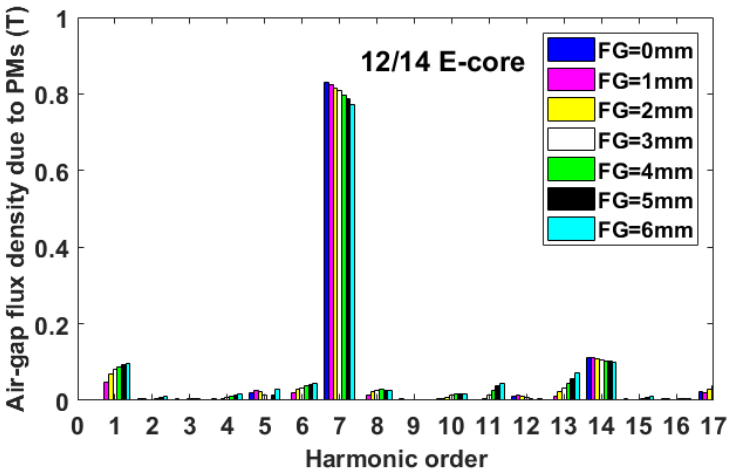

(a) due to PMs only

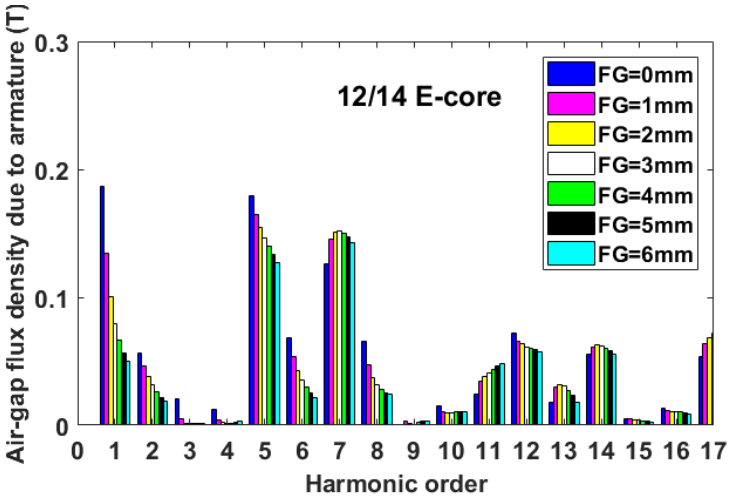

(b) due to armature only

Fig. 3.21. Spectra of the air-gap flux densities, the E-core 12-slot/14-pole modular CPMs.

3.5. Dynamic Characteristics

Apart from the above static electromagnetic characteristics, the dynamic performances are also key factors to evaluate the electrical machines. The dynamic characteristics of all the investigated CPMs including the torque-speed curves and the power-speed curves have been calculated, as shown in Fig. 3.22 to Fig. 3.25. It is assumed that the maximum inverter current (10.38A) and the maximum DC-bus voltage (40V) are the same for all investigated modular CPMs.

It has found that the modular structure has almost no improvement for the flux-weakening capability of the 12-slot/10-pole E-core modular CPMs. For the 12-slot/10-pole C-core modular CPM, the flux weakening capability can even be worsened when

the FG width equals to 2mm or 4mm. This is mainly due to the fact that the relatively higher phase flux linkages in comparison with the E-core modular CPMs can lead to higher φ_m/L_d which will result in a finite speed rather than infinite speed.

However, due to the advantage of the flux-focusing effect of the modular structure, for the 12-slot/14-pole modular CPM machines, both the E-core and C-core structures can achieve better flux weakening capabilities by choosing proper FG width while keeping the advantages of higher torque and power.

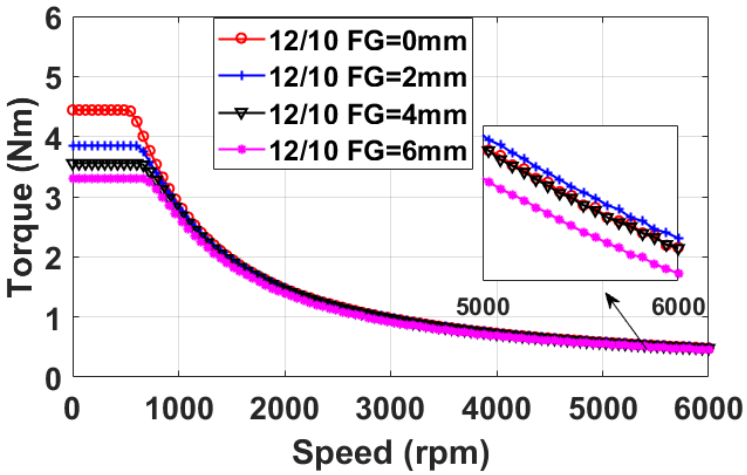

(a) 12-slot/10-pole E-core CPM

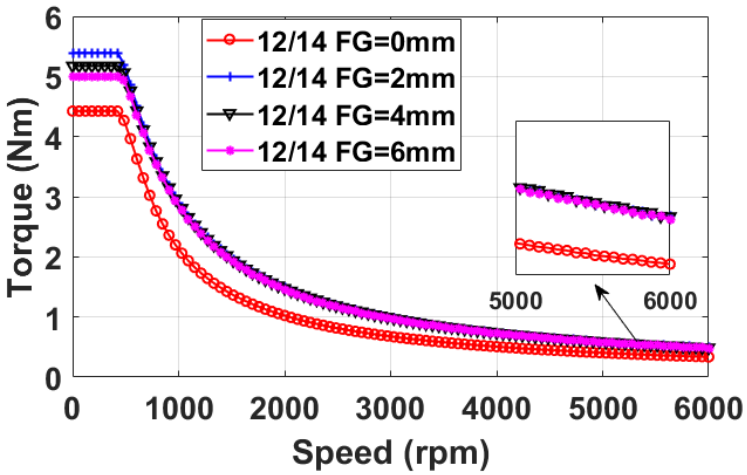

(b) 12-slot/14-pole E-core CPM

Fig. 3.22. Torque-speed curves of the E-core modular CPMs with different FG widths.

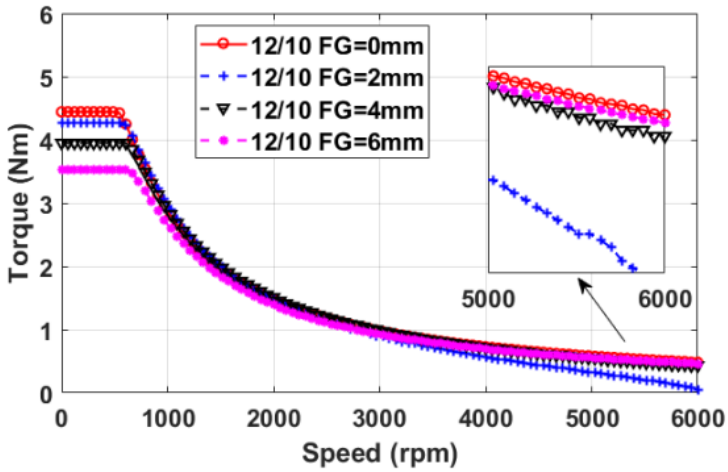

(a) 12-slot/10-pole C-core CPM

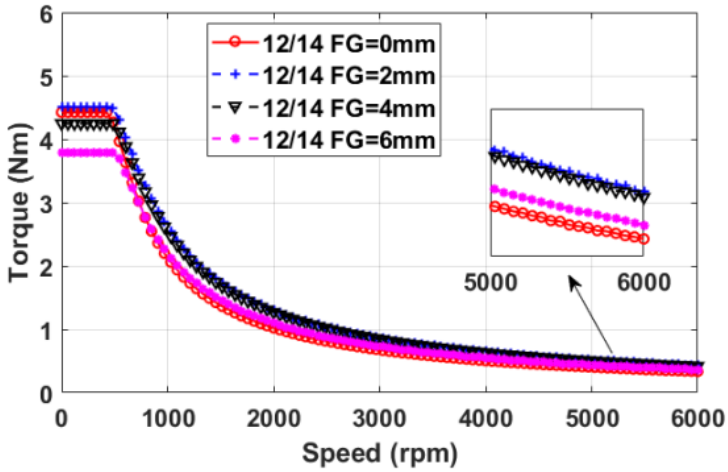

(b) 12-slot/14-pole C-core CPM

Fig. 3.23. Torque-speed curves of the C-core modular CPMs with different FG widths.

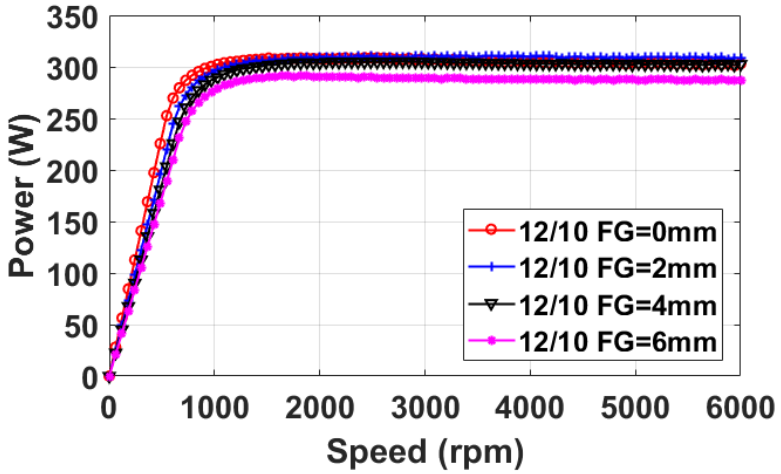

(a) 12-slot/10-pole E-core CPM

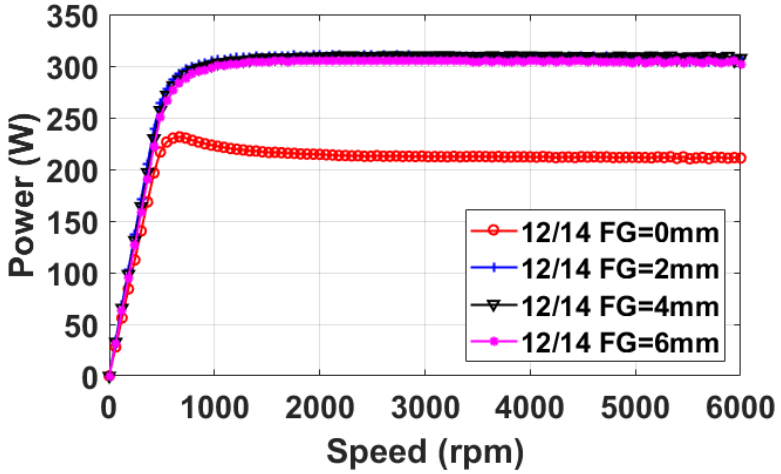

(b) 12-slot/14-pole E-core CPM

Fig. 3.24. Power-speed curves of the E-core modular CPMs with different FG widths.

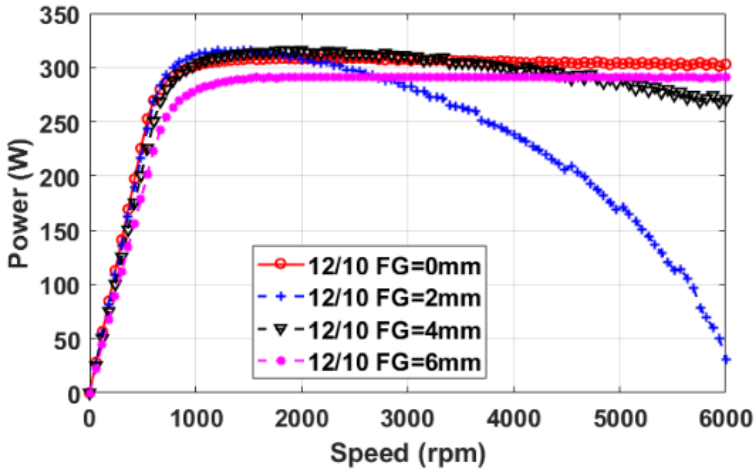

(a) 12-slot/10-pole C-core CPM

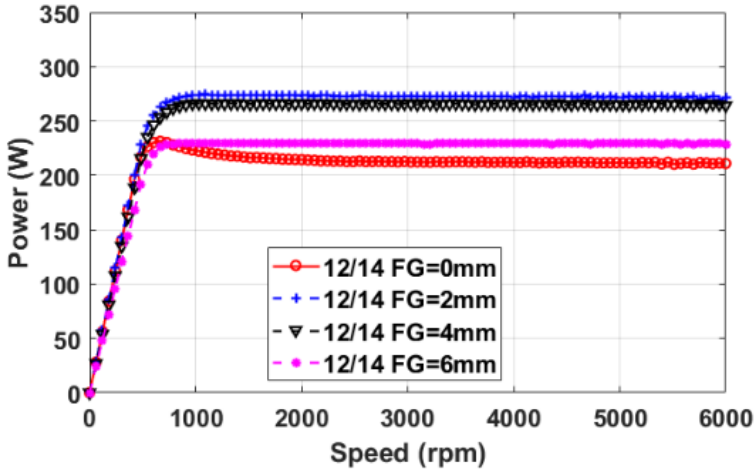

(b) 12-slot/14-pole C-core CPM

Fig. 3.25. Power-speed curves of the C-core modular CPMs with different FG widths.

The power factor is also a critical design parameter for electrical machines, which can determine the capacity requirement of the inverter and also its cost. Therefore, the influence of FGs on the power factors of different modular CPMs within the full speed range has been investigated and power factor-speed curves are shown in Fig. 3.26. On one hand, for the 12-slot/10-pole CPMs with both E-core and C-core structures, the existence of the FGs almost has no positive effect on the power factors, and can even lead to lower power factors when the FG is relatively large, (e.g. FG=6mm) in the C-core. On the other hand, for the 12-slot/14-pole CPMs, the introduction of FGs could significantly increase the power factors with the E-core structure. As for the C-core structure, the FGs can also significantly improve the power factors when an appropriate FG width is chosen, especially within the low speed range. However, if the FG width becomes too large, the power factors will be decreased (e.g. FG=6mm).

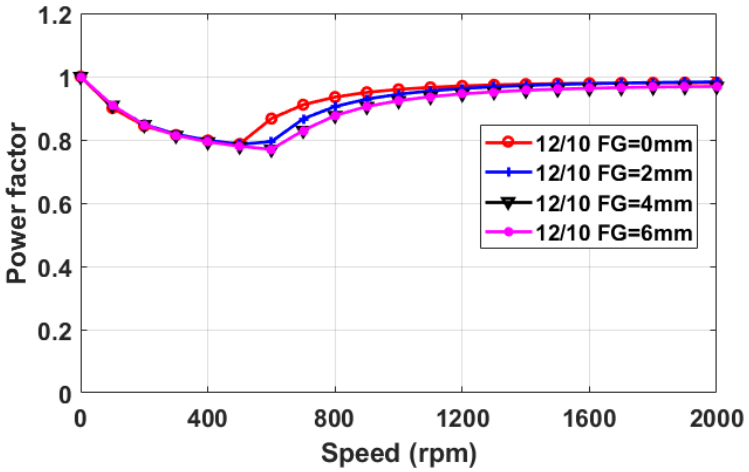

(a) 12-slot/10-poe E-core CPM

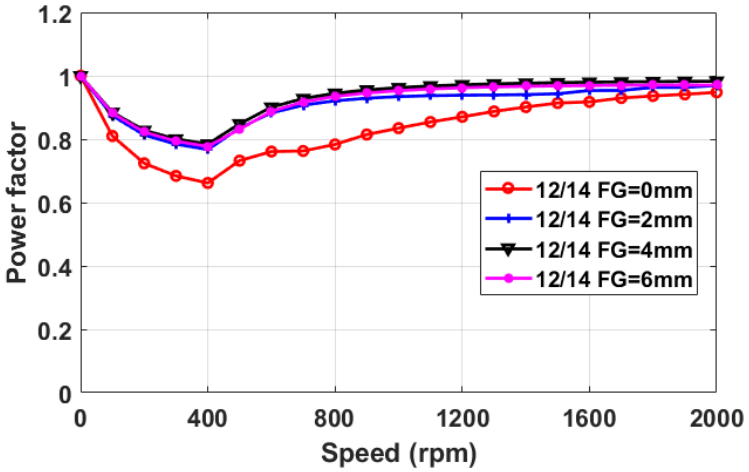

(b) 12-slot/14-pole E-core CPM

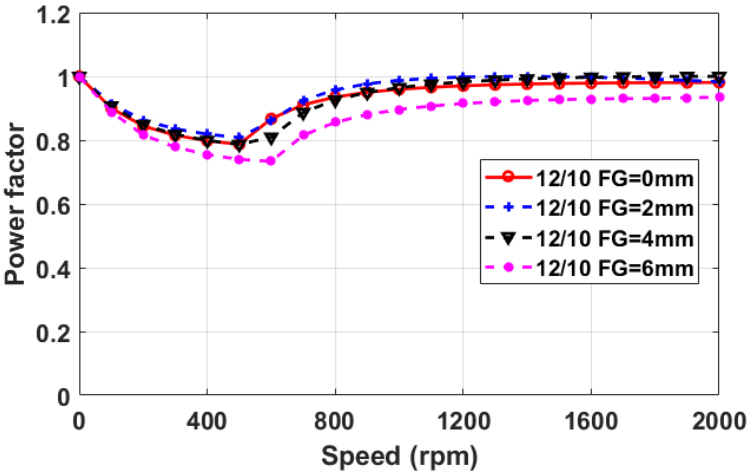

(c) 12-slot/10-pole C-core CPM

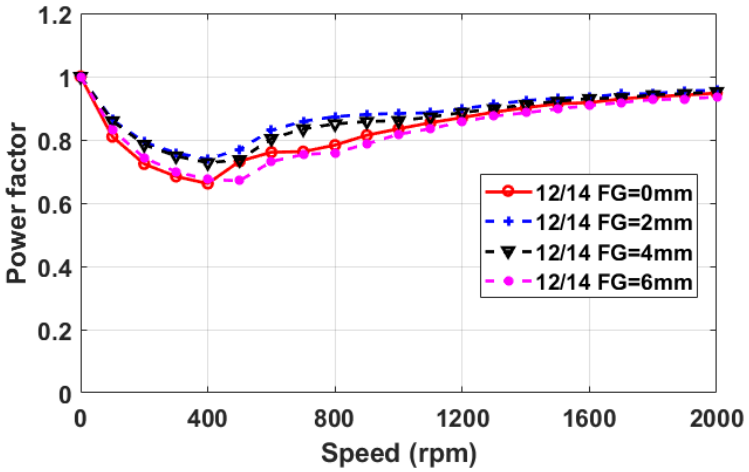

(d) 12-slot/14-pole C-core CPM

Fig. 3.26. Power factor-speed curves of the investigated modular CPMs with different FG width.

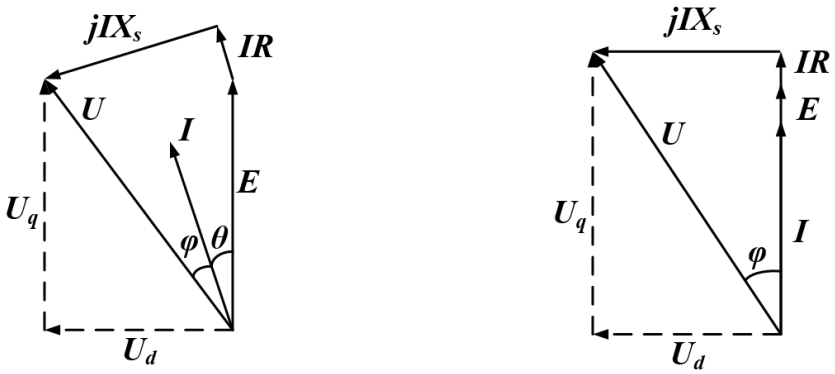

(a) I_d and $I_q \neq 0$ (b) $I_d=0$ but $I_q \neq 0$

Fig. 3.27. Phasor diagrams of PM synchronous machines.

This phenomenon can be explained using (3.10) and (3.11). Since the investigated CPM is a synchronous machine and the phasor diagrams are shown in Fig. 3.27. It is generally known in the synchronous PM machines that:

$$\begin{cases} U_d = \omega\psi_q - RI_d \\ U_q = \omega(L_d I_d + \psi_m) + RI_q \end{cases} \text{ and}$$
$$P_f = \cos\varphi = \cos\left[\tan^{-1}(U_d/U_q) - \theta\right] \tag{3.10}$$

where U_d and U_q are d- and q-axis voltages, I_d and I_q are the d- and q-axis currents, respectively. P_f is the power factor, ω is the rotation speed, ψ_q is the q-axis flux linkages, L_d is the d-axis inductance, ψ_m is the flux linkages produced by the PMs and θ is the current advance angle. In the constant torque region under maximum torque

per ampere (MTPA) control, the *d*-axis currents of all the investigated modular CPMs are quite small and can be neglected. In the meantime, if the influence of phase resistance is neglected, P_f can be expressed as:

$$P_f = \frac{U_q}{\sqrt{{U_d}^2 + {U_q}^2}} = \frac{1}{\sqrt{1 + (\psi_q/\psi_m)^2}} \tag{3.11}$$

It can be seen that the power factor is determined by the ratio of ψ_q to ψ_m. For the investigated modular CPMs, it is evident that ψ_q/ψ_m can be considered to be equal to $\psi_{a\_fund}/\psi_{f\_fund}$. ψ_{a_fund} and ψ_{f_fund} represent the fundamental values of the flux linkages only produced by the armature winding and the PMs, respectively. Therefore, the ratio of ψ_{f_fund} to ψ_{a_fund} against FG width of the investigated modular CPMs at rated condition are shown in Fig. 3.28. As larger $\psi_{f\_fund}/\psi_{a\_fund}$ leads to higher power factors, it is evident that the FG can increase the power factors significantly in the 12-slot/14-pole CPMs, especially with the E-core structure. This can validate the aforementioned influences of FGs on the power factors of the investigated modular CPMs.

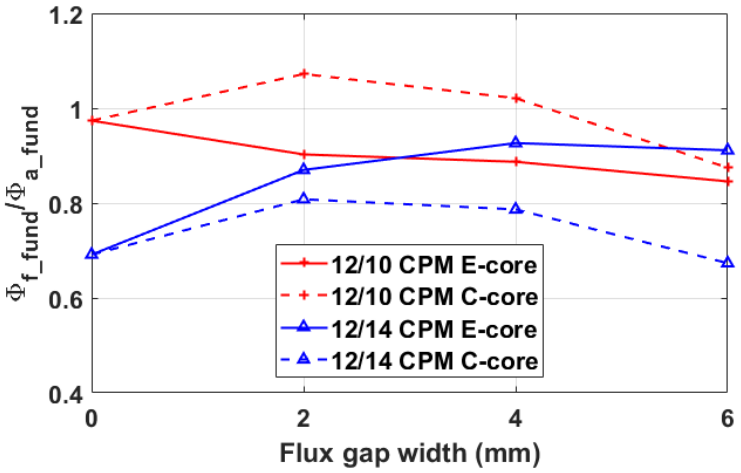

Fig. 3.28. Ratio of ψ_{f_fund} to ψ_{a_fund} *vs* FG width of the investigated modular CPMs at rated condition (I_{rms}=7.34A) @400rpm.

The above results have indicated the influences of FG width on each machine, and it is important to have a comparison between different machines in terms of dynamic performances as well. Thus, the best candidate from each machine type (with optimal FG width) has been selected and shown in Fig. 3.29.

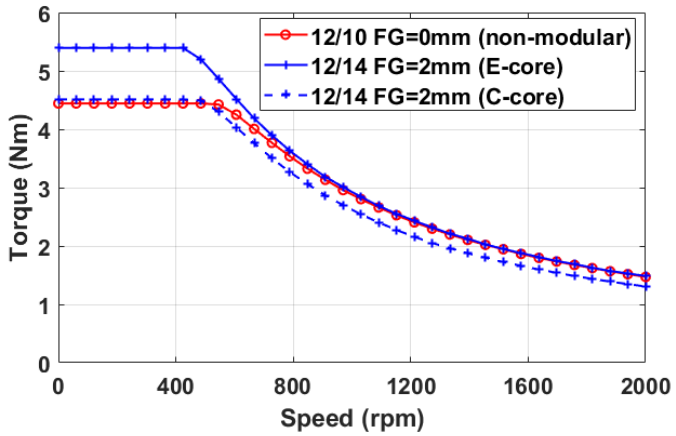

(a) Torque-speed curves comparison

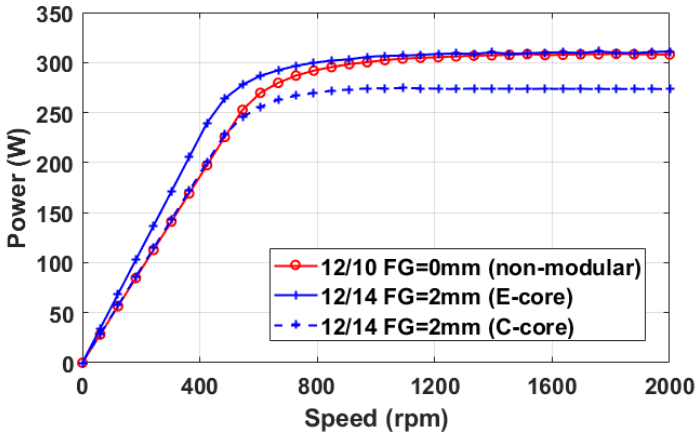

(b) Power-speed curves comparison

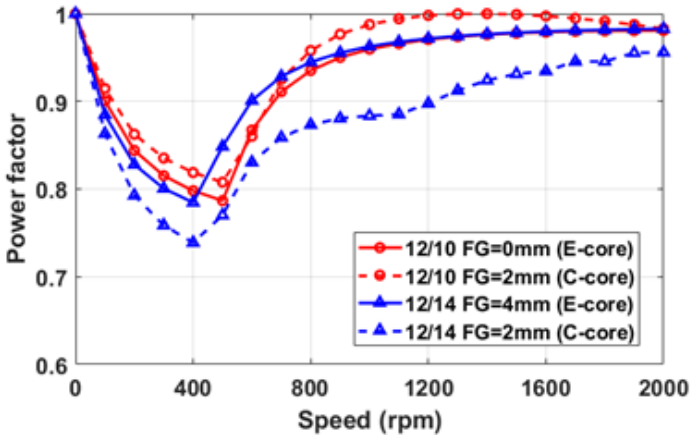

(c) Power factor-speed curves comparison

Fig. 3.29. Comparison of the different machines in terms of dynamic performances (best candidate selected).

Although the 12-slot/14-pole E-core machine achieves the highest torque within the constant-torque region, the performances such as torque and power of the 12-slot/10-pole non-modular machine (FG=0mm) within the flux-weakening region is still

comparable due to its higher base speed compared with the 12-slot/14-pole machines. Therefore, it should be noted that only the 12-slot/10-pole non-modular machines (FG=0mm) are shown in Fig. 3.29 (a), (b), without the feature of E-core or C-core. Moreover, except the 12-slot/14-pole C-core machine, all other machines can have decent power factors over the speed range.

Last but not the least, the efficiency maps also play an important role in the dynamic performances. Therefore, the efficiency maps of the investigated E-core and C-core modular CPMs with different FG widths, e.g. FG=0mm, 2mm, 4mm and 6mm, have been calculated, as shown in Fig. 3.30 to Fig. 3.33. It is worth noting that the efficiency differences of the investigated modular CPMs are small which is mainly due to the relatively small size of the investigated machines leading to negligible PM eddy current losses. Nevertheless, the variation trend can be observed and some useful conclusions can be drawn.

For the 12-slot/10-pole E-core CPMs, the influence of FGs on the efficiency can be neglected. However, for all other machines, their efficiencies could be improved by selecting a proper FG width. For instance, the highest efficiencies of the 12-slot/14-pole E-core CPMs with 2mm, 4mm and 6mm FG width are 4% higher than that of the non-modular one, i.e. 0mm FG width. This is mainly due to the reduction in stator iron losses which has been elaborated in section 3.4.3. Due to the same reason, the 12-slot/10-pole C-core CPMs can achieve 2% improvement in the efficiencies while the efficiencies of the 12-slot/14-pole C-core CPMs can be 3% higher if an appropriate FG width is selected.

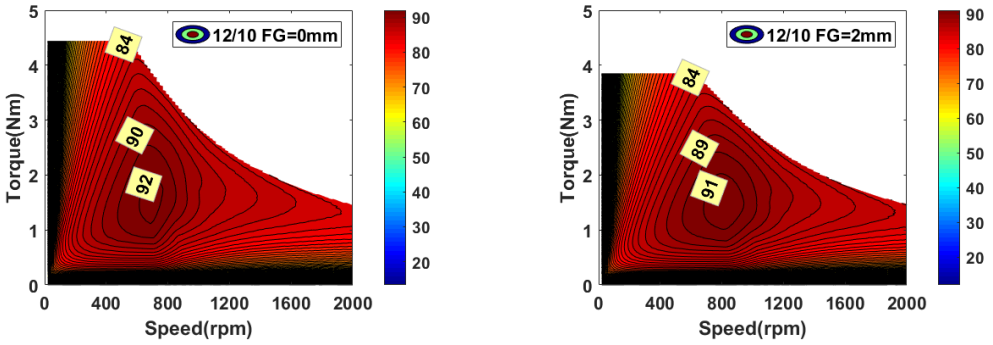

(a) FG=0mm

(b) FG=2mm

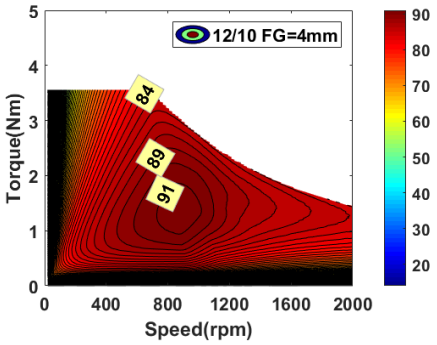

(c) FG=4mm

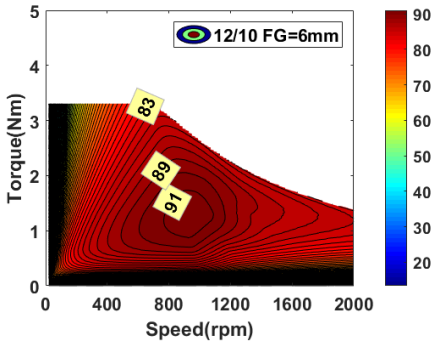

(d) FG=6mm

Fig. 3.30. Efficiency maps of 12-slot/10-pole E-core CPMs with different FG widths.

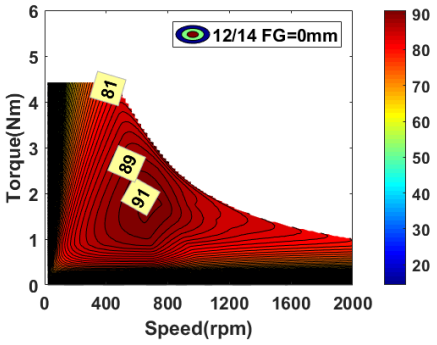

(a) FG=0mm

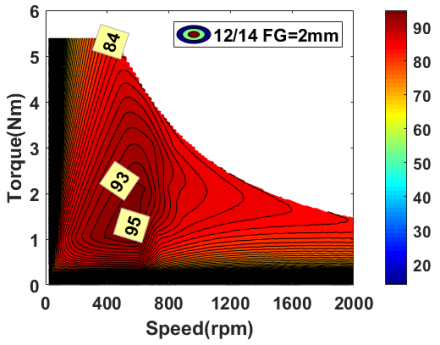

(b) FG=2mm

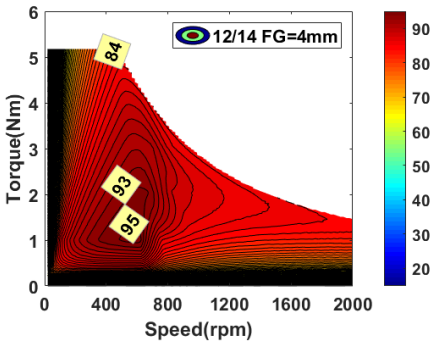

(c) FG=4mm

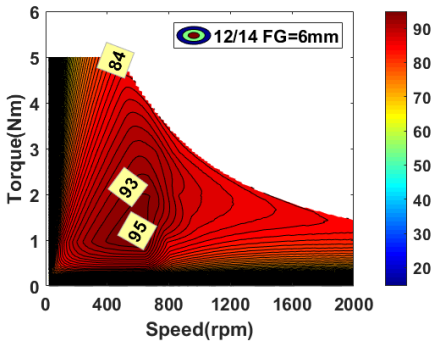

(d) FG=6mm

Fig. 3.31. Efficiency maps of 12-slot/14-pole E-core CPMs with different FG widths.

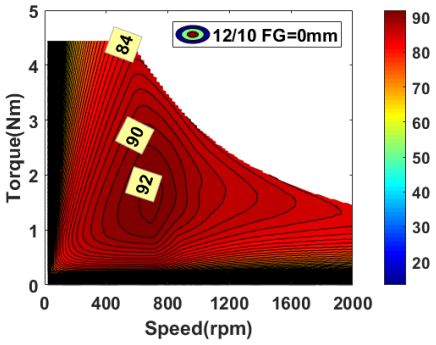

(a) FG=0mm

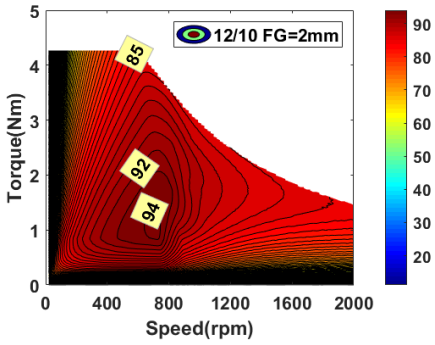

(b) FG=2mm

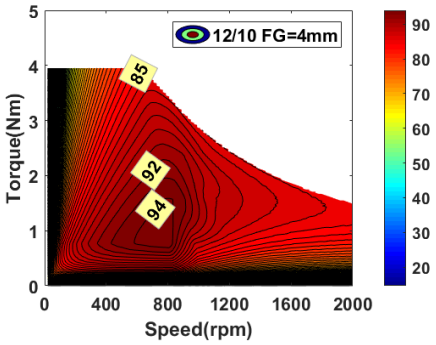

(c) FG=4mm

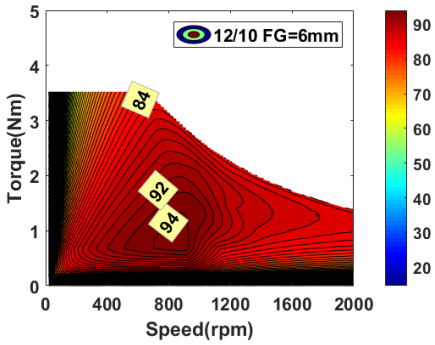

(d) FG=6mm

Fig. 3.32. Efficiency maps of 12-slot/10-pole C-core CPMs with different FG widths.

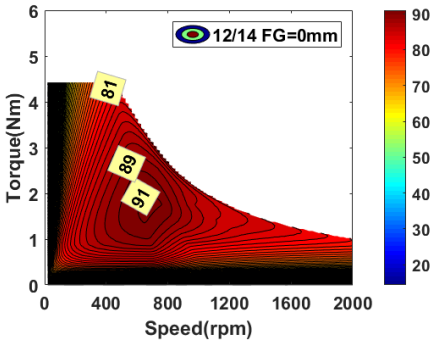

(a) FG=0mm

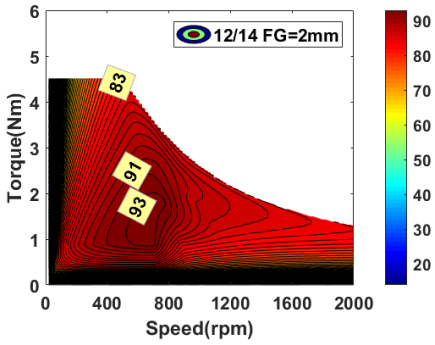

(b) FG=2mm

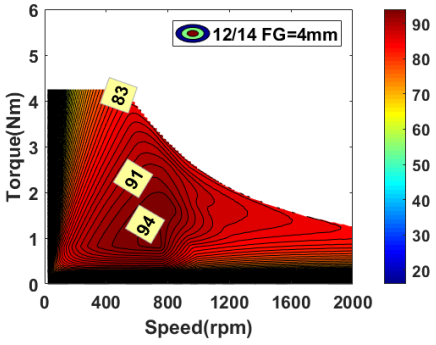

(c) FG=4mm

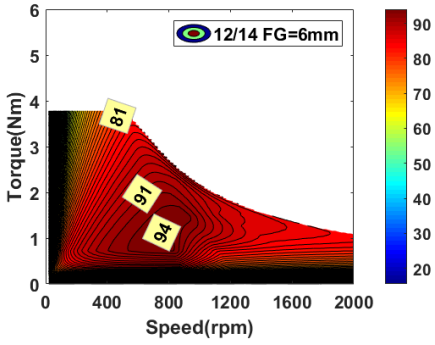

(d) FG=6mm

Fig. 3.33. Efficiency maps of 12-slot/14-pole C-core CPMs with different FG widths.

3.6. Scaling Effect

It should be noted that the dimensions of the modular CPMs investigated in aforementioned sections are relatively small, it is essential to figure out if the influence of FGs are the same for modular CPMs with large dimensions. This is to see the full potential of modular machines in a wide range of applications. Since EV is a potential application for such machines, the stator outer diameter is extended to 3 times larger which is 150mm and usually a normal size for traction motors [135]. For simplification, the split ratio is fixed as the same and the general specifications of the large-scale machines are listed in Table 3.3.

Table 3.3 General specifications of the modular CPMs with large dimensions

Stator outer radius (mm)	150	Split ratio	0.57
Tooth body width (mm)	20	Stator yoke height (mm)	10
Air-gap length (mm)	1	Stack length (mm)	200
Rated current (A_{rms})	70.5	Number of turns per phase	132

Since torque is the most critical requirement in such machines, the average torque and torque ripple coefficient *vs* different FG width are shown in Fig. 3.34 and Fig. 3.35, respectively. It can be easily seen that the FGs have a significant torque improvement effect on the E-core 12-slot/14-pole CPM if a proper FG width is selected. Moreover, the FGs can also improve the torque in C-core 12-slot/14-pole CPMs with an appropriate width chosen, but the improvement is not significant compared with the E-core 12-slot/14-pole CPMs. However, for all the other machines, the torque performance will be deteriorated when the FG width is increased. In terms of the torque ripple, for all modular CPMs, the adoption of C-core structure can reduce the torque ripple, especially for the 12-slot/10-pole CPMs. Therefore, it can be concluded that the influences of the FGs are the same for modular machines regardless of their dimensions and power ratings.

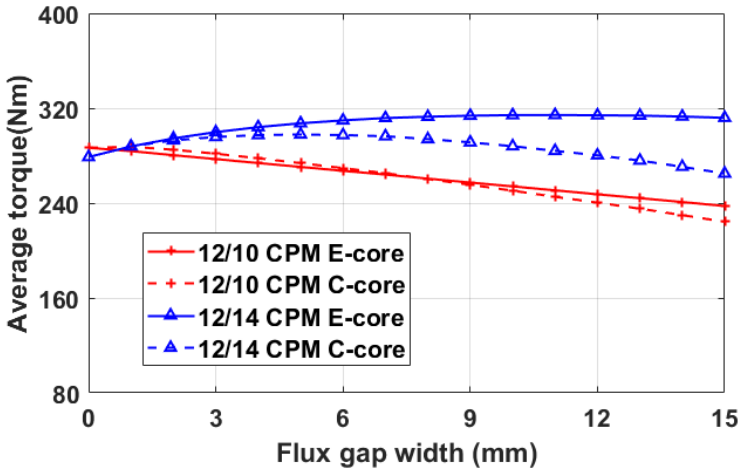

Fig. 3.34. Average torque *vs* FG width of the modular CPMs with large dimensions at the rated current (I_{rms}=70.5A).

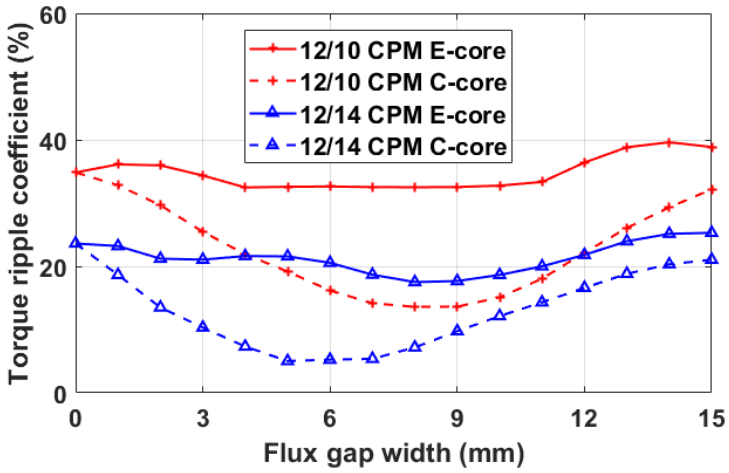

Fig. 3.35. Torque ripple coefficient *vs* FG width of the investigated modular CPMs at the rated current (I_{rms}=70.5A).

3.7. Experimental Validation

3.7.1. Prototype Machines

In order to verify the FEA predictions in the previous sections, both 12-slot/14-pole E-core and C-core CPMs have been prototyped and then detailed dimensions are listed in Table 3.4.The two prototype machines share a 14-pole CP rotor which is shown in Fig. 3.36. Fig. 3.37 shows the two modular stators: E-core and C-core. It should be noted that 2mm is chosen as the FG width here, which is the same as the slot opening.

Table 3.4 Dimensions of the prototype machines

Stator outer radius (mm)	50	Split ratio	0.57
Tooth body width (mm)	7.2	Stator yoke height (mm)	3.7
Air-gap length (mm)	1	Stack length (mm)	50
Magnet thickness (mm)	3	Pole arc to pole pitch ratio	1.34
Flux gap (FG) width (mm)	2	Number of turns per phase	132

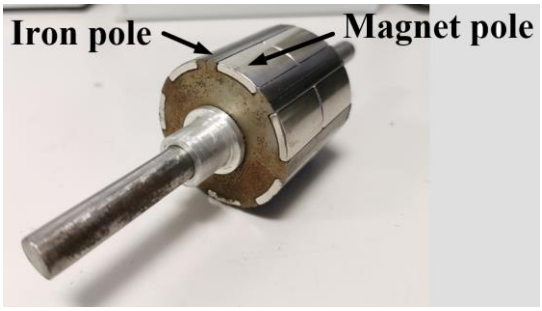

Fig. 3.36. The 14-pole CP rotor of the prototype machines.

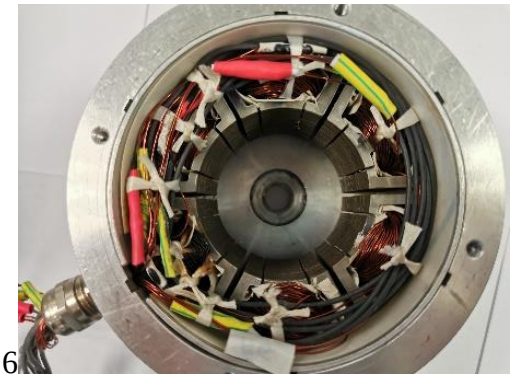

(a) E-core stator with FG=2mm

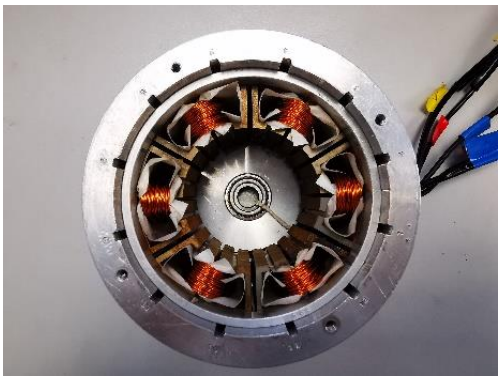

(b) C-core stator with FG=2mm

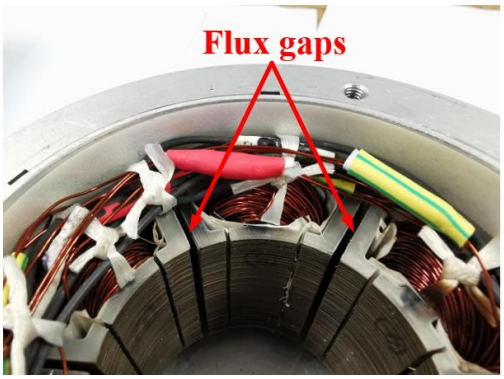

(c) E-core stator with FG=2mm

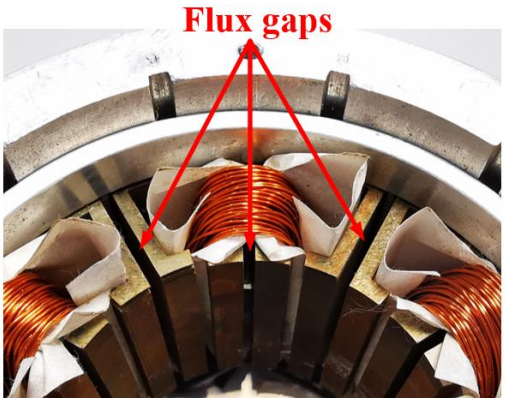

(d) C-core stator with FG=2mm

Fig. 3.37. E-core stator and C-core stators of the prototype machines with FG=2mm. (a), (c) E-core stator with FG=2mm, (b), (d) C-core stator with FG=2mm.

3.7.2. Phase Back-EMFs

The phase back-EMFs of prototype machines are shown in Fig. 3.38. A good agreement between the predicted and measured results can be observed. The slight differences are mainly due to neglecting the magnet end-effect in the 2D FEA models.

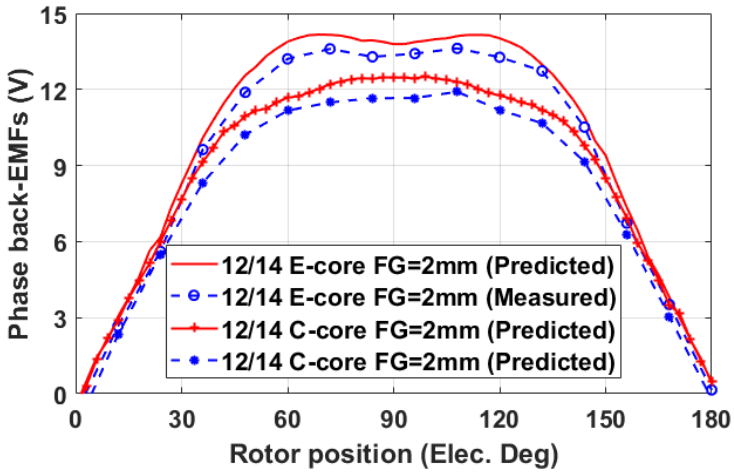

Fig. 3.38. Predicted and measured phase back-EMFs at 400rpm.

3.7.3. Cogging Torques

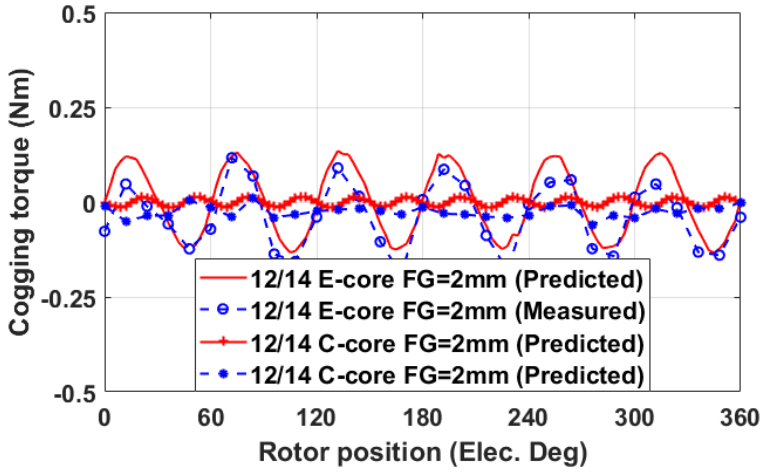

Fig. 3.39. Predicted and measured cogging torques.

By using the same test rig set-up which has been stated in the chapter 2, the cogging torques of the modular machines are measured. It can be seen that the measured and predicted results generally have the same trend. It should be noted that for the 12/14 C-core CPM, the discrepancy is mainly due to the small torque magnitude which makes

measurement process not accurate enough. Meanwhile, the manufacturing tolerances can also result in slight differences.

3.7.4. Inductances

Both self and mutual inductances versus rotor positions are measured using the method mentioned in the previous chapter and compared with the predicted results as shown in Fig. 3.40 and Fig. 3.41. In general, the measured inductances match with the predicted results well. The differences are due to the fact that the end-winding has not been taken into account in the 2D FEA models.

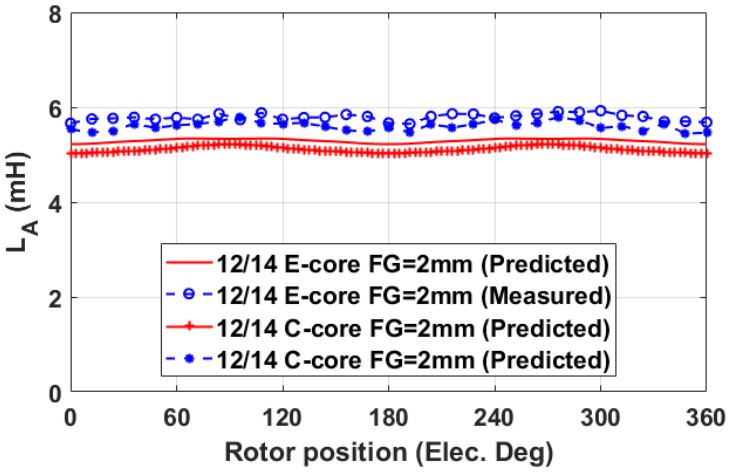

Fig. 3.40. Predicted and measure self-inductances.

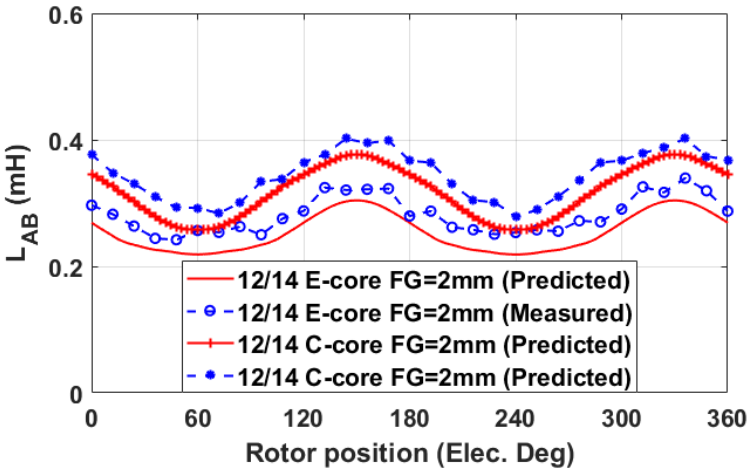

Fig. 3.41. Predicted and measure mutual inductances.

3.7.5. Static Torques

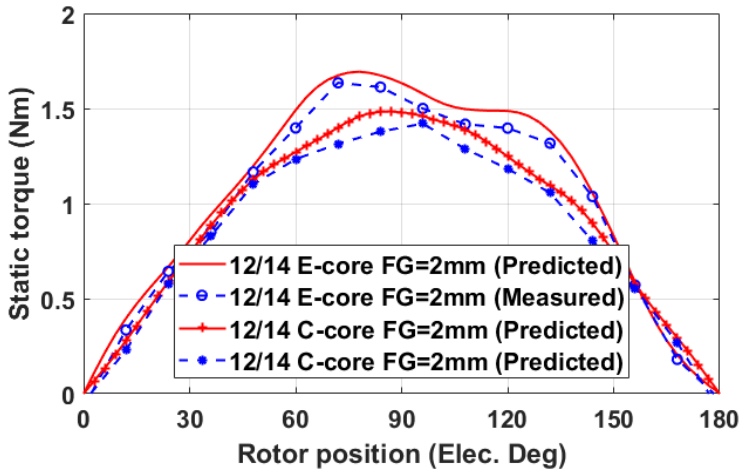

Fig. 3.42. Predicted and measured static torque *vs* rotor positions with $I_A = 3A$, $I_B = I_C = -1.5A$.

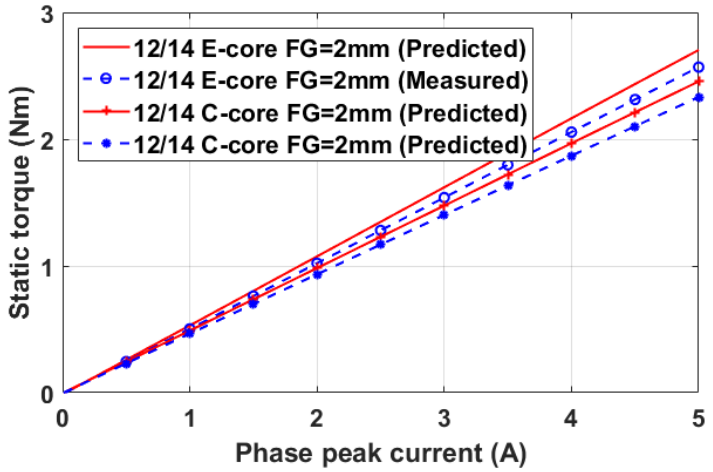

Fig. 3.43. Predicted and measured static torque *vs* phase peak current.

The on-load static torque has also been measured using the method mentioned in the cogging torque section, while supplying the 3-phase currents $I_A = I$, $I_B = -I/2$ and $I_C = -I/2$, where I is a dc current, which can be changed to simulate different load conditions. I also represents the current amplitude of an equivalent 3-phase sinewave current supply. To avoid the overheating of the prototype machine, 3A is selected as the dc current to achieve the waveform of static torque versus rotor position which is presented Fig. 3.42. The different rotor positions here can be regarded as different equivalent current phase angle. Moreover, the static torque under different phase peak currents are measured and

compared with the predicted results. The predicted and measured results are shown in Fig. 3.43 where general good agreement can be observed.

3.7.6. Dynamic Tests

The torque-speed curves of the prototypes are also measured and the results are shown in Fig. 3.44. The test rig is shown in Fig. 3.45. The dc link voltage is set to 18 V and the maximum phase peak current is 6 A, which are the same as the specifications used in the previous chapter. Again, a generally good match can be observed between the measured and predicted results.

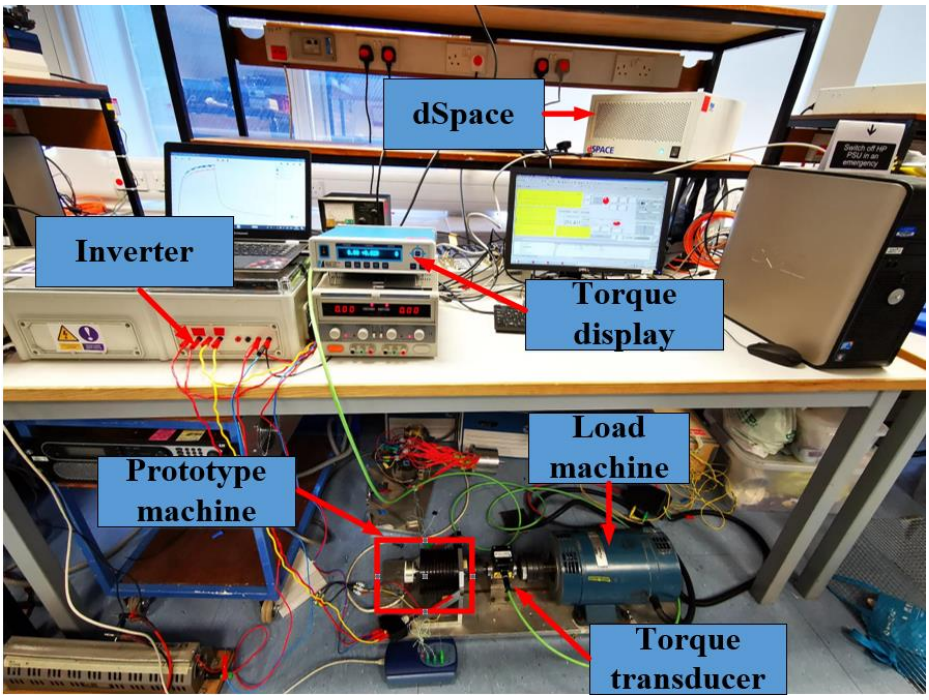

Fig. 3.45. Test rig set-up.

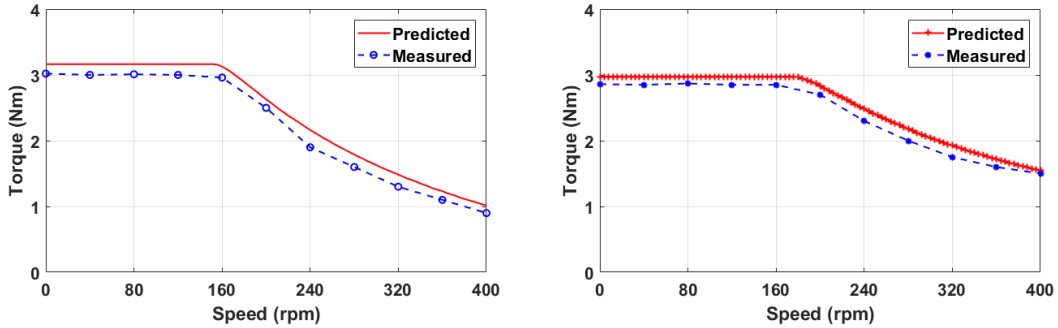

(a) E-core stator (b) C-core stator

Fig. 3.46. Predicted and measured torque-speed curves of 12-slot/14-pole E-core and C-core modular CPMs.

3.8. Conclusion

In this chapter, the modular consequent pole PM machines (CPMs) with both E-core and C-core stators are comprehensively compared. Two typical slot/pole number combinations including 12-slot/10-pole ($Ns>2p$) and 12-slot/14-pole ($Ns<2p$) have been taken into consideration. Both static and dynamic performances such as torque-speed curves, power-speed curves, power factor-speed curves and efficiency maps have been investigated. In addition, to achieve more general conclusion about the impact of flux gaps on machine performance, modular CPMs with large dimensions have also been investigated. It has been found that, for machines with different sizes, their average torque can be improved by using the E-core stator, whilst the torque ripple can be significantly reduced by using the C-core stator. Together with a CP rotor, PM material usage can be further reduced, making the modular CPMs ideal candidates for a wide range of industry applications. The simulation results of static and dynamic performances have been validated by a series of experimental tests.

In order to achieve optimal performance and provides some guidelines, some recommendations under different criteria are given as following for selecting the best candidates:

- Best candidate for maximizing the average torque: 12-slot/14-pole with E-core, the average torque increases by 17.3% from 4.424Nm (FG=0mm) to 5.191Nm (FG=3mm).
- Best candidate for minimizing torque ripple: 12-slot/10-pole with C-core, the torque ripple reduces by 68.7% from 9.43% (FG=0mm) to 2.95%(FG=3mm).
- Best candidate for achieving the highest efficiency: 12-slot/14-pole with E-core, the efficiency increases by 4.4% from 91% (FG=0mm) to 95% (FG=2mm).
- Best candidates for achieving the best dynamic performances are recommended in Table 3.5.

Table 3.5 Best candidates for dynamic performances

Flux-weakening capability	Power factor
12-slot/14-pole E-core (FG=2mm)	12-slot/10-pole C-core (FG=2mm)

To get a better understanding of performance improvements, a comparison is shown in Fig. 3.47. The 12-slot/10-pole C-core with 3mm FG and 12-slot/14-pole E-core with 2mm FG machines are selected for their outstanding performances in minimizing torque ripple and maximizing average torque, and their performances are compared with respect to the corresponding benchmark machines (non-modular machines).

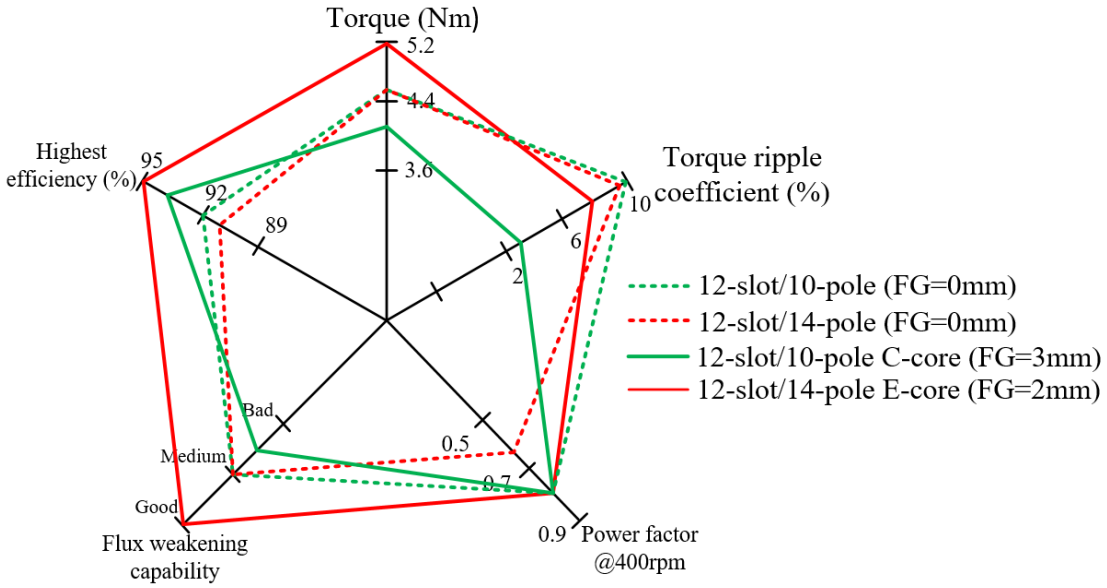

Fig. 3.47. Featured spider comparison.

Chapter 4 Forced Air and Liquid Cooling in Modular CPM Machines

4.1. Introduction

As discussed in previous chapters, PM machines have been widely used due to the advantages such as high torque, power density and high efficiency. However, higher power/torque density requirements are often limited by the thermal performances of the PM machines. Thermal management of electrical machines is always recognized as a vital aspect in machine design. Local high temperatures in the machines may shorten the winding insulation life and demagnetize the PMs. In other words, the performances of the electrical machines could be deteriorated due to the influence of high temperatures. Therefore, effective cooling methods are essential for electrical machines in order to reduce the temperature rise. In general, the cooling methods in electrical machines can be broadly classified into two groups, i.e. stator cooling and/or rotor cooling.

Significant efforts have been made for stator cooling. This is mainly because the windings, especially the slot center and end-windings are usually the hottest parts due to relatively low equivalent thermal conductivity resulting from the existence of insulation, impregnation and residual air in stator slots. Cooling jackets with water or other coolants circulating inside is the most commonly used method for housing and stator cooling [136]. The stator iron core is wrapped in the water jacket, which can effectively remove the heat generated in the machine. A lot of researches have been done to design and optimize the water jackets [137-141]. Although the water jacket is a good solution for the machine cooling, the aforementioned hot spots such as the active winding parts in the slot center and end-windings still cannot get direct cooling. Thus, several more direct cooling methods for the windings such as stator slot cooling channels [105, 142-144] and end-winding oil spray cooling [108, 145, 146] are proposed. They have been proven to be very effective cooling methods which can reduce the winding temperature and hence to reduce the overall temperature rise within the electrical machines.

Due to the existence of the airgap, the heat dissipation of the rotor is usually quite poor which could lead to high temperature in the rotor, causing potential irreversible PM demagnetization. With the aim of preventing the PMs from being demagnetized by high temperature, various rotor cooling methods have been proposed. [147] investigates the feasibility of integrating a fan on the shaft and stator/rotor ventilation holes to increase the air circulation which can increase the heat transfer within the machine, especially in the end-winding regions and provide effective cooling to both the stator and the rotor. Moreover, [148] proposes an electrical machine with a hollow shaft where the coolant is designed to flow through the shaft in order to provide sufficient cooling to the rotor.

The electromagnetic performances of modular CPMs have been comprehensively investigated in previous chapters. It has proven that the FGs can be beneficial for improving the electromagnetic performances of the modular CPMs such as average torque, power factor and efficiency if the width of the FGs is properly. Since the electromagnetic performances can be improved, it is worthwhile looking into the thermal performances of the modular machines. The existing literature [80] provides some feasible cooling methods using the FGs such as standard cooling jacket, axial cooling, radial cooling and direct air-gap oil-cooling. It proves that the machines can be effectively cooled when the FGs are used as cooling channels. However, only few 2D results are shown and several drawbacks can be observed such as high pressure drop in the cooling jacket, increased friction loss due to the viscosity of oil in the air-gap and so on. This chapter proposes a novel forced air cooling method utilizing the flux gaps (FG) of modular electrical machines as cooling channels to improve the internal cooling in such machines. The E-core modular CPM with FGs inserted into alternate stator tooth bodies as investigated in previous chapters has been used as an example.

This chapter is organized as follows: firstly, the proposed cooling structure is introduced and the CFD solution domain is established. Then, the effectiveness of utilizing the FGs as cooling channels is proven. Moreover, the influence of FG width, inlet position and inlet dimension are also investigated.

4.2. Proposed Forced Air Cooling Utilizing FGs

As discussed in previous chapter, the electromagnetic performances such as average torque, dynamic capability can be significantly improved by selecting appropriate FG

width in the 12-slot/14-pole E-core modular CPMs. Thus, by way of example, this machine has been selected for the investigation and its topology is shown in Fig. 4.1(a). Table 4.1 lists the general specification of this machine. The FGs are inserted in the middle of alternate stator teeth and hence the machine has 6 FGs in total.

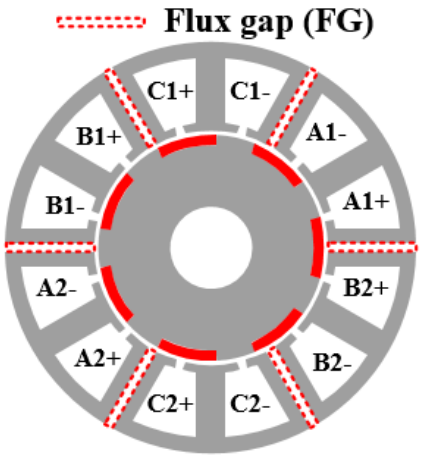

Fig. 4.1. Topology of the 12-slot/14-pole E-core modular CPM.

Table 4.1. General specifications of the modular CPMs

Stator outer radius (mm)	100	Split ratio	0.57
Tooth width (mm)	7.2	Stator yoke height (mm)	3.7
Air-gap length (mm)	1	Stack length (mm)	50
Rated current (A_{rms})	7.34	Number of turns/phase	132

4.2.1. Model Structure

The idea of using FGs as cooling channels is to let the coolant pass through the FGs in order to increase the wall heat transfer coefficient (HTC) of the FGs and to improve the heat dissipation rate from the stator to the coolant, in this case it is air. For the initial proposed cooling structure, the inlets are positioned facing the FGs which are aligned with the FGs in the axial direction as can be seen from Fig. 4.2 (a). The corresponding outlets are on the opposite side of the endcaps. Thus, the machine will have in total 6 inlets and 6 corresponding outlets, as shown in Fig. 4.2 (b).

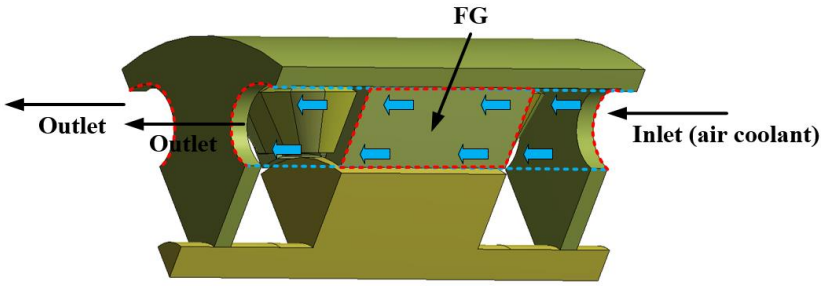

(a) 1/6 partial model

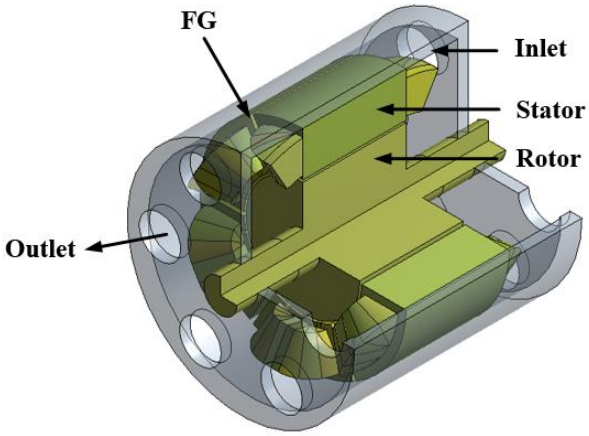

(b) Detailed view of 3D model

Fig. 4.2. Models of the proposed forced air cooling with inlets and outlets on endcaps.

Due to the fact that FEA method is only accurate enough in the field where solid conduction heat transfer is dominant, while the investigation in this chapter includes both solid and fluid mediums, it is essential to carry out the research using 3D computational fluid dynamics (CFD) software. The package used in this investigation is CFX package which is embedded in the commercial software Ansys. The CFD method is based on the finite-volume and can be accurate enough to predict the fluid velocity distributions and the wall HTC within boundaries. It is known that the 3D CFD analysis is accurate but quite time-consuming and therefore a partial model is usually used to reduce computer hardware requirement and also computation time. Due to the fact that the modular CPM has an asymmetric consequent-pole (CP) rotor structure and the number of pole pairs is 7 which is an odd number, it is not adequate to build the 1/6 model to reduce the computation burden (which is however possible from the stator point of view as there are 6 FGs in the stator). However, the focus of this investigation is to evaluate the general cooling effect of the modular stator structure by using the FGs as cooling channels rather than focusing on the rotor PMs, therefore, the PMs are replaced by the same material as rotor iron core. This means that the “virtual” rotor is

treated as a smooth cylinder and a 1/6 partial model is built as can be seen in Fig. 4.2(a). This will significantly simplify the modelling and reduce the computation time, which is particularly beneficial as large number of cases need to be investigated in this chapter.

4.2.2. Governing Equations and Boundary Conditions

Following the governing equations such as the mass conservation equation, momentum conservation equation and energy conservation equation, the CFD method is able to accurately predict the characteristics of different fluid flow. Generally, these governing equations are expressed as [149]:

$$\frac{\partial \rho}{\partial t} + \nabla \cdot (\rho \boldsymbol{u}) = 0 \tag{4.1}$$

$$\begin{cases} \dfrac{\partial(\rho u)}{\partial t} + \nabla \cdot (\rho \boldsymbol{u} v) = \nabla \cdot (\mu \nabla u) - \dfrac{\partial P}{\partial x} + S_u \\ \dfrac{\partial(\rho v)}{\partial t} + \nabla \cdot (\rho \boldsymbol{u} v) = \nabla \cdot (\mu \nabla v) - \dfrac{\partial P}{\partial y} + S_v \\ \dfrac{\partial(\rho w)}{\partial t} + \nabla \cdot (\rho \boldsymbol{u} w) = \nabla \cdot (\mu \nabla w) - \dfrac{\partial P}{\partial z} + S_w \end{cases} \tag{4.2}$$

$$\frac{\partial(\rho T)}{\partial t} + \nabla \cdot (\rho \boldsymbol{u} T) = \nabla \cdot (\frac{\lambda}{c} \nabla T) + S_T \tag{4.3}$$

where ρ is the fluid density, and t is the time in (4.1). In (2), x-, y- and z-components of the fluid velocity are represented as u, v, and w and u is the fluid velocity vector, μ is the fluid dynamic viscosity, P is the fluid pressure; S_u, S_v, and S_w are the source terms of the momentum equation. In (3), T is the temperature, c is the specific heat capacity, λ is the thermal conductivity, S_T is the volumetric heat source.

4.2.3. Turbulence Model and Mesh Treatment

Due to the complex fluid flow path and the relatively narrow FGs, the shear stress transport (SST) $k-\omega$ turbulence model is selected to accurately calculate the flow field and the temperature rise. Most turbulence models are based on Reynolds-averaged Navier–Stokes (RANS) equations which are used to deal with the 3D turbulent flow and the heat transfer. According to [82, 150], in comparison with the standard $k-\epsilon$ and $k-\omega$ turbulence model, the SST $k-\omega$ model is more accurate for swirling flows and the specialized wall functions are not required.

The tetrahedron mesh generation technology is applied to this model. Careful considerations should be taken near the narrow air-gap and FG regions in order to guarantee the accuracy of the CFD model. The inflation boundary layers method has been adopted and 8 mesh layers have been created in both the air-gap and the FGs in order to achieve acceptable accuracy. Moreover, the `skewness` is an important criterion to assess the mesh quality. The grid is refined iteratively until the solution becomes grid-independent and the maximum skewness of the generated grid is less than 0.4 which is good enough to achieve accurate calculation. Finally, the resultant mesh grid will have nearly 7 million mesh elements. The detailed view of the overall mesh generation is shown in Fig. 4.3.

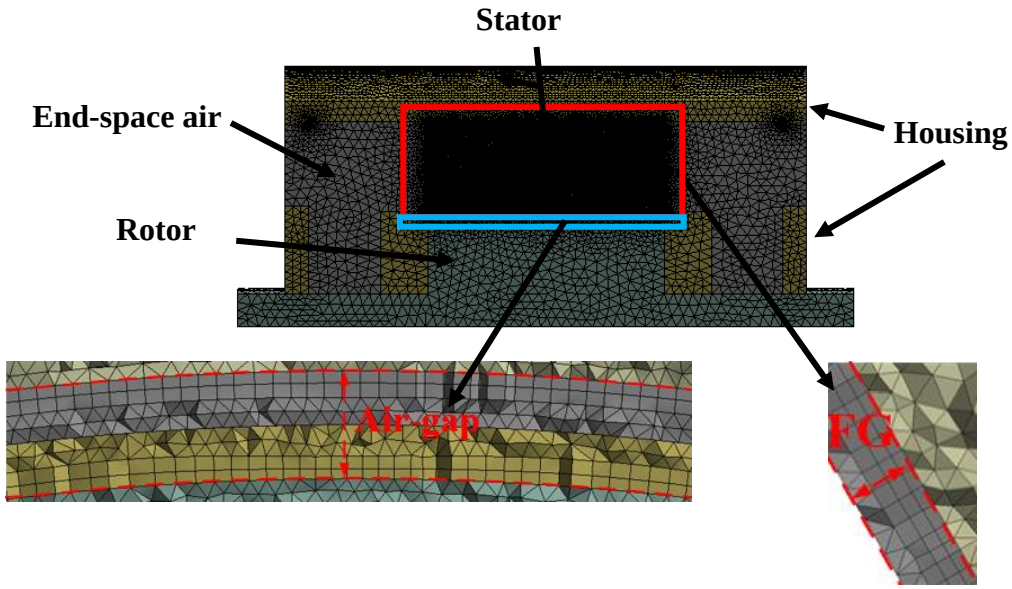

Fig. 4.3. Generated mesh of the CFD model

4.2.4. Thermal Properties of Different Materials and End-Winding Treatment

Windings in the stator slot will usually include different materials such copper, insulation, slot liner, etc. and it is difficult and time-consuming to model each individual conductor, particularly for random wound windings. Thus, the commonly used equivalent thermal conductivity method is adopted to model the windings. The idea of equivalent thermal conductivity method is to take all materials including copper, insulation, impregnation, residual air etc. into account and use an equivalent thermal conductivity to represent the slot as shown in Fig. 4.4.

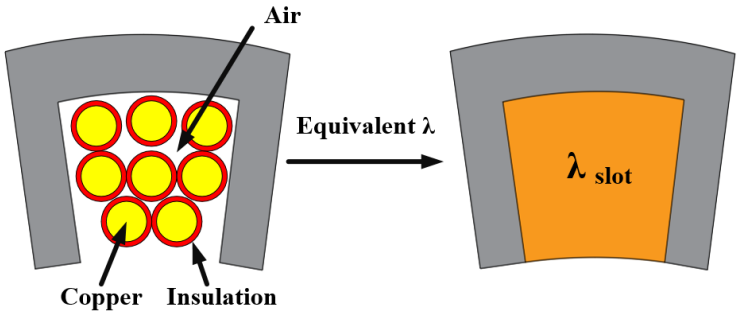

Fig. 4.4. Illustration of equivalent thermal conductivity in stator slot [151].

According to [152], a good data correlation to estimate the equivalent thermal conductivity can be expressed in (4.4):

$$\lambda_{\text{slot}} = 0.24[(1 - k_f)S_{\text{slot}}L]^{-0.04} \tag{4.4}$$

where λ_{slot} is the slot equivalent thermal conductivity, k_f is the slot fill factor, S_{slot} represents the slot area and L is the active length.

It is worth noting that the windings will have orthotropic thermal conductivities. For most radial-flux electrical machines, the thermal conductivity in axial direction is much higher than that in the radial direction. The thermal conductivity in the axial direction is almost the same as the thermal conductivity of copper wire while equivalent thermal conductivity in the radial direction is largely determined by the insulation material, impregnation, residual air and slot liner, etc. As a result, it is much smaller than the axial equivalent thermal conductivity.

Another problem with the windings is the modelling of end-windings. Due to the fact that the end-windings are wound on the stator tooth as seen in Fig. 4.5 (a), thermal conductivities are changing gradually along the end-winding, i.e., radial conductivity should be increasing while the axial conductivity should be decreasing. In order to model this, the entire end-windings is divided into several segments and one specific local coordinate system is applied to each segment, as shown in Fig. 4.5 (b). By doing this, the radial and tangential directions (corresponding to radial conductivity) represent the X-Y plane while the axial direction (corresponding to axial conductivity) is the Z-axis.

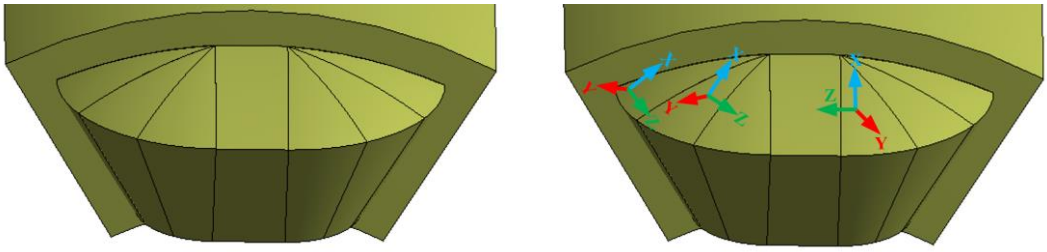

(a) End-winding segments (b) different local coordinate systems along the end-winding

Fig. 4.5. End-winding treatments with the orthotropic thermal conductivity being considered.

Table 4.2 lists the thermal properties of the used materials including their thermal conductivity, specific heat capacity, density and dynamic viscosity for the fluid.

Table 4.2 Thermal properties of related materials

Materials	Thermal conductivity (W/m/K)	Specific heat capacity (J/kg)	Density (kg/m^3)	Dynamic viscosity ($N s/m^2$)
Steel	60.5	434	7854	/
Air (20°C)	0.026	1004	1.185	1.831E-05
Aluminium	237	903	2702	/
Equivalent slot (Copper wires, varnish and air included)	0.39 (radial and tangential), 401 (axial)	385	8900	/

4.2.5. Heat Sources and Boundary Conditions

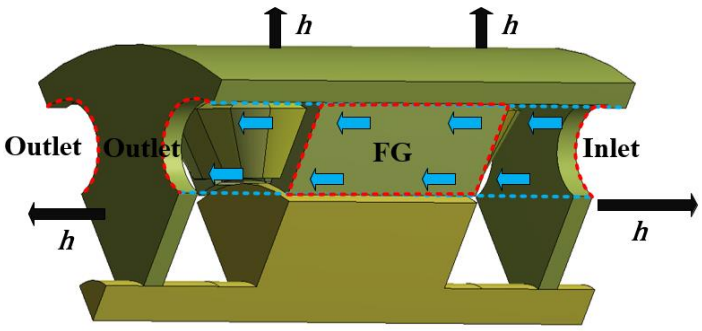

Fig. 4.6. Illustration of boundary conditions.

Heat sources within the CFD model are the losses of different components in the machines. For simplification, only the copper losses and stator iron losses are taken into consideration in this investigation. As stated in previous sections, for general modelling, the PMs are replaced by the same material as rotor iron core and the "virtual" rotor is treated as a smooth cylinder which means there is no need to consider the PM eddy current losses. Moreover, according to the calculated results shown in chapter 3, the PM eddy current losses are very small which means it is safe to neglect them without seriously affecting the accuracy of the model. For the same reason, the very small rotor iron losses have also been neglected.

The copper losses (Joule losses) are calculated based on the current and phase resistance. The stator iron loss are calculated by FEA, as already investigated in chapter 3. Moreover, some assumptions and the boundary conditions are listed as following:

1) For model simplification, mechanical components such as eye bolts, small fillet, junction boxes, bearings, etc. are removed from the CFD model;

2) In the solution domains, the air is treated as incompressible fluid;

3) Due to the limit of computation resources and with the aim of saving time, only the steady state is taken into account. The rotating-reference frame technique, also called 'frozen rotor' method, was used to consider the rotation of the rotor. Thus, the air within the machine is separated into two parts. One part is used to envelop the rotor and set to rotate with the rotor while the other part is set as stationary and an interface is created to allow data to be transferred between the rotating and stationary parts;

4) The losses are distributed within the machine homogenously. The iron losses are calculated at the rated condition (400rpm, I_{rms}=7.34A) and the copper losses per phase of all machines are the same (I_{rms}=7.34A, R_{phase}=0.6Ω, P_{copper_phase}=32.3W);

5) The thermal property of materials is not influenced by the temperature rise;

6) $\boldsymbol{h}$ is the heat transfer coefficient (HTC) from the housing outer surface to the ambient air. It is assumed to be natural convection and $\boldsymbol{h}$ is set to be 20 W/m^2/K considering the machine dimensions according to [153, 154] and the ambient air temperature is 20 ℃;

7) The type of inlet is set as speed inlet and coolant air is set to be 60 ℃, which is the commonly used coolant temperature in industry [155], outlet is set as pressure outlet with static pressure of 1 atm;

8) The temperatures of critical locations are monitored such as the slot centre, end-winding hot spot and the criteria of solver convergence is set as 1e-04 considering the computing power and accuracy of the results.

4.3. Influence of FG Width

Since the modular machines have FGs as extra cooling channels, the temperature rise of modular machines are expected to be lower in comparison with that of non-modular machines. Same as the influence of FGs on the electromagnetic performances investigated in previous chapters, the influence of FG width on the cooling effect in modular machines are investigated in this section. Although it might be evident that higher inlet speed will lead to better cooling effect which means lower temperature rise, it is still useful to investigate the cooling effect under different inlet speeds.

Table 4.3 shows the highest temperature within the machines with different FG widths and inlet speeds. It worth noting that the highest temperature within machines often locates at slot centre or at the end-winding. It can be seen that with increasing inlet speed, the highest temperature within the machines keeps decreasing which is due to the increasing mass flow of air coolant. Meanwhile, it can be found that, for the same inlet speed, better cooling effect can be observed in the modular machines compared with the non-modular machines (FG=0mm). This is independent of the FG width. These results have proven the effectiveness of utilizing FGs as cooling channels in modular machines.

Table 4.3 Highest temperature within the machines (inlets facing FGs)

FG width / **Inlet speed**	**0mm**	**1mm**	**2mm**	**3mm**	**4mm**	**5mm**	**6mm**
0m/s	126.71	126.6	126.19	126.6	126.6	126.5	126.2
2.5m/s	91.22	85.59	84	84.87	85.21	85.72	85.91
5m/s	85.36	81.02	80.61	81.3	81.63	82.02	82.32
7.5m/s	82.69	79.44	78.94	79.72	79.47	80.19	80.11
10m/s	81.35	78.27	77.90	78.69	78.76	78.92	79.05

Moreover, the highest temperatures within the machines versus FG widths for different inlet speeds are also shown in Fig. 4.7. It can be seen that the modular machines with 2mm FG will always have the lowest hot spot temperature compared with the other modular machines. In other words, there will be an optimal FG width to achieve the best cooling effect for the modular machines with forced air cooling. This is a phenomenon which is quite similar to the electromagnetic performances, where an optimal FG width also exists.

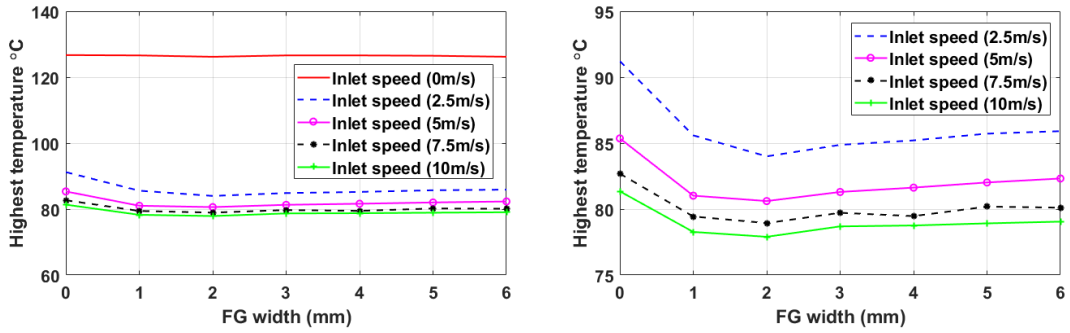

(a) 0m/s included (b) 0m/s excluded

Fig. 4.7. Highest temperatures within the machines *vs* FG width for different inlet speeds.

The results can be explained by using a series of contour plots. Firstly, the streamlines of the investigated machines with selected FG width 0mm (non-modular), 2mm, 4mm and 6mm are shown in Fig. 4.8. The flow path of the air passing through the FGs in modular machines can be easily observed. The temperature distributions with the selected FG widths are shown in Fig. 4.9. Meanwhile, the temperature distributions of the end-windings are presented in Fig. 4.10 and Fig. 4.11, these two figures show the same results but from different angles.

From Fig. 4.9, the flow path of the low temperature air can be easily seen and the extra circulating air in the FGs in modular machines is able to remove more heat from the stator iron and windings compared with the non-modular machines. Fig. 4.10 and Fig. 4.11 clearly show that the end-windings are the main hot spots and the temperatures can be significantly reduced in the modular machines with the proposed forced air cooling. For example, the highest temperature within the modular machine with 2mm FG width can be reduced to 84℃, down by nearly 7℃ compared with 91.22℃ in the non-modular machine (0mm FG width).

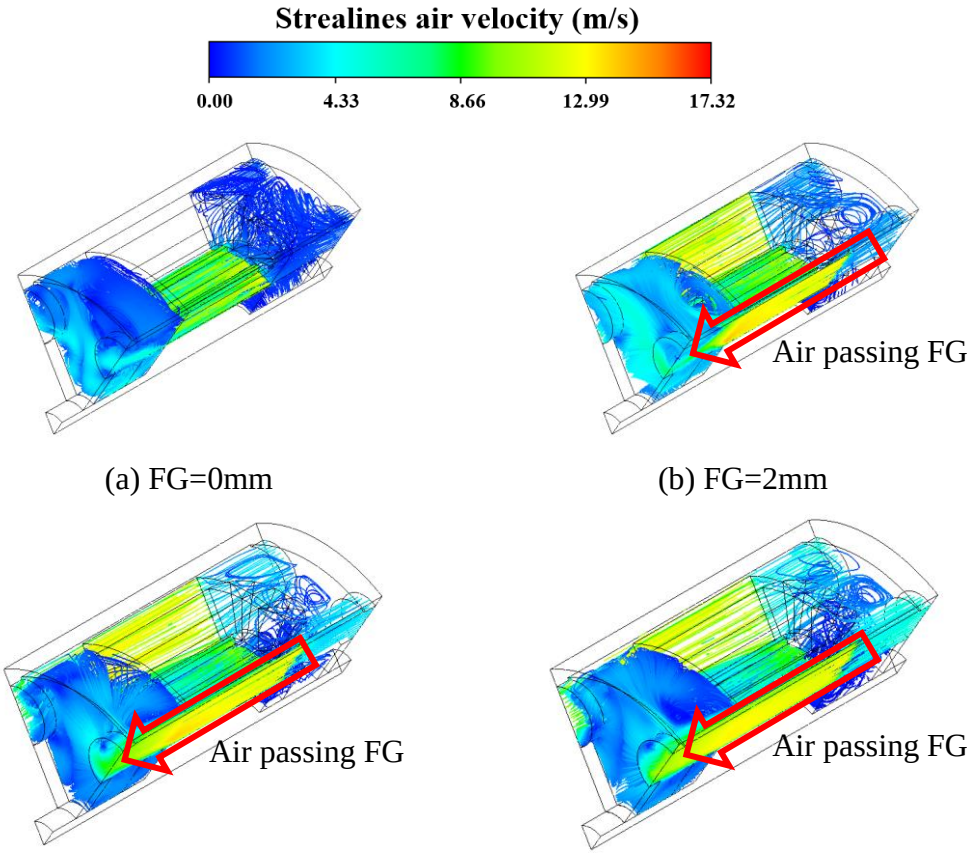

(a) FG=0mm (b) FG=2mm

(c) FG=4mm (d) FG=6mm

Fig. 4.8. Streamlines of the machines with different FG widths.

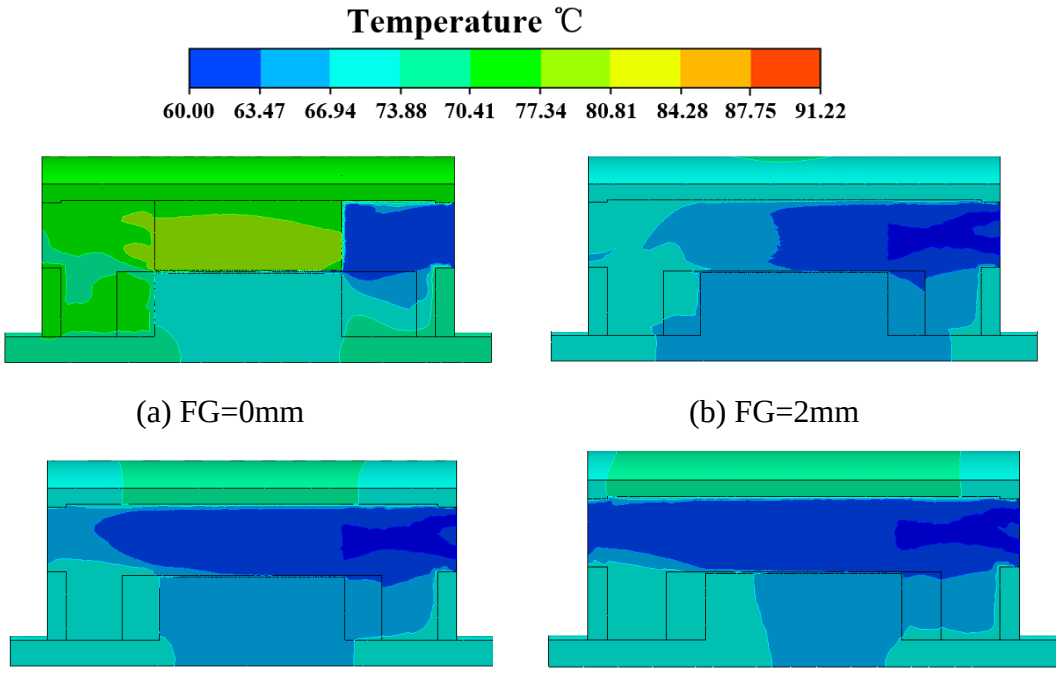

(a) FG=0mm (b) FG=2mm

(c) 4mm (d) 6mm

Fig. 4.9. Temperature distributions within machines with different FG widths.

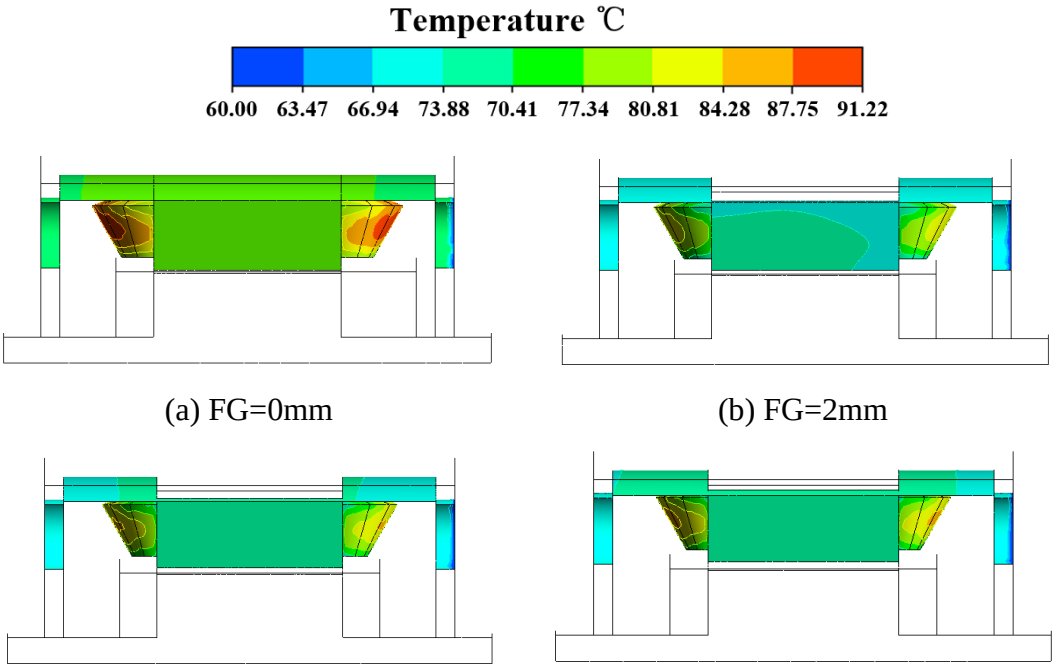

(a) FG=0mm (b) FG=2mm

(c) FG=4mm (d) FG=6mm

Fig. 4.10. End-winding temperature distributions of the machines with different FG widths.

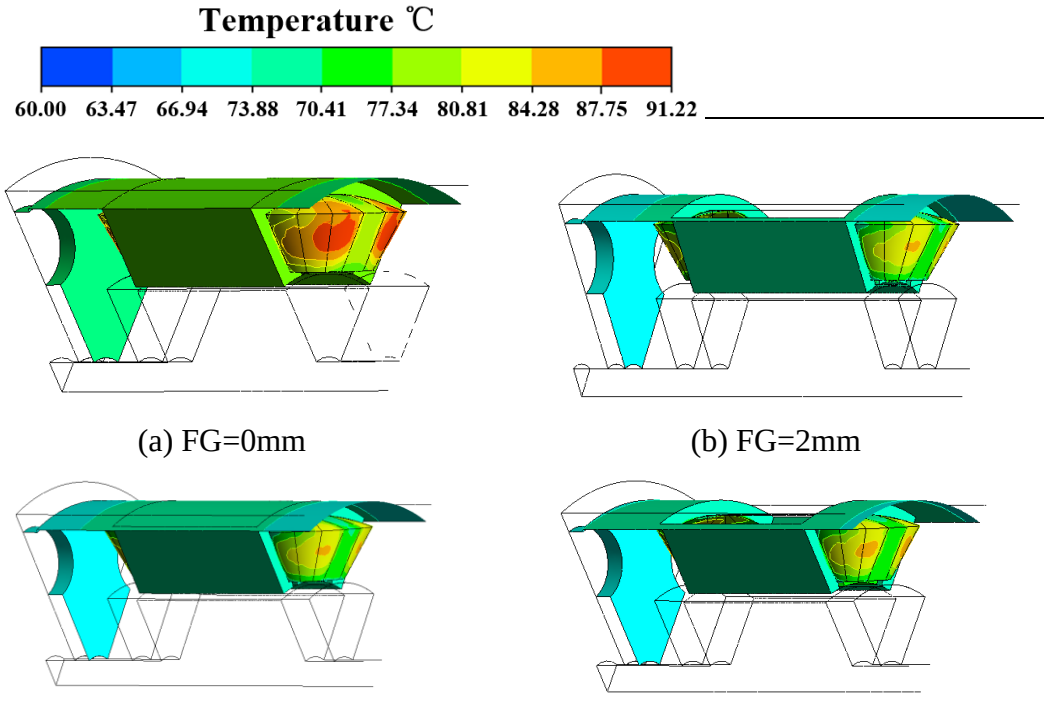

(a) FG=0mm (b) FG=2mm

(c) FG=4mm (d) FG=6mm

Fig. 4.11. End-winding temperature distributions of machines with different FG width.

As can be seen from Fig. 4.7, there will be an optimal FG width (2mm) for the modular machines with the forced air cooling to achieve the best cooling effect. In order

to explain this phenomenon, the distributions of air velocity vector on the specified plane which is aligned with the middle of FG are plotted in Fig. 4.12.

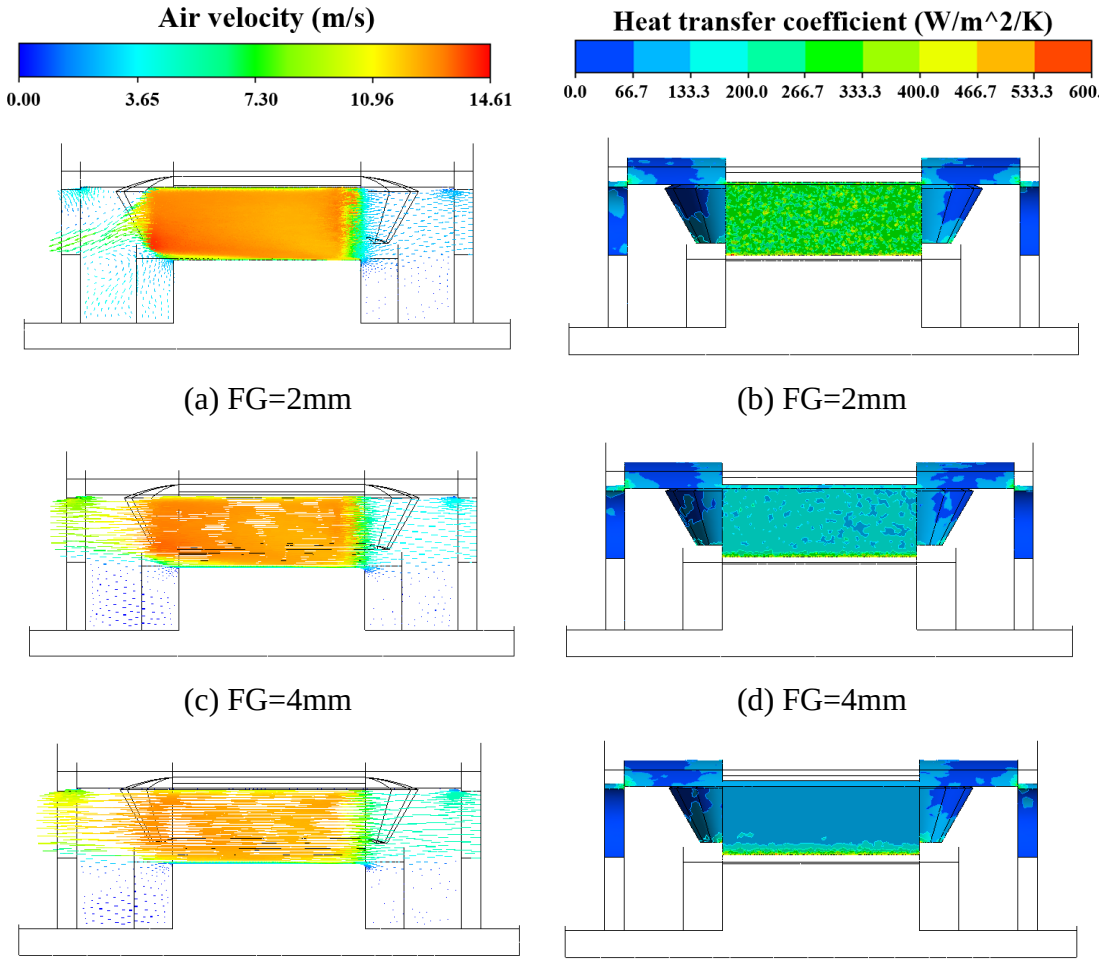

(a) FG=2mm (b) FG=2mm

(c) FG=4mm (d) FG=4mm

(e) FG=6mm (f) FG=6mm

Fig. 4.12. (a), (c), (e) Distributions of air velocity vector in modular machines with different FG widths. (b), (d), and (f) HTCs on the wall of FGs in modular machines with different FG widths.

Meanwhile, the HTCs on the wall of FGs are also shown in Fig. 4.12. It should be noted that only the modular machines with 2mm, 4mm and 6mm FG widths are shown here and because the non-modular machine (0mm FG width) does not have FGs. The machine with 2mm FG has the highest air velocities in the FGs. As a result, the HTCs on the wall of FG in the modular machine with 2mm FG width ranges from 266-333 $W/m^2/K$, which is higher compared with those in the modular machine with 4mm, 6mm FG widths, as shown in Fig. 4.12 (d) and (f), respectively. Higher HTC means better heat dissipation rate which leads to the fact that the modular machine with 2mm FG width has the most significant temperature drop and the best cooling effect.

However, apart from the temperature, the pressure drop between the inlet and outlet should also be included. This is because the pressure drop determines the efficiency of the external heat exchanger equipment, and higher pressure drop means lower cooling system efficiency. It is pointed out in [156] that an increased pressure drop could lower the coolant flow rate if the external heat exchanger has a limited pressure supply. Although the external heat changer equipment has not been taken into considerations in the investigation, it is still meaningful to gain some insight into the influence of FGs on the pressure drop and also on the efficiency of the external heat exchanger equipment. In addition, it is established that usually the friction losses can be reflected on the pressure drop and lower pressure drop is desirable which roughly represents higher cooling system efficiency. Therefore, the pressure drops versus FG width with 2.5m/s inlet speed have been calculated, as shown in Fig. 4.13. It can be easily found that larger FG width can lead to lower pressure drop which means higher cooling system efficiency. Therefore, considering both the best cooling effect (highest temperature drop) and lowest pressure drop (highest cooling system efficiency), a compromise should be made when selecting the FG width. In this case, FG width of 2mm is considered to be a good option.

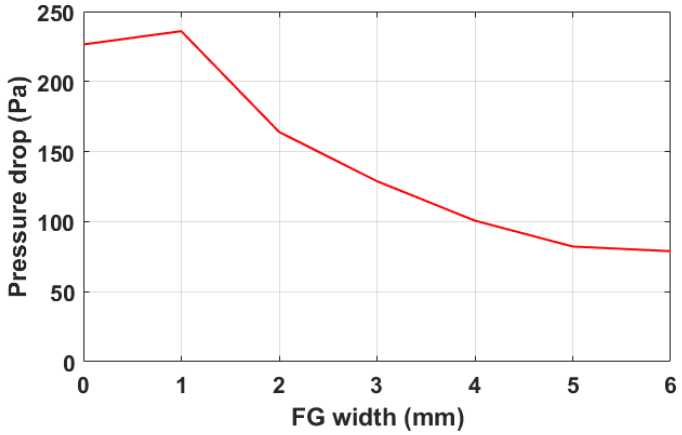

Fig. 4.13. Pressure drop between the inlet and outlet *vs* FG width. The inlet speed is 2.5m/s.

4.4. Influence of Inlet Position

As mentioned previously, the influence of the FG width has been investigated and it is found out that 2mm FG width is optimal to achieve the best cooling effect. However, the investigation is based on the scenarios when the inlet is aligned with the FGs and

the air coolant goes directly into the FGs from the inlet which can be easily observed from the streamlines shown in Fig. 4.14 (a). With this structure, the EWs, where the hot spots are usually located, have not been provided with sufficient cooling. Therefore, it is essential to investigate the influence of the inlet position. As the EWs are the locations where effective cooling is mostly desired, a reasonable alternative for the inlet position is aligned with the central line of the EWs, as shown in Fig. 4.14 (b). It is worth pointing out that when inlet position changes, the outlet position will change accordingly, as shown in Fig. 4.14.

It has already been pointed out in section 4.3 that higher inlet speed will lead to better cooling effect which means lower temperature rise. And the focus of this section is the influence of inlet positions, thus only 2.5m/s and 5m/s inlet speeds are taken into consideration for the following analyses.

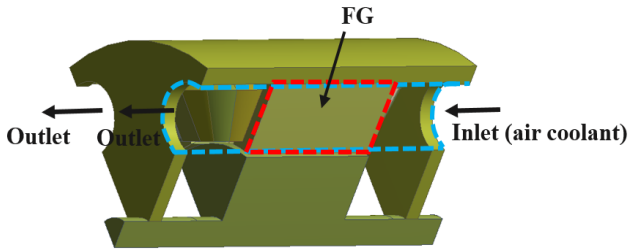

(a) inlet facing FGs

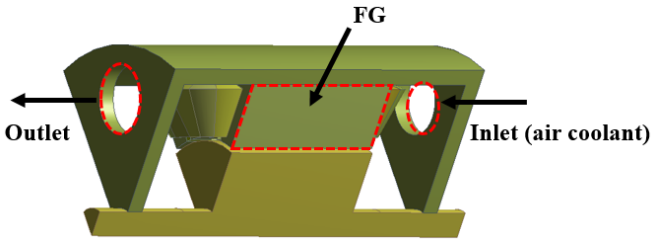

(b) inlet facing EWs

Fig. 4.14. CFD models with different inlet positions.

Table 4.4 Highest temperature within the machines (inlets facing FGs)

FG width / Inlet speed	0mm	1mm	2mm	3mm	4mm	5mm	6mm
2.5m/s	91.22	85.59	84	84.87	85.21	85.72	85.91
5m/s	85.36	81.02	80.61	81.3	81.63	82.02	82.32

Table 4.5 Highest temperature within the machines (inlets facing EWs)

FG width / Inlet speed	0mm	1mm	2mm	3mm	4mm	5mm	6mm
2.5m/s	90.35	85.38	84.09	83.85	83.73	83.72	83.45
5m/s	84.84	80.83	80.64	80.69	80.45	80.53	80.3

The highest temperatures within the machines with inlet facing FGs and inlet facing EWs for different FG width are listed in Table 4.4 and Table 4.5, respectively. To make the comparison clearer, these results are also shown in Fig. 4.15. It is obvious that higher inlet speed leads to better cooling effect, regardless of the inlet positions.

As already explained before, when the inlet is facing FGs, in terms of the influence of FG width, it can be seen that the highest temperature will first decrease and then increase. This is mainly due to the variation trend of HTCs on the wall of FGs. However, it should be observed that if the inlet is facing the EWs, the highest temperatures within the machines will first reduce with the increasing FG width and then remain almost unchanged when the FG width becomes larger (e.g. ≥2mm).

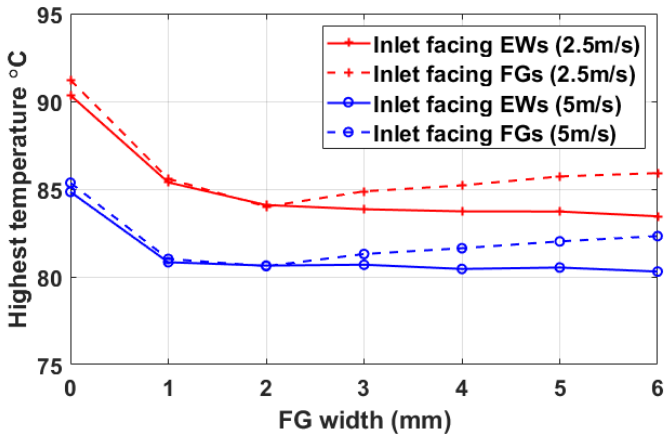

Fig. 4.15. Highest temperatures within the machines for different inlet positions.

The EW temperature distributions for both inlet positions, i.e. inlet facing FGs and inlet facing EWs, are shown in Fig. 4.16 and Fig. 4.17, where 2mm and 6mm are the selected FG widths, respectively.

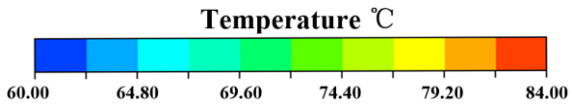

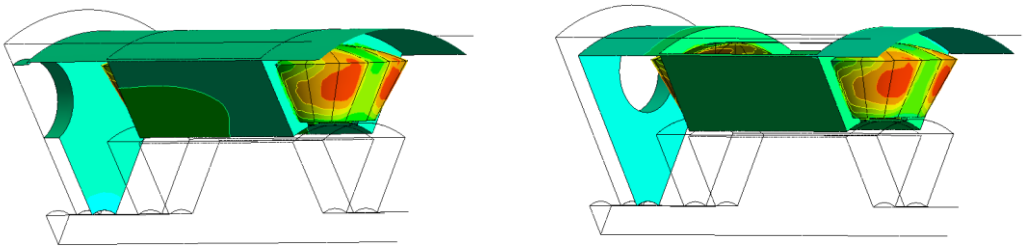

(a) Inlet facing FGs, (2mm FG) (b) Inlet facing EWs, (2mm FG)

Fig. 4.16. EW temperature distributions for both inlet positions, FG=2mm.

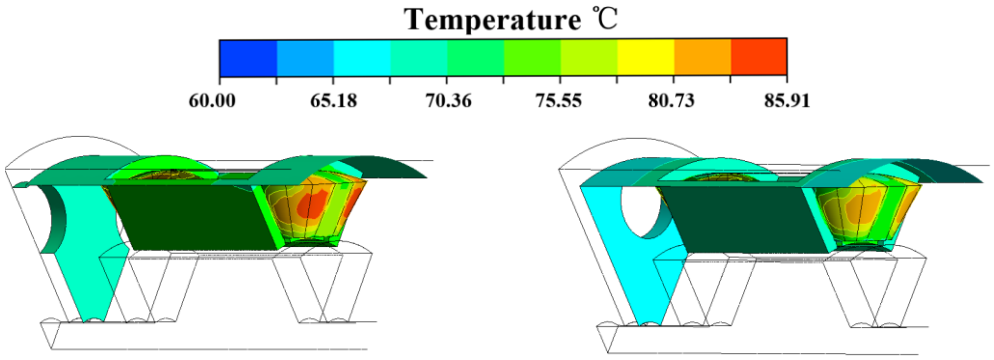

(a) Inlet facing FGs, (6mm FG) (b) Inlet facing EWs, (6mm FG)

Fig. 4.17. EW temperature distributions for both inlet positions, FG=6mm.

The HTCs of the FGs for both inlet positions and FG width are compared in Fig. 4.18. It can be seen that for both inlet positions, the HTCs of FGs with different FG widths are at the same level and quite similar.

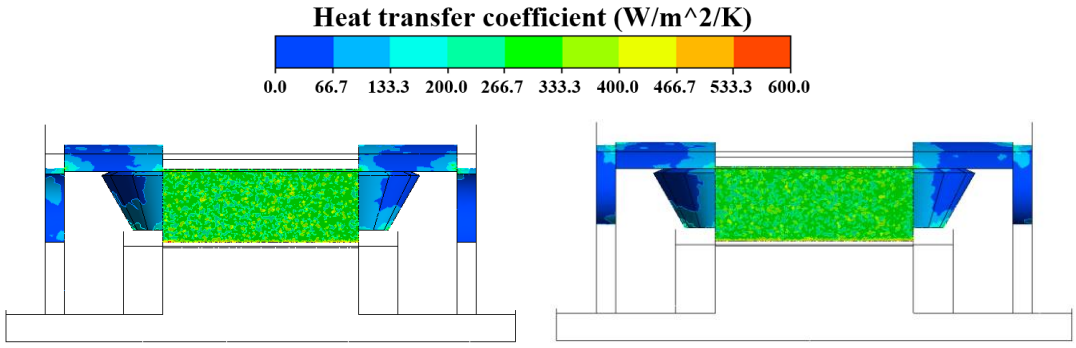

(a) FG=2mm (b) FG=2mm

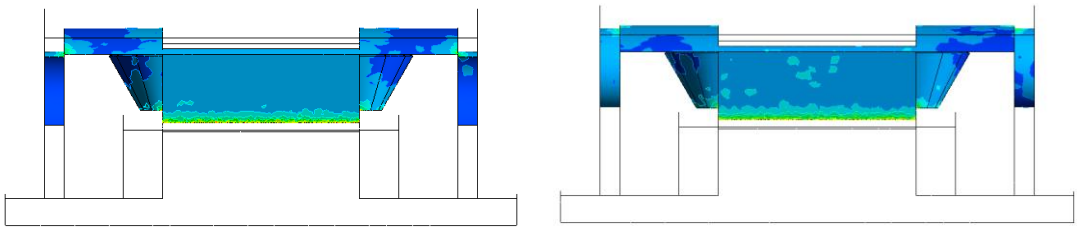

(c) FG=6mm (d) FG=6mm

Fig. 4.18. HTCs of FGs. (a) FG=2mm and (c) FG=6mm with inlet facing FGs, (b) FG=2mm and (d) FG=6mm with inlet facing EWs.

It is worth noting that in the investigated modular machines, the heat generated within the windings (including active winding and end-winding) is dissipated through three paths: (1) from active winding to stator iron core and the housing via thermal conduction, (2) from stator core to the FGs via thermal convection and (3) from EWs to the end-space air via thermal convection. Since the boundary conditions of the machine housings are fixed the same for all machines as shown in Fig. 4.6 and HTCs of FGs are quite similar as shown in Fig. 4.18, the HTCs of surfaces of EWs should be considered to see the different impact of different inlet positions. Therefore, the figures highlighting HTCs of the surfaces of EWs for both inlet positions and FG widths are shown in Fig. 4.19.

It should be noted that when the inlet is facing the EWs, compared with the 2mm FG width, although the 6mm FG width has smaller HTC in FGs, its HTC on EWs is higher. In other words, when the inlet is facing EWs, although the HTCs in FGs will be slightly lower, the HTCs on the surfaces of EWs can be increased when the FG width becomes larger and as a result, the overall influence of FG width is quite slight. This is the reason why when the inlet faces the EWs, the highest temperatures within the machines will first reduce with the increasing FG width and then stay almost the same when FG width becomes larger (e.g. $\geqslant$2mm).

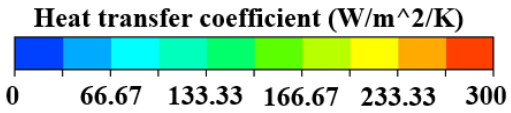

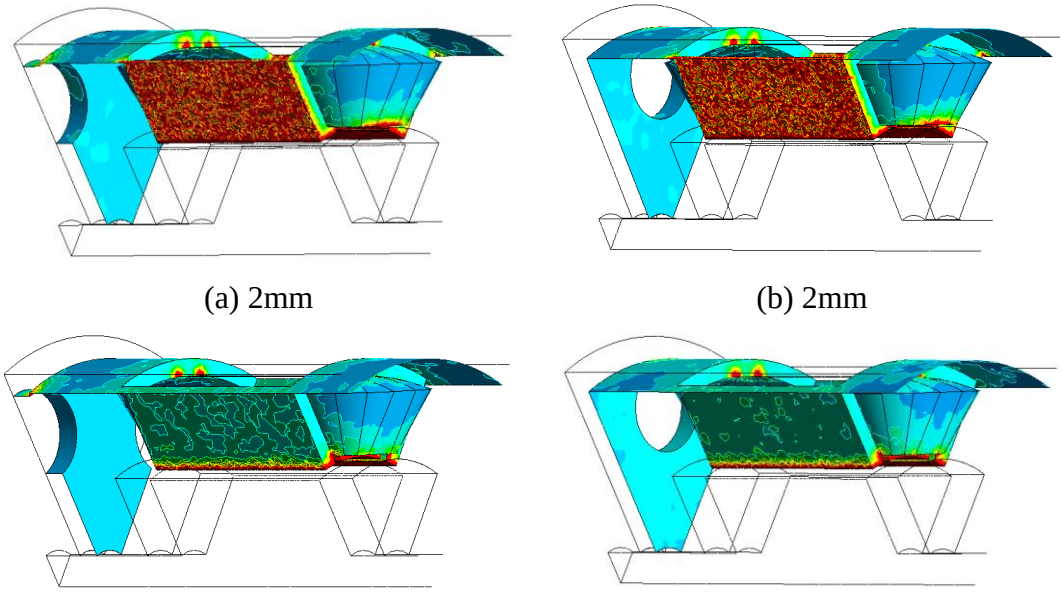

(a) 2mm (b) 2mm

(c) 6mm (d) 6mm

Fig. 4.19. HTCs of surfaces of EWs. (a) FG=2mm and (c) FG=6mm with inlet facing FGs, (b) FG=2mm and (d) FG=6mm with inlet facing EWs.

Meanwhile, the pressure drop between the inlet and outlet for both inlet positions against different FG widths is shown in Fig. 4.20. For both inlet positions, the pressure drop will decrease with increasing FG width. However, the pressure drop for the case where the inlet is facing FGs is always lower compared with the case where the inlet is facing EWs. The reason can be explained as follows. If the inlet faces the EWs, the EWs will block the air flow and separate it before entering the FGs. This obviously will increase the resistance of the air flow path and as a result, the pressure drop will be higher compared with the case where the inlet faces the FGs.

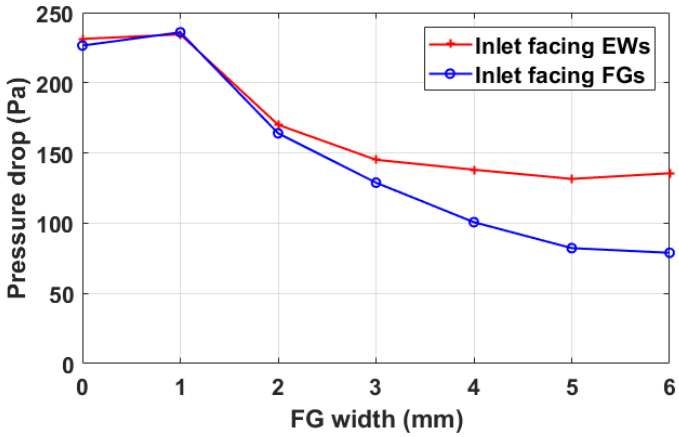

Fig. 4.20. Pressure drops between the inlet and outlet of the machines having different inlet positions.

4.5. Influence of Inlet Dimensions

The machines with inlets and outlets in the end-caps are quite similar to the open fan cooled (OFC) motor discussed in [150]. A typical feature of this kind of machines is that the cooling air is continuously being blown from the ambient or heat exchanger into the machine via the inlets and discharged from the outlets. Although this method can enhance the heat exchange between the machine and external environment and provide sufficient cooling effect, a main drawback is that the particles or contaminants could be attracted into the machine [33]. Therefore, a hood is usually employed to filter the air coolant but in fact the pollutants cannot be totally filtered. Thus, the OFC machines normally need a clean-up process every two or three years.

The proposed modular machines with inlets and outlets in the end-caps in this chapter can also be regarded as an OFC machine. Meanwhile, due to the presence of FGs and they are utilized as the cooling channels, it is essential to ensure that they are not blocked by the pollutants. Although the heat exchanger is not in the scope of this research, it can be easily understood that smaller inlet will be better for preventing the pollutants from entering the machines if the pollutant is not filtered by the hood. Therefore, the influence of the inlet dimension has been investigated in this section. Fig. 4.21 shows structures with different inlet dimensions. Since the shape of inlet is round, the radius of the inlet is the dimension which needs to be changed. It should be noted that the focus of this section is the inlet dimension and 2mm has been proven to be the optimal FG width in the previous section, thus, the FG width is fixed at 2mm in this section. This can significantly reduce the time and effort for CFD modelling.

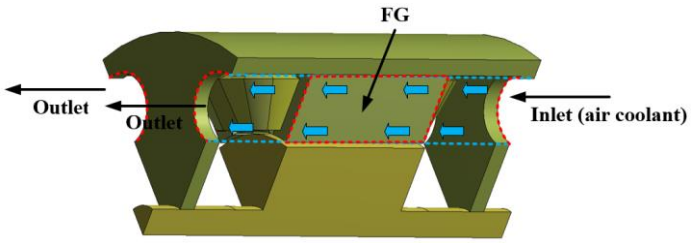

(a) Machine with 10mm inlet radius

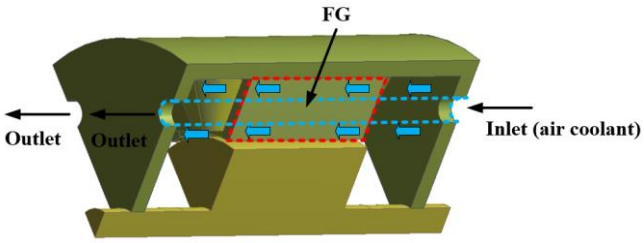

(b) Machine with 2mm inlet radius

Fig. 4.21. Illustration of machines with different inlet radii.

Two cases have been studied in this section. In the first case, the inlet type used in the CFD model is set to be the speed inlet type since the inlet dimension is fixed and the mass flow rate is proportional to the air density as the air is treated as incompressible fluid. However, if the inlet dimension is changing, smaller inlet means less air flow into the machine with the same inlet speed. Fig. 4.22 shows the highest temperature within the machine versus the inlet radius. In this case, the inlet speed is fixed at 2.5m/s as an example. As expected, the highest temperature in the machine will reduce with increased inlet radius as more air flows into the machine.

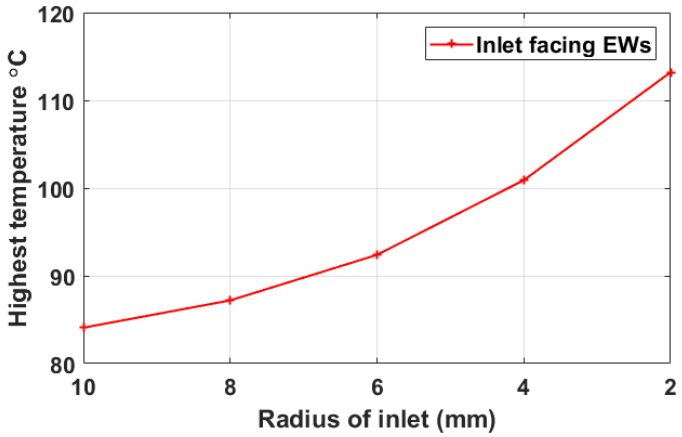

Fig. 4.22. Highest temperature (at EWs) *vs* inlet radius. The inlet speed is 2.5m/s.

In the second case, in order to have a fairer comparison, the same mass flow rate of air coolant is used when the inlet dimension varies. The input mass flow rate is set as 0.72L/s, which is calculated from the initial condition when the inlet has a 10mm radius and an inlet speed of 2.5m/s. Two scenarios with different inlet positions, i.e. inlet facing the EWs and inlet facing the FGs, are also taken into consideration here.

The temperature results are shown in Fig. 4.23. It can be found that, if the inlet faces the FGs, the influence of inlet dimensions is quite small. However, the highest

temperature within the machines will decrease with the decreasing inlet radius if the inlet faces the EWs. In other words, when the inlet faces the EWs, inlets with smaller dimensions can have better cooling effect.

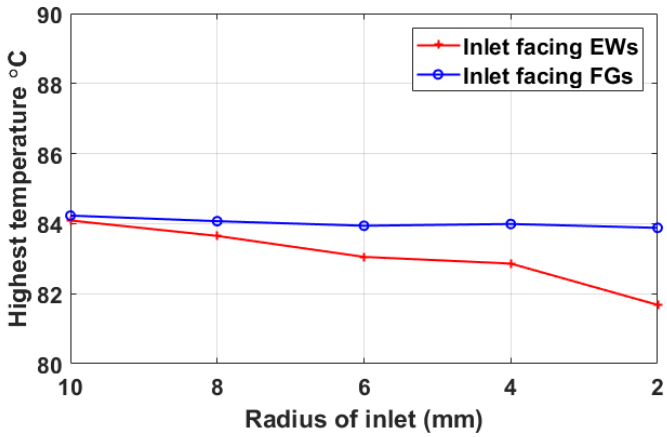

Fig. 4.23. Highest temperature *vs* inlet radius within the machines. The inlet flow rate is 0.7L/s.

For the machines with inlet facing FGs, further analyses have been carried out. The temperature distributions of the entire CFD models and the ones highlighting the EWs are shown in Fig. 4.24 and Fig. 4.25, respectively. In addition, the HTCs of the FGs and the surfaces of EWs are shown in Fig. 4.26. Inlet radii of 10mm and 2mm are selected as example here. It can be seen that the differences of HTCs either in the FGs or on the surfaces of EWs are quite small. This is true for both inlet radii (10mm and 2mm). The similar level of HTCs indicates similar level of heat dissipation rate. This is the reason why the influence of inlet dimensions on the cooling effect is quite small and can be neglected if the inlet is facing the FGs.

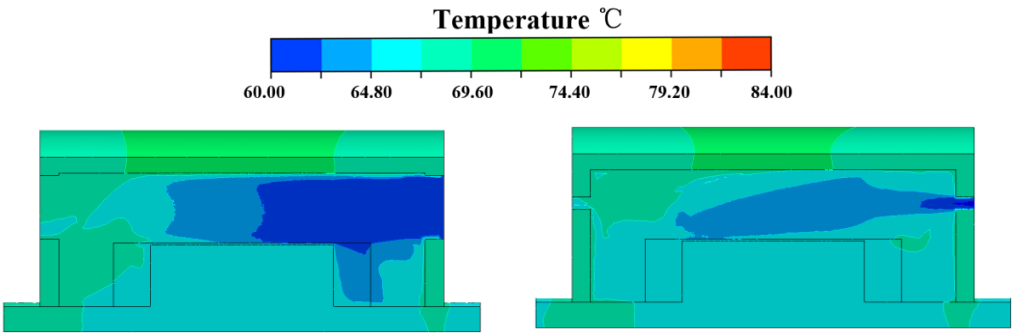

(a) inlet radius is 10mm (b) inlet radius is 2mm

Fig. 4.24. Temperature distribution of the entire CFD models with inlet facing FGs.

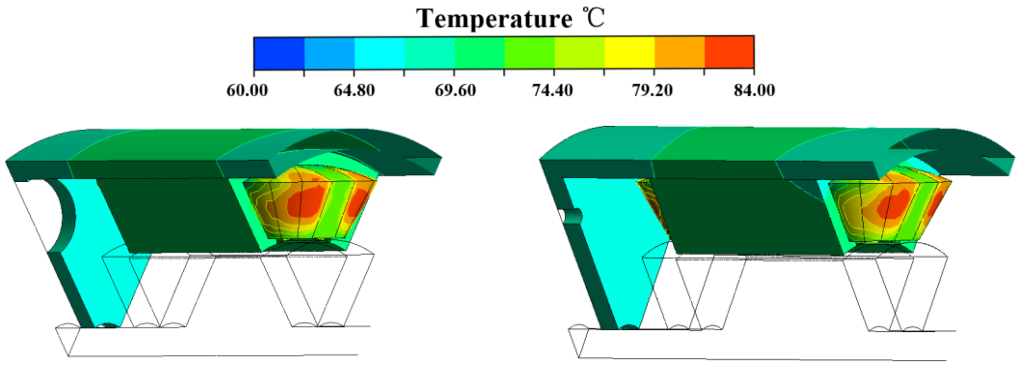

(a) inlet radius is 10mm (b) inlet radius is 2mm

Fig. 4.25. Temperature distribution of the EWs with inlet facing FGs.

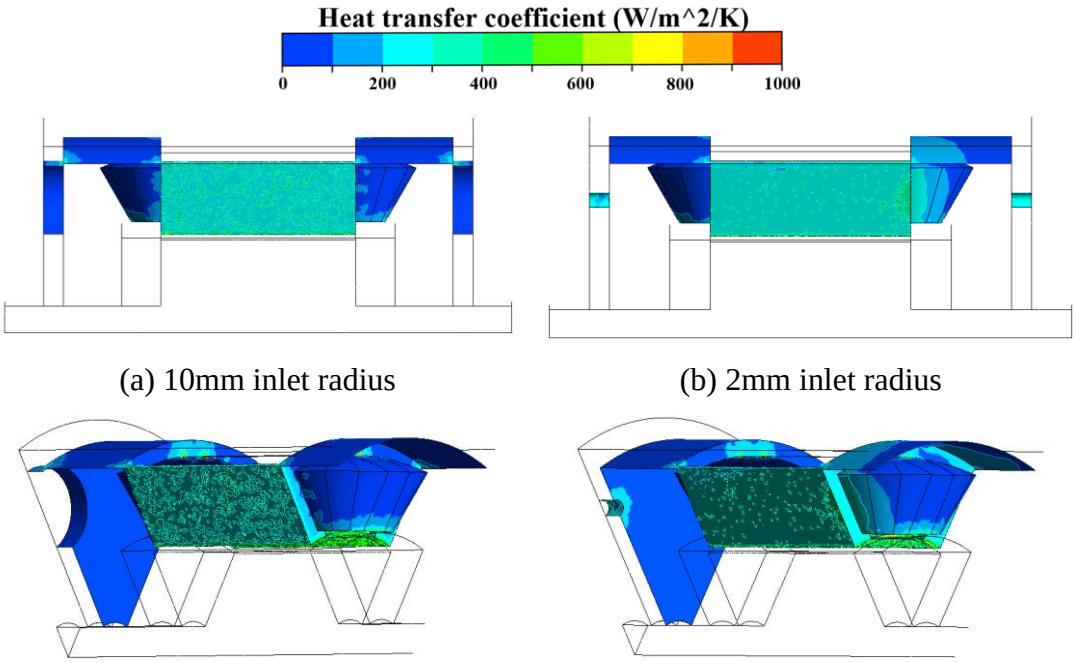

(a) 10mm inlet radius (b) 2mm inlet radius

(c) 10mm inlet radius (d) 2mm inlet radius

Fig. 4.26. HTCs of FGs and surfaces of EWs from two different angles. (a) and (c) show the same results but from different angles. This is the same for (b) and (d).

However, the conclusion is very much different when the inlet faces the EWs. The temperature distributions of the entire CFD models and the ones highlighting the EWs are shown in Fig. 4.27 and Fig. 4.28, respectively. It is clear that the EWs can get better cooling effect when the inlet radius is 2mm. Compared with 10mm inlet radius, highest temperature at end-winding drops from around 84 ℃ to 82 ℃.

This is mainly due to the fact that, for the same flow rate, the inlet speed is significantly increased when the inlet radius reduces and the EWs can be more effectively cooled. This can also be validated by the axial air velocity vectors on the

middle plane, which is aligned with the centre line of the EWs, as shown in Fig. 4.29. It can be observed that the air velocity in the end-space with the 2mm inlet radius is much higher compared with that having 10mm inlet radius.

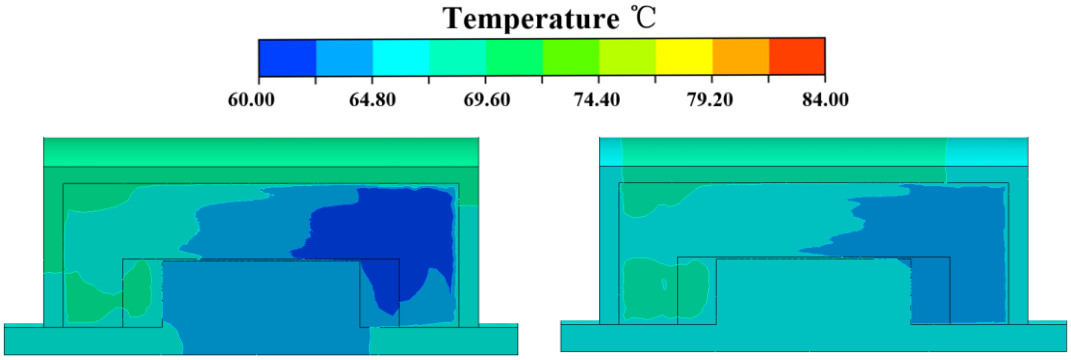

(a) inlet radius is 10mm (b) inlet radius is 2mm

Fig. 4.27. Temperature distribution of the entire CFD models with inlet facing EWs.

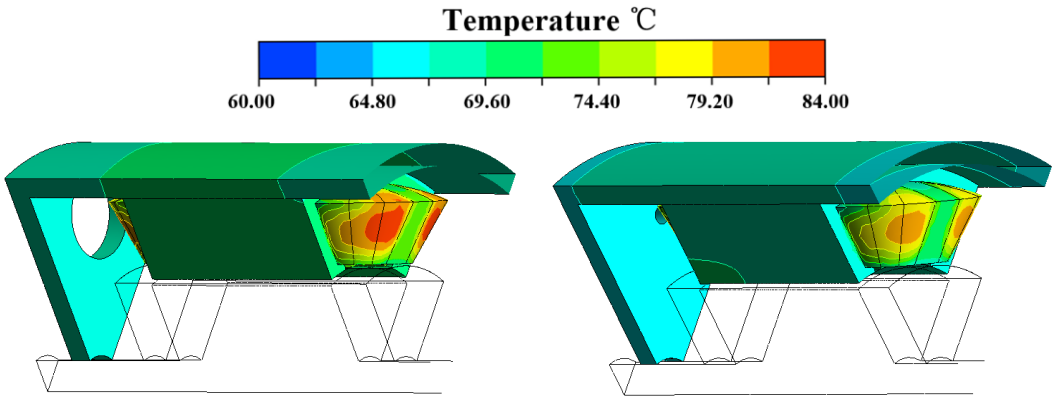

(a) inlet radius is 10mm (b) inlet radius is 2mm

Fig. 4.28. Temperature distribution highlighting the end-windings with inlet facing EWs.

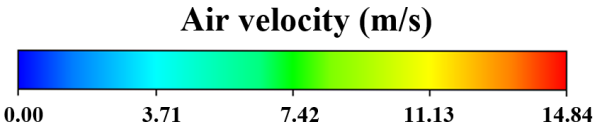

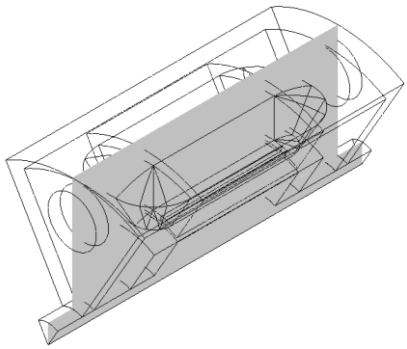

(a) illustration of plane position

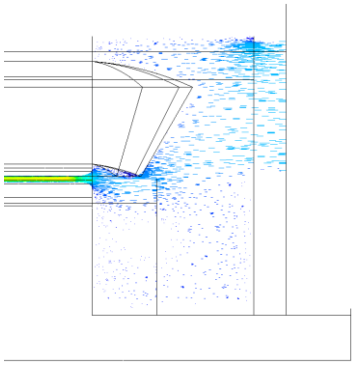

(b) 10mm inlet radius

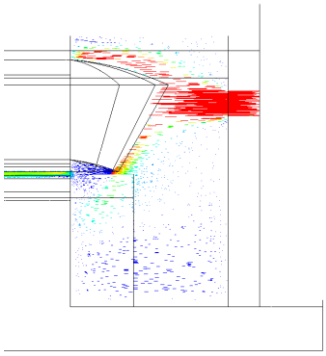

(c) 2mm inlet radius

Fig. 4.29. Air velocity vectors on the middle plane.

The HTCs on the surfaces of EWs are also compared in Fig. 4.30 for different inlet radii. It can be clearly seen that the HTCs on the surfaces of EWs are much higher (almost twice as high) when the inlet radius is 2mm compared with that having a 10mm inlet radius. As a result, the EWs can get better cooling when the inlet radius is 2mm. So to conclude, for the same flow rate, if the inlet faces the EWs, EWs can be directly cooled by the air coolant, higher air velocity due to smaller inlets can achieve better cooling effect.

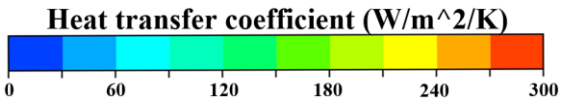

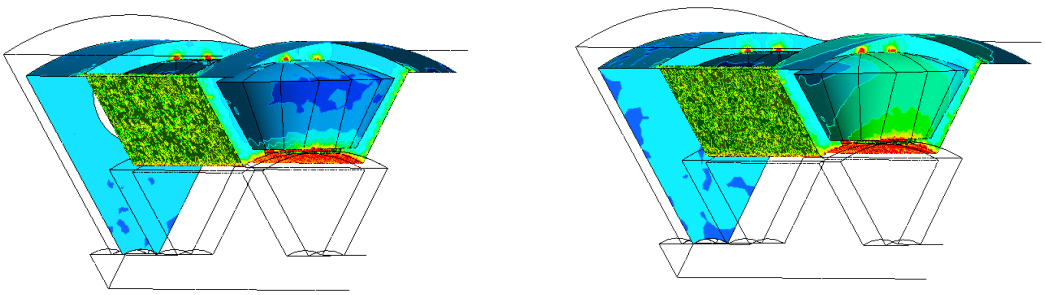

(a) inlet radius is 10mm (b) inlet radius is 2mm

Fig. 4.30. HTCs on surfaces of EWs with inlet facing EWs.

However, the pressure drops between the inlet and outlet against the inlet radius have been calculated, as shown in Fig. 4.31. It can be found that the pressure drop can be significantly increased if the inlet is small. For example, when the inlet radius reduces from 4mm to 2mm, the pressure drop can be increased by several times, regardless of the inlet position. Therefore, considering the cooling system efficiency and the capability of the heat exchanger, the dimension of inlet should be within a reasonable range rather than being as small as possible. In this case, a 4mm inlet radius is considered to be a good option.

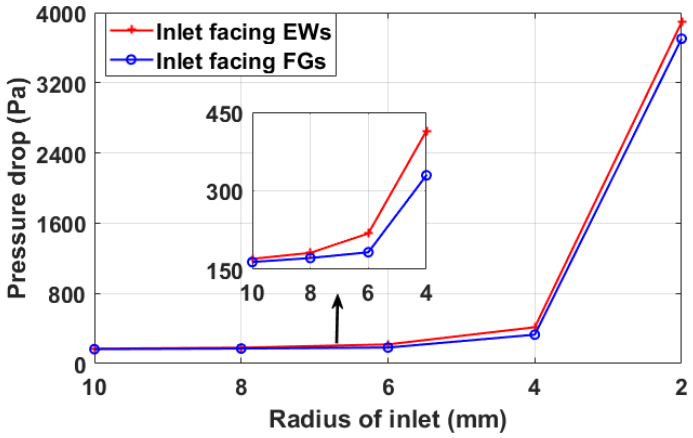

Fig. 4.31. Pressure drop between the inlet and outlet *vs* inlet radius. The inlet flow rate is 0.72L/s.

4.6. Assessments Based on the Same Torque

It should be noted that in the previous sections of this chapter, all investigations are based on the assumption that all machines have the same copper losses. However, it is already found in the previous chapters that the average torque of such modular machines can be significantly improved by selecting a proper FG width. The average

torque of the 12-slot/14-pole E-core modular CPMs against FG width is shown in Fig. 4.32. The average torque at rated condition can be improved by 17.3% from 4.42Nm (FG=0mm) to 5.19Nm (FG=3mm). In other words, if the modular CPM with a 3mm FG width is required to achieve the same torque as the non-modular CPM with 0mm FG, its needed current will be smaller. This means relatively lower copper losses might be generated by the modular CPMs. Therefore, in order to make the investigation more complete, in this section, the copper losses for all machines are calculated based on the assumption that all the modular machines will produce the same torque (4.42Nm, rated condition) as the non-modular machine (FG=0mm).

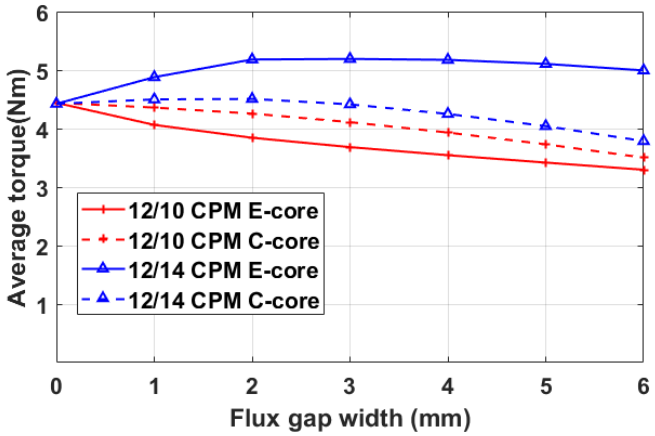

Fig. 4.32. The average torque *vs* FG width, I_{rms}=7.34A.

The CFD results are compared with that obtained for the same copper losses (as investigated in section 4.3), as shown in Fig. 4.33. It can be seen that the modular machines will have lower temperatures compared with that of non-modular machines even without forced air cooling (flow speed is 0 m/s). This is quite evident due to their reduced copper losses for the same average torque. Therefore, the benefits of modular machines can be featured from two aspects. On one hand, if all machines have the same copper losses and the proposed forced air cooling method is adopted, the modular machines can achieve better torque performances while having lower temperatures compared with the non-modular machines. In this case, an optimal FG width exists for achieving the lowest temperature. On the other hand, if all modular machines are designed to achieve the same rated torque as the non-modular machine, their intrinsic thermal performances without cooling will be better compared with the non-modular machine due to the resultant relatively lower copper losses. Moreover, their

temperatures can be further reduced if the forced air cooling method is adopted and an optimal FG width exists as well.

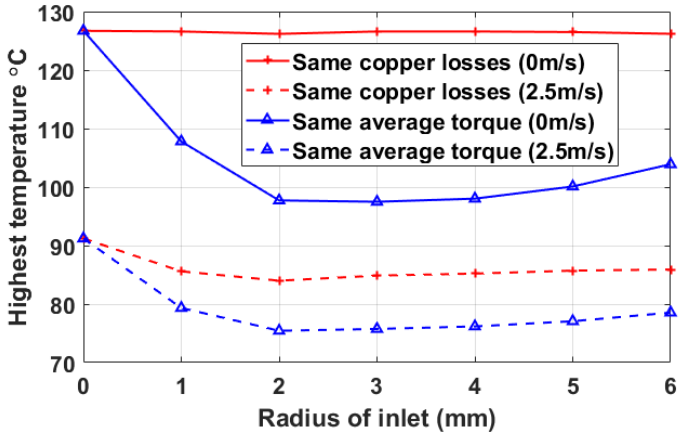

Fig. 4.33. Comparisons based on the same copper loss or the same average torque.

4.7. Assessment of Inlet Shape

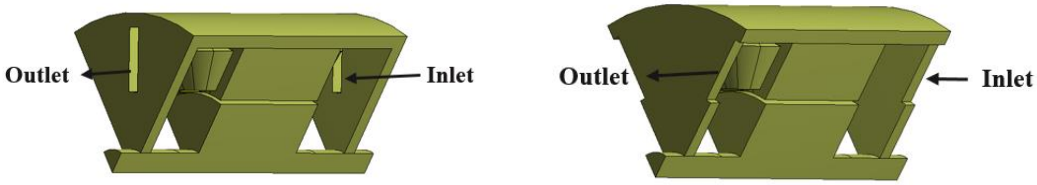

(a) inlet facing EWs (b) inlet facing FGs

Fig. 4.34. FG-shaped inlets and outlets.

All inlets and outlets in the previous sections are round-shaped. It would be interesting to assess some other inlet shapes. Considering the shape of the FGs, it is reasonable to adopt the FG-shaped inlets and outlets as shown in Fig. 4.34. Here, the shape of inlets and outlets is designed as the same as the FGs. Fig. 4.35 shows the highest temperature versus inlet width. The pressure drop between the inlet and outlet is shown in Fig. 4.36. All the results are obtained for an inlet flow rate of 0.72L/s with a 2mm FG width and the copper losses are the rated losses. In terms of the cooling effect, the case when the FG-shaped inlets face the EWs could have better cooling effect compared with the case when the FG-shaped inlets face the FGs. This is the same phenomenon as the round-shaped case. Regarding the inlet width, it has very slight influence on the temperature reduction but larger FG width could have lower pressure drop as can be seen in Fig. 4.36. Therefore, to conclude, if the inlets and outlets are designed as FG-shaped, they should be facing the EWs for achieving better cooling

effect and should be as wide as possible to minimize the pressure drop. It is also found that both round-shaped and FG-shaped inlets and outlets have similar effect in terms of cooling.

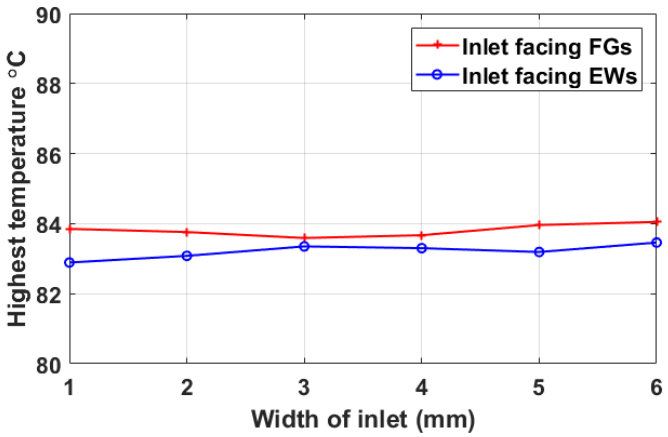

Fig. 4.35. Highest temperature *vs* inlet width (FG-shaped inlet) with 0.72L/s flow rate.

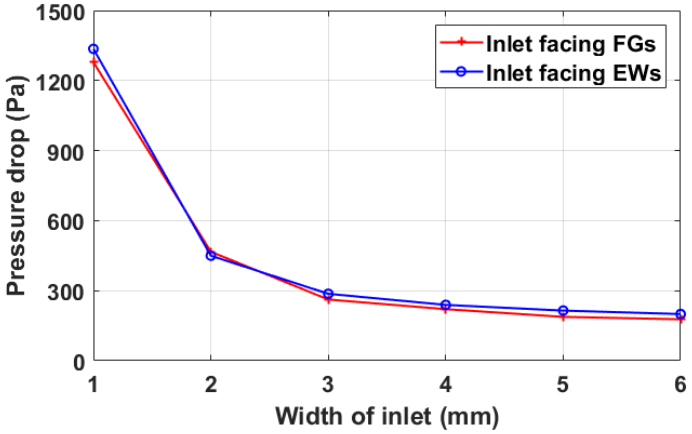

Fig. 4.36. Pressure drop between the inlet and outlet *vs* inlet width (FG-shaped inlet) with 0.72L/s flow rate.

4.8. Issue about EWs

It should be noted that the treatment of EWs has been illustrated in section 4.2.4 and the model used in this chapter is shown in Fig. 4.37 (a). In this model, the middle segment of EWs is assumed to have a perfect contact with the stator iron. This is a safe assumption considering the relatively small dimensions of the investigated machines. However, the winding process could not be so ideal. In order to be more realistic, the case where the middle EW segment not contacting the stator iron has been taken into consideration, as shown in Fig. 4.37 (b).

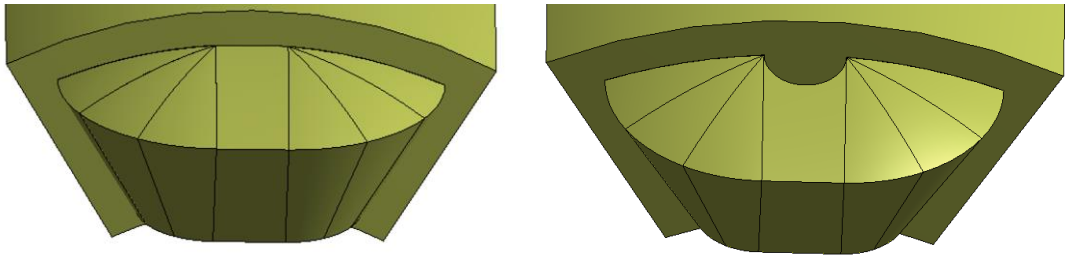

(a) EW contacting the stator iron (b) EW not contacting the stator iron

Fig. 4.37. Both models of EW segments.

The highest temperatures within the machines versus FG widths considering both cases are listed in Table 4.6 and shown in Fig. 4.38. It can be seen that the resultant temperature differences of the two models are quite small, which can be neglected. Meanwhile, the temperature distributions of EWs are shown in Fig. 4.39 and Fig. 4.40. Here 0mm and 2mm FG are selected as examples. It can be found that when the EW segment does not contact the stator iron, the middle segment will have highest temperatures. Thus, areas with high temperatures are relatively larger compared with the case when EW segment contacts the stator iron. However, the overall difference between the highest temperatures of both models is very small.

Table 4.6. Highest temperature within the machines (both EW models)

FG width / **Inlet speed**	**0mm**	**1mm**	**2mm**	**3mm**	**4mm**	**5mm**	**6mm**
EW contacting stator	91.2	85.6	84	84.9	85.2	85.7	85.9
EW not contacting stator	90.8	85.4	84.1	84.7	85.1	85.5	85.7

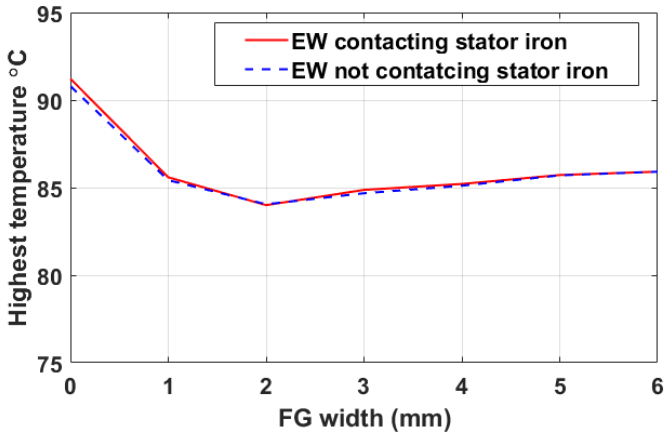

Fig. 4.38. Highest temperatures within the machines *vs* FG width (both EW models).

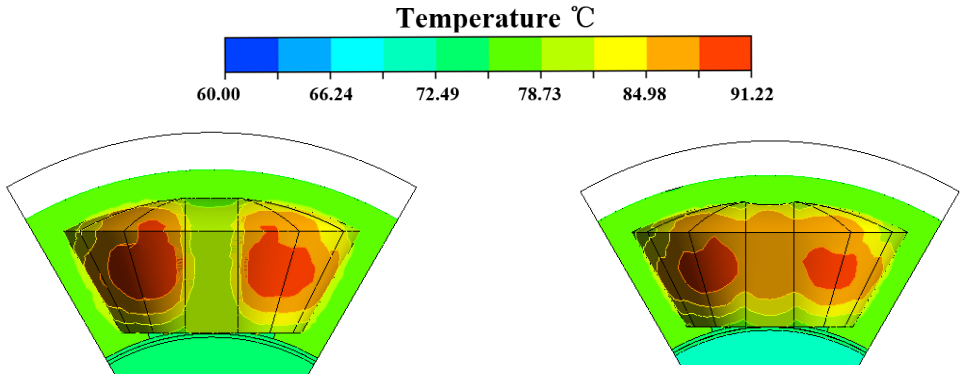

(a) EW contacting the stator iron (b) EW not contacting the stator iron

Fig. 4.39. Temperature distributions of both models (FG=0mm).

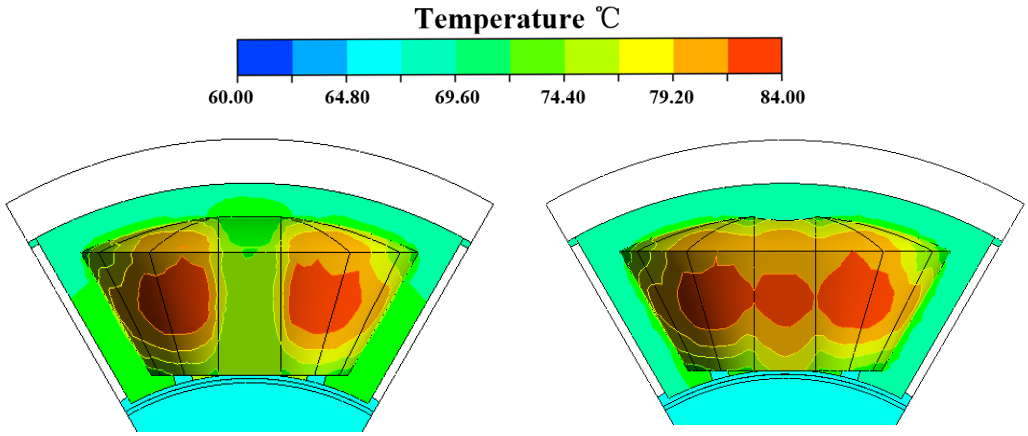

(a) EW contacting the stator iron (b) EW not contacting the stator iron

Fig. 4.40. Temperature distributions of both models (FG=2mm).

4.9. Proposed Forced Oil Cooling Utilizing FGs

A forced air cooling with inlets and outlets on the end-caps is proposed in previous sections. This cooling method can fully take advantage of the FGs and integrate them into the cooling circuit in order to improve machine cooling efficiency. Due to the extra convection of FGs in modular machines, the temperature rise of the modular machines can be significantly reduced compared with the non-modular machines. It has been proven by the numerical results obtained by CFD analyses.

However, as reviewed in the introduction chapter, high torque/power density electrical machines are usually cooled by various forced liquid cooling methods including: water jacket, slot heat pipe, spray nozzle, hollow shaft, etc. Due to the high relative heat capacity of liquid, the forced liquid cooling methods are more powerful which can remove more heat and therefore are more preferable for high torque/power density application, compared with the forced air cooling. Amongst all the forced liquid cooling methods, authors in [157] have proposed a submerged wet stator for an electrical machine. This machine is used in an aircraft starter-generator system where high power density and efficiency are required. The stator is separated from the rotor by placing a carbon sleeve in the airgap. The stator is submerge in the oil and can be directly cooled by the circulating oil. In theory, by using this structure, the thermal resistance between the coolant and the main heat source (windings) is minimized and the best heat dissipation rate could be achieved. However, the method used in [157] has limited cooling circuit as it uses the slot openings and part of the airgap to circulate the cooling oil. This seriously impedes the cooling efficiency. To address this issue, the FGs of the modular machines can be utilized as cooling channels for the oil to pass through, which could significantly improve the internal cooling in such machines. Similar as the forced air cooling, the 12-slot/14-pole E-core machine has been selected as example for the investigations in the following sections.

4.9.1. Model Structure

The idea of the proposed forced oil cooling is to submerge the stator in the cooling oil and the stator is separated from the rotor by placing a sleeve in the airgap, as shown in Fig. 4.41(a). The FGs are used as cooling channels let the oil pass through freely. This can increase the wall heat transfer coefficient (HTC) of the FGs and to improve the heat dissipation rate from the stator to the cooling oil. For the initial design, the inlets and outlets are positioned directly above the end-windings (EWs) and are aligned with the middle plane of each E-core segment in the axial direction, as shown in Fig. 4.41 (b) and (c). It should be noted that the rotor part is not included in the solution model. This is mainly because on one hand, the stator is separated from the rotor by placing a sleeve in the airgap which can avoid the oil leakage towards the rotor. With this structure, the rotor structure will not have significant influence on the stator part and it is safe to neglect it. On the other hand, similar as the forced air cooling in the previous sections, the 3D CFD analysis is used to assess the thermal performances in this investigation. 3D CFD is accurate but quite time-consuming. For example, to guarantee the accuracy of results, nearly 5 million elements will be generated for the mesh grid and it takes nearly 7 hours for a case to reach stable results after ~1200 iterations. Therefore, to reduce the computation burden, it is reasonable here to not include the rotor part. Moreover, the sleeve is assumed to contact the stator inner surface perfectly and the sleeve thickness is selected as 0.5mm due to the fact that the 0.5mm carbon fibre sleeve can be able to withstand a maximum pressure of around 2 bar (200 kPa) [157] which is quite safe for this investigation. The slot opening is still 2mm which is used in the electromagnetic investigations.

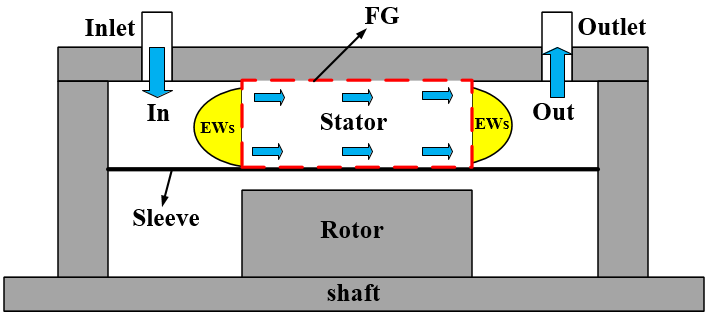

(a) Proposed forced oil cooling concept

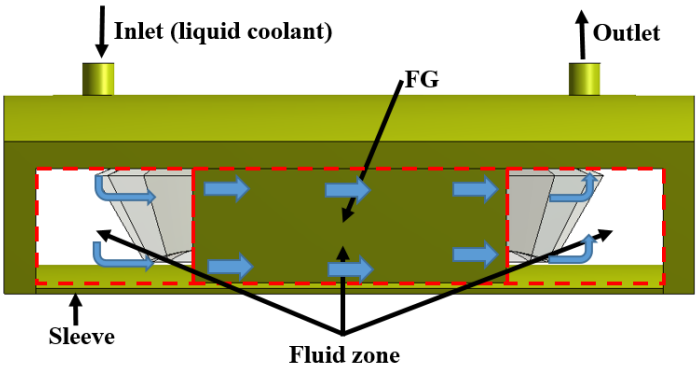

(b) Detailed view of 3D model

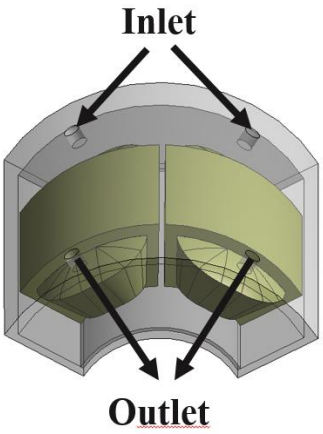

(c) position of inlets and outlets

Fig. 4.41. Models of the proposed forced oil cooling.

4.9.2. Thermal Properties of Different Materials

Table 4.7 lists the thermal properties of the used materials including their thermal conductivity, specific heat capacity, density and dynamic viscosity for the fluid. The oil selected here is the lubricating oil [155] and the sleeve is made of carbon fibre [157]. Being the same as the air cooling section, it is assumed that the thermal properties of materials are not influenced by the temperature rise for model simplifications.

Table 4.7 Thermal properties of related materials [155]

Materials	Thermal conductivity (W/m/K)	Specific heat capacity (J/kg)	Density (kg/m^3)	Dynamic viscosity (Pa·s)
Steel	60.5	434	7854	/
Aluminium	237	903	2702	/
Equivalent slot (Copper wires, varnish and air included)	0.39 (radial and tangential), 401 (axial)	385	8900	/
Lubricating oil [155]	0.155	2100	845	0.015
Sleeve (carbon fibre)	0.87	170	1600	/

4.9.3. Heat Sources and Boundary Conditions

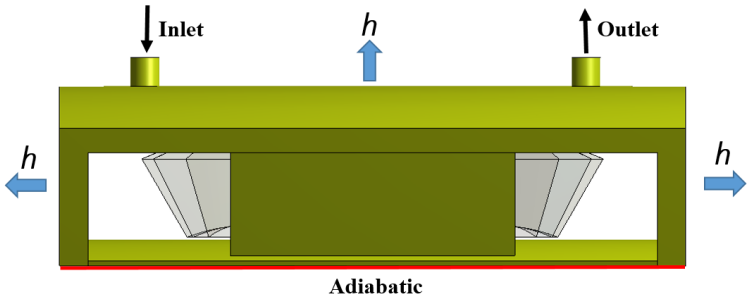

Fig. 4.42. Illustration of boundary conditions.

Same as the forced air cooling method, only the copper losses and stator iron losses are taken into consideration in this investigation. Moreover, the some assumptions for model simplification and the boundary conditions very much the same as the forced air cooling part which is shown in section 4.2.5.

4.10. Influence of FG Width

Same as the influence of FGs on the electromagnetic performances investigated in previous chapters, the influence of FG width on the cooling effect in modular machines are investigated in this section. Since the modular machines have FGs as extra cooling

channels, the temperature rises of modular machines are expected to be lower in comparison with that of non-modular machines.

Table 4.3 shows the highest temperature within the machines with different FG widths and inlet flow rates. The initial flow rate 0.16L/min is obtained using expression (4.5) and (4.6), when the initial temperature rise ΔT of oil coolant from the inlet to the outlet is assumed to be 20℃. This is to consider the fact that operating temperature of fluid is usually between 60℃ and 90℃ which is a common practice in automotive drives [155].

$$Q = \dot{m}_r c_p (T_{out} - T_{in}) = \dot{m}_r c_p \Delta T \tag{4.5}$$

$$\dot{V}_r = \frac{\dot{m}_r}{\rho} \tag{4.6}$$

where Q is the thermal power (total losses), $\dot{m}_r$ is the mass flow rate of coolant, c_p is the specific heat of coolant, T_{out}, T_{in} are the temperatures of the outlet and inlet, respectively. ΔT is the temperature rise of coolant, ρ is the density of coolant and $\dot{V}_r$ is the volumetric flow rate of coolant.

It is worth noting that the highest temperature within machines often locates at slot centre or at the end-winding. It can be seen that with the increasing inlet flow rate, the highest temperature within the machines (with the same FG width) keeps decreasing.

Table 4.8 Highest temperature within the machines

FG width / **Flow rate**	**0mm**	**1mm**	**2mm**	**3mm**	**4mm**	**5mm**	**6mm**
0.16L/min	88.5	83.57	81.91	81.51	81.25	81.11	80.99
0.32L/min	82.35	78.59	78.02	78.12	78.13	78.09	77.88
0.48L/min	79.59	76.65	76.48	76.67	76.74	76.77	76.64
0.64L/min	78.09	75.6	75.6	75.84	76.00	76.06	75.83
0.80L/min	77.13	74.91	75.02	75.32	75.53	75.51	75.15

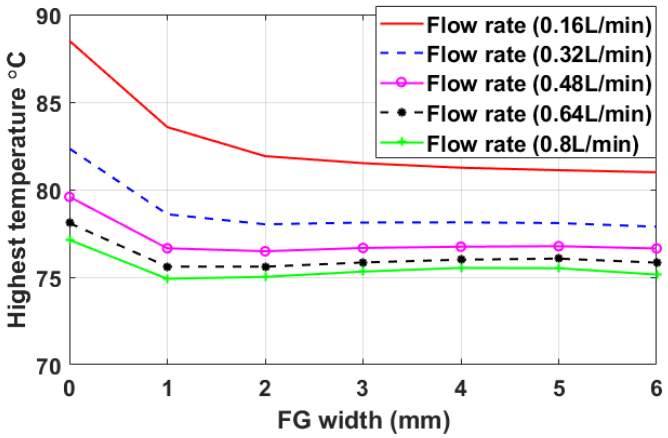

Fig. 4.43. Highest temperatures within the machines *vs* FG widths under different inlet flow rates.

Moreover, the highest temperatures within the machines versus FG widths under different inlet flow rates are also shown in Fig. 4.43. It can be seen that, as expected, the modular machines have lower highest temperatures compared with the non-modular machines, regardless of inlet flow rate. The reason is quite evident that the FGs are utilized as extra cooling channels to let the oil coolant passing through which can improve the heat dissipation. The streamlines of the modular machines with FG width 0mm (non-modular) and 2mm are shown in Fig. 4.44 as examples. The flow path of the oil passing through the FGs in modular machines can be easily observed. The temperature distributions with the selected FG widths are shown in Fig. 4.45. Meanwhile, the temperature distributions highlighting the EWs are shown in Fig. 4.46. It is found that the EWs are the main hot spots and the temperatures can be significantly reduced in the modular machines with the proposed forced oil cooling. For example, the highest temperature within the modular machine with 6mm FG width can be reduced to 80.99℃, down by nearly 7.5℃ compared with 88.5℃ in the non-modular machine (0mm FG width).

However, it can be observed that the reduction in temperature is very small when the FG width is increasing, except for the case with relative low inlet flow rate, e.g. 0.16L/min. When the inlet flow rate is 0.16L/min, the highest temperature will see a significant decrease until the FG width is increased to 2mm and then the variation versus FG width becomes also small. Generally speaking, the FGs can have good cooling effect in the modular machines, but the influence of FG width on the temperature reduction is not significant. This is mainly due to the variation trend of

HTCs on the wall of FGs in modular machines. 2mm, 4mm and 6mm FG widths are selected as examples. It can be observed from Fig. 4.47 that the HTCs on the wall of FGs are at the same level and remain almost unchanged in modular machines.

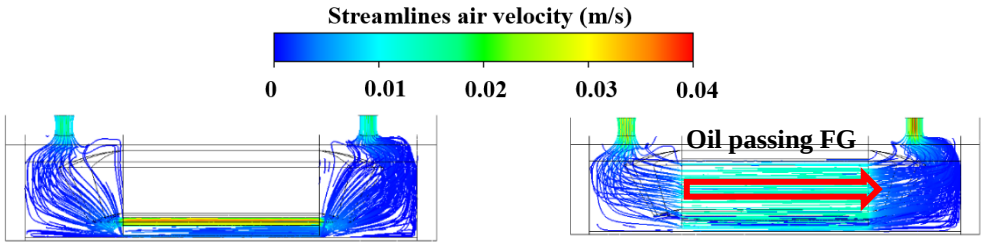

(a) FG=0mm (b) FG=2mm

Fig. 4.44. Streamlines of the selected modular machines.

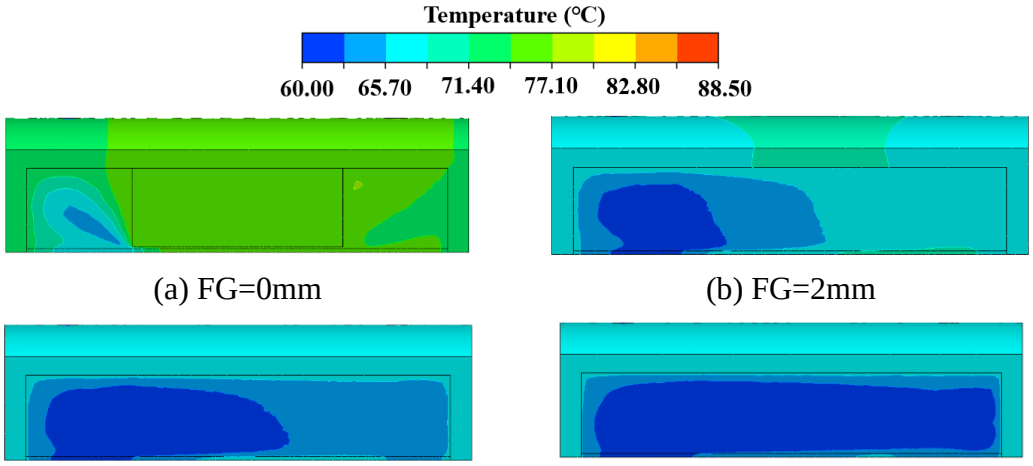

(a) FG=0mm (b) FG=2mm

(c) FG=4mm (d) FG=6mm

Fig. 4.45. Temperature distributions of the machines with different FG widths.

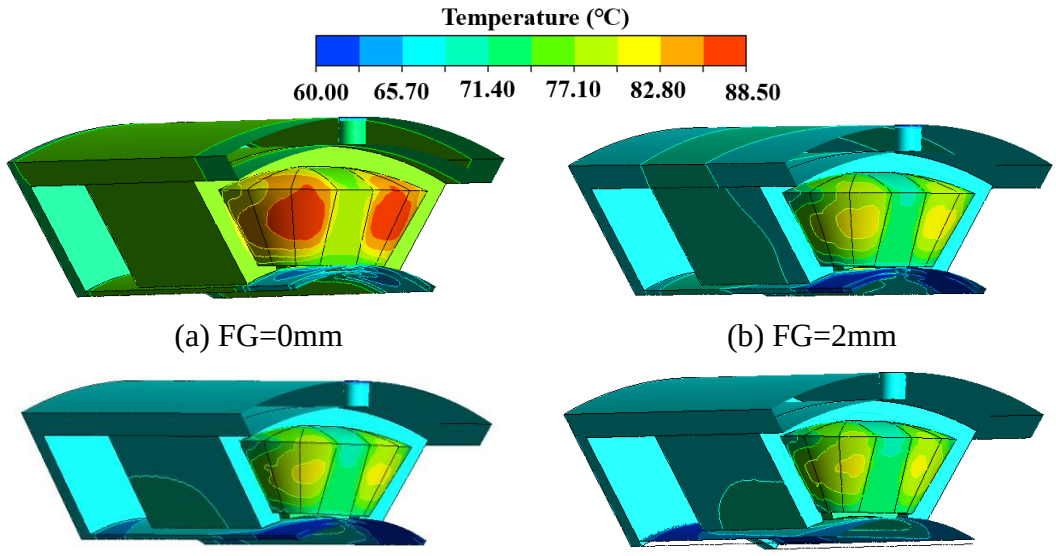

(a) FG=0mm (b) FG=2mm

(c) FG=4mm (d) FG=6mm

Fig. 4.46. Temperature distribution highlighting the end-windings with different FG widths.

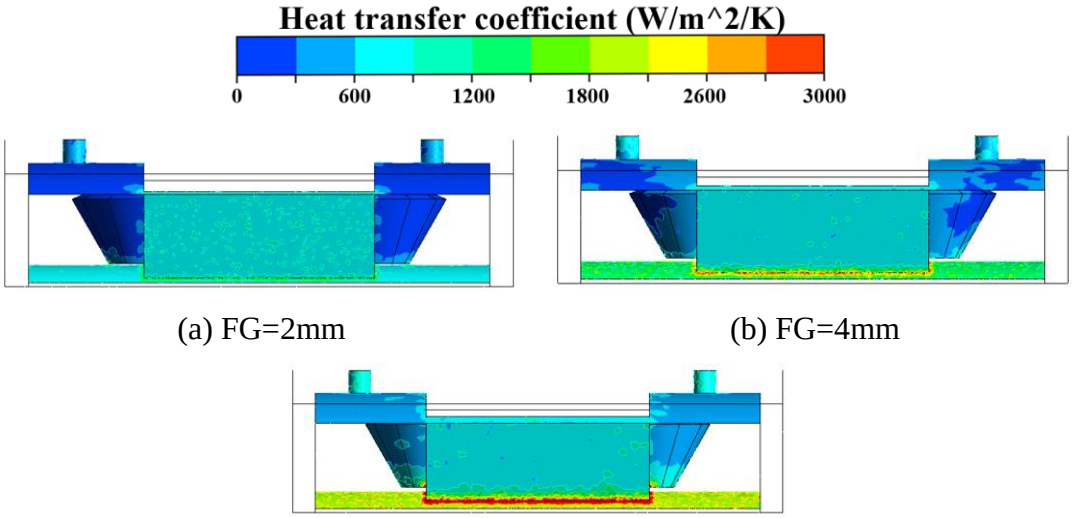

(a) FG=2mm (b) FG=4mm

(c) FG=6mm

Fig. 4.47. HTCs of FG walls with different FG widths.

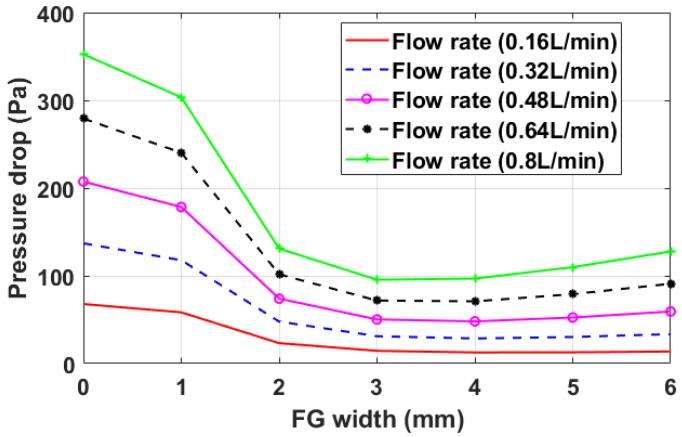

Fig. 4.48. Pressure drop between inlet and outlet *vs* FG width under different flow rates.

Apart from the temperature reduction, the pressure drop between the inlet and outlet should also be investigated. It can be found that, for all inlet flow rates, the pressure drop could be significantly reduced with increasing FG width until it reaches to 2mm. The pressure drop will be generally stable when the FG width is ≥ 2mm. Therefore, considering the lower pressure drop (higher cooling system efficiency), the FG width should be at least 2mm.

4.11. Different Loadings

The results shown in previous section is calculate based on the rated copper losses. However, sometimes the machines may need to operate under overload conditions. Since the oil cooling is more effective to remove more heat compared with the forced

air cooling, it is meaningful to investigate the effect of the proposed forced oil cooling method under overload conditions. In this model, copper losses are the main heat sources. Therefore, different copper losses are considered for different load conditions. The highest temperatures within machines versus FG width under different copper losses are shown in Fig. 4.49. The flow rate here is fixed at 0.16L/min. The legend x1.5, x2, x2.5 and x3 represent 1.5 times, 2 times, 2.5 times and 3 times the rated copper losses, respectively. It can be seen that the cooling effect can be more remarkable if the loadings are increased. To make the cooling effect clearer, the percentages of temperature reduction under different loadings have been shown in Fig. 4.50, 0mm and 6mm FG widths are selected as examples. The percentage of temperature reduction can be increased from 8.5% to 19.6% if the loading is increased by 3 times from the rated condition. Thus, the forced oil cooling together with modular stator structure will see greater potential in high torque/power density applications.

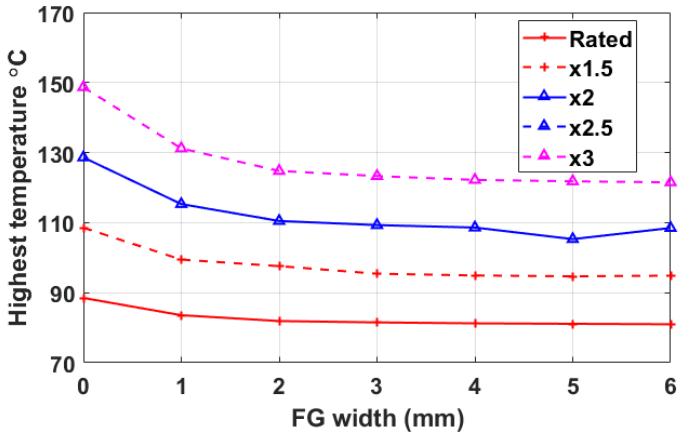

Fig. 4.49. Highest temperatures *vs* FG width under different loadings.

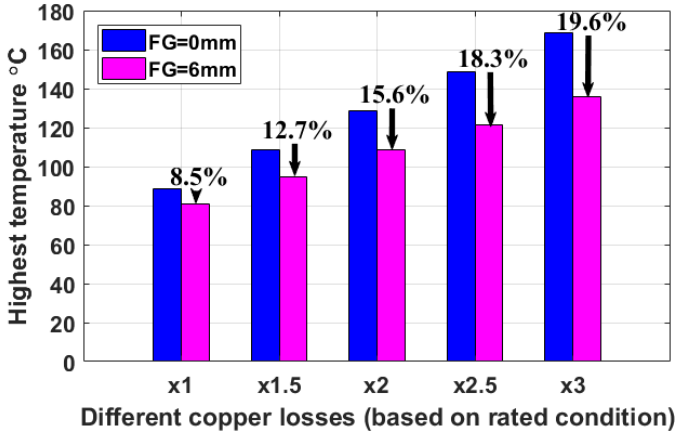

Fig. 4.50. Temperature reduction under different loadings. The FG width are 0 and 6mm.

4.12. Influence of Inlet Position

Similar as the forced air cooling, it would be also useful to investigate the cooling effect when the inlets are aligned with the FGs and the oil coolant goes directly into the FGs from the inlets as shown in Fig. 4.51 (b). The models shown in (a), (b) are named as configurations 1 and 2, respectively. Configuration 1 is the original design. Both configurations have the same number of inlets and outlets, i.e. 6 in total. The focus of this section is the influence of inlet positions, thus only 0.16L/min flow rate is taken as example.

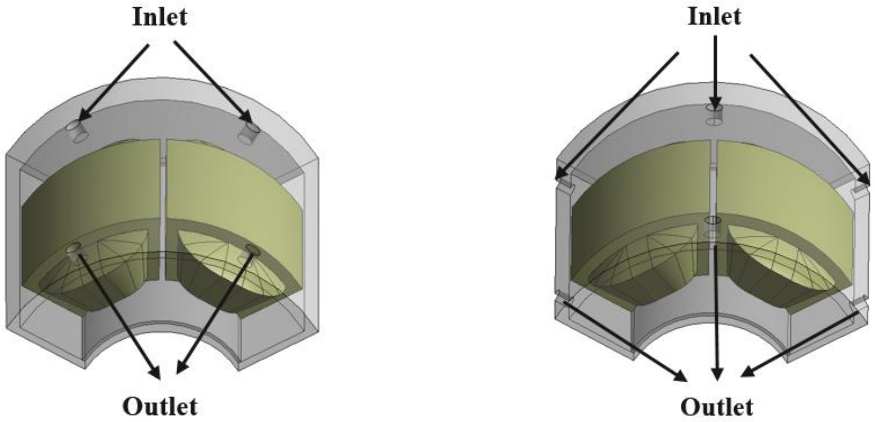

(a) configuration 1 (b) configuration 2

Fig. 4.51. Two positions of inlets and outlets.

The highest temperatures within the machines versus FG width with both configurations are shown in Fig. 4.52. It can be found that the configuration 1 will always have lower highest temperature and thus better cooling efficiency. This is mainly due to the fact that in configuration 1, the EWs are just below the inlets and can be cooled by the cold oil coolant directly. It is evident that the hot spot can get better cooling effect if they are closer to the inlets.

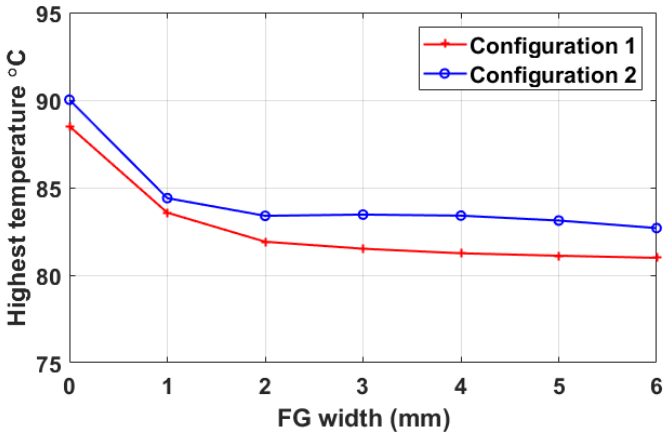

Fig. 4.52. Highest temperature within the machines *vs* FG width for both configurations.

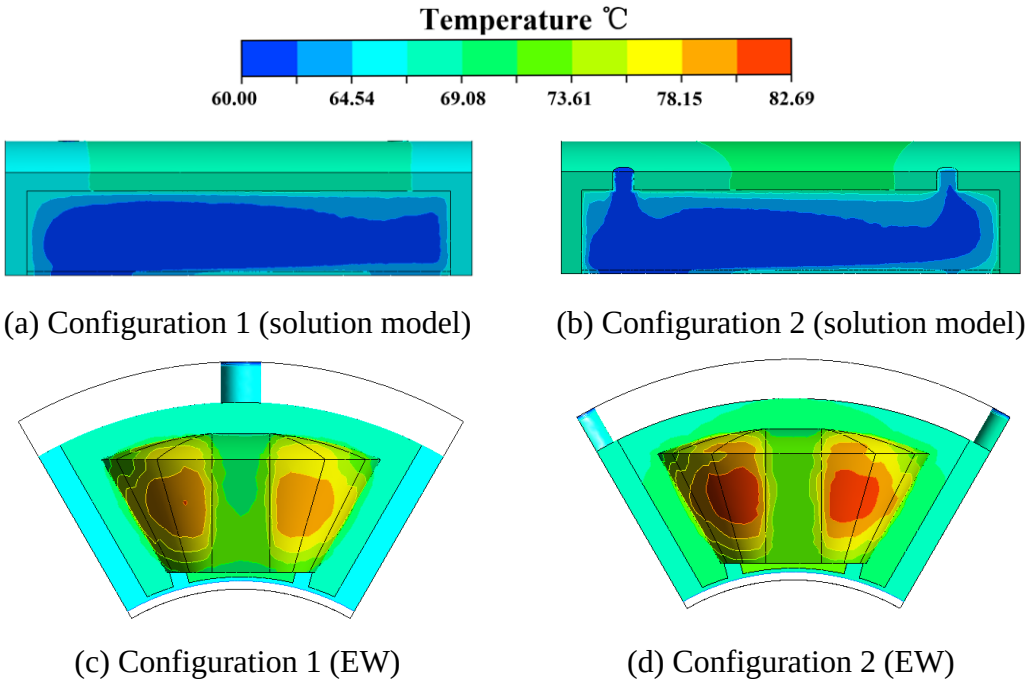

(a) Configuration 1 (solution model)

(b) Configuration 2 (solution model)

(c) Configuration 1 (EW)

(d) Configuration 2 (EW)

Fig. 4.53. Temperature distributions of the machines for both configurations with different FG widths.

Moreover, it is also found that the pressure drop differences between these two configurations are quite small and can be neglected, as shown in Fig. 4.54.

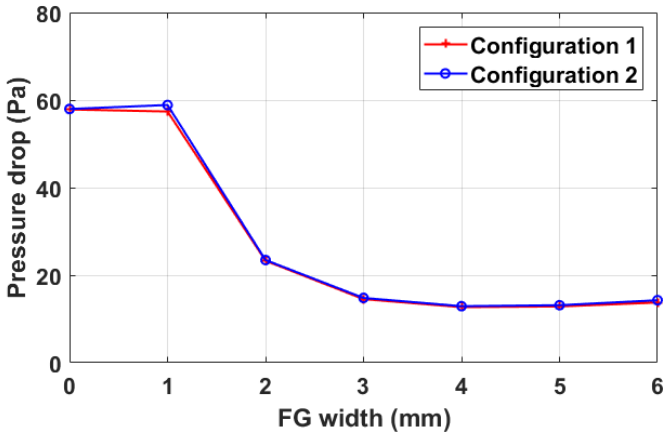

Fig. 4.54. Pressure drop *vs* FG width for both configurations.

4.13. Issues about EWs

Same as the investigations carried out for forced air cooling in section 4.8, the scenario where the middle EW segment does not contact the stator iron should also be investigated here and the models are shown in Fig. 4.55.

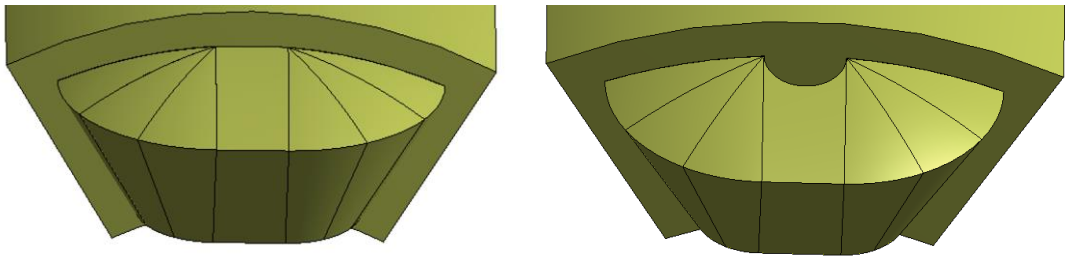

(a) EW contacting stator iron (b) EW not contacting stator iron

Fig. 4.55. Both models of EW segments.

The highest temperatures within the machines versus FG widths considering both models shown in Fig. 4.56. It is found that the highest temperature is slightly lower when the EW segment does not contact the stator iron due to increased contact area with the oil coolant. However, this temperature difference between these two models is quite small and can be neglected. Meanwhile, the pressure drop difference of the two models can also be neglected.

The temperature distributions of EWs of both models are shown in Fig. 4.57 and Fig. 4.58, 0mm and 6mm FG width are selected as examples. The same phenomenon as the forced air cooling can be observed. When the EW segment does not contact the stator iron, the middle segment will have higher temperatures. Thus, areas with high

temperatures are relatively larger compared with the case when EW segment contacts the stator iron. In addition, the pressure drop differences of both models are quite small and can be neglected, as shown in Fig. 4.59.

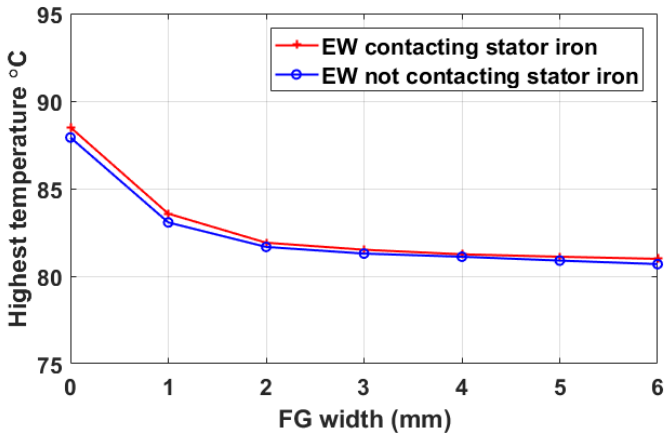

Fig. 4.56. Highest temperature within the machines *vs* FG width (both EW models).

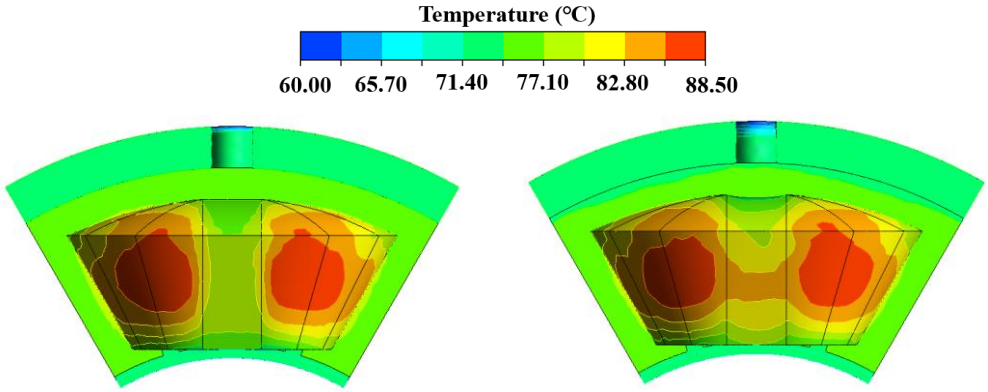

(a) EW contacting stator iron (b) EW not contacting stator iron

Fig. 4.57. Temperature distributions of both models (FG=0mm).

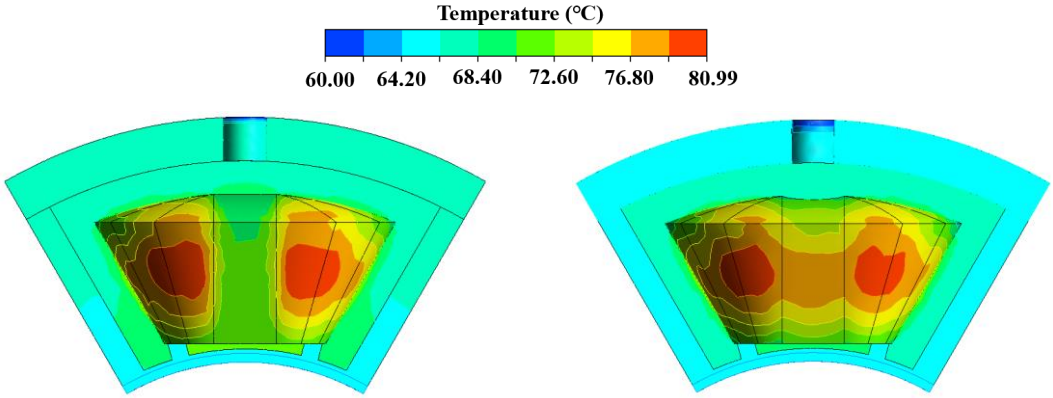

(a) EW contacting stator iron (b) EW not contacting stator iron

Fig. 4.58. Temperature distributions of both models (FG=6mm).

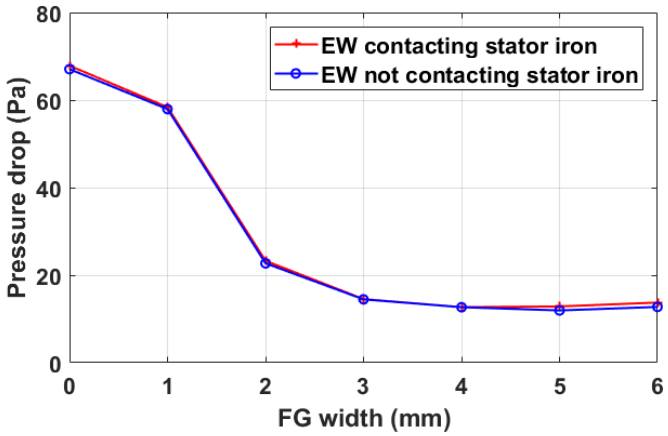

Fig. 4.59. Pressure drop *vs* FG width (both EW models).

4.14. Other Configurations of Inlets and Outlets

It should be noted that the proposed initial design only has one inlet on one side and one outlet on the other side per stator segment as shown in Fig. 4.60 (a). This will lead to an asymmetric temperature distribution within the machines. In other words, the region close to the inlet side (front) will have lower temperatures compared with the region next to outlet side (back). The front and back sides are indicated in Fig. 4.60 (a). It is pointed in [108] that the temperature uniformity is important in the thermal design of electrical machines. Unexpected hot spots may be caused under uneven temperature distribution, which could be higher than the temperature limit of winding insulations, causing early failures. Therefore, it is essential to make sure the temperature distribution is as uniform as possible.

In order to realize the temperature uniformity, two other configurations for different positions of inlets and outlets are proposed and shown in Fig. 4.60 (b), (c). They are named as configurations 3 and 4 in order to be distinguished from the configuration 1 and 2 as investigated in section 4.12. It should be noted that the initial design shown in Fig. 4.60 (a) is named as configuration 1.

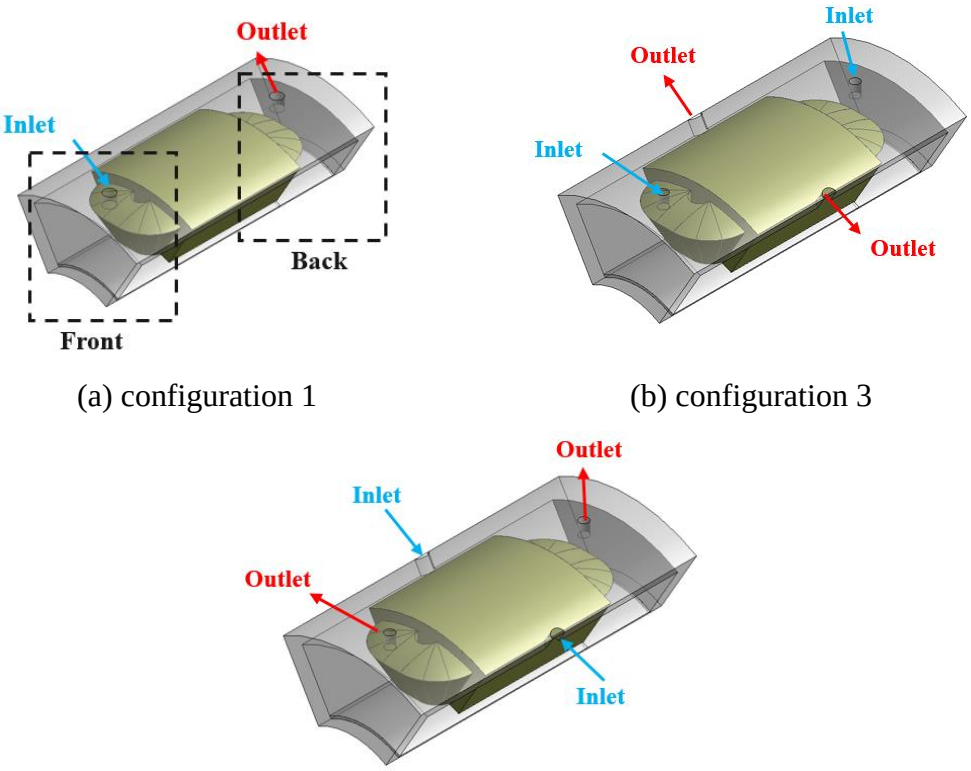

(a) configuration 1

(b) configuration 3

(c) configuration 4

Fig. 4.60. The initial configuration 0 and two other configurations (3, 4).

The highest temperatures within the machines versus FG width with different configurations are shown in Fig. 4.61. It can be seen that the configurations 3 and 4 will have relatively higher temperatures compared with the configuration 1. This is mainly due to that the comparison is based on the same total flow rate. For the configuration 3, there are two inlets which means the flow rate per inlet will be halved compared with the configuration 1. Thus, the highest temperature of the configuration 3 is slightly higher than that of the configuration 1. In terms of the configuration 4, the inlet is positioned above the FG and is far from the hot spots such as EWs. This leads to the relatively higher peak temperature.

The temperature distributions of the investigated configurations from both back and front sides are compared, as shown in Fig. 4.62 and Fig. 4.63. Although the configurations 3 and 4 have relatively higher peak temperatures compared with the configuration 1, they can eliminate the asymmetric temperature distributions existing in the configuration 1. Moreover, the pressure drop difference between the different configurations is quite small and can be neglected, as shown in Fig. 4.64. Therefore, to conclude, the configurations 3 and 4 can be good solutions to realize the temperature

uniformity within the machines. However, they will have slightly higher temperatures, which can be addressed by increasing the total flow rates.

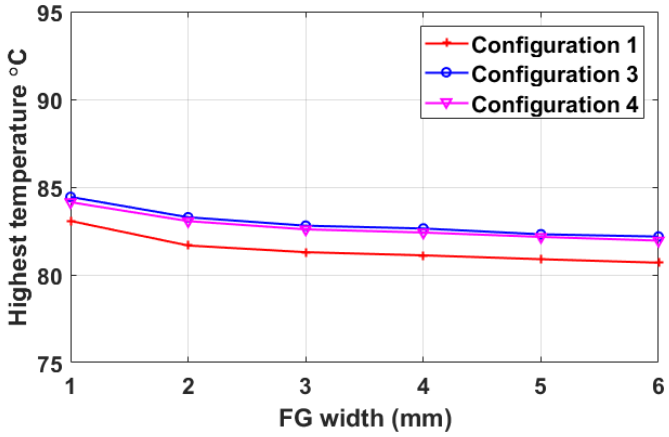

Fig. 4.61. Highest temperature within the machines *vs* FG width for different configurations.

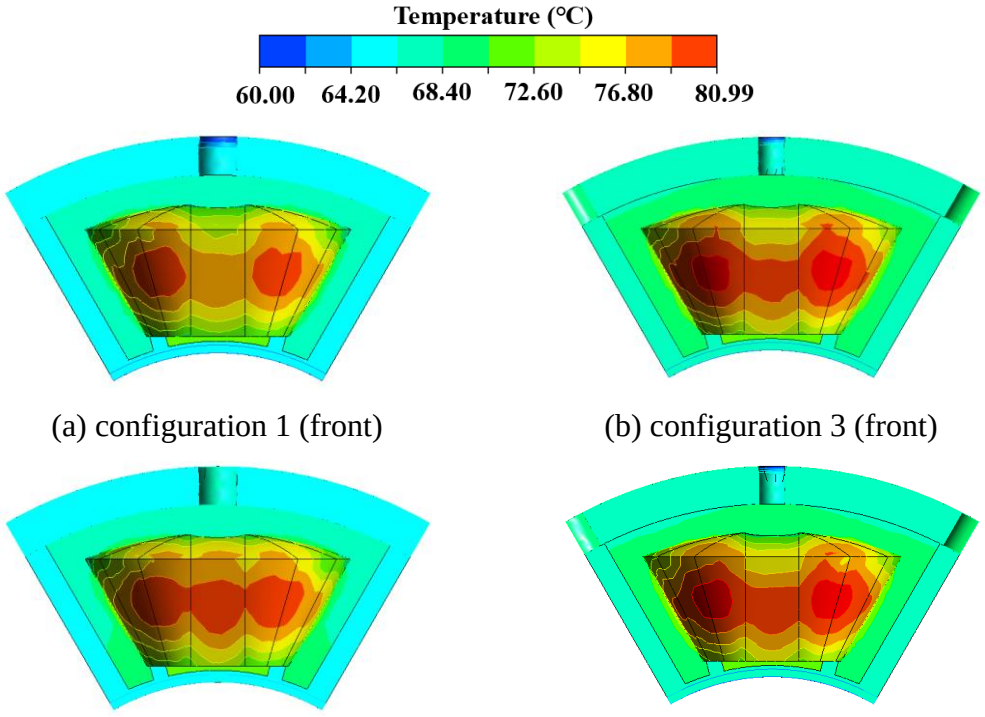

(a) configuration 1 (front) (b) configuration 3 (front)

(c) configuration 1 (back) (d) configuration 3 (back)

Fig. 4.62. Temperature distributions of EWs with configurations 1 and 3 on both sides, FG=6mm.

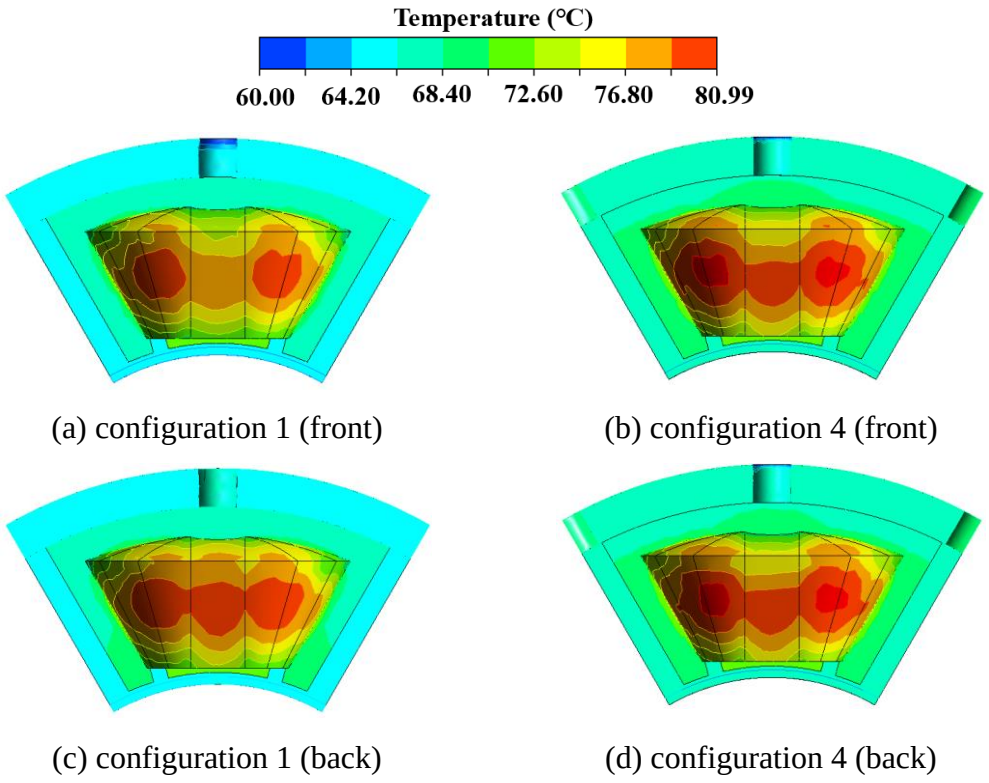

(a) configuration 1 (front) (b) configuration 4 (front)

(c) configuration 1 (back) (d) configuration 4 (back)

Fig. 4.63. Temperature distributions of EWs for configurations 0 and 4 on both sides, FG=6mm.

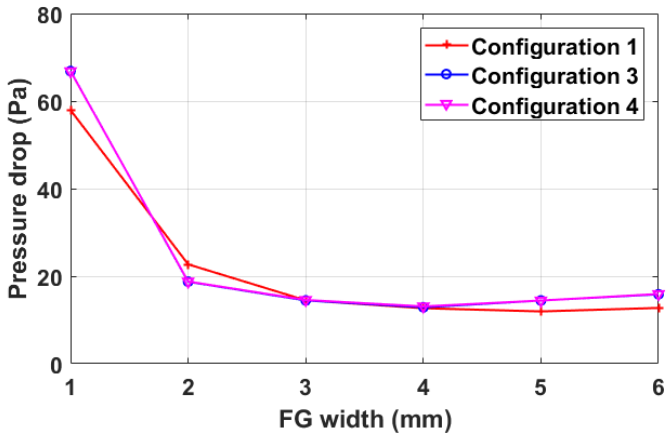

Fig. 4.64. Pressure drop *vs* FG width for different configurations.

4.15. Conclusion

Based on the modular machines investigated in previous chapters, a forced air cooling with inlets and outlets on the end-caps is proposed in the preceding sections of this chapter and a submerged wet stator with forced oil cooling method is proposed in the later part of this chapter. The effectiveness of has been proven by the numerical results obtained by CFD analyses. According to the results, the conclusions and some

design guidelines of such modular machines considering particularly the thermal performance can be given:

Forced air cooling:

- For the initial design when the inlet faces FGs, there will be an optimal FG width to achieve the best cooling effect. However, larger FG width can lead to lower pressure drop which is also desirable;
- Better cooling effect can be achieved when the inlet faces EWs, especially at larger FG width. However, the pressure drop of this case is always higher compared with that when the inlet faces FGs.
- The influence of inlet radius is quite small and can be neglected when the inlet faces FGs. However, if the inlet faces EWs, the inlet with smaller radius can have better cooling effect, but the pressure drop is also increased.

At last, some recommendations for best cooling effect and lowest pressure drop (or highest cooling system efficiency) are given in Table 4.9 and

Table 4.10, respectively.

Table 4.9. Configuration having best cooling effect

Inlet position	FG width	Inlet radius
Facing EWs	2-6mm	4mm

Table 4.10. Configuration having lowest pressure drop

Inlet position	FG width	Inlet radius
Facing FGs	6mm	10mm

Forced oil cooling:

- Generally speaking, the FGs can have good cooling effect in the modular machines, but the influence of FG width on the temperature reduction is very slight. However, larger FG width can lead to lower pressure drop which is also desirable. Moreover, it is found that the cooling effect would be much better if the loadings are increasing.
- Better cooling effect can be achieved when the inlets are just above EWs.

- The configurations 3 and 4 are proposed to realize the temperature uniformity within machines. Although they could have slightly higher temperatures, this can be easily improved by increasing the total flow rates.

At last, some recommendations for best cooling effect are given in Table 4.11. The pressure drop is not a major problem in the forced oil cooling due to relatively lower flow speed, as along as the FG≥2mm.

Table 4.11. Configuration having best cooling effect

Inlet position	FG width	Inlet configuration (temperature uniformity)
Above EWs	1-6mm	Configuration 3&4

Chapter 5 General Conclusion and Future Works

5.1. Conclusions

In this thesis, the consequent pole machines (CPMs) have been investigated. The influences of different winding configurations and rotor structures on electromagnetic performances of the CPMs are studied. Furthermore, the modular CPMs are investigated which can potentially ease the manufacture, assembly and transportation processes for large-dimension machines. Finally, two forced cooling methods, i.e. forced air cooling and force liquid cooling, have been proposed for the investigated modular CPMs and their effectiveness has been proven by CFD analyses. The conclusion drawn in this thesis can provide some guidelines for designing CPMs which could be used in a wide range of applications. For example, they can be used for electric vehicles where high torque/power density and low cost are desirable; large direct-drive wind power generators where modular technology is pivotal for easing the manufacture.

5.1.1. Winding Configuration and Rotor Structure

The thesis starts from the investigation of the influences of winding configurations on electromagnetic performances of fractional-slot (FS-) and integer-slot (IS-) CPMs. Their static and dynamic performances are thoroughly investigated. It is found that the torque capability of the IS-CPMs is better than the FS-CPMs. However, by adopting the double layer (DL) winding configuration, the armature field reaction of the FS-CPM can be significantly reduced and the torque performance can be improved as a result. Moreover, the IS-CPMs have much lower PM eddy current losses in comparison with the FS-CPMs, which can lead to higher efficiency. However, with larger *d*-axis inductances, the flux-weakening capability of the FS-CPMs are much better than the IS-CPMs, leading to wider constant power speed range.

Apart from the aspect of winding configurations, the influences of rotor structures on electromagnetic performances of the FS- and IS-CPMs have also been investigated. It shows that with the same PM volume, the CPMs with SPM rotor have better torque capability in comparison with IPM rotors, regardless of FS or IS winding structures. With the same rotor structures, the torque performances of CPMs with IS winding are

better compared with CPMs with FS windings. In terms of the PM eddy current losses, the CPMs with IPM rotors have much lower PM eddy current losses compared with the CPMs having SPM rotors, regardless of FS or IS winding. In addition, the PM eddy current losses of the IS-CPMs are lower than those of the corresponding FS-CPMs. Regarding the dynamic performances, with lower phase flux linkages, the flux-weakening capabilities of the CPMs with IPM rotors are better than their SPM counterparts. With larger *d*-axis inductances, the flux-weakening capability of the FS-CPMs are better than the IS-CPMs. In addition, by taking the influence of temperature on the magnet working point into consideration, it is found that the demagnetization withstand capabilities of the CPMs with IPM rotors are much better than their SPM counterparts. The FE predictions have been validated by experiments using the FS-SPM prototype machines.

Based on the investigations, some recommendations for the best candidates in CPMs under different criteria are given in Table 5.1.

Table 5.1. Best candidates under different criteria

Criteria	**FS**	**IS**	**SPM**	**IPM**
Torque performance		●	●	
Torque ripple		●		●
PM losses		●		●
Efficiency		●		●
Flux-weakening capability	●			●
Demagnetization withstand capability	●	●		●
Winding process	●	●	●	●
Manufacture	●		●	

●: Best candidate

5.1.2. Modular CPMs

Based on the aforementioned electromagnetic investigations, the great potential of CPMs in various applications has been recognized. Thus, this thesis also attempts to combine the modular stator with the CP rotor to achieve an even higher PM utilization and to cope with the manufacture, assembly and transportation challenges in large-

dimension machines, especially the large direct-drive wind power generators. The modular CPMs with both E-core and C-core stators are investigated. Two typical slot/pole number combinations including 12-slot/10-pole ($Ns>2p$) and 12-slot/14-pole ($Ns<2p$) have been taken into consideration. To be specific, their static and dynamic performances such as torque-speed curves, power factor-speed curves and efficiency maps have been comprehensively investigated. It is found that most performances can be improved by selecting proper FG width in modular structures. The simulated static and dynamic performances have been validated by a series of experimental tests.

Also, some guidelines and recommendations under different criteria are given as following for selecting the best candidates:

- Best candidate for maximizing the average torque: 12-slot/14-pole with E-core, the average torque increases by 17.3% from 4.4Nm (FG=0mm) to 5.2Nm (FG=3mm).
- Best candidate for minimizing torque ripple: 12-slot/10-pole with C-core, the torque ripple reduces by 68.7% from 9.4% (FG=0mm) to 2.9% (FG=3mm).
- Best candidate for minimizing on-load UMF: 12-slot/14-pole with C-core, the UMF reduces by 84.8% from 58.2N (FG=0mm) to 8.8N (FG=6mm).
- Best candidate for achieving the highest efficiency: 12-slot/14-pole with E-core, the efficiency increases by 4% from 91% (FG=0mm) to 95% (FG=2mm).
- Best candidates for achieving the optimal dynamic performances are recommended in Table 5.2.

Table 5.2 Best candidates for dynamic performances

Flux-weakening capability	Power factor
12-slot/14-pole E-core (FG=2mm)	12-slot/10-pole E-core (FG=2mm)

To get a better understanding of performance improvements, a comparison is shown in Fig. 5.1. The 12-slot/10-pole C-core with 3mm FG and 12-slot/14-pole E-core with 2mm FG machines are selected for their outstanding performances in minimizing torque ripple and maximizing average torque, and their performances are compared with respect the corresponding benchmark machines (non-modular machines).

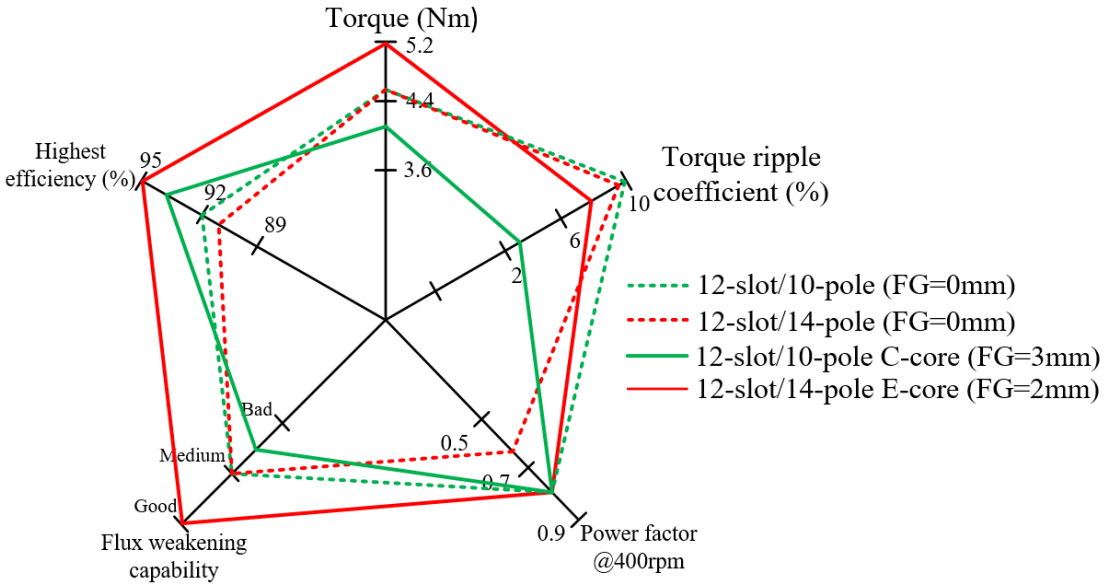

Fig. 5.1. Featured spider comparison.

5.1.3. Forced Air and Liquid Cooling for the Modular CPMs

The electrical machines should not only be evaluated from the aspect of electromagnetic performances, but also be evaluated from the aspect of thermal management. Based on the modular machines investigated in chapter 3, a forced air cooling with inlets and outlets on the end-caps and a submerged wet stator with forced oil cooling method are proposed in this thesis in order to address the thermal management issue. Both cooling methods can fully take advantage of the FGs and integrate them into the cooling circuit in order to improve machine cooling efficiency. Effectiveness of both cooling methods has been proven by the numerical results obtained by CFD analyses. To provide a full picture of the potential of the proposed cooling methods, the influences of the FG width and also several other design parameters have been investigated aiming to provide some design guidelines for engineers to perform thermal management of such modular machines. The main findings can be summarized as following:

1) Forced air cooling:

- For the initial design when the inlet faces FGs, there will be an optimal FG width to achieve the best cooling effect. However, larger FG width can lead to lower pressure drop which is also desirable;

• Better cooling effect can be achieved when the inlet faces EWs, especially at larger FG width. However, the pressure drop of this case is always higher compared with that when the inlet faces FGs.

• The influence of inlet radius is quite small and can be neglected when the inlet faces FGs. However, if the inlet faces EWs, the inlet with smaller radius can have better cooling effect, but the pressure drop is also increased.

2) Forced liquid cooling:

• The FGs can have good cooling effect in the modular machines, but the influence of FG width on the temperature reduction is small. However, larger FG width can lead to lower pressure drop which is also desirable. Moreover, it is found that the cooling effect would be much better if the loadings are increased.

• Better cooling effect can be achieved when the inlets are just above the EWs.

• The configurations 3 and 4 as shown in Fig. 5.2 are proposed to realize the temperature uniformity within the machines. Although they could have slightly higher temperatures, this can be easily improved by increasing the total flow rates.

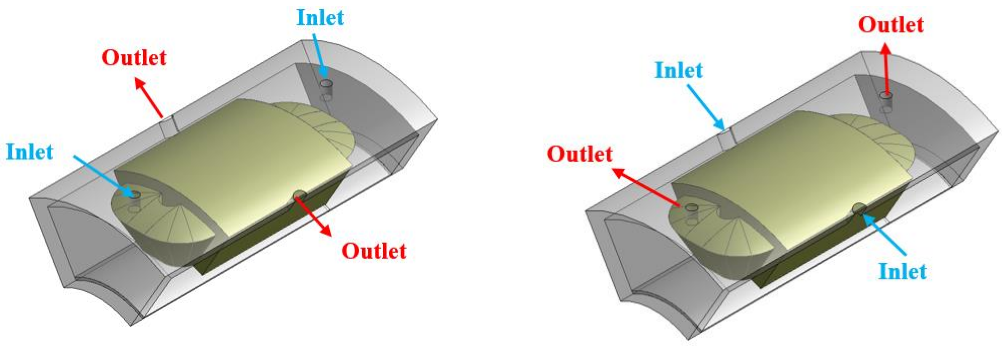

(a) configuration 3 (b) configuration 4

Fig. 5.2. Proposed configurations 3 and 4.

5.2. Future Works

Although a lot of works have been performed in this thesis, there are still some research to be carried out in the future to reveal the full potential of CPMs, such as:

1) Experimental tests should be carried out to validate the CFD results.

2) The vibration and acoustic noise of modular CPMs could be investigated.

3) Works can be done in order to reduce the saturation level in CPMs, especially at overloads conditions. This is because the CPMs are sensitive to the armature field, leading to limited overload capability.

4) Some work can be done related to the proposed forced air and liquid cooling methods. For example, the PMs on the rotor and rotation speed can be fully considered in order to see its potential in high-speed applications. Moreover, the electromagnetic-thermal coupling effect could be taken into account to consider the influence of temperatures on the electromagnetic characteristics.

References:

[1] J. d. Santiago, H. Bernhoff, B. Ekergård, S. Eriksson, S. Ferhatovic, R. Waters, *et al.*, "Electrical motor drivelines in commercial all-electric vehicles: a review," *IEEE Transactions on Vehicular Technology*, vol. 61, no. 2, pp. 475-484, 2012.

[2] A. M. Bazzi, "Electric machines and energy storage technologies in EVs and HEVs for over a century," in *International Electric Machines & Drives Conference (IEMDC)*, 12-15 May, 2013, pp. 212-219.

[3] A. Pouramin, R. Dutta, and M. F. Rahman, "Preliminary study on differences in the performance characteristics of concentrated and distributed winding IPM machines with different rotor topologies," in *2017 IEEE Energy Conversion Congress and Exposition (ECCE)*, 2017, pp. 3565-3570.

[4] W. L. Soong and N. Ertugrul, "Field-weakening performance of interior permanent-magnet motors," *IEEE Trans. Ind. Appl.*, vol. 38, no. 5, pp. 1251-1258, 2002.

[5] T. Burress, "Benchmarking EV and HEV technologies," Oak Ridge National LaboratoryJune 9th 2015.

[6] T. Burress, "Benchmarking EV and HEV technologies," Oak Ridge National LaboratoryJune 7th 2016.

[7] D. Staton and J. Goss, "Open source electric motor models for commercial EV & hybrid traction motors," in *CWIEME*, Berlin, 2017.

[8] A. M. El-Refaie, "Motors/generators for traction/propulsion applications: A review," *IEEE Vehicular Technology Magazine*, vol. 8, no. 1, pp. 90-99, 2013.

[9] S. Estenlund, M. Alaküla, and A. Reinap, "PM-less machine topologies for EV traction: a literature review," in *2016 International Conference on Electrical Systems for Aircraft, Railway, Ship Propulsion and Road Vehicles & International Transportation Electrification Conference (ESARS-ITEC)*, 2016, pp. 1-6.

[10] T. A. Huynh and M. Hsieh, "Comparative study of PM-assisted synRM and IPMSM on constant power speed range for EV applications," *IEEE Trans. Magn.*, vol. 53, no. 11, pp. 1-6, 2017.

[11] L. Ge, X. Zhu, W. Wu, F. Liu, and Z. Xiang, "Design and comparison of two non-rare-earth permanent magnet synchronous reluctance motors for EV applications," in *2017 20th International Conference on Electrical Machines and Systems (ICEMS)*, 2017, pp. 1-5.

[12] Y. Kong, M. Lin, M. Yin, and L. Hao, "Rotor structure on reducing demagnetization of magnet and torque ripple in a PMa-synRM With ferrite permanent magnet," *IEEE Trans. Magn.*, vol. 54, no. 11, pp. 1-5, 2018.

[13] F. Xing, W. Zhao, and B. Kwon, "Design and optimisation of a novel asymmetric rotor structure for a PM-assisted synchronous reluctance machine," *IET Electric Power Applications*, vol. 13, no. 5, pp. 573-580, 2019.

[14] Z. Yang, F. Shang, I. P. Brown, and M. Krishnamurthy, "Comparative study of interior permanent magnet, induction, and switched reluctance motor drives for EV and HEV applications," *IEEE Transactions on Transportation Electrification*, vol. 1, no. 3, pp. 245-254, 2015.

[15] Q. Yu, B. Bilgin, and A. Emadi, "Loss and Efficiency Analysis of Switched Reluctance Machines Using a New Calculation Method," *IEEE Trans. Ind. Electron.*, vol. 62, no. 5, pp. 3072-3080, Jan. 2015.

[16] K. Zhang, G. J. Li, Z. Q. Zhu, and G. W. Jewell, "Analytical modelling of dynamic performance with harmonic current injection for doubly salient SynRMs," *IEEE Trans. Ind. Appl.*, vol. no. pp. 1-1, 2020.

[17] H. Yang, Y. Lim, and H. Kim, "Acoustic noise/vibration reduction of a single-phase SRM using skewed stator and rotor," *IEEE Trans. Ind. Electron.*, vol. 60, no. 10, pp. 4292-4300, 2013.

[18] K. Wang, Z. Q. Zhu, G. Ombach, M. Koch, S. Zhang, and J. Xu, "Optimal slot/pole and flux-barrier layer number combinations for synchronous reluctance machines," in *2013 Eighth International Conference and Exhibition on Ecological Vehicles and Renewable Energies (EVER)*, 2013, pp. 1-8.

[19] G. Pellegrino, A. Vagati, B. Boazzo, and P. Guglielmi, "Comparison of induction and PM synchronous motor drives for EV application including design examples," *IEEE Trans. Ind. Appl.*, vol. 48, no. 6, pp. 2322-2332, 2012.

[20] D. G. Dorrell, "Combined thermal and electromagnetic analysis of permanent-magnet and induction machines to aid calculation," *IEEE Trans. Ind. Electron.*, vol. 55, no. 10, pp. 3566-3574, May. 2008.

[21] T. J. E. M. J. R. Hendershot Jr, *Design of brushless permanent-magnet motors*, 1995.

[22] L. Papini, F. Papini, P. Bolognesi, and C. Gerada, "Comparison of surface mounted and uneven consequent-pole PM high-speed machines," in *IEEE Workshop on Electrical Machines Design, Control and Diagnosis (WEMDCD)*, 20-21 Apr., 2017, pp. 52-57.

[23] P. Bolognesi, F. Papini, and V. Biagini, "Consequent-pole brushless machines featuring uneven magnet-pole width ratio," in *International Conference on Electrical Machines (ICEM)*, Sep., 2010, pp. 1-6.

[24] S. U. Chung, J. M. Kim, D. H. Koo, B. C. Woo, D. K. Hong, and J. Y. Lee, "Fractional slot concentrated winding permanent magnet synchronous machine with consequent pole rotor for low speed direct drive," *IEEE Trans. Magn.*, vol. 48, no. 11, pp. 2965-2968, Nov. 2012.

[25] S. U. Chung, J. W. Kim, Y. D. Chun, B. C. Woo, and D. K. Hong, "Fractional slot concentrated winding PMSM with consequent pole rotor for a low-speed direct drive: reduction of rare earth permanent magnet," *IEEE Trans. Energy Convers.*, vol. 30, no. 1, pp. 103-109, Sep. 2015.

[26] S. U. Chung, S. H. Moon, D. J. Kim, and J. M. Kim, "Development of a 20-pole-24-slot SPMSM with consequent pole rotor for in-wheel direct drive," *IEEE Trans. Ind. Electron.*, vol. 63, no. 1, pp. 302-309, Jan. 2016.

[27] L. Wu and R. Qu, "Comparison of conventional and consequent pole interior permanent magnet machines for electric vehicle application," in *International Conference on Electrical Machines and Systems (ICEMS)*, 22-25 Oct., 2014, pp. 70-74.

[28] G. Qu, Y. Fan, and R. Cui, "Design and analysis of a new consequent-pole interior permanent magnet synchronous motor," in *International Conference on Electrical Machines and Systems (ICEMS)*, 2018, pp. 376-381.

[29] M. Chiu, J. Chiang, and C. Lin, "Design and optimization of a novel V-type consequent-pole interior permanent magnet synchronous motor for applying to refrigerant compressor," in *2018 21st International Conference on Electrical Machines and Systems (ICEMS)*, 2018, pp. 413-418.

[30] F. Li, K. Wang, J. Li, and H. J. Zhang, "Suppression of even-order harmonics and torque ripple in outer rotor consequent-pole PM machine by multilayer winding," *IEEE Trans. Magn.*, vol. no. pp. 1-5, Jun. 2018.

[31] J. Li, K. Wang, F. Li, S. Zhu, and C. Liu, "Elimination of even-order harmonics and unipolar leakage flux in consequent-pole PM machines by employing N-S-Iron-S-N-Iron rotor," *IEEE Trans. Ind. Electron.*, vol. no. pp. 1-1, May 2018.

[32] J. Li, K. Wang, and C. Liu, "Comparative study of consequent-pole and hybrid-pole permanent magnet machines," *IEEE Trans. Energy Convers.*, vol. 34, no. 2, pp. 701-711, 2019.

[33] K. Wang, J. Li, S. S. Zhu, and C. Liu, "Novel hybrid-pole rotors for consequent-pole PM machines without unipolar leakage flux," *IEEE Trans. Ind. Electron.*, vol. 66, no. 9, pp. 6811-6823, 2019.

[34] J. Li, K. Wang, and H. Zhang, "Flux-focusing permanent magnet machines with modular consequent-poe rtor," *IEEE Trans. Ind. Electron.*, vol. 67, no. 5, pp. 3374-3385, 2020.

[35] J. Li, K. Wang, and C. Liu, "Torque improvement and cost reduction of permanent magnet machines with a dovetailed consequent-pole rotor," *IEEE Trans. Energy Convers.*, vol. 33, no. 4, pp. 1628-1640, 2018.

[36] F. Li, K. Wang, J. Li, H. Y. Sun, and P. C. K. Luk, "Electromagnetic performance analysis of PMSM with eccentric consequent pole rotor," in *International Conference on Power Electronics Systems and Applications - Smart Mobility, Power Transfer & Security (PESA)*, 12-14 Dec., 2017, pp. 1-7.

[37] J. Li and K. Wang, "A novel spoke-type PM machine employing asymmetric modular consequent-pole rotor," *IEEE Trans. Mech.*, vol. 24, no. 5, pp. 2182-2192, 2019.

[38] F. Li, K. Wang, H. Sun, and J. Kong, "Influence of various magnetic pole on electromagnetic performance of consequent-pole permanent magnet machine," *IEEE Access*, vol. 7, no. pp. 121853-121862, 2019.

[39] N. Baloch, B. Kwon, and Y. Gao, "Low-cost high-torque-density dual-stator consequent-pole permanent magnet vernier machine," *IEEE Trans. Magn.*, vol. 54, no. 11, pp. 1-5, 2018.

[40] W. Tao, H. Zhou, and G. Liu, "A novel stator-PM vernier fault-tolerant machine with consequent pole structure," in *2019 22nd International Conference on Electrical Machines and Systems (ICEMS)*, 2019, pp. 1-4.

[41] S. U. Chung, J. W. Kim, B. C. Woo, D. K. Hong, J. Y. Lee, and D. H. Koo, "A novel design of modular three-Phase permanent magnet vernier machine with consequent pole rotor," *IEEE Trans. Magn.*, vol. 47, no. 10, pp. 4215-4218, 2011.

[42] D. Li, R. Qu, J. Li, and W. Xu, "Consequent-pole toroidal-winding outer-rotor vernier permanent-magnet machines," *IEEE Trans. Ind. Appl.*, vol. 51, no. 6, pp. 4470-4481, 2015.

[43] Y. Yu, Y. Pei, L. Chen, F. Chai, and G. Han, "Design and comparative analysis of consequent pole rotor configurations in PM vernier motors for in-wheel drive application," in *2019 22nd International Conference on Electrical Machines and Systems (ICEMS)*, 2019, pp. 1-6.

[44] H. Zhou, W. Tao, C. Zhou, Y. Mao, G. Li, and G. Liu, "Consequent pole permanent magnet vernier machine with asymmetric air-gap field distribution," *IEEE Access*, vol. 7, no. pp. 109340-109348, 2019.

[45] H. Wang, S. Fang, H. Yang, H. Lin, Y. Li, L. Qin, *et al.*, "Loss calculation and temperature field analysis of consequent-pole hybrid excited vernier machine," *IEEE Trans. Magn.*, vol. 53, no. 11, pp. 1-5, 2017.

[46] D. Li, R. Qu, J. Li, and W. Xu, "Design of consequent pole, toroidal winding, outer rotor vernier permanent magnet machines," in *2014 IEEE Energy Conversion Congress and Exposition (ECCE)*, 2014, pp. 2342-2349.

[47] W. Liu, L. Sun, and T. A. Lipo, "On the scaling of consequent pole vernier machines eith dpoke type magnets," in *2018 IEEE Energy Conversion Congress and Exposition (ECCE)*, 2018, pp. 3294-3301.

[48] Y. Mei, Y. Fan, Q. Zhang, G. Qu, and C. Mao, "Design and analysis of a new consequent-pole permanent-magnet servo motor based on field modulation," in *2019 22nd International Conference on Electrical Machines and Systems (ICEMS)*, 2019, pp. 1-5.

[49] H. Wang, S. Fang, H. Yang, H. Lin, D. Wang, Y. Li, *et al.*, "A novel consequent-pole hybrid excited vernier machine," *IEEE Trans. Magn.*, vol. 53, no. 11, pp. 1-4, 2017.

[50] L. Xu, W. Fan, S. Zheng, J. Wu, Y. Hua, and S. Zhou, "Investigation of a partitioned-stator hybrid-excited flux-switching permanent magnet machine with consequent poles," in *2019 22nd International Conference on Electrical Machines and Systems (ICEMS)*, 2019, pp. 1-5.

[51] Y. Gao, D. Li, R. Qu, H. Fang, H. Ding, and L. Jing, "Analysis of a novel consequent-pole flux switching permanent magnet machine with flux bridges in stator core," *IEEE Trans. Energy Convers.*, vol. 33, no. 4, pp. 2153-2162, 2018.

[52] H. Yang, H. Lin, Z. Q. Zhu, S. Fang, and Y. Huang, "A winding-switching concept for flux weakening in consequent magnet pole switched flux memory machine," *IEEE Trans. Magn.*, vol. 51, no. 11, pp. 1-4, 2015.

[53] W. Ullah, F. Khan, E. Sulaiman, M. Umair, N. Ullah, and B. Khan, "Influence of various rotor pole on electromagnetic performance of consequent pole switched flux permanent magnet machine," in *2019 International Conference on Electrical, Communication, and Computer Engineering (ICECCE)*, 2019, pp. 1-6.

[54] H. Yang, Z. Q. Zhu, H. Lin, H. Li, and S. Lyu, "Analysis of consequent-pole flux reversal permanent magnet machine with biased flux modulation theory," *IEEE Trans. Ind. Electron.*, vol. 67, no. 3, pp. 2107-2121, 2020.

[55] Z. Z. Wu and Z. Q. Zhu, "Partitioned stator flux reversal machine with consequent-pole PM stator," *IEEE Trans. Energy Convers.*, vol. 30, no. 4, pp. 1472-1482, Jan. 2015.

[56] Z. Z. Wu and Z. Q. Zhu, "Comparative analysis of end Effect in partitioned stator flux reversal machines having surface-mounted and consequent pole permanent magnets," *IEEE Trans. Magn.*, vol. 52, no. 7, pp. 1-4, 2016.

[57] H. Qu, Z. Q. Zhu, and H. Y. Li, "Analysis of novel consequent pole flux reversal permanent magnet machine," in *2019 IEEE Energy Conversion Congress and Exposition (ECCE)*, 2019, pp. 5223-5230.

[58] H. Li and Z. Zhu, "Investigation of stator slot/rotor pole combination of flux reversal permanent magnet machine with consequent-pole PM structure," *The Journal of Engineering*, vol. 2019, no. 17, pp. 4267-4272, 2019.

[59] Y. Gao, R. Qu, D. Li, J. Li, and G. Zhou, "Consequent-pole flux-reversal permanent-magnet machine for electric vehicle propulsion," *IEEE Trans. Appl. Supercond.*, vol. 26, no. 4, pp. 1-5, Jun. 2016.

[60] Y. Terao, M. Sekino, and H. Ohsaki, "Comparison of Conventional and Superconducting Generator Concepts for Offshore Wind Turbines," *IEEE Transactions on Applied Superconductivity*, vol. 23, no. 3, pp. 5200904-5200904, 2013.

[61] H. Akita, Y. Nakahara, N. Miyake, and T. Oikawa, "New core structure and manufacturing method for high efficiency of permanent magnet motors," in *38th IAS Annual Meeting on Conference Record of the Industry Applications Conference, 2003.*, 2003, pp. 367-372 vol.1.

[62] H. Akita, Y. Nakahara, N. Miyake, and T. Oikawa, "A new core," *IEEE Industry Applications Magazine*, vol. 11, no. 6, pp. 38-43, 2005.

[63] J. Yuan, C. Shi, and J. Shen, "Analysis of cogging torque in surface-mounted permanent magnet machines with segmented stators," in *2014 17th International Conference on Electrical Machines and Systems (ICEMS)*, 2014, pp. 2513-2516.

[64] T. Lee, M. Seo, Y. Kim, and S. Jung, "Cogging torque of surface-mounted permanent magnet synchronous motor according to segmented-stator core effect," in *2016 XXII International Conference on Electrical Machines (ICEM)*, 2016, pp. 200-206.

[65] N. J. Baker, D. J. B. Smith, M. C. Kulan, and S. Turvey, "Design and performance of a segmented stator permanent magnet alternator for aerospace," *IEEE Trans. Energy Convers.*, vol. 33, no. 1, pp. 40-48, 2018.

[66] G. Dajaku and D. Gerling, "A novel 12-teeth/10-poles PM machine with flux barriers in stator yoke," in *Electrical Machines (ICEM), 2012 XXth International Conference on*, 2012, pp. 36-40.

[67] G. Dajaku, X. Wei, and D. Gerling, "Reduction of low space harmonics for the fractional slot concentrated windings using a novel stator design," *IEEE Trans. Magn.*, vol. 50, no. 5, pp. 1-12, Dec. 2014.

[68] G. Dajaku and D. Gerling, "Different novel methods for reduction of low space harmonics for the fractional slot concentrated windings," in *Electrical Machines and Systems (ICEMS), 2012 15th International Conference on*, 2012, pp. 1-6.

[69] F. Libert and J. Soulard, "Manufacturing methods of stator cores with concentrated windings," in *2006 3rd IET International Conference on Power Electronics, Machines and Drives - PEMD 2006*, 2006, pp. 676-680.

[70] G. Heins, D. M. Ionel, and M. Thiele, "Winding factors and magnetic fields in permanent-magnet brushless machines with concentrated windings and modular stator cores," *IEEE Trans. Ind. Appl.*, vol. 51, no. 4, pp. 2924-2932, Jan. 2015.

[71] M. Zheng, Z. Q. Zhu, S. Cai, and S. S. Xue, "A novel modular stator hybrid-excited doubly salient synchronous machine with stator slot permanent magnets," *IEEE Trans. Magn.*, vol. 55, no. 7, pp. 1-9, 2019.

[72] S. R. Mousavi-Aghdam, M. R. Feyzi, N. Bianchi, and M. Morandin, "Design and analysis of a novel high-torque stator-segmented SRM," *IEEE Trans. Ind. Electron.*, vol. 63, no. 3, pp. 1458-1466, 2016.

[73] Z. Q. Zhu, Z. Azar, and G. Ombach, "Influence of additional air gaps between stator segments on cogging torque of permanent-magnet machines having modular stators," *IEEE Trans. Magn.*, vol. 48, no. 6, pp. 2049-2055, 2012.

[74] Z. Chen and E. Spooner, "A modular, permanent-magnet generator for variable speed wind turbines," in *1995 Seventh International Conference on Electrical Machines and Drives (Conf. Publ. No. 412)*, 1995, pp. 453-457.

[75] E. Spooner, A. C. Williamson, and G. Catto, "Modular design of permanent-magnet generators for wind turbines," *IEE Proc.-Electr. Power Appl.*, vol. 143, no. 5, pp. 388-395, Sep. 1996.

[76] E. Spooner and A. Williamson, "Modular, permanent-magnet wind-turbine generators," in *IAS '96. Conference Record of the 1996 IEEE Industry Applications Conference Thirty-First IAS Annual Meeting*, 1996, pp. 497-502 vol.1.

[77] G. Geng and E. Spooner, "Cancellation of noise and vibration in modular permanent-magnet wind turbine generators," in *1995 Seventh International Conference on Electrical Machines and Drives (Conf. Publ. No. 412)*, 1995, pp. 467-471.

[78] E. Spooner and A. C. Williamson, "Parasitic losses in modular permanent-magnet generators," in *1997 Eighth International Conference on Electrical Machines and Drives (Conf. Publ. No. 444)*, 1997, pp. 165-169.

[79] G. Dajaku and D. Gerling, "Low costs and high-efficiency electric machines," in *International Conference on Electric Drives Production Conference (EDPC)*, 15-18 Oct., 2012, pp. 1-7.

[80] A. Nollau and D. Gerling, "Novel cooling methods using flux-barriers," in *2014 IEEE International Conference on Electrical Machines (ICEM)*, 2014, pp. 1328-1333.

[81] G. Dajaku and D. Gerling, "Analysis of different PM machines with concentrated windings and flux barriers in stator core," in *2014 International Conference on Electrical Machines (ICEM)*, 2014, pp. 375-384.

[82] A. Nollau and D. Gerling, "A flux barrier cooling for traction motors in hybrid drives," in *2015 IEEE International Electric Machines & Drives Conference (IEMDC)*, 2015, pp. 1103-1108.

[83] J. W. Gerold and D. Gerling, "Analysis of different arrangements of flux barriers and different pole pairs in a stator with concentrated wnding," in *2018 XIII International Conference on Electrical Machines (ICEM)*, 2018, pp. 58-64.

[84] G. J. Li, Z. Q. Zhu, W. Q. Chu, M. P. Foster, and D. A. Stone, "Influence of flux gaps on electromagnetic performance of novel modular PM machines," *IEEE Trans. Energy Convers.*, vol. 29, no. 3, pp. 716-726, April. 2014.

[85] G. J. Li, Z. Q. Zhu, M. Foster, and D. Stone, "Comparative studies of modular and unequal tooth PM machines either with or without tooth tips," *IEEE Trans. Magn.*, vol. 50, no. 7, pp. 1-10, March. 2014.

[86] G. J. Li and Z. Q. Zhu, "Analytical modeling of modular and unequal tooth width surface-mounted permanent magnet machines," *IEEE Trans. Magn.*, vol. 51, no. 9, pp. 1-9, 2015.

[87] G. J. Li, B. Ren, Z. Q. Zhu, Y. X. Li, and J. Ma, "Cogging torque mitigation of modular permanent magnet machines," *IEEE Trans. Magn.*, vol. 52, no. 1, pp. 1-10, Sept. 2016.

[88] G. J. Li, B. Ren, Z. Q. Zhu, M. P. Foster, and D. A. Stone, "Demagnetization withstand capability enhancement of surface mounted PM machines using stator modularity," *IEEE Trans. Ind. Appl.*, vol. 54, no. 2, pp. 1302-1311, Nov. 2018.

[89] G. J. Li, Z. Q. Zhu, M. P. Foster, D. A. Stone, and H. L. Zhan, "Modular permanent-magnet nachines with alternate teeth having tooth tips," *IEEE Trans. Ind. Electron.*, vol. 62, no. 10, pp. 6120-6130, April. 2015.

[90] T. Albers and A. H. Bonnett, "Motor temperature considerations for pulp and paper mill applications," *IEEE Trans. Ind. Appl.*, vol. 38, no. 6, pp. 1701-1713, 2002.

[91] G. C. Montanari, G. Mazzanti, and L. Simoni, "Progress in electrothermal life modeling of electrical insulation during the last decades," *IEEE Transactions on Dielectrics and Electrical Insulation*, vol. 9, no. 5, pp. 730-745, 2002.

[92] D. Huger and D. Gerling, "On the effects of high-temperature-induced aging on electrical machine windings," in *2015 IEEE International Electric Machines & Drives Conference (IEMDC)*, 2015, pp. 1018-1021.

[93] S. Ruoho, J. Kolehmainen, J. Ikaheimo, and A. Arkkio, "Interdependence of demagnetization, loading, and temperature rise in a permanent-magnet synchronous motor," *IEEE Trans. Magn.*, vol. 46, no. 3, pp. 949-953, 2010.

[94] D. A. Staton and A. Cavagnino, "Convection heat transfer and flow calculations suitable for electric machines thermal models," *IEEE Trans. Ind. Electron.*, vol. 55, no. 10, pp. 3509-3516, Sept. 2008.

[95] G. M. Gilson, T. Raminosoa, S. J. Pickering, C. Gerada, and D. B. Hann, "A combined electromagnetic and thermal optimisation of an aerospace electric motor," in *The XIX International Conference on Electrical Machines - ICEM 2010*, 2010, pp. 1-7.

[96] M. A. Valenzuela and J. A. Tapia, "Heat transfer and thermal design of finned frames for TEFC variable-speed motors," *IEEE Trans. Ind. Electron.*, vol. 55, no. 10, pp. 3500-3508, 2008.

[97] D. A. Staton and E. So, "Determination of optimal thermal parameters for brushless permanent magnet motor design," in *Conference Record of 1998 IEEE Industry Applications Conference. Thirty-Third IAS Annual Meeting (Cat. No.98CH36242)*, 1998, pp. 41-49 vol.1.

[98] D. V. d. Pol and J. Tierney, "Free convection heat transfer from vertical fin-arrays," *IEEE Transactions on Parts, Hybrids, and Packaging*, vol. 10, no. 4, pp. 267-271, 1974.

[99] Y. Gai, M. Kimiabeigi, Y. C. Chong, J. Widmer, X. Deng, M. Popescu, *et al.*, "Cooling of automotive traction motors: schemes, examples and computation methods- a review," *IEEE Trans. Ind. Electron.*, vol. no. pp. 1-1, 2018.

[100] C. Micallef, S. J. Pickeringt, K. A. Simmons, and K. J. Bradley, "An alternative cooling arrangement for the end region of a totally enclosed fan cooled (TEFC) induction motor," in *2008 4th IET Conference on Power Electronics, Machines and Drives*, 2008, pp. 305-309.

[101] C. Yung, "Cool facts about cooling electric motors: improvements in applications that fall outside the normal operating conditions," *IEEE Industry Applications Magazine*, vol. 21, no. 6, pp. 47-56, 2015.

[102] S. Noda, S. Mizuno, T. Koyama, and S. Shiraishi, "Development of a totally enclosed fan cooled traction motor," in *2010 IEEE Energy Conversion Congress and Exposition*, 2010, pp. 272-277.

[103] X. Yang, A. Fatemi, T. Nehl, L. Hao, W. Zeng, and S. Parrish, "Comparative study of three stator cooling jackets for electric machine of mild hybrid vehicle," in *2019 IEEE International Electric Machines & Drives Conference (IEMDC)*, 2019, pp. 1202-1209.

[104] S. I. Yoshinori Sato, Takahito Okubo,Makoto Abe,Katsunori Tamai, "Development of high response motor and inverter system for the Nissan LEAF electric vehicle," *SAE international*, vol. no. pp. 2011.

[105] M. Schiefer and M. Doppelbauer, "Indirect slot cooling for high-power-density machines with concentrated winding," in *2015 IEEE International Electric Machines & Drives Conference (IEMDC)*, 2015, pp. 1820-1825.

[106] S. A. Semidey and J. R. Mayor, "Experimentation of an electric machine technology demonstrator incorporating direct winding heat exchangers," *IEEE Trans. Ind. Electron.*, vol. 61, no. 10, pp. 5771-5778, 2014.

[107] P. Lindh, I. Petrov, A. Jaatinen-Värri, A. Grönman, M. Martinez-Iturralde, M. Satrústegui, *et al.*, "Direct liquid cooling method verified with an axial-flux permanent-magnet traction machine prototype," *IEEE Trans. Ind. Electron.*, vol. 64, no. 8, pp. 6086-6095, 2017.

[108] C. Liu, Z. Xu, D. Gerada, J. Li, C. Gerada, Y. C. Chong, *et al.*, "Experimental investigation on oil spray cooling with hairpin windings," *IEEE Trans. Ind. Electron.*, vol. no. pp. 1-1, Sep. 2019.

[109] Y. Gai, M. Kimiabeigi, Y. C. Chong, J. D. Widmer, J. Goss, U. SanAndres, *et al.*, "On the measurement and modeling of the heat transfer coefficient of a hollow-shaft rotary cooling system for a traction motor," *IEEE Trans. Ind. Appl.*, vol. 54, no. 6, pp. 5978-5987, 2018.

[110] Y. Gai, M. Kimiabeigi, Y. C. Chong, J. Goss, M. C. Kulan, J. D. Widmer, *et al.*, "Pressure loss modelling in a water-cooled hollow-shaft rotor for an automotive traction motor," in *2018 XIII International Conference on Electrical Machines (ICEM)*, 2018, pp. 1297-1302.

[111] Y. Gai, J. D. Widmer, A. Steven, Y. C. Chong, M. Kimiabeigi, J. Goss, *et al.*, "Numerical and experimental calculation of CHTC in an oil-based shaft cooling system for a high-speed high-power PMSM," *IEEE Trans. Ind. Electron.*, vol. 67, no. 6, pp. 4371-4380, 2020.

[112] Y. Gai, Y. C. Chong, H. Adam, J. Goss, and M. Popescu, "Power losses and thermal analysis of a hollow-shaft rotor cooling system," in *2019 22nd International Conference on Electrical Machines and Systems (ICEMS)*, 2019, pp. 1-6.

[113] Y. Li, Z. Q. Zhu, and G. J. Li, "Influence of stator topologies on average torque and torque ripple of fractional-slot SPM machines with fully closed slots," *IEEE Trans. Ind. Appl.*, vol. 54, no. 3, pp. 2151-2164, Jan. 2018.

[114] C. Hwang, S. Hung, C. Liu, and S. Cheng, "Optimal design of a high speed SPM motor for machine tool applications," *IEEE Trans. Magn.*, vol. 50, no. 1, pp. 1-4, Dec. 2014.

[115] Z. Q. Zhu, Z. P. Xia, Y. F. Shi, D. Howe, A. Pride, and X. J. Chen, "Performance of Halbach magnetized brushless ac motors," *IEEE Trans. Magn.*, vol. 39, no. 5, pp. 2992-2994, Sep. 2003.

[116] A. Vagati, G. Pellegrino, and P. Guglielmi, "Comparison between SPM and IPM motor drives for EV application," in *International Conference on Electrical Machines (ICEM)*, 2010, pp. 1-6.

[117] P. Zhang, D. M. Ionel, and N. A. O. Demerdash, "Saliency ratio and power factor of IPM motors with distributed windings optimally designed for high efficiency and low-cost applications," *IEEE Trans. Ind. Appl.*, vol. 52, no. 6, pp. 4730-4739, Nov. 2016.

[118] S. U. Chung, H. J. Lee, B. C. Woo, J. W. Kim, J. Y. Lee, S. R. Moon, *et al.*, "A feasibility study on a new doubly salient permanent magnet linear synchronous machine," *IEEE Trans. Magn.*, vol. 46, no. 6, pp. 1572-1575, Jun. 2010.

[119] K. I. Laskaris and A. G. Kladas, "Internal permanent magnet motor design for electric vehicle drive," *IEEE Trans. Ind. Electron.*, vol. 57, no. 1, pp. 138-145, Jan. 2010.

[120] A. M. E.-. Refaie, "Fractional-slot concentrated-windings synchronous permanent magnet machines: opportunities and challenges," *IEEE Trans. Ind. Electron.*, vol. 57, no. 1, pp. 107-121, Jan. 2010.

[121] Z. Q. Zhu and D. Howe, "Influence of design parameters on cogging torque in permanent magnet machines," *IEEE Trans. Energy Convers.*, vol. 15, no. 4, pp. 407-412, Dec. 2000.

[122] D. M. Ionel, M. Popescu, M. I. McGilp, T. J. E. Miller, S. J. Dellinger, and R. J. Heideman, "Computation of core losses in electrical machines using improved models for laminated steel," *IEEE Trans. Ind. Appl.*, vol. 43, no. 6, pp. 1554-1564, Nov. 2007.

[123] G. Bertotti, "General properties of power losses in soft ferromagnetic materials," *IEEE Trans. Magn.*, vol. 24, no. 1, pp. 621-630, Jan. 1988.

[124] S. Steentjes, S. Boehmer, and K. Hameyer, "Permanent magnet eddy-current Losses in 2-D FEM simulations of electrical machines," *IEEE Trans. Magn.*, vol. 51, no. 3, pp. 1-4, May 2015.

[125] G. Qi, J. T. Chen, Z. Q. Zhu, D. Howe, L. B. Zhou, and C. L. Gu, "Influence of skew and cross-coupling on flux-weakening performance of permanent-magnet brushless AC machines," *IEEE Trans. Magn.*, vol. 45, no. 5, pp. 2110-2117, May 2009.

[126] Y. Hu, S. Zhu, and C. Liu, "Magnet eddy-current loss analysis of interior PM machines for electric vehicle application," *IEEE Trans. Magn.*, vol. 53, no. 11, pp. 1-4, May 2017.

[127] Z. Q. Zhu and D. Howe, "Electrical machines and drives for electric, hybrid, and fuel cell vehicles," *Proceedings of the IEEE*, vol. 95, no. 4, pp. 746-765, Apr. 2007.

[128] Z. Q. Zhu, "A simple method for measuring cogging torque in permanent magnet machines," in *2009 IEEE Power & Energy Society General Meeting*, 2009, pp. 1-4.

[129] Z. Q. Zhu and D. Wu, "On-load voltage distortion in fractional-slot interior permanent magnet machines," *IEEE Trans. Magn.*, vol. 51, no. 10, pp. 1-9, Oct. 2015.

[130] K. T. Chau, C. C. Chan, and C. Liu, "Overview of permanent-magnet brushless drives for electric and hybrid electric vehicles," *IEEE Trans. Ind. Electron.*, vol. 55, no. 6, pp. 2246-2257, Jun. 2008.

[131] S. Jianxin, W. Canfei, M. Dongmin, J. Mengjia, S. Dan, and W. Yunchong, "Analysis and optimization of a modular stator core with segmental teeth and solid back iron for pm electric machines," in *IEEE International Electric Machines & Drives Conference (IEMDC)*, 15-18 May, 2011, pp. 1270-1275.

[132] B. Ren, G. Li, Z. Zhu, M. Foster, and D. Stone, "Performance comparison between consequent-pole and inset modular permanent magnet machines," *The Journal of Engineering*, vol. 2019, no. 17, pp. 3951-3955, Jun. 2019.

[133] S. Cai, Z. Q. Zhu, C. Wang, J. C. Mipo, and S. Personnaz, "A novel fractional slot non-overlapping winding hybrid excited machine with consequent-pole PM rotor," *IEEE Trans. Energy Convers.*, vol. no. pp. 1-1, 2020.

[134] Y. Wang, Z. Q. Zhu, J. Feng, S. Guo, Y. F. Li, and Y. Wang, "Investigation of unbalanced magnetic force in fractional-slot PM machines having an odd number of stator slots," *IEEE Trans. Energy Convers.*, vol. no. pp. 1-1, May 2020.

[135] N. Zhao, R. Yang, N. Schofield, and R. Gu, "Investigation of DC-link voltage and temperature variations on EV traction system design," *IEEE Trans. Ind. Appl.*, vol. 53, no. 4, pp. 3707-3718, Jul. 2017.

[136] A. Tüysüz, F. Meyer, M. Steichen, C. Zwyssig, and J. W. Kolar, "Advanced cooling methods for high-speed electrical machines," *IEEE Trans. Ind. Appl.*, vol. 53, no. 3, pp. 2077-2087, May 2017.

[137] W. Tong, R. Tang, Z. An, and Q. Shen, "Water cooling system design and thermal analysis for low speed permanent magnet machines," in *2011 IEEE International Conference on Electrical Machines and Systems (ICEMS)*, 2011, pp. 1-4.

[138] L. Ye, F. Tao, W. Xuhui, and L. Yong, "Numerical research on hydraulic and thermal performance of the motor water jackets based on the orthogonal experiment," in *2013 IEEE International Conference on Electrical Machines and Systems (ICEMS)*, 2013, pp. 860-863.

[139] D. P. Kulkarni, G. Rupertus, and E. Chen, "Experimental investigation of contact resistance for water cooled jacket for electric motors and generators," *IEEE Trans. Energy Convers.*, vol. 27, no. 1, pp. 204-210, May 2012.

[140] P. Liang, F. Chai, K. Shen, and W. Liu, "Thermal design and optimization of a water-cooling permanent magnet synchronous in-wheel motor," in *2019 IEEE International Conference on Electrical Machines and Systems (ICEMS)*, 2019, pp. 1-6.

[141] B. Zhang, R. Qu, X. Fan, and J. Wang, "Thermal and mechanical optimization of water jacket of permanent magnet synchronous machines for EV application," in *2015 IEEE International Electric Machines & Drives Conference (IEMDC)*, 2015, pp. 1329-1335.

[142] R. Vlach, R. Grepl, and P. Krejci, "Control of Stator Winding Slot Cooling by Water Using Prediction of Heating," in *2007 IEEE International Conference on Mechatronics*, 2007, pp. 1-5.

[143] N. A. Rahman, E. Bostanci, and B. Fahimi, "Thermal analysis of switched reluctance motor with direct in-winding cooling system," in *2016 IEEE Conference on Electromagnetic Field Computation (CEFC)*, 2016, pp. 1-1.

[144] M. Diana, J. Colussi, A. L. Ganga, and P. Guglielmi, "An innovative slot cooling for integrated electric drives," in *2019 IEEE Workshop on Electrical Machines Design, Control and Diagnosis (WEMDCD)*, 2019, pp. 191-196.

[145] B. Assaad, K. Mikati, T. V. Tran, and E. Negre, "Experimental Study of Oil Cooled Induction Motor for Hybrid and Electric Vehicles," in *2018 XIII International Conference on Electrical Machines (ICEM)*, 2018, pp. 1195-1200.

[146] L. Ye, F. Tao, L. Qi, and W. Xuhui, "Experimental investigation on heat transfer of directly-oil-cooled permanent magnet motor," in *2016 19th International Conference on Electrical Machines and Systems (ICEMS)*, 2016, pp. 1-4.

[147] Y. J. Wei Chen, Dong Yan, Liyan Guo, Qiang Geng, Tingna Shi, "Design and optimization of dual-cycled cooling structure for fully-enclosed permanent magnet motor," *Applied Thermal Engineering*, vol. 152, no. 10, pp. 338-349, Feb. 2019.

[148] P. H. Connor, A. L. Rocca, Z. Xu, M. Degano, C. N. Eastwick, S. J. Pickering, *et al.*, "Air-cooling of a hollow high-speed permanent magnet rotor," in *2019 IEEE International Electric Machines & Drives Conference (IEMDC)*, 2019, pp. 1216-1221.

[149] X. Fan, R. Qu, J. Li, D. Li, B. Zhang, and C. Wang, "Ventilation and thermal improvement of radial forced air-cooled FSCW permanent magnet synchronous wind generators," *IEEE Trans. Ind. Appl.*, vol. 53, no. 4, pp. 3447-3456, Mar. 2017.

[150] Y. Gai, M. Kimiabeigi, Y. C. Chong, J. D. Widmer, X. Deng, M. Popescu, *et al.*, "Cooling of automotive traction motors: schemes, examples, and computation methods," *IEEE Trans. Ind. Electron.*, vol. 66, no. 3, pp. 1681-1692, Mar. 2019.

[151] G. Li, "Contribution à la Conception des Machines Electriques à Rotor Passif pour des Applications Critiques: Modélisations Electromagnétiques et Thermiques sur Cycle de Fonctionnement, Etude du Fonctionnement en Mode Dégradé," *PhD Thesis*, vol. no. pp. 2011.

[152] A. Boglietti, A. Cavagnino, and D. Staton, "Determination of critical parameters in electrical machine thermal models," *IEEE Trans. Ind. Appl.*, vol. 44, no. 4, pp. 1150-1159, Jul. 2008.

[153] M. Markovic, L. Saunders, and Y. Perriard, "Determination of the thermal convection coefficient for a small electric motor," in *Conference Record of the 2006 IEEE Industry Applications Conference Forty-First IAS Annual Meeting*, 2006, pp. 58-61.

[154] D. Liang, Z. Q. Zhu, J. H. Feng, S. Y. Guo, Y. F. Li, J. Q. Wu, *et al.*, "Influence of critical parameters in lumped-parameter thermal models for electrical machines," in *2019 22nd International Conference on Electrical Machines and Systems (ICEMS)*, 2019, pp. 1-6.

[155] W.-R. Canders, J. Hoffmann, and M. Henke, "Cooling Technologies for High Power Density Electrical Machines for Aviation Applications," *Energies*, vol. 12, no. 23, pp. 4579, 2019.

[156] P. L. Stephenson, "An experimental study of the pressure drop in generator rotor cooling ducts," in *1989 IEEE International Electric Machines & Drives Conference (IEMDC)*, 1989, pp. 154-158.

[157] Z. Xu, A. L. Rocca, P. Arumugam, S. J. Pickering, C. Gerada, S. Bozhko, *et al.*, "A semi-flooded cooling for a high speed machine: Concept, design and practice

of an oil sleeve," in *IECON 2017 - 43rd Annual Conference of the IEEE Industrial Electronics Society*, 2017, pp. 8557-8562.